Notion of representative volume element for heterogeneous materials: statistical and numerical approach

Toufik Kanit

ECOLE DES MINES
DE PARIS

Collège Doctoral

N° attribué par la bibliothèque
/__/__/__/__/__/__/__/__/__/__/

THESE

Pour obtenir le grade de
Docteur de l'Ecole Nationale Supérieure des Mines de Paris
Spécialité Mécanique Numérique

Présentée et soutenue publiquement par

Toufik KANIT

le 12 mai 2003

Notion de Volume Elémentaire Représentatif pour les Matériaux Hétérogènes : Approche Statistique et Numérique

Directeurs de thèse : ***Dominique JEULIN***
Samuel FOREST

Jury

M. P. PILVIN	Rapporteur	Université de Bretagne-Sud IUP-LG2M, France
M. K. SAB	Rapporteur	Ecole Nationale des Ponts et Chaussées, France
M. M. OSTOJA-STARZEWSKI	Examinateur	Mc-Gill University, Montreal, Canada
M. S. SINGLETON	Examinateur	Unilever, Grande Bretagne
M. M. REED	Invité	Unilever, Grande Bretagne
Mme V. MOUNOURY	Invitée	Ecole des Mines de Paris, France
M. D. JEULIN	Examinateur	ISTASE-Université Jean Monnet, France
M. S. FOREST	Examinateur	Ecole des Mines de Paris, France

Centre des Matériaux P.M. FOURT de l'Ecole des Mines de Paris,
B.P. 87, 91003 EVRY Cedex

ECOLE DES MINES
DE PARIS

Doctoral College

N° given by the library
/__/__/__/__/__/__/__/__/__/__/

PhD THESIS

To obtain the grade of
Doctor of Ecole Nationale Supérieure des Mines de Paris
Speciality Computational Mechanics

Presented by

Toufik KANIT

the May 12th, 2003

Notion of Representative Volume Element for Heterogeneous Materials : Statistical and Numerical Approach

PhD Advisors : ***Dominique JEULIN***
Samuel FOREST

Jury

M. P. PILVIN	Referee	Université de Bretagne-Sud IUP-LG2M, France
M. K. SAB	Referee	Ecole Nationale des Ponts et Chaussées, France
M. M. OSTOJA-STARZEWSKI	Examinator	Mc-Gill University, Montreal, Canada
M. S. SINGLETON	Examinator	Unilever, United Kingdom
M. M. REED	Invited member	Unilever, United Kingdom
Mme V. MOUNOURY	Invited member	Ecole des Mines de Paris, France
M. D. JEULIN	Examinator	ISTASE - Université Jean Monnet, France
M. S. FOREST	Examinator	Ecole des Mines de Paris, France

Centre des Matériaux P.M. FOURT de l'Ecole des Mines de Paris,
B.P. 87, 91003 EVRY Cedex

Remerciements

Je souhaiterais d'abord remercier chaleureusement Monsieur Jean-Pierre Trottier, Directeur du Centre des Matériaux de l'Ecole des Mines de Paris, pour m'avoir accepté dans son laboratoire et pour la confiance qu'il a su me témoigner.

Je voudrais exprimer ma gratitude à Monsieur Karam Sab et à Monsieur Philipe Pilvin pour avoir accepté de rapporter sur le manuscrit, leur présence parmi les membres de jury m'a fait un grand plaisir.

Je tiens également à remercier Monsieur Martin Ostoja-Starzewski pour avoir présidé le jury de soutenance et pour l'intérêt qu'il a porté à ce travail et pour ces remarques pertinentes.

Special thanks are due to Mr. Scott Singleton and Mr. Mattew Reed of Unilever for the very stimulating scientific and industrial atmosphere during my PhD, and for accepting to take part in the jury.

Je ne saurais exprimer ma reconnaissance à mes chers encadreurs : Monsieur Dominique Jeulin, Monsieur Samuel Forest et Madame Valérie Mounoury qui m'ont supporté et suivi tout au long de ces trois années de recherche, ainsi qu'à notre chef de groupe Georges Cailletaud.

Un grand merci à Franck N'Guyen qui a encadré la partie analyse d'images des travaux de ma thèse, pour notamment son esprit chaleureux et sa grande patience, merci infiniment Franck!

Je remercie également toutes les personnes que j'ai côtoyées : Francçoise, Sylvain, Thierry, Andrei, Kamel, Farida, Asmahana, Fouad, Fabrice, Olivier, ainsi que tous les chercheurs, enseignants et administratif, et notamment Frédéric Feyel, Stéphane Quilici et Isabelle Galliet.

Je réserve un remerciement tout spécial à ma femme *Radia* qui m'a supporté tout au long des derniers moments et je lui transmets tout l'amour du monde.

Résumé

Le Volume Elémentaire Représentatif (VER) joue un rôle important dans la mécanique et la physique des milieux hétérogènes aléatoires dans le but de déterminer leurs propriétés effectives. Une définition quantitative de la taille du VER est proposée dans ce travail en utilisant une approche numérique et statistique. La taille du VER peut être associée à une précision donnée sur l'estimation de la propriété macroscopique recherchée et à un nombre de réalisations d'un volume donné V de la microstructure. Cette taille dépend de la propriété morphologique ou physique étudiée, du contraste dans les propriétés des constituants et de leur fraction volumique. La méthodologie est développée sur une microstructure aléatoire bi-phasée spécifique, à savoir les mosaïques de Voronoï en $3D$. Elle est appliquée ensuite à un matériau bi-phasé issu de l'industrie agro-alimentaire. Des simulations par la méthode des éléments finis à grand nombre de degrés de liberté sur des volumes de tailles différentes sont faites dans le cas de l'élasticité linéaire et la conductivité thermique. Les volumes sont simulés avec différentes conditions aux limites : déformations homogènes au contour, contraintes homogènes au contour et des conditions aux limites périodiques. Les propriétés effectives peuvent être déterminées sur des gros volumes et un faible nombre de réalisations. D'autre part, il est possible d'utiliser des petits volumes à condition d'avoir un nombre suffisant de réalisations. Un *biais* dans l'estimation des propriétés effectives a été remarqué pour les volumes qui sont trop faibles quelles que soient les conditions aux limites. La variance des propriétés apparentes pour chaque taille de volume est utilisée pour définir la précision de l'estimation. La notion-clé de *portée intégrale* est introduite pour relier l'erreur de l'estimation à la définition de la taille du VER. Pour une précision et un nombre de réalisations donnés, il est possible de donner une taille minimale des volumes à utiliser pour le calcul des propriétés effectives. Les résultats peuvent être aussi utilisés pour trouver le nombre minimal de réalisations à considérer pour une taille donnée de volume pour estimer la propriété effective avec une précision donnée. Les tailles du VER trouvées pour les modules élastiques, la conductivité thermique et la fraction volumique sont comparées. Une comparaison générale des propriétés élastiques et thermiques est présentée pour trois types de microstructures, les mosaïques de Voronoï, un exemple de matériau issu de l'industrie agro-alimentaire et un autre modèle booléen de microstructures à base de prismes hexagonaux. Ce travail peut être vu comme une introduction aux approches de design de microstructures qui ont des propriétés macroscopiques souhaitées. L'objectif est d'explorer des morphologies nouvelles succeptibles de conduire à des propriétés de rigidité ou conductivité exceptionnelles, ou toute autre propriété à contrôler.

Abstract

The Representative Volume Element (RVE) plays a central role in the mechanics and physics of random heterogeneous materials with a view to predicting their effective properties. A quantitative definition of its size is proposed in this work using a numerical and statistical approach. A RVE size can be associated with a given precision of the estimation of the wanted overall property and the number of realizations of a given volume V of microstructure that one is able to consider. It is shown to depend on the investigated morphological or physical property, the contrast in the properties of the constituents, and their volume fractions. The methodology is developed on a specific random microstructure, namely a two–phase three–dimensional Voronoï mosaic and applied to a real two-phase heterogeneous material from food industry. Large scale finite element simulations of volumes of different sizes are performed in the case of linear elasticity (thermal conductivity respectively), using parallel computing. The volumes are subjected to homogeneous strain (gradient of temperature respectively), stress (heat flux respectively) at the boundary or periodic boundary conditions. The effective properties can be determined for large volumes and a small number of realizations. Conversely, smaller volumes can be used providing that a sufficient number of realizations is considered. A *bias* in the estimation of the effective properties is observed for too small volumes for all types of boundary conditions. The variance of computed apparent properties for each volume size is used to define the precision of the estimation. The key–notion of *integral range* is introduced to relate this error estimation and the definition of the RVE size. For given precision and number of realizations, one is able to provide a minimal volume size for the computation of effective properties. The results can also be used to predict the minimal number of realizations that must be considered for a given volume size in order to estimate the effective property for a given precision. The RVE sizes found for elastic and thermal properties, but also for a geometrical property like volume fraction, are compared. A general comparison of the elastic and thermal properties of three different microstructures is given, Voronoï mosaics, real material from food industry and another virtual model, a boolean model of hexagonal prismatic rods and plates. Computation homogenization technique is used to predict the effective properties from $3D$ confocal images of real samples. An analysis of the percolation strain fields in deformed samples is proposed to select stiffer or higher conductive products. The present work can be regarded as a first step towards a computational approach of the design of microstructures for wanted overall properties. The aim is to explore new morphologies that can lead to unexpected properties like outstanding stiffness or conductivity, or controlled compliance.

Contents

List of Figures

List of Tables

Introduction

The mechanical behavior of multi-phase materials is of considerable economic importance. A better understanding of the mechanics of multi-phase materials will allow these materials to be used in an optimal manner. The objective of the mechanics of heterogeneous materials is to estimate the macroscopic properties of an equivalent homogeneous material. In the case of the random materials, the evaluation of these properties from the properties of the constituents has reached a high level of precision. One of the first systematic works in this domain are due to Hill (Hill, 1952).

Important progress in the way of substituting a homogenized medium to a heterogeneous material was made with the mathematical theory of homogenization (Beran, 1968), (Sanchez-Palencia, 1974), (Bensoussan et al., 1978) and (Sanchez-Palencia, 1980). Since these pioneering studies, the method has been extended to plastic materials (Suquet, 1983) and (Bouchitte and Suquet, 1991). Some of the arguments developed for homogenization were general and found applications in other fields. These works spawned a large body of numerical studies (Bourgat, 1977), (Marigo et al., 1987), (Bendsoe and Kikuchi, 1988), (Devries et al., 1989) and (Guedes and Kikuchi, 1990) which were developed independently from earlier micromechanical studies. Several theoretical formulae have been proposed that are relevant for interpenetrating phases in heterogeneous media. For example, effective medium theories (Hashin, 1983) were developed to extend exact results for dilute inclusions to higher volume fractions. Certain microstructures were shown (Milton, 1984) to have properties that coincide with exact theoretical results, but the proposed microstructures are physically very unusual. A different class of theories is rigorously based on realistic microstructural information. These are the classic variational bounds (Milton and Phan-Thien, 1982), which only provide an upper bound for porous media, and the recent expansions of Torquato (Torquato, 1998). The microstructural information needed to evaluate the results is quite difficult to obtain, so in practice the bounds and expansions are evaluated only up to third-order. Even with limited information, the upper bounds and expansions are thought to give good predictions for dispersions (Torquato, 1991), (Torquato, 1998). The accuracy of these theories is difficult to determine for a real double-percolating heterogeneous medium. This uncertainty has limited the application of these results. However, effective medium theories are commonly used, and the rigorous theories

are attractive because of their relative simplicity. Modeling a composite and estimating numerically its macroscopic properties is a complex procedure. This could be avoided if accurate analytical structure-property relations could be theoretically or empirically obtained. Many studies have focused on this problem (Hashin, 1983). In general the results are reasonable for a particular class of composites or porous media. The self-consistent (or effective medium) method of Hill (Hill, 1965) and Budiansky (Budiansky, 1965) and its generalization by Christensen and Lo (Christensen and Lo, 1979) is one of the most common for particulate media (Hashin, 1983).

Further techniques for bounding overall properties are elaborated then in (Paul, 1960), (Hashin and Shtrikman, 1963), (Hill, 1963), (Walpole, 1966), (Kröner, 1972), (Kröner, 1977), (Willis, 1981), (Willis and Talbot, 1989), (Nemat-Nasser and Hori, 1993). Such bounds depend only on the relative volume fractions and do not reflect any particular geometry. When one phase is a dispersion of ellipsoidal inclusions, a much more direct approach is available. This is the self-consistent method of Hershey (Hershey, 1954) and (Kröner, 1958). Originally proposed for aggregates of crystals, it has been reviewed and elaborated by Hill (Hill, 1965). More precise bounds (second order and third order) were developed later. Third order bounds, in the case of random media, were obtained in the general case by Beran (Beran, 1968) and for models of random function (Jeulin, 1998), and later for two-phase materials by Miller (Miller, 1969), Milton (Milton, 1982) and Jeulin (Jeulin and Savary, 1997). On the other hand more theories were developed for the linear properties of random materials like the systematic theory of Kröner (Kröner, 1980) and in many other works (Torquato and Stell, 1983), (Torquato and Lado, 1986), (Torquato, 1991) and (Sab, 1992). Other alternative to direct property prediction has been the development of analytical rigorous bounds (reviewed by Willis (Willis, 1981), Hashin (Hashin, 1983) and Torquato (Torquato, 1991). There is a whole hierarchy of these bounds, each set tighter than the next, but depending on higher order correlation functions of the microstructure. The original Hashin and Shtrikman (Hashin and Shtrikman, 1963) bounds that have been widely used by experimentalists implicitly depend on the two-point correlation function of the microstructure, although the only quantities appearing in the formulae are the individual properties of each phase and their volume fraction. To go beyond these bounds to higher-order, more restrictive bounds, it is necessary that detailed information be known about the composite in the form of three-point or higher statistical correlation functions (Beran and Molyneux, 1966); (Milton and Phan-Thien, 1982), which do appear explicitly in the relevant formulae. Evaluation of even the three-point function is a formidable task, so use of these bounds has in the past been restricted to composites with spherical inclusions. It is now possible to evaluate the bounds for non-particulate composites (Roberts and Teubner, 1995), and it is interesting to compare the results with experimental and numerical data. If the properties of each phase are not too dissimilar the bounds are quite restrictive and can be used for predictive purposes (Hashin and Shtrikman, 1963). Sometimes experimental properties closely follow one or the other of the bounds, so that the upper or lower bound often provides a reasonable prediction of the actual property even when the

phases have very different properties (Torquato, 1991); (Roberts and Knackstedt, 1995).

Computational homogenization is a practical tool to estimate effective properties from simulations on samples of heterogeneous materials. Important works were made for the effective mechanical moduli in different cases of boundary conditions (uniform static, kinematic and mixed loading). Especially in (Huet, 1990) and (Hazanov and Huet, 1994), where it is shown that overall properties given by mixed boundary conditions are between the static and kinematic ones. In the nonlinear behavior, an example of study of the size effects on the intragranular behavior, is given in (Quilici et al., 1998), by the simulation of torsion in multicrystals. Other studies in the homogenization of polycrystalline aggregates are given in (Forest et al., 2000), (Barbe et al., 2001a), (Barbe et al., 2001b) and in (Gusev, 1997) for the case of periodic media. Some works developed numerical methods based on models of random structures. Ghosh (Ghosh and Moorthey, 1995) developed a finite element method based on the Voronoï cells. The homogenization of heterogeneous media in which the constituents were fluids is also studied, an example being given in (Terada et al., 1998).

Computational homogenization requires a proper determination of the typical size of a socalled *Representative Volume Element* (RVE). From such a volume we can determine the overall macroscopic properties of the heterogeneous material. Two different definitions of the RVE are used in the mechanics of heterogeneous materials. The first one can be derived from the principle that in order to characterize the macroscopic constitutive response of a composite, one must know the statistical nature of the microstructure of actual composites. This principle leads to the conclusion that the RVE for which an effective constitutive theory could apply is one that is sufficiently large to be statistically representative of the composite, that is, to effectively include a sampling of all microstructural heterogeneities that occur in the composite. This is generally the principle adopted, and it leads to the fact that the RVE must include a large number of the composite microheterogeneities (grains, inclusions, voids, fibers, etc.). The response of the RVE must be independent of the boundary conditions, and its size is given for a specific effective property. A more accurate definition of the RVE, which is used later in this work, is based on a statistical definition : the RVE must ensure a given accuracy to the estimated property obtained by spatial averaging of the stress, the strain, or the energy fields in a given domain. Another definition of the RVE is given by Drugan and Willis in (Drugan and Willis, 1996) : *It is the smallest material volume element of the composite for which the usual spatially constant (overall modulus) macroscopic constitutive representation is a sufficiently accurate model to represent mean constitutive response*. They studied the smallest volume size for a two-phase composite with an isotropic matrix and isotropic spherical inclusions by comparing the local and the nonlocal parts of effective constitutive equations. They mentioned that, with a maximum error of 5% of the overall modulus, the RVE size is twice the inclusion diameter at most for any reinforcement concentration level, for many sets of matrix and inclusion moduli characterizing large classes of structural composites. In contrast to the

large RVE sizes deduced from the statistical principle given in the first definition, the estimates of RVE size for the definition adopted in (Drugan and Willis, 1996) are much smaller. In the present work we show that this definition is not sufficient. The overall moduli obtained by averaging over small domains inside a composite, using a sufficient number of realizations for each of the studied boundary conditions, is not the same, in general, as that obtained by a sufficiently large size of the RVE.

In many practical cases, knowledge of microscopic fields, such as stress fields, strain fields, thermal fields, within mesoscale structural components are desired. However, difficulties arise in the numerical simulation of such problems, which has irregular fine scale heterogeneous microstructure. This is due to the fact that the spatial discretization mesh size must be smaller than the intrinsic micromechanical length scales for reasonable accuracy. This gives rise to large memory requirements to store the numerical systems. Alternatively, the use of smaller volumes of heterogeneous material must be compensated by averaging over several realizations of the microstructure to get the same accuracy, provided no bias is introduced in the estimation by some edge effect generated from the boundary conditions. This is illustrated at several places in this work.

Direct numerical computations using the finite element method have been developed for heterogeneous media with periodic microstructures (Adams and Doner, 1967), (Needleman, 1972) and opened the way to several studies. Recently, efforts have been made to study composites with more complex morphologies (Brockenborough et al., 1991), (Moulinec and Suquet, 1995) and (Moulinec and Suquet, 1997). There now exist large-scale computational methods for calculating the properties of composites given a digital representation of their microstructure; for example permeability in (Adler et al., 1990) and (Bentz and Martys, 1994), conductivity in (Adler et al., 1992) and (Roberts and Teubner, 1995) and elastic moduli (Garboczi and Day, 1995); (Poutet et al., 1996); (Meille and Garboczi, 2001).

For particular materials it may be possible to simulate microstructure formation from first principles. Generally this relies on the detailed knowledge of the physics and chemistry of the system, with accurate modeling of each material requiring a significant amount of research. Three-dimensional models have also been directly reconstructed from samples by combining digitized serial sections obtained by scanning electron microscopy (Kwiecien et al., 1990), or using the relatively new technique of X-ray microtomography (Flannery et al., 1987). In the absence of sophisticated experimental facilities for microstructure imaging, another alternative is to employ a statistical model of the microstructure. This method is named statistical reconstruction since the statistical properties of the model are matched to those of a two-dimensional image (Quiblier, 1984); (Adler et al., 1992); (Bentz and Martys, 1994); (Roberts, 1997). Statistical reconstruction is a promising approach of producting three-dimensional models, but there remain outstanding theoretical and numerical questions regarding its application. The simulation of finite size heterogeneous material samples provides only apparent properties that do not necessary

coincide with the wanted effective ones.

In (Huet, 1990), Huet showed that the apparent modulus tensor of a sub-volume of the material body subject to boundary tractions associated with a uniform stress tensor or boundary displacements associated with a uniform strain tensor on the boundary of the sub-volume overestimates or underestimates the effective modulus tensor, respectively. These two types of apparent moduli depend on the size of sub-volumes. They approach the effective moduli as the sub-volume size increases. Similar results have been reported by other authors, (Nemat-Nasser and Hori, 1993) and (Pecullan et al., 1998). Huet used then the above concept to define the minimum RVE size (Hazanov and Huet, 1994), without giving a quantitative estimate. Similar problems were studied by Ostoja-Starzewski in (Ostoja-Starzewski, 1993), (Ostoja-Starzewski, 1996) and (Ostoja-Starzewski, 1998).

The present work aims at studying the representativity of the measurements obtained from a limited domain of the random linear elastic two-phase heterogeneous material (the hard phase is named P_1, the soft one is P_2), and to precise the statistical definition of the Representative Volume Element. These measurements of the specimen concern the morphology (volume fraction), and the effective physical properties (elastic moduli and thermal conductivity). In this work, the notion of integral range is associated with the notion of the RVE. To define it, we use the curves of variance of the volume fraction, the elastic moduli : bulk modulus k and shear modulus μ and the thermal conductivity λ obtained in windows of increasing sizes. This is applied to a model of random medium, the Voronoï mosaics (Matheron, 1968), (Miller, 1969), (Jeulin, 1987) and (Jeulin, 1991). The Voronoï mosaic model is a good candidate to generate random media, for geometrical considerations, since it provides planar boundaries separating grains. To generate such microstructures, an original method is used with numerous extensions of the classical model (Decker and Jeulin, 2000). Its main advantages, as compared to standard procedures, is to be able to generate textures with a very large number of grains, at a low computational cost.

The theoretical and numerical results of this work are applied to a two-phase material from food industry. Applying a material science approach to the characterization of material of the food industry requires consideration of its constituents on a microstructural level. Any change in this material formulation or processing parameters gives rise to different microstructures, which in turn dictate both the mechanical and sensory properties. Hence, via materials science, relationships may be established between the microstructure of this material, and physical properties or the sensory attributes. These data may then be used as a predictive tool for the development of new microstructures that satisfy predetermined sensory criteria. This work (especially chapter 2) is part of a wider study that aims at linking physical properties of a given material to its microstructure.

In the first chapter, after a brief reminder on the homogenization theory and of the covariance of random media, to introduce the notion of integral range, we

present the principle of construction of the Voronoï mosaics, and some numerical parameters used later in the finite element method to simulate the elastic and thermal behavior of a two-phase material based on the Voronoï mosaic. We mainly study the effect of the contrast and of the mesh density on the results of the homogenization.

From the curves of variance of the apparent properties, the volume fraction, the elastic moduli and the thermal conductivity, the values of the integral ranges are determined. A statistical approach is used to determine the size of the RVE. It consists in using a sufficient number of realizations on smaller volumes, and to avoid the bias of apparent properties observed in windows with a too small size.

In the second chapter, a more detailed application of the numerical and statistical approach is proposed for a real heterogeneous material. $3D$ real images are obtained from confocal microscopy and directly simulated by the finite element method to estimate the effective linear elastic properties and the effective thermal conductivity. The mixture of the heterogeneous material is considered as a two-phase linear elastic material, with a hard and highly conductive phase P_1 with volume fraction around 70%, and another soft phase and less conductive named P_2 with volume fraction 30%. Two different microstructures of this material have been studied that have equal volume fractions and different morphologies with three different samples of each type. The direct computation of elastic matrices of each sample shows some anisotropy in these matrices because of the insufficient size of these samples.

That is why we applied our approach, developed in the first chapter and in (Kanit et al., 2003a), (Kanit et al., 2002), to estimate sizes for the RVE of the real material. One sample of each type of the material is studied. With the help of values of the integral ranges found with the numerical simulations we give the necessary sizes of the RVE for each sample and for each physical property. All the Huet's results, concerning relationships existing between the apparent physical properties obtained on smaller samples than the RVE and the effective properties of the heterogeneous material (Huet, 1990), (Huet, 1991), will be tested with two different methods of decomposition into smaller volumes : regular and random in the case of our real material and Voronoï mosaics.

An introduction to percolation phenomena in microstructures is given. Two types of percolation phenomena are studied, the geometrical percolation and the mechanical percolation of the local strain fields to try to explain the different behaviors observed in the studied real microstructures.

In the last chapter we proposed another model of virtual microstructures. This model is constructed with hexagonal prismatic rods and plates with volume fractions around 70% for the hard phase represented by hexagons. Direct computations of elastic moduli of these microstructures allow us to say that the used sizes are representative. A comparison between the three heterogeneous microstructures models is given as general conclusion. This illustrates the concept of design of microstruc-

tures using computational homogenization tools.

Chapter -I-

QUANTITATIVE ESTIMATION OF REPRESENTATIVE VOLUME ELEMENT SIZE FOR RANDOM MATERIALS : APPLICATION TO VORONOI MOSAICS

Contents

I.1 Introduction

One important goal of the mechanics and physics of heterogeneous materials is to derive their effective properties from the knowledge of the constitutive laws and spatial distribution of their components. Homogenization methods have been designed for this purpose. They have reached a high level of sophistication and efficiency, especially in the case of linear properties such as thermal conductivity or elasticity. They can be found in reference extended papers and textbooks like (Willis, 1981; Sanchez-Palencia and Zaoui, 1987; Nemat-Nasser and Hori, 1993) or, more recently, (Suquet, 1997; Ponte Castañeda and Suquet, 1998; Bornert et al., 2001), (Besson et al., 2001), (Jeulin and Ostoja-Starzewski, 2002), where extensions to nonlinear properties are also proposed.

On the one hand, rigorous bounds for the macroscopic linear properties of composites are available. They include the well–known Voigt and Reuss bounds that take only the volume fraction of the components into account. Hashin and Shtrikman's bounds incorporate the notion of isotropic distribution of phases (Hashin and Shtrikman, 1963). Third order bounds, in the case of random media, were obtained in the general case by (Beran, 1968), and later for two-phase materials by (Miller, 1969) and (Milton, 1982). The incorporation of more and more statistical information on the distribution of heterogeneities in random materials leads to a hierarchy of bounds, as suggested by the systematic theory of (Kröner, 1980), and also in (Torquato and Stell, 1983; Torquato and Lado, 1986; Torquato, 1991). Note that some of these bounds are optimal in the sense that specific morphologies can be designed that give exactly the value of the bound as effective property.

On the other hand, direct estimations of the wanted effective properties can be proposed. The Mori–Tanaka model for instance favors one phase as a matrix. In contrast, the self–consistent scheme, presented by (Beran, 1968) for thermal conductivity and by (Hershey, 1954) and (Kröner, 1958) for linear polycrystals, refers to a disordered distribution of phases. A geometrical construction given by (Milton, 1985) for two-phase composites is obtained by a multiscale stacking of spheres of every phase with the appropriate volume fractions; for this disordered morphology, and for the estimations of the self-consistent model, the role of every component is symmetric.

In all these theories, the proposed estimations are given for random composite media with an infinite extension, and can therefore be denoted as asymptotic estimates. A different way to solve homogenization problems is to use numerical techniques and simulations on samples of the microstructure. In that case, the

notion of Representative Volume Element (RVE) is of paramount importance. The RVE is usually regarded as a volume V of heterogeneous material that is sufficiently large to be statistically representative of the composite, i.e., to effectively include a sampling of all microstructural heterogeneities that occur in the composite. This is generally the principle adopted, and it leads to the fact that the RVE must include a large number of the composite micro-heterogeneities (grains, inclusions, voids, fibers, etc.). It must however remain small enough to be considered as a volume element of continuum mechanics. Several types of boundary conditions can be prescribed on V to impose a given mean strain or mean stress to the material element. As a matter of fact, the response of the RVE must be independent of the type of boundary conditions, as proved by (Sab, 1992). This also pleads for a rather large size of RVE.

Another definition of the RVE was recently proposed by (Drugan and Willis, 1996) : *"It is the smallest material volume element of the composite for which the usual spatially constant (overall modulus) macroscopic constitutive representation is a sufficiently accurate model to represent mean constitutive response"*. This approach uses the solution of the homogenization for an infinite medium, and does not consider statistical fluctuations of the effective properties over finite domains. In contrast to the large RVE sizes expected from the previous definitions, the estimates of RVE size found by (Drugan and Willis, 1996) turn out to be much smaller (a small number of fibers for disordered fiber composite for instance).

Numerical techniques can help determining a critical size of volume V and choosing among the previous conflicting definitions. Monte–Carlo simulations were used by (Gusev, 1997) to generate independent realizations of disordered distributions of spheres in a matrix. A few dozen of spheres were necessary to obtain small scatter in the averaged property. In (Forest et al., 2000), the stress–strain curves of polycrystalline wires in torsion were simulated as a function of the number of grains within the cross–section : about 30 grains in the cross–section were necessary to reach stationary responses. Other examples of convergence of overall properties as the unit cell size is increased can be found in (Povirk, 1994; Terada et al., 1998). In (Zeman and Sejnoha, 2001), the numerical simulations are combined with the use of statistical information like the two–point probability. In (Roberts and Garboczi, 2000), the finite element method is used to estimate the elastic properties for various models of porous ceramics. Statistical fluctuation is briefly investigated but not related to estimations of RVE sizes. Examples of microstructural dependence of Young's modulus and Poisson's ratio, computed via the finite element method, can be found in (Roberts and Garboczi, 1999), (Roberts and Garboczi, 2000), (Roberts and Garboczi, 2001), (Meille and Garboczi, 2001) and (Roberts and Garboczi, 2002).

For microstructures with a high contrast of properties, the bounds are too far apart to give a useful estimate of the effective properties. On the other hand, estimates like the self-consistent model can give a fair prediction but correspond to a very specific morphology of the components. For these reasons, we have to use

a numerical method. In the present work, computational homogenization methods are used to determine the effective properties of heterogeneous materials.

In some experiments but also in many simulations, large size volumes V cannot be handled, so that one has to work with apparent moduli obtained on volumes smaller than the RVE. This situation has been extensively studied by (Huet, 1990), (Huet, 1991) and (Hazanov and Huet, 1994). Bounding relations between apparent and effective properties are derived for several types of strain, stress or mixed boundary conditions.

The aim of the present chapter is to propose and illustrate a more quantitative definition of the RVE, which is based on statistical arguments : the RVE must ensure a given accuracy of the estimated property obtained by spatial averaging of the stress, the strain, or the energy fields in a given domain V. Alternatively, the use of smaller volumes v must be compensated by averaging over several realizations of the microstructure to get the same accuracy, provided no bias is introduced in the estimation by some edge effects generated by the boundary conditions. It will appear that the overall moduli obtained by averaging over small domains of composite material, using a sufficient number of realizations for each of the studied boundary conditions, is not the same, in general, as that obtained by a sufficiently large RVE. Note that, in general, the size of a RVE depends on the investigated morphological or physical property. For the same microstructure, it will be shown that the RVE size differs if thermal or elastic properties are considered. It makes sense also to define the notion of RVE for a morphological property like volume fraction. Again, it will appear that the corresponding size is different from that found for a physical property. The key–notion that will be used for a precise definition of the RVE is the *integral range* classically used in mathematical morphology and recalled in section I.3.2 in this chapter. The notion of integral range has already been used for the homogenization, by simulations, of the elastic properties of two-dimensional random composites, but without explicit reference to the notion of RVE in (Cailletaud et al., 1994).

The example of microstructure chosen in this chapter to illustrate the methodology of determination of RVE is a three–dimensional two–phase Voronoï mosaics. Three–dimensional Voronoï cells are simple representations of grains in a polycrystals and have been used in the past to study the elastoplastic behavior of polycrystals in (Forest et al., 2000; Barbe et al., 2001a) and (Barbe et al., 2001b). Here only two phases are considered with a high contrast of properties to enhance the variability of apparent properties on small volumes. Because of the high value of contrast in properties, large volume sizes V must be investigated. The numerical simulations are performed using the finite element method. This means that it will be necessary to use gigantic meshes with a huge amount of degrees of freedom ($d.o.f.$). The resolution is possible only by means of parallel computing (see appendix 2).

The representativity of the measurements obtained from limited domains of the random two-phase heterogeneous material, is investigated. These measurements of

the specimen concern the morphology (volume fraction P), and the following effective physical properties : elastic moduli (shear modulus μ and bulk modulus k) and thermal conductivity λ. The variances of the apparent volume fraction, elastic moduli and thermal conductivity are obtained in windows of increasing sizes. In all this work, the hard phase (resp. highly conductive) is labeled 1, with volume fraction P_1. The soft one (resp. less conductive) is called 2, with volume fraction P_2.

The chapter is organized as follows. The second section recalls the main definitions, boundary conditions and notations of the whole chapter for the determination of effective elastic and thermal properties. A brief statistical description of heterogeneous materials is provided in section I.3 focusing on covariance and integral range. The case of Voronoï mosaics is introduced in section I.3.3. The numerical tools necessary for the Monte–Carlo simulations follow in section I.4 with special attention to the meshing of Voronoï polyhedra, mesh size and parallel computing techniques. The effective properties for this type of microstructure are obtained in section I.5 for volume fraction, elasticity and thermal conductivity. The stress is led on the study of dispersion (variance) as a function of volume size and on the determination of corresponding integral ranges. A quantitative definition of RVE size based on the notion of integral range is introduced in section 5.2. The different RVE sizes found for the different properties are compared. Their dependence on volume fraction and contrast of properties is also addressed.

I.2 Effective Linear Properties

The elements and notations of homogenization theory necessary for the numerical determination of effective properties carried out in section I.5 are presented below for linear elasticity and for thermal conductivity. Special attention is focussed on boundary conditions to be prescribed on volume elements and to the definition of effective and apparent properties. More details and the proofs of the given results can be found in the textbooks and reference articles mentioned at the beginning of the introduction.

I.2.1 Linear Elasticity

A volume element V made of heterogeneous material is considered. Conditions are prescribed at its boundary ∂V in order to estimate its overall properties.

a) Boundary Conditions

In this work, three types of boundary conditions to be prescribed on individual volume element V are considered :

- Kinematic uniform boundary conditions (KUBC) : the displacement $\underline{\boldsymbol{u}}$ is imposed at point $\underline{\boldsymbol{x}}$ belonging to the boundary ∂V such that :

$$\underline{\boldsymbol{u}} = \underset{\sim}{\boldsymbol{E}}.\underline{\boldsymbol{x}} \quad \forall \underline{\boldsymbol{x}} \in \partial V \tag{I.1}$$

$\underset{\sim}{\boldsymbol{E}}$ is a symmetrical second–rank tensor that does not depend on $\underline{\boldsymbol{x}}$. This implies that :

$$< \underset{\sim}{\boldsymbol{\varepsilon}} > \hat{=} \frac{1}{V} \int_V \underset{\sim}{\boldsymbol{\varepsilon}} \, dV = \underset{\sim}{\boldsymbol{E}} \tag{I.2}$$

The symbol $\hat{=}$ means *equals by definition to*.

The macroscopic stress tensor is then defined by the spatial average :

$$\underset{\sim}{\boldsymbol{\Sigma}} \hat{=} < \underset{\sim}{\boldsymbol{\sigma}} > = \frac{1}{V} \int_V \underset{\sim}{\boldsymbol{\sigma}} \, dV \tag{I.3}$$

- Static uniform boundary conditions (SUBC) : the traction vector is prescribed at the boundary :

$$\underset{\sim}{\boldsymbol{\sigma}}.\underline{\boldsymbol{n}} = \underset{\sim}{\boldsymbol{\Sigma}}.\underline{\boldsymbol{n}} \quad \forall \underline{\boldsymbol{x}} \in \partial V \tag{I.4}$$

$\underset{\sim}{\boldsymbol{\Sigma}}$ is a symmetrical second–rank tensor independent of $\underline{\boldsymbol{x}}$. The vector normal to ∂V at $\underline{\boldsymbol{x}}$ is denoted by $\underline{\boldsymbol{n}}$. This implies that :

$$< \underset{\sim}{\boldsymbol{\sigma}} > \hat{=} \frac{1}{V} \int_V \underset{\sim}{\boldsymbol{\sigma}} \, dV = \underset{\sim}{\boldsymbol{\Sigma}} \tag{I.5}$$

The macroscopic strain tensor is then defined as the spatial average :

$$\underset{\sim}{\boldsymbol{E}} \hat{=} < \underset{\sim}{\boldsymbol{\varepsilon}} > = \frac{1}{V} \int_V \underset{\sim}{\boldsymbol{\varepsilon}} \, dV \tag{I.6}$$

- Periodicity conditions (PERIODIC) : the displacement field over the entire volume V takes the form

$$\underline{\boldsymbol{u}} = \underset{\sim}{\boldsymbol{E}}.\underline{\boldsymbol{x}} + \underline{\boldsymbol{v}} \quad \forall \underline{\boldsymbol{x}} \in V \tag{I.7}$$

where the fluctuation $\underline{\boldsymbol{v}}$ is periodic. It takes the same values at two homologous points on opposite faces of V. The traction vector $\underset{\sim}{\boldsymbol{\sigma}}.\underline{\boldsymbol{n}}$ takes opposite values at two homologous points on opposite faces of V.

When the constitutive behavior of the components is described by linear elasticity, each micromechanical problem (KUBC, SUBC and PERIODIC) admits a single solution, up to a rigid body motion for problem SUBC and a translation for PERIODIC. Accordingly, there exists a four–rank concentration tensor field $\underset{\approx}{\boldsymbol{A}}$ such that :

$$\underset{\sim}{\boldsymbol{\varepsilon}}(\underline{\boldsymbol{x}}) = \underset{\approx}{\boldsymbol{A}}(\underline{\boldsymbol{x}}) : \underset{\sim}{\boldsymbol{E}} \quad \forall \underline{\boldsymbol{x}} \in V \quad \text{and} \quad \forall \underset{\sim}{\boldsymbol{E}} \tag{I.8}$$

for the KUBC problem, and a four–rank concentration tensor field $\underset{\approx}{\boldsymbol{B}}$ such that :

$$\underset{\sim}{\boldsymbol{\sigma}}(\underline{\boldsymbol{x}}) = \underset{\approx}{\boldsymbol{B}}(\underline{\boldsymbol{x}}) : \underset{\sim}{\boldsymbol{\Sigma}} \quad \forall \underline{\boldsymbol{x}} \in V \quad \text{and} \quad \forall \underset{\sim}{\boldsymbol{\Sigma}} \tag{I.9}$$

for the SUBC problem. From the equations (I.3) and (I.6), the concentration tensors satisfy :

$$< \underset{\approx}{\boldsymbol{A}} > = < \underset{\approx}{\boldsymbol{B}} > = \underset{\approx}{\boldsymbol{I}} \tag{I.10}$$

$\underset{\approx}{\boldsymbol{I}}$ is the fourth-rank identity tensor operating on symmetric second-rank tensors.

b) Apparent and Effective Moduli

Let $\underset{\sim}{\underset{\sim}{\boldsymbol{c}}}(\underline{\boldsymbol{x}})$ and $\underset{\sim}{\underset{\sim}{\boldsymbol{s}}}(\underline{\boldsymbol{x}})$ be the four–rank tensor fields of elastic moduli and compliances in the volume V of heterogeneous material :

$$\underset{\sim}{\boldsymbol{\sigma}}(\underline{\boldsymbol{x}}) = \underset{\sim}{\underset{\sim}{\boldsymbol{c}}}(\underline{\boldsymbol{x}}) : \underset{\sim}{\boldsymbol{\varepsilon}}(\underline{\boldsymbol{x}}), \quad \underset{\sim}{\boldsymbol{\varepsilon}}(\underline{\boldsymbol{x}}) = \underset{\sim}{\underset{\sim}{\boldsymbol{s}}}(\underline{\boldsymbol{x}}) : \underset{\sim}{\boldsymbol{\sigma}}(\underline{\boldsymbol{x}}) \quad \forall \underline{\boldsymbol{x}} \in V \tag{I.11}$$

For the KUBC problem, one has then :

$$\underset{\sim}{\boldsymbol{\Sigma}} = < \underset{\sim}{\boldsymbol{\sigma}} > = < \underset{\sim}{\underset{\sim}{\boldsymbol{c}}} : \underset{\sim}{\underset{\sim}{\boldsymbol{A}}} : \underset{\sim}{\boldsymbol{E}} > = < \underset{\sim}{\underset{\sim}{\boldsymbol{c}}} : \underset{\sim}{\underset{\sim}{\boldsymbol{A}}} > : \underset{\sim}{\boldsymbol{E}} = \underset{\sim}{\underset{\sim}{\boldsymbol{C}}}_E^{app} : \underset{\sim}{\boldsymbol{E}} \tag{I.12}$$

and for the SUBC problem :

$$\underset{\sim}{\boldsymbol{E}} = < \underset{\sim}{\boldsymbol{\varepsilon}} > = < \underset{\sim}{\underset{\sim}{\boldsymbol{s}}} : \underset{\sim}{\underset{\sim}{\boldsymbol{B}}} : \underset{\sim}{\boldsymbol{\Sigma}} > = < \underset{\sim}{\underset{\sim}{\boldsymbol{s}}} : \underset{\sim}{\underset{\sim}{\boldsymbol{B}}} > : \underset{\sim}{\boldsymbol{\Sigma}} = \underset{\sim}{\underset{\sim}{\boldsymbol{S}}}_\Sigma^{app} : \underset{\sim}{\boldsymbol{\Sigma}} \tag{I.13}$$

which defines unambiguously apparent moduli $\underset{\sim}{\underset{\sim}{\boldsymbol{C}}}_E^{app}$ and apparent compliances $\underset{\sim}{\underset{\sim}{\boldsymbol{S}}}_\Sigma^{app}$ for a given volume V. The relations show that the apparent properties are not given in general by a simple law of mixtures, but involve a more complex averaging process.

A definition of apparent moduli based on strain energy e is also possible :

$$e \hat{=} < \underset{\sim}{\boldsymbol{\sigma}} : \underset{\sim}{\boldsymbol{\varepsilon}} > = < \underset{\sim}{\boldsymbol{\varepsilon}} : \underset{\sim}{\underset{\sim}{\boldsymbol{c}}} : \underset{\sim}{\boldsymbol{\varepsilon}} > = \underset{\sim}{\boldsymbol{E}} : < \underset{\sim}{\underset{\sim}{\boldsymbol{A}}}^T : \underset{\sim}{\underset{\sim}{\boldsymbol{c}}} : \underset{\sim}{\underset{\sim}{\boldsymbol{A}}} > : \underset{\sim}{\boldsymbol{E}} \tag{I.14}$$

for the KUBC problem, and :

$$e = < \underset{\sim}{\boldsymbol{\sigma}} : \underset{\sim}{\boldsymbol{\varepsilon}} > = < \underset{\sim}{\boldsymbol{\sigma}} : \underset{\sim}{\underset{\sim}{\boldsymbol{s}}} : \underset{\sim}{\boldsymbol{\sigma}} > = \underset{\sim}{\boldsymbol{\Sigma}} : < \underset{\sim}{\underset{\sim}{\boldsymbol{B}}}^T : \underset{\sim}{\underset{\sim}{\boldsymbol{s}}} : \underset{\sim}{\underset{\sim}{\boldsymbol{B}}} > : \underset{\sim}{\boldsymbol{\Sigma}} \tag{I.15}$$

for the SUBC problem. The exponent T denotes transposition. This leads to the following definition of apparent moduli :

$$\underset{\sim}{\underset{\sim}{\boldsymbol{C}}}_E^{app} = < \underset{\sim}{\underset{\sim}{\boldsymbol{A}}}^T : \underset{\sim}{\underset{\sim}{\boldsymbol{c}}} : \underset{\sim}{\underset{\sim}{\boldsymbol{A}}} >, \quad \underset{\sim}{\underset{\sim}{\boldsymbol{S}}}_\Sigma^{app} = < \underset{\sim}{\underset{\sim}{\boldsymbol{B}}}^T : \underset{\sim}{\underset{\sim}{\boldsymbol{s}}} : \underset{\sim}{\underset{\sim}{\boldsymbol{B}}} > \tag{I.16}$$

The symmetry of the apparent moduli is clear in these formula. However, the application of so–called Hill–Mandel lemma shows that both definitions are in fact equivalent ((Sanchez-Palencia and Zaoui, 1987)).

For sufficiently large volumes V, the apparent moduli do not depend any more on the type of boundary conditions and coincide with the wanted effective properties of the medium ((Sab, 1992)) :

$$\underset{\sim}{\underset{\sim}{\boldsymbol{C}}}_E^{app} = \underset{\sim}{\underset{\sim}{\boldsymbol{S}}}_\Sigma^{app-1} = \underset{\sim}{\underset{\sim}{\boldsymbol{C}}}^{eff} = \underset{\sim}{\underset{\sim}{\boldsymbol{S}}}^{eff-1} \tag{I.17}$$

For intermediate volumes V, one simply has the following bounding inequations ((Huet, 1990)) :

$$\underset{\sim}{\underset{\sim}{\boldsymbol{S}}}_\Sigma^{app-1} \leq \underset{\sim}{\underset{\sim}{\boldsymbol{C}}}^{eff} \leq \underset{\sim}{\underset{\sim}{\boldsymbol{C}}}_E^{app} \tag{I.18}$$

The inequalities must be understood in the sense of quadratic forms. In the computations presented in section b), it will be checked that these relations hold. The periodic estimation for a given volume V also lies between $\underset{\sim}{\underset{\sim}{\boldsymbol{S}}}_\Sigma^{app-1}$ and $\underset{\sim}{\underset{\sim}{\boldsymbol{C}}}_E^{app}$.

c) Elementary Problems on V for Isotropic Effective Properties

Specific boundary value problems are defined in this sub-section that will be used for the determination of isotropic effective elastic properties in section b). These are special cases of the previous KUBC, SUBC and PERIODIC boundary conditions, for which specific values of $\underset{\sim}{\boldsymbol{E}}$ and $\underset{\sim}{\boldsymbol{\Sigma}}$ are chosen.

In the case of KUBC and PERIODIC boundary conditions prescribed to a given volume V, one takes :

$$\underset{\sim}{\boldsymbol{E}}_k = \begin{pmatrix} \frac{1}{3} & 0 & 0 \\ 0 & \frac{1}{3} & 0 \\ 0 & 0 & \frac{1}{3} \end{pmatrix}, \qquad \underset{\sim}{\boldsymbol{E}}_\mu = \begin{pmatrix} 0 & \frac{1}{2} & 0 \\ \frac{1}{2} & 0 & 0 \\ 0 & 0 & 0 \end{pmatrix} \tag{I.19}$$

An "apparent bulk modulus" k^{app} and an "apparent shear modulus" μ^{app} can be defined as :

$$k^{app} \hat{=} e(\underset{\sim}{\boldsymbol{E}}_k) = <\underset{\sim}{\boldsymbol{\sigma}}> : \underset{\sim}{\boldsymbol{E}}_k = \frac{1}{3}\mathrm{trace} <\underset{\sim}{\boldsymbol{\sigma}}> \tag{I.20}$$

$$\mu^{app} \hat{=} e(\underset{\sim}{\boldsymbol{E}}_\mu) = <\underset{\sim}{\boldsymbol{\sigma}}> : \underset{\sim}{\boldsymbol{E}}_\mu = <\sigma_{12}> \tag{I.21}$$

In the case of SUBC boundary conditions, one takes :

$$\underset{\sim}{\boldsymbol{\Sigma}}_k = \begin{pmatrix} 1 & 0 & 0 \\ 0 & 1 & 0 \\ 0 & 0 & 1 \end{pmatrix} \qquad \underset{\sim}{\boldsymbol{\Sigma}}_\mu = \begin{pmatrix} 0 & 1 & 0 \\ 1 & 0 & 0 \\ 0 & 0 & 0 \end{pmatrix} \tag{I.22}$$

In this case an "apparent bulk modulus" k^{app} and an "apparent shear modulus" μ^{app} can also be defined as :

$$\frac{1}{k^{app}} \hat{=} e(\underset{\sim}{\boldsymbol{\Sigma}}_k) = \underset{\sim}{\boldsymbol{\Sigma}}_k : <\underset{\sim}{\boldsymbol{\varepsilon}}> = \mathrm{trace} <\underset{\sim}{\boldsymbol{\varepsilon}}> \tag{I.23}$$

$$\frac{1}{\mu^{app}} \hat{=} e(\underset{\sim}{\boldsymbol{\Sigma}}_\mu) = \underset{\sim}{\boldsymbol{\Sigma}}_\mu : <\underset{\sim}{\boldsymbol{\varepsilon}}> = 2 <\varepsilon_{12}> \tag{I.24}$$

The physical meaning of these quantities is actually that of bulk and shear moduli only when the response of volume V is isotropic, which is generally not the case. The problem of the determination of isotropic apparent moduli from simulations on small volumes is discussed in subsection b).

I.2.2 Thermal Conductivity

For the thermal problem, the temperature, its gradient and the heat flux vector are denoted by $T, \nabla T$ and $\underline{\boldsymbol{q}}$ respectively. The heat flux vector and the temperature gradient are related by Fourier's law, that reads :

$$\underline{\boldsymbol{q}} = \lambda \nabla T \tag{I.25}$$

in the isotropic case. The scalar λ is the thermal conductivity coefficient of the considered phase.

A volume V of heterogeneous material is considered again. Three types of boundary conditions are used in the study of the effective thermal conductivity :

- Uniform gradient of temperature at the boundary (UGT) :

$$T = \underline{\boldsymbol{G}}.\underline{\boldsymbol{x}} \quad \forall \underline{\boldsymbol{x}} \in \partial V \tag{I.26}$$

$\underline{\boldsymbol{G}}$ is a constant vector independent of $\underline{\boldsymbol{x}}$. This implies that :

$$< \nabla T >= \frac{1}{V}\int_V \nabla T dV = \underline{\boldsymbol{G}} \tag{I.27}$$

The macroscopic flux vector is defined by the spatial average :

$$\underline{\boldsymbol{Q}} \hat{=} < \underline{\boldsymbol{q}} >= \frac{1}{V}\int_V \underline{\boldsymbol{q}}\, dV \tag{I.28}$$

- Uniform heat flux at the boundary (UHF) :

$$\underline{\boldsymbol{q}}.\underline{\boldsymbol{n}} = \underline{\boldsymbol{Q}}.\underline{\boldsymbol{x}} \quad \forall \underline{\boldsymbol{x}} \in \partial V \tag{I.29}$$

$\underline{\boldsymbol{Q}}$ is a constant vector independent on $\underline{\boldsymbol{x}}$. This implies that :

$$< \underline{\boldsymbol{q}} >= \frac{1}{V}\int_V \underline{\boldsymbol{q}}\, dV = \underline{\boldsymbol{Q}} \tag{I.30}$$

The macroscopic temperature gradient is given by the spatial average :

$$\underline{\boldsymbol{G}} \hat{=} < \nabla T >= \frac{1}{V}\int_V \nabla T dV \tag{I.31}$$

- Periodic boundary conditions (PERIODIC) : the temperature field takes the form

$$T = \underline{\boldsymbol{G}}.\underline{\boldsymbol{x}} + t \quad \forall \underline{\boldsymbol{x}} \in V \tag{I.32}$$

The fluctuation temperature t is periodic.

Concentration tensors $\underset{\sim}{\boldsymbol{A}}$ and $\underset{\sim}{\boldsymbol{B}}$ exist such that :

$$\nabla T(\underline{\boldsymbol{x}}) = \underset{\sim}{\boldsymbol{A}}(\underline{\boldsymbol{x}}).\underline{\boldsymbol{G}}, \quad \text{and} \quad \underline{\boldsymbol{q}}(\underline{\boldsymbol{x}}) = \underset{\sim}{\boldsymbol{B}}(\underline{\boldsymbol{x}}).\underline{\boldsymbol{Q}} \tag{I.33}$$

for the problems UGT and UHF respectively. Apparent conductivity tensors can be defined as :

$$\underset{\sim}{\boldsymbol{\lambda}}_G^{app} =< \lambda \underset{\sim}{\boldsymbol{A}} >, \quad \text{and} \quad \underset{\sim}{\boldsymbol{\lambda}}_Q^{app-1} =< \frac{1}{\lambda}\underset{\sim}{\boldsymbol{B}} > \tag{I.34}$$

Apparent conductivities coincide with the wanted effective properties for sufficiently large volumes V.

In the case of isotropic effective properties, as considered in sub-section c), the following test temperature gradient and flux will be prescribed :

$$\underline{\boldsymbol{G}}_\lambda = (1\,1\,1)^T \quad \text{and} \quad \underline{\boldsymbol{Q}}_\lambda = (1\,1\,1)^T \tag{I.35}$$

They are used respectively to define the following “apparent conductivities” :

$$\lambda^{app} = \frac{1}{3}\text{trace} < \underline{\boldsymbol{q}} >, \quad \lambda^{app-1} = \frac{1}{3}\text{trace} < \nabla T > \tag{I.36}$$

I.3 Statistical Description of Random Heterogeneous Media

Models of random media may be useful at two different levels : to provide a description of the heterogeneous structure, and to predict some macroscopic properties of materials. In this part, basic morphological tools that are available to quantitatively characterize the geometry of random media ar introduced. They can be easily obtained from the analysis of images of the microstructure. They are illustrated in the last sub-section by an estimation of the integral range for a Voronoï mosaic model.

I.3.1 Reminder on the Covariance of a Random Set

To describe the geometrical dispersion, the state of two points x_1 and x_2 with the separation h can be tested, without considering what happens between the two points ((Matheron, 1971; Jeulin, 1981; Serra, 1982; Coster and Chermant, 1989; Jeulin, 2001)). The morphological approach based on the covariance is, in general, suitable to study the dispersion.

The covariogram $K(X,h)$ is the measure Mes of the intersection of the set X (surface in $2D$, volume in $3D$) and of the translated set of X by $-h$, X_{-h}.

We have :

$$K(X,h) = Mes(X \cap X_{-h}) = \int k(x)k(x+h)dx \tag{I.37}$$

$k(x)$ is defined as :

$$k(x) = \begin{cases} 1 & \text{if } x \in X \\ 0 & \text{else} \end{cases} \tag{I.38}$$

Properties of the Covariogram

- For $h = 0$, we have :

$$K(X,0) = Mes(X \cap X_{-0}) = Mes(X) \tag{I.39}$$

- For a bounded set X :

$$K(X,\infty) = 0, \quad K(X,h) = 0 \text{ for } h > A \tag{I.40}$$

  A is the largest distance between two points in X in the direction of h.

- The integral of the covariogram is given by :

$$\int_{R^n} K(X,h)dh = (Mes(X))^2 \tag{I.41}$$

The probabilistic version of the covariogram for a stationary set X is the *covariance function*, noted $C(X,h)$. The covariance function is the probability for the two points x and $x+h$ to be in the set X :

$$C(X,h) = P\{x \in X, x+h \in X\} \tag{I.42}$$

If X is defined in R^3 :

$$C(X,0) = V_V(X) = P \tag{I.43}$$

V_V is the volume fraction of X in $\mathbb{R}^3$. One has also :

$$C(X,h) = C(X,-h) \leq C(X,0) \tag{I.44}$$

and :

$$\lim_{h\to\infty} C(X,h) = (V_V(X))^2 \tag{I.45}$$

The covariance presents an asymptotic theoretical value equals to the square of the volume fraction of X.

If this limit is reached before :

$$h \to \infty \tag{I.46}$$

for example, for a value :

$$h = L \tag{I.47}$$

the points of the structure with a distance larger than L are not correlated ((Matheron, 1971; Jeulin, 1981; Serra, 1982; Jeulin, 2001)). This distance is the range of the covariance. We can estimate the covariance from images (like plane sections) inside a mask, by means of the geometrical covariogram (two examples are given in figure I.1). The covariance is characteristic of the size and of the arrangement of connected objects building the set X. In figure I.1a the range is close to :

$$L_1 = 37\ \mu m \tag{I.48}$$

while in figure I.1b it is close to :

$$L_2 = 19\ \mu m \tag{I.49}$$

The range for the coarse microstructure L_1 being larger than for the fine microstructure L_2. In addition, from the measurement of the covariance in two orthogonal directions given in figure I.1, it can be seen that the microstructure is isotropic.

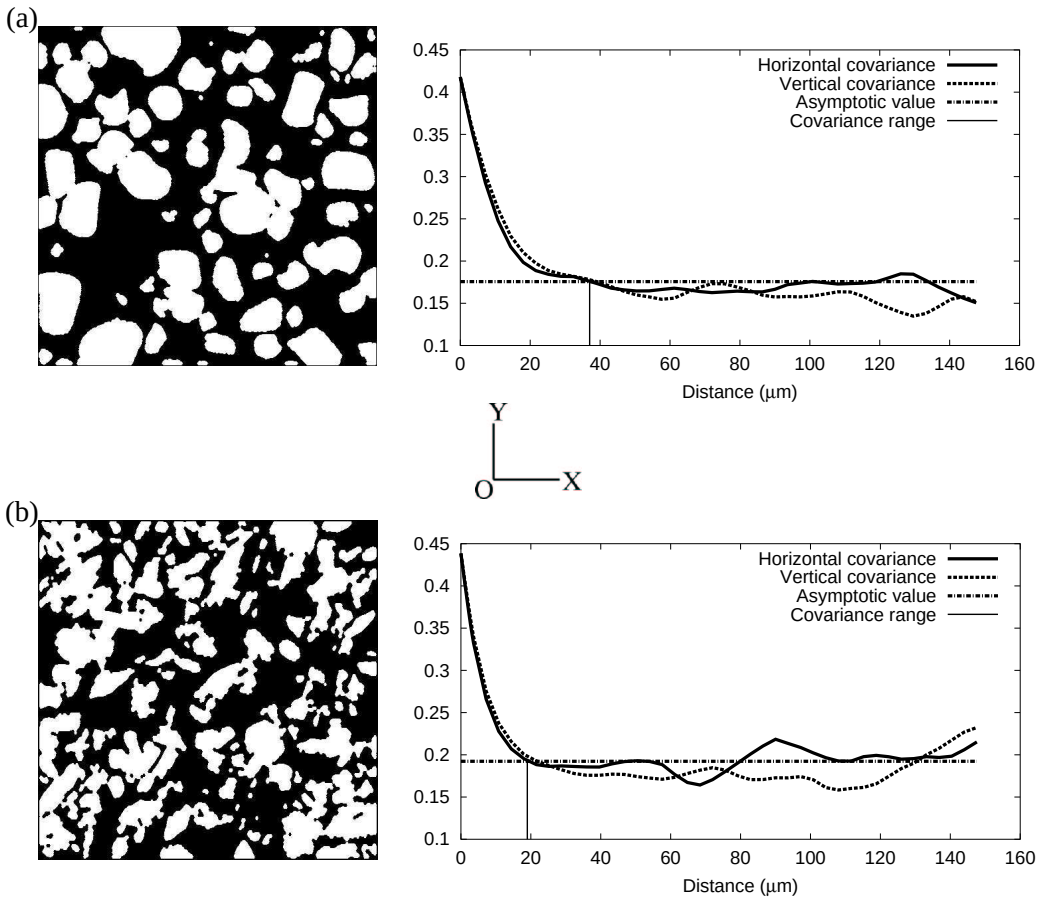

Figure I.1 : Microstructures (with the same volume fraction and different morphologies) and their covariances in horizontal and vertical directions; the image size is $150\mu m$x$150\mu m$. The asymptotic value is equal to the square of the volume fraction (of the white phase); for the fine (a) and coarse (b) microstructures (material from food industry, (Colworth, 2000)).

I.3.2 Notion of Integral Range

It is possible to define a range which gives information on the domain size of the structure for which the parameters measured in this volume have a good statistical representativity. This range is called the integral range ((Matheron, 1971; Matheron, 1975; Matheron, 1989; Lantuéjoul, 1991; Cailletaud et al., 1994; Jeulin, 2001)) . The definition of the integral range in the space R^n is :

$$A_n = \frac{1}{C(X,0) - C(X,0)^2} \int_{R^n} (C(X,h) - C(X,0)^2) dh \tag{I.50}$$

This notion is very useful to predict the variability of properties of a material as a function of the geometry of parts. For instance, the variance $D_P^2(V_V^*)$ of the local volume fraction V_V^* :

$$V_V^* = \frac{Mes(X \cap V)}{Mes(V)} \tag{I.51}$$

of a sample with volume V in an infinite domain, for a microstructure with the covariance $C(X,h)$ is given by ((Matheron, 1971)) :

$$D_P^2(V_V^*) = \frac{1}{V^2} \int_V \int_V (C(X, x-y) - P^2)\ dxdy \tag{I.52}$$

For a large specimen :

$$V \gg A_n \tag{I.53}$$

$D_P^2(V)$ can be expressed as a function of the integral range in the space R^n, A_n, by :

$$D_P^2(V) = \frac{P(1-P)A_n}{V} \tag{I.54}$$

Therefore, the specimen V is statistically equivalent to :

$$N \simeq \frac{V}{A_n} \tag{I.55}$$

uncorrelated samples. From the variance, it is easy to work out the confidence interval of the average of the volume fraction P ($P \pm 2D_P(V)$) as a function of the volume V and of the integral range. This gives the relative precision of the estimation. Conversely, the volume V to be used to get a given precision is obtained as a function of P and of A_n.

This is the reason for interpreting A_n as the scale of the phenomenon, V being the scale of observation. The integral range A_n is a good measure of the notion of scale. It is a convenient measurement of the size of a RVE of a stationary and ergodic random structure.

I.3.3 Case of the Voronoï Mosaics

The previous notions of mathematical morphology can be illustrated in the case of the microstructure considered in the numerical simulations of this work, namely three-dimensional Voronoï mosaics.

To generate such microstructures, an original method is proposed, with numerous extensions of the classical model ((Decker and Jeulin, 2000)). Its main advantage, as compared to standard procedures, is to generate textures with very large numbers of grains, at a low computational cost.

First pick points $M_1, M_2, ...$ in space at random according to a Poisson process of density ρ points per unit volume. Next subdivide space into cells (crystals) $C_1, C_2, ...$ by the rule : C_i contains all points in space closer to M_i than to any $M_i (j \neq i)$. In the cell model C_i is a convex polyhedron because it is the intersection of several half-spaces (points closer to M_i than to M_j form a half-space). M_i will be called the center of C_i. This builds a Voronoï tessellation of space ((Gilbert, 1962)).

In practice M_i represents the location of the original seed crystal from which C_i grew. One assumes :

- the seeds for all crystals start growing at the same instant;
- seeds grow at the same rate in all directions;
- seeds remain fixed in space without pushing apart as they grow into contact (see figure I.2a).

Coloring every cell C of the tessellation at random generates a random Voronoï mosaic. In what follows, the colors will in fact correspond to the physical properties of the components of a random composite. To study two-phase materials, two colors are used.

Note that it is possible to superimpose a constraint of periodicity at the boundary of the volume in the generation of the Voronoï mosaic ((Decker and Jeulin, 2000; Forest et al., 2000)). In the simulations of this work with periodic boundary conditions, such periodic Voronoï mosaics are used.

In the case of the Voronoï mosaic model, the covariance $C(h)$ of the composite and covariogram $K(h)$ of the random cell C are related by the following equation ((Jeulin, 1981)) :

$$C(h) = P(1-P)\frac{K(h)}{K(0)} + P^2 \tag{I.56}$$

From the definition of the integral range (equation (I.50)) :

$$A_3 = \frac{1}{P(1-P)} \int (C(h) - P^2) dh = \int_{R^3} \frac{K(h)}{K(0)} dh \tag{I.57}$$

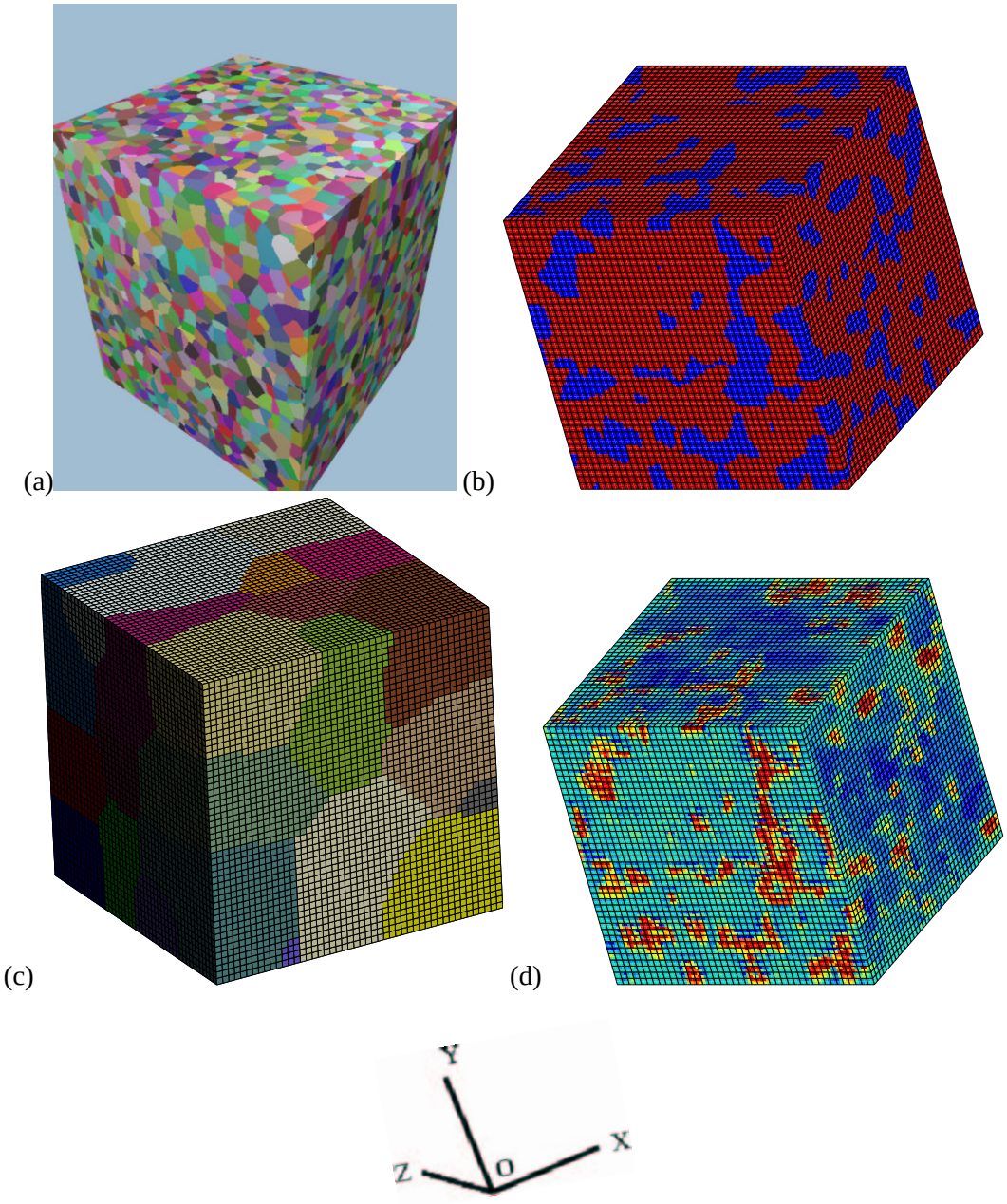

Figure I.2 : Voronoï mosaic model and finite element computations : (a) random distribution of 8000 grains in space; (b) image of the same microstructure with two phases distributed randomly among the grains for a given volume fraction of phase 1, with the superimposed finite element mesh; (c) sub-division of the microstructure into 32 sub-domains for parallel computing; (f) example of computation of the effective shear modulus with KUBC boundary conditions (von Mises equivalent strain distribution for prescribed mean strain $E_{12} = 0.1$).

Finally, one obtains :

$$A_3 = \frac{E\{V^2\}}{E\{V\}} \tag{I.58}$$

$E\{Z\}$ is the mathematical expectation of property Z. The value of the integral range in the case of the Voronoï mosaic model is deduced from the variance of the volume of the random cell C given by (Gilbert, 1962) :

$$A_3 = 1.179 \tag{I.59}$$

I.4 Numerical Tools for the Homogenization

The finite element method is chosen for the computations presented in this work. This requires meshing techniques for microstructures. They are described in the first subsection. The question of mesh refinement is also discussed here. The last sub-section presents the parallel computing tools that are necessary to handle large enough meshes.

I.4.1 Finite Element Meshing of Microstructures

a) Free Mesh and Multi-Phase Elements

Two types of meshes were used and compared in the case of the Voronoï mosaic : the multi-phase element technique and free meshing with tetrahedral elements. Figure I.3 shows them in the case of an aggregate of 20 Voronoï cells. In the multi–phase element technique, an image of the microstructure is used to attribute the proper phase property to each integration point ($i.p.$) of a regular mesh, according to the color of the underlying voxel. The figure I.3a shows an example of regular mesh with linear 8–node elements and 8 integration points per finite element. The main drawback of this simple technique is that in the same finite element two different phases can be present. The element edges do not necessarily follow the interfaces of grains in the microstructure. Such meshes have been used extensively in ((Lippmann et al., 1997)) and ((Barbe et al., 2001a)). The second type is the free meshing technique with tetrahedral elements (see figure I.3b, and ((Thompson et al., 1999))). The faces of all Voronoï cells are meshed using two–dimensional Delaunay triangles. After that, the individual cell volumes are meshed with tetrahedral elements with the constraint that they are built on the $2D$ meshes of the faces. Accordingly, all integration points of one element belong to the same phase. This technique usually leads to larger numbers of elements. Both methods are compared in ((Lippmann et al., 1997)) for inclusion–matrix microstructures. Note that (Ghosh and Moorthey, 1995) developed a finite element method based on Voronoï cells.

For illustration, an example of tensile test is computed in linear elasticity with mixed boundary conditions (traction load is prescribed on one face, the opposite one is fixed and all the other faces are free of forces). Phases 1 and 2 were randomly distributed among the 20 grains of figure I.3 according to a volume fraction of 70% of hard phase P_1. The contrast in Young's modulus is :

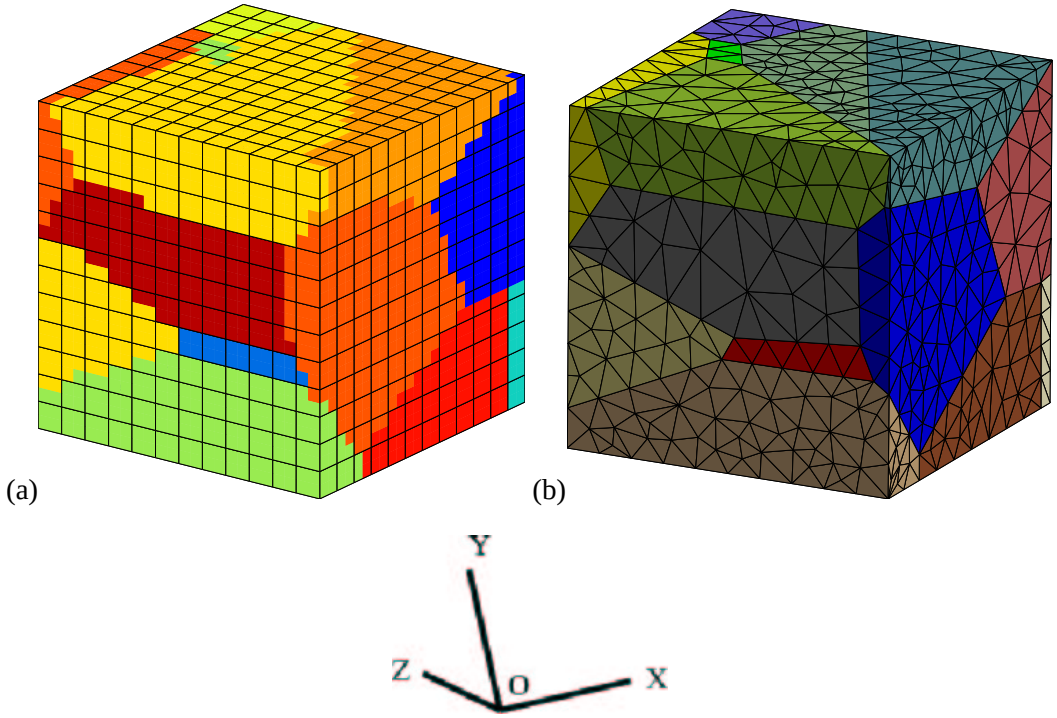

Figure I.3 : Two meshes of the same microstructure (20 Voronoï cells) with approximatively the same number of integration points ($i.p.$) and the same number of degrees of freedom ($d.o.f.$) : (a) multi-phase elements (13824 $i.p.$ and 6591 $d.o.f.$), (b) free meshing (10326 $i.p.$ and 6387 $d.o.f.$).

$$c_E = \frac{E_1}{E_2} = \frac{2500}{25} = 100 \tag{I.60}$$

and the Poisson ratio is :

$$\nu_1 = 0.3 \tag{I.61}$$

and :

$$\nu_1 = 0.49 \tag{I.62}$$

The obtained average stress and strain are found to be identical for both meshes. However slight differences exist for the local fields. The local distributions of von Mises stress are compared in figure I.4. The local differences are also explained by the insufficient mesh density used in each case. As a result, and for the sake of simplicity, the multi-phase element technique is used in the sequel. Quadratic bricks with reduced integration (20 nodes and 8 integration points per element) are used in all following simulations, contrary to the simple previous test. Since only $3D$ simulations are presented, the number of degrees of freedom in one brick is 60 (the number of nodes multiplied by the three components of displacement at each node). For a large regular cubic grid made of twenty–node bricks, the number of nodes is approximately equal to four times the number of bricks. The total number of degrees of freedom is then three times the number of nodes.

b) Determination of the Mesh Density

The effect of the mesh density (average number of finite elements used to mesh one Voronoï cell) is studied. Three microstructures of 1000 grains are used for three different volume fractions (72.5%, 66.7% and 52.5% of phase P_1). The material properties are the same as in the previous sub-section. Tensile tests are simulated. The number of cells and the geometry of the microstructure is unchanged but different mesh resolutions are used. The number of finite elements was changed from 1728 to 85184 (the corresponding number of degrees of freedom was changed from 24843 to 1075275). The results given in figure I.5 show the convergence of the apparent Young's modulus as a function of the number of degrees of freedom. This figure also shows that one must use about 50 quadratic elements to mesh one grain, for the variation of the overall effective elastic response to be smaller than 1%. In the sequel, about 14 finite elements per grain were retained as mesh density, which corresponds to a precision better than 5% in the results. It has been checked also that this mesh density is sufficient to get a precision better than 1% on the statistical fluctuations and variance of the results when many realizations are considered.

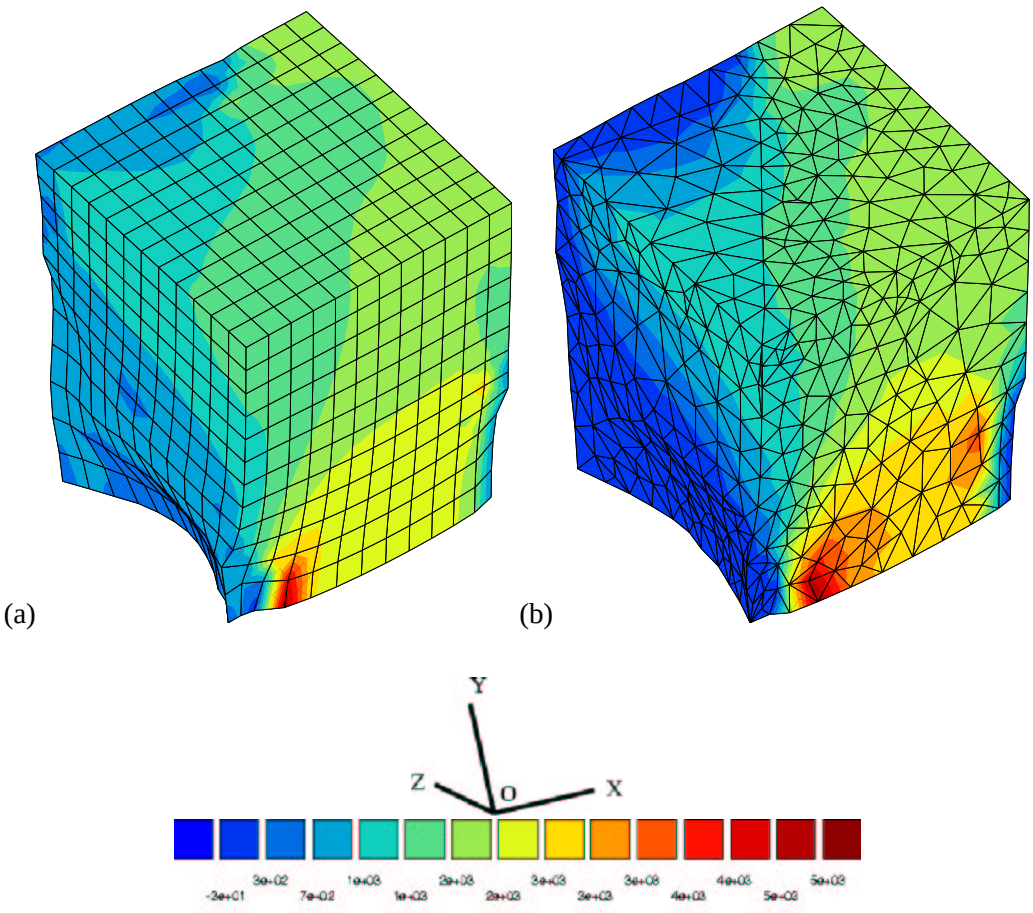

Figure I.4 : Distribution of von Mises equivalent stress (MPa) for mean tensile deformation $E_{33} = 0.1$ in OY direction : (a) multi-phase elements, (b) free mesh.

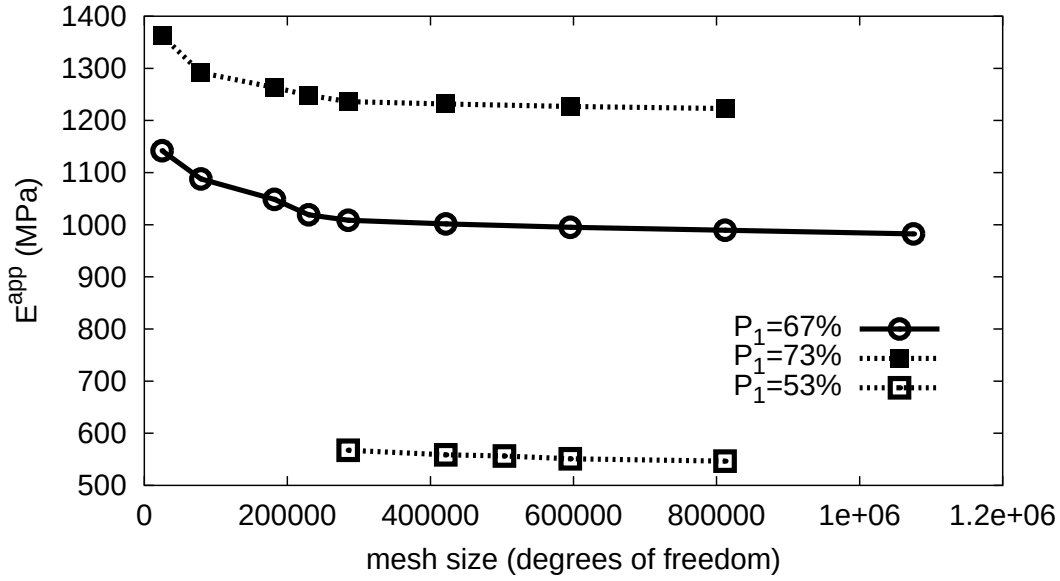

Figure I.5 : Effect of mesh size and of the volume fraction of hard phase ($P_1 = P$) on the value of apparent Young's modulus.

I.4.2 Parallel Computing

In order to characterize the size of the RVE, one must be able to carry out computations with a very large amount of finite elements. For that purpose, we have chosen to resort to parallel computation.

The retained method is the FETI solver (Finite Element Tearing and Interconnecting method, (Farhat and Roux, 1994), (Feyel et al., 1997), (Feyel, 1998)), which is a dual sub-division method well–known for its numerical scalability. Subdivision means the process of dividing a large finite element mesh into sub-domains. The large algebraic system is replaced by a succession of smaller ones related to the sub-domains and to the interface between the sub-domains. The numerical scalability of FETI allows us to solve problems with a large number of sub-domains. The individual problems on sub-domains are computed simultaneously on different processors. For a good speed-up, sub-division must give the same amount of work to all processors which must have the same velocity. The aim of the interface problem is to ensure continuity of displacement at the interface between sub-domains. FETI is called dual method because the interface problem is posed in terms of forces that glue the sub-domains. This interface problem is solved iteratively by a conjugate gradient method.

The large contrast of properties considered in this work can lead to ill–conditioned matrices. This numerical difficulty is solved by using a conjugate gradient algorithm with a preconditionning procedure. Unfortunately, the preconditionning is less efficient for an increasing number of sub-domains.

A cluster of 32 PC under Linux was available for the computations of this work. The largest volume computed in this work, in the case of linear elasticity, is a cube with :

$$48 \times 48 \times 48 = 110592 \tag{I.63}$$

quadratic bricks for the mesh of about 8000 Voronoï cells (i.e. about 14 elements per cell). This corresponds to almost 1,4 million of degrees of freedom. This mesh and the distribution of the two phases are shown in figure I.2b. The mesh is decomposed into 32 sub-domains (see figure I.2c). The resolution of the linear elastic problem is done in one single increment, using a multi–frontal solver. About 850 Mo RAM memory are necessary for each processor, so that the whole resolution requires more than 27 Go memory. The entire computation time for one resolution (reading of the mesh, parallel resolution, writing of the output files) is about 1 hour and 30 minutes. An example of result is shown in the case of a shear test with KUBC conditions in figure I.2 d.

I.5 Determination of Morphological and Effective Physical Properties of a Two-Phase Voronoï Mosaic

Three types of overall properties are studied in this part for a large range of volume sizes V and a large number of realizations N of the random microstructures. The first one is a geometrical property, namely the overall volume fraction P^{app} . The motivation for studying this simple property lies on the fact that the integral range is known in the case of the Voronoï mosaic (see equation (I.59)). This a good test for the random generation procedure of the microstructure. Furthermore, this illustrates in a simple way the methodology proposed in this work. The investigated physical properties are the elastic moduli (bulk modulus k and shear modulus μ), and the thermal conductivity λ.

For each property, the dispersion of the results when increasing volume V is reported in section II.5.1. The integral ranges are then identified in sub-section II.5.2. The link between these results and the notion of RVE is postponed to section II.5.3.

The convention is made that the mean volume of one Voronoï cell is fixed equal to 1 and kept constant. So, a volume V contains $N = V$ Voronoï cells. The results will be given as a function of volume V, which is also equivalent to a number of cells :

$$N = V \tag{I.64}$$

As a result, an increasing volume means an increasing number of grains.

I.5.1 Study of the Average Properties

a) Volume Fraction

Consider a microstructure in which there is a given number of Voronoï cells, with a given probability :

$$P_1 = P \tag{I.65}$$

and :

$$P_2 = 1 - P \tag{I.66}$$

for the random attribution of the two phases 1 and 2. When working with domains of finite size, estimations of P_1 or P_2 are obtained for each realization. So, the obtained volume fraction found for a given realization of the Voronoï mosaic in a finite volume V will differ from P_1. The number of cells in a volume V is chosen to obey to a Poisson distribution with mean value $N = V$. It means that in a microstructure with N grains, there may not be enough grains to regard it as a representative domain from the point of view of volume fraction of phase 1.

Many realizations of $3D$ Voronoï mosaic were simulated for increasing volume sizes. The mean volume fraction and its dispersion found for a given volume V (or equivalently mean number of grains N) are given in figure I.6, as a function of V. It can be seen that the mean volume fraction does not depend on volume size. The mean volume fraction for phase 1 found for small volumes coincides with that found for large ones, provided that a sufficient number of realizations of small volumes are considered. However, the variance decreases with increasing volume size. This study was carried out for the following target mean volume fractions :

$$P = 50\%,\ 70\%,\ 90\% \tag{I.67}$$

The number of realizations considered for each volume size are given in table I.1. This number is chosen so that the obtained mean value and variance do not vary any longer up to a given precision (less than 0.5% here).

As a result, the overall volume fraction of a phase in a heterogeneous material can be determined either by a few number of measurements on large volumes, or by many realizations for small volumes of material. We investigate in the two next subsections whether this reasoning can be extended to physical properties.

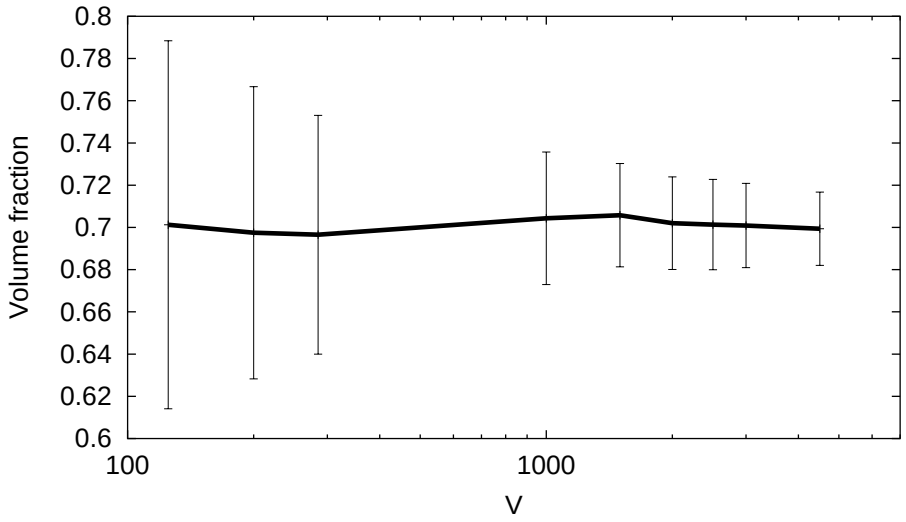

Figure I.6 : Mean value and intervals of confidence for volume fraction $P = 70\%$ (results from simulations).

Size of the domain (V)	n
6	2500
10	1653
15	1488
37	1238
50	1200
100	1152
125	1020
200	277
285	118
500	35
1000	25
2000	12
2500	14
4000	12
4500	15
8000	13
10000	13
12000	11
14000	10

Table I.1 : Number of realizations n used for all considered domain sizes.

b) Elastic Moduli

In this sub-section, the Voronoï mosaic is considered as a two–phase linear elastic material. The chosen mechanical properties of the phases are

$$(E_1,\ \nu_1,\ k_1,\ \mu_1) = (2500\ MPa,\ 0.3,\ 2083\ MPa,\ 962\ MPa) \tag{I.68}$$

$$(E_2,\ \nu_2,\ k_2,\ \mu_2) = (25\ MPa,\ 0.49,\ 417\ MPa,\ 8\ MPa) \tag{I.69}$$

So the chosen contrast in the Young's modulus is :

$$c_E = \frac{E_1}{E_2} = 100 \tag{I.70}$$

Note that the contrast in shear modulus μ is very high, whereas the contrast in bulk modulus k is weaker :

$$c_\mu = 120.25 \tag{I.71}$$

and :

$$c_k = 5 \tag{I.72}$$

The same microstructures used in the previous study for the volume fraction (in the cases of $P_1 = 70\%$ and $P_2 = 1 - P_1 = 30\%$) are simulated and are introduced in the finite element method for various boundary conditions. The objective of this part is to estimate the apparent mechanical properties (the bulk modulus k^{app} and the shear modulus μ^{app}), as a function of the size of the domain V.

Isotropy of Mean Apparent Moduli

If a small volume element V of a given composite material is considered, it will not *a priori* exhibit an isotropic behavior. Even if the microstructure is expected to be macroscopically isotropic, the tensor of apparent moduli obtained for a finite domain V is generally not isotropic. We show here however that the mean value of a sufficient number of realizations is isotropic. For that purpose, microstructures of volume V with an average number of 200 Voronoï cells are considered. The anisotropic matrix of the apparent mechanical properties relating mean stress and strain tensors is computed for each realization. Six computations are necessary for each realization to find the 21 apparent elastic coefficients, using here kinematic uniform boundary conditions KUBC. The mean value of the matrix of overall mechanical properties is given below.

From averaging over 10 different realizations, the obtained matrix is (components in MPa) :

$$[C_{10}^{app}] = \begin{pmatrix} 2034 & 935 & 939 & 5 & 2 & 7 \\ 935 & 1997 & 934 & 1 & 3 & 1 \\ 939 & 934 & 2035 & 1 & 1 & 3 \\ 5 & 1 & 1 & 531 & 1 & 1 \\ 2 & 3 & 1 & 1 & 531 & 1 \\ 7 & 1 & 3 & 1 & 1 & 542 \end{pmatrix} \tag{I.73}$$

after 30 and 60 different realizations the matrix becomes :

$$[C_{30}^{app}] = \begin{pmatrix} 2001 & 928 & 928 & 3 & 2 & 7 \\ 928 & 1991 & 927 & 3 & 2 & 0 \\ 928 & 927 & 1995 & 0 & 2 & 4 \\ 3 & 3 & 0 & 526 & 1 & 1 \\ 2 & 2 & 2 & 1 & 525 & 0 \\ 7 & 0 & 4 & 1 & 0 & 528 \end{pmatrix} \tag{I.74}$$

$$[C_{60}^{app}] = \begin{pmatrix} 2015 & 935 & 934 & 2 & 1 & 3 \\ 935 & 2013 & 934 & 2 & 1 & 0 \\ 934 & 934 & 2012 & 0 & 1 & 2 \\ 2 & 2 & 0 & 533 & 1 & 0 \\ 1 & 1 & 1 & 1 & 532 & 1 \\ 3 & 0 & 2 & 0 & 1 & 533 \end{pmatrix} \tag{I.75}$$

The last matrix shows the structure of an isotropic elasticity matrix with bulk and shear moduli equal to :

$$k^{app} = 1289\ MPa \tag{I.76}$$

and :

$$\mu = 533\ MPa \tag{I.77}$$

To estimate these effective values, it is not necessary to compute the whole matrix (6 tests on each volume). Instead, for the boundary conditions KUBC for instance, the two deformations $\underset{\sim}{\boldsymbol{E}}_k$ and $\underset{\sim}{\boldsymbol{E}}_\mu$ defined by equation (I.19) can be imposed successively to each realization with volume V. For each realization, two values k^{app} and μ^{app} are obtained (see equations (I.20) and (I.21)). The mean values $(\overline{k}^{app}, \overline{\mu}^{app})$ over all realizations provide the wanted estimation (associated with the given volume V) of the isotropic effective linear properties. This is the procedure adopted in what follows.

Estimation of the Apparent Elastic Moduli

The numerical simulations based on the finite element method are carried out for three different boundary conditions: kinematic uniform boundary conditions (KUBC), static uniform boundary conditions (SUBC) and the periodic boundary conditions (PERIODIC). The studied volume fraction of hard phase is $P = 70\%$. The number of realizations for each volume is given in table I.1. Figure I.7 gives the obtained mean values and variances of the apparent moduli k^{app} and μ^{app} as a function of the volume size (or equivalently the number of Voronoï cells). It shows that the dispersion of the results decreases when the size of the domain increases for all boundary conditions. As opposite to the case of volume fraction previously studied, the obtained mean values depend on the volume size, but also on the type of boundary conditions. For each modulus, the three values converge towards the same limit for large volumes V, which is the wanted effective modulus. The values k^{eff} and μ^{eff} found for large volume sizes are reported in table I.2 and compared to the Voigt-Reuss and Hashin–Shtrikman bounds. The self–consistent model (SC), also given in table I.2, provides a fair estimate in most cases, except for the volume fraction $P = 50\%$, where it underestimates the moduli. This is due to the fact that the SC model does not properly reproduce the percolation threshold of the mosaic model (which is close to 50%).

Property	Simulation	Upper B.	Lower B.	HS+	HS-	SC
$\mu\ (P = 0.7,\ E_1/E_2 = 100)$	433	676	27	534	39	435
$\mu\ (P = 0.7,\ E_1/E2 = 1000)$	398	673	3	529	6	404
$\mu\ (P = 0.5,\ E_1/E2 = 100)$	193	485	17	338	28	147
$k\ (P = 0.7,\ E_1/E2 = 100)$	1198	1583	947	1318	955	1194
$k\ (P = 0.7,\ E_1/E2 = 1000)$	743	1471	133	1019	135	737
$k\ (P = 0.5,\ E_1/E2 = 100)$	833	1250	694	976	699	770
$\lambda\ (P = 0.7,\ \lambda_1/\lambda_2 = 100)$	1.346	1.715	0.079	1.498	0.180	1.363

Table I.2 : Values of numerical results, bounds of Voigt-Reuss or Wiener (upper and lower bounds), Hashin-Shtrikman's bounds (HS+, HS-) and self–consistent estimate (SC) for elastic and thermal properties studied in this work. The elastic moduli are given in (MPa), the thermal conductivity in (W/mK).

It can be noticed that the mean value given by the periodic boundary conditions varies slightly as a function of the size of the domain, as compared to the other boundary conditions. Figure I.7 gives the corresponding confidence intervals $[\overline{Z} - 2D_Z, \overline{Z} + 2D_Z]$, where Z is one of the apparent moduli, $\overline{Z}$ its mean value and D_Z^2 its variance.

Finally, an important bias is found in the mean value given by all boundary conditions for small volume sizes, the value being different from the effective one obtained for large specimens. For small volumes, the average moduli obtained by simulations depend on the boundary conditions : KUBC produces results close to the upper Voigt bound, while SUBC gives results close to the lower Reuss bound.

(a)

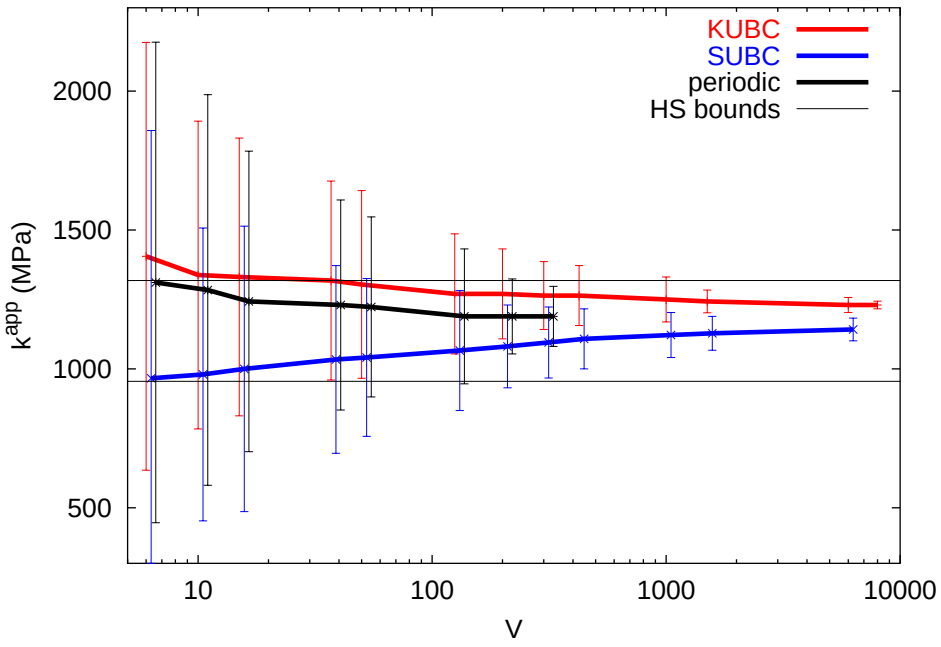

(b)

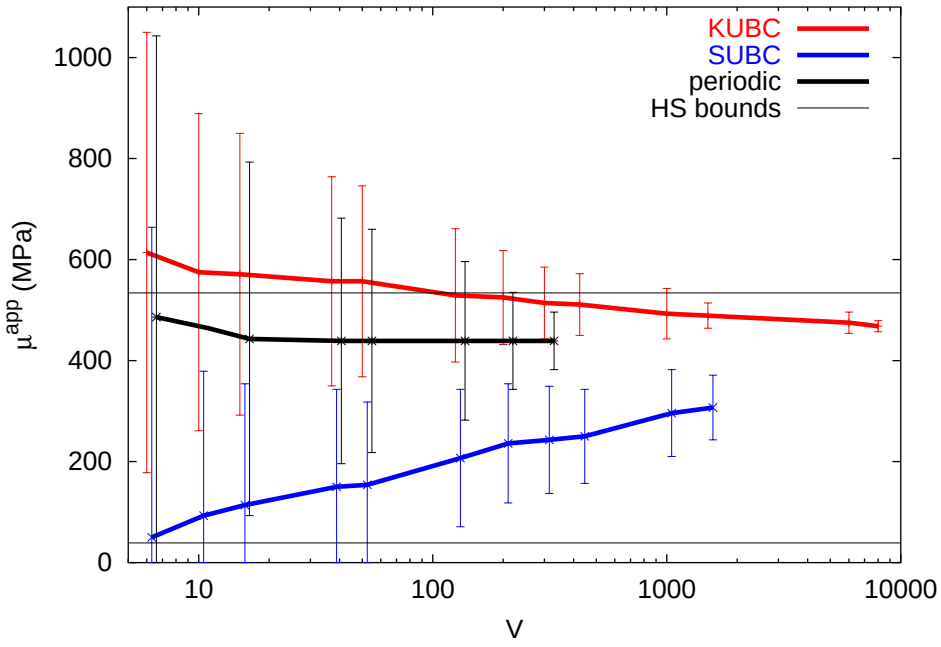

Figure I.7 : Mean values and intervals of confidence on the mean value for the bulk modulus k^{app} (a) and (b) for the shear modulus μ^{app}, as a function of domain size ($P_1 = 70\%$). Three different types of boundary conditions are considered. For clarity, the errorbars are slightly shifted around each studied domain size.

This bias is well–known ((Huet, 1990; Sab, 1992; Ostoja-Starzewski, 1998)). It must be taken into account for the definition of the RVE. The result is that the mean value computed on small specimens cannot represent the effective response for the composite material even using the periodic boundary conditions and a sufficient number of realizations. It appears also that for sufficiently large sizes, here around :

$$V = 15 \tag{I.78}$$

the mean value obtained with the periodic boundary conditions practically does not depend on the size of simulations.

c) Thermal Conductivity

Different thermal conductivities are now attributed to the phases of the Voronoï mosaic in order to predict the effective one. The same microstructures used in the study of the RVE for the volume fraction and elasticity ($P = 70\%$), are simulated to determine the apparent thermal properties. The aim of this part is to estimate the apparent thermal conductivity λ^{app} of the homogeneous equivalent medium, as a function of the size of the domain. The chosen thermal conductivities of the phases are

$$(\lambda_1, \lambda_2) = (2.44\text{W/mK}, 0.0244\text{W/mK}) \tag{I.79}$$

generating a contrast :

$$c_\lambda = \frac{\lambda_1}{\lambda_2} = 100 \tag{I.80}$$

The numerical results are obtained for three boundary conditions : uniform temperature gradient at the boundary (UGT), uniform heat flux at the boundary (UHF) and periodic boundary conditions (PERIODIC). Figure I.8 gives the mean apparent conductivities and associated variances as a function of the domain size. It shows that the dispersion of results decreases when the size of the volume increases. The mean value given by the periodic boundary conditions does not vary very much, as compared to the other boundary conditions. The three mean values converge towards the effective thermal conductivity :

$$\lambda^{eff} = 1.346\, W/mK \tag{I.81}$$

which is compared to Wiener's and Hashin–Shtrikman's bounds in table I.2. It can be noticed also that the self-consistent model (SC) gives a very good estimate (see table I.2). For small volume elements, the average thermal conductivity obtained by simulations depends on the boundary conditions : UGT gives results close to the upper Wiener bound $\lambda_{Wiener+}$, and UHF produces results close to the lower Wiener bound $\lambda_{Wiener-}$:

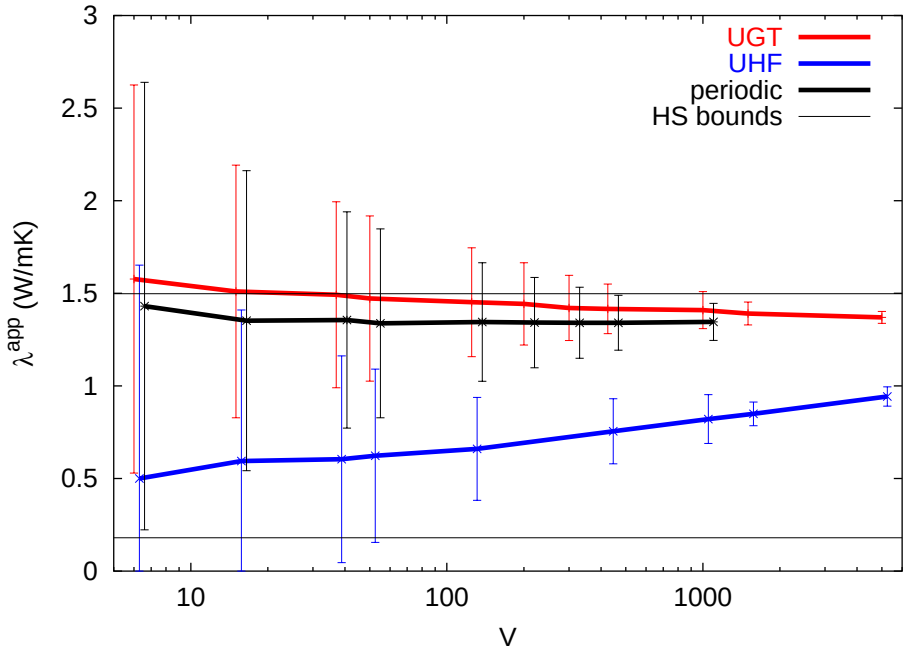

Figure I.8 : Dispersion and mean value of the apparent effective thermal conductivity as a function of domain size for different boundary conditions $(c = \lambda_1/\lambda_2 = 100,\ P = 70\%)$.

$$\lambda_{Wiener+} = P_1\lambda_1 + P_2\lambda_2 \tag{I.82}$$

$$\lambda_{Wiener-} = \frac{\lambda_1\lambda_2}{P_1\lambda_2 + P_2\lambda_1} \tag{I.83}$$

The self-consistent model gives the overall thermal conductivity λ^{eff} as the solution of the equation ((Beran, 1968)) :

$$\frac{\lambda_1 - \lambda^{eff}}{\lambda_1 + 2\lambda^{eff}}P_1 + \frac{\lambda_2 - \lambda^{eff}}{\lambda_2 + 2\lambda^{eff}}P_2 = 0 \tag{I.84}$$

We have to notice that, as for the apparent elastic moduli, volumes larger than $V = 15\ grains$ enable us to get an unbiased estimation of λ^{eff}.

I.5.2 Fluctuation of Effective Properties and Determination of the Integral Ranges

a) Volume Fraction

In this section, we come back to the variance of the volume fraction for the Voronoï mosaic, which is given by equation (I.54). In the three-dimensional case, it becomes :

$$D_P^2(V) = \frac{P(1-P)A_3}{V} \tag{I.85}$$

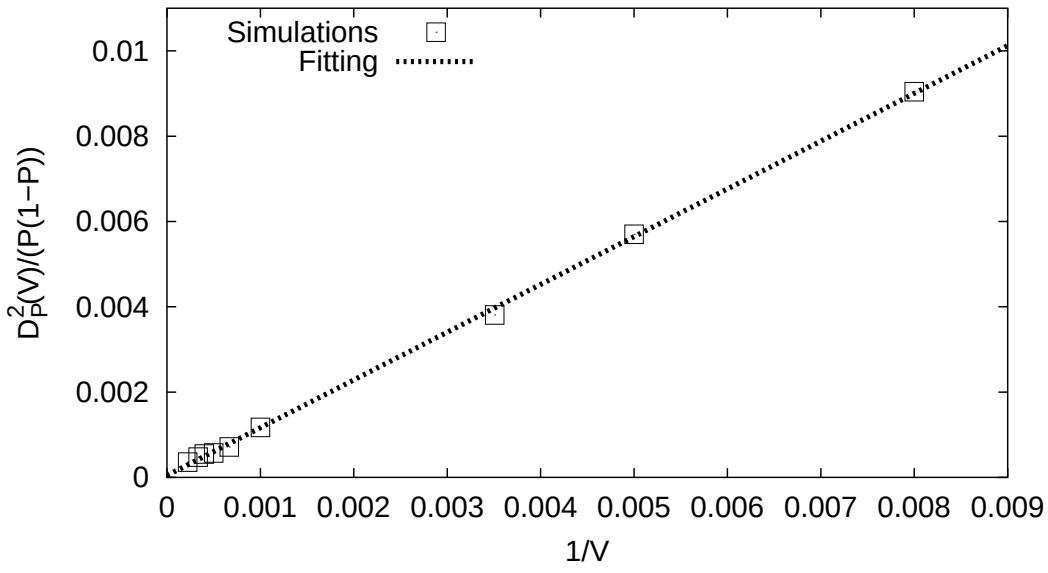

Figure I.9 : Fitting of $\frac{D_P^2(V)}{P(1-P)}$ as a function of the inverse of the volume of the field for volume fraction $P = 70\%$. The slope provides the value of the integral range A_3 for the volume fraction.

where P is the true volume fraction, A_3 is the integral range in $3D$ for the Voronoï mosaic, and V is the volume of the field containing N cells in average. With the convention that the average volume of one cell is one, the conditions $N = V$ can be substituted in equation (I.85). Figure I.9 is then used to identify A_3 from the simulations presented in section a).

Table I.3 gives the integral range A_3 estimated from figure I.9. It is close to the result given by the semi–analytical calculations deduced from ((Gilbert, 1962), equation (I.59)), with a larger experimental error for the case $P = 70\%$.

b) Elastic Moduli

As recalled in section I.3.2, the effective properties are defined from spatial averages of fields $Z(x)$ over a volume V. We will have to consider now fluctuations of the average values over different realizations of the random composite material inside the volume V.

In geostatistics, it is well known that for an ergodic stationary random function $Z(x)$, one can compute the variance $D_Z^2(V)$ of its average value $\bar{Z}(V)$ over the volume V (Matheron, 1971), (Matheron, 1989), (Lantuéjoul, 1991) :

$$D_Z^2(V) = D_Z^2 \frac{A_3}{V} \tag{I.86}$$

where D_Z^2 is the point variance of $Z(x)$ and A_3 is the integral range of the random function $Z(x)$. This is a generalization to any random function $Z(x)$ of the notion

Property	Integral Range A_3	Coefficient α
$P = 50\%$	1.178 ± 0.023	1.
$P = 70\%$	1.111 ± 0.014	1.
$P = 90\%$	1.177 ± 0.070	1.
k ($P = 70\%,\ E_1/E_2 = 100$) KUBC	2.088 ± 0.045	1.029 ± 0.051
k ($P = 70\%,\ E_1/E_2 = 100$) SUBC	1.267 ± 0.023	0.915 ± 0.044
k ($P = 70\%,\ E_1/E_2 = 100$) PERIODIC	1.020 ± 0.011	0.780 ± 0.037
μ ($P = 70\%,\ E_1/E_2 = 100$) KUBC	1.863 ± 0.046	0.992 ± 0.049
μ ($P = 70\%,\ E_1/E_2 = 100$) SUBC	0.820 ± 0.026	0.735 ± 0.066
μ ($P = 70\%,\ E_1/E_2 = 100$) PERIODIC	1.322 ± 0.009	0.763 ± 0.021
k ($P = 70\%,\ E_1/E_2 = 1000$) PERIODIC	1.650 ± 0.017	0.900 ± 0.038
μ ($P = 70\%,\ E_1/E_2 = 1000$) PERIODIC	2.097 ± 0.015	0.862 ± 0.023
k ($P = 50\%,\ E_1/E_2 = 100$) PERIODIC	1.589 ± 0.050	0.875 ± 0.010
μ ($P = 50\%,\ E_1/E_2 = 100$) PERIODIC	1.637 ± 0.016	1.009 ± 0.036
λ ($P = 70\%,\ \lambda_1/\lambda_2 = 100$) UGT	2.335 ± 0.258	1.070 ± 0.021
λ ($P = 70\%,\ \lambda_1/\lambda_2 = 100$) UHF	2.036 ± 0.407	0.978 ± 0.031
λ ($P = 70\%,\ \lambda_1/\lambda_2 = 100$) PERIODIC	2.619 ± 0.200	1.033 ± 0.018

Table I.3 : Values of the integral range A_3 and of the coefficient α for different properties and different boundary conditions, identified from the simulation results.

introduced for the volume fraction in section I.3.2.

The scaling law (I.86) is valid for an additive combination of the variable Z over the region of interest V, when its size is such that :

$$V > A_3 \tag{I.87}$$

and when A_3 is finite.

For an infinite integral range, V can be replaced in many cases by V^α, with :

$$\alpha \neq 1 \tag{I.88}$$

in relation I.86) ((Lantuéjoul, 1991)).

As the composition of elastic moduli in the change of scale is not additive in general, relation (I.86) cannot be applied. Instead we propose to test a power law (called “model” in what follows) according to the relation :

$$D_Z^2(V) = D_Z^2 \left(\frac{A_3}{V}\right)^\alpha \tag{I.89}$$

A similar relation was proposed and tested by (Cailletaud et al., 1994). In the case of a two-phase material with elastic property Z_1 for phase 1 and Z_2 for phase 2, the point variance D_Z^2 of the random variable Z is given by :

$$D_Z^2 = P(1-P)(Z_1 - Z_2)^2 \tag{I.90}$$

The relation (I.89) becomes :

$$D_Z^2(V) = P(1-P)(Z_1 - Z_2)^2 \left(\frac{A_3}{V}\right)^{\alpha} \tag{I.91}$$

For the elastic properties (I.68) and (I.69) chosen in this work, the equation (I.90) yields :

$$D_k^2 = 583329\ (MPa)^2 \tag{I.92}$$

and :

$$D_\mu^2 = 190784\ (MPa)^2 \tag{I.93}$$

Equation (I.89) can be written as :

$$log(D_Z^2(V)) = -\alpha\ log(V) + (log(D_Z^2) + \alpha\ log(A_3)) \tag{I.94}$$

Our data were fit to relation (I.94) for the elastic moduli k^{app} and μ^{app} and different boundary conditions. The found parameters A_3 and α are given in table I.3. The quality of the model can be seen in figure I.10, where the variances of simulated results and the model are compared for all considered boundary conditions. The power law is especially well-suited for PERIODIC boundary conditions.

It is clear, from the coefficients given in table I.3, that the proposed scaling law in relation (I.89) can be accepted for our simulations. The value of the integral range depends on the boundary conditions. It is of the order of the integral range of the volume fraction for periodic and SUBC conditions. The largest integral range of the elastic moduli is found for the periodic boundary conditions and the coefficient α is close to (but generally smaller than) 1. It means that the variance decreases more slowly with the volume than the variance of the volume fraction in all cases. Note that the value of the coefficient α found by (Cailletaud et al., 1994) is also close to 1 for a $2D$ random mosaic. Another conclusion is that larger domains (or more realizations) must be used to estimate the elastic moduli with a given precision, for SUBC than for KUBC boundary conditions. This will be illustrated later.

I.5.3 Effect of the Volume Fraction and Contrast on the Integral Ranges

The apparent properties and integral ranges obtained for elasticity depend on the volume fraction of phases. A second volume fraction :

$$P_1 = P_2 = P = 50\% \tag{I.95}$$

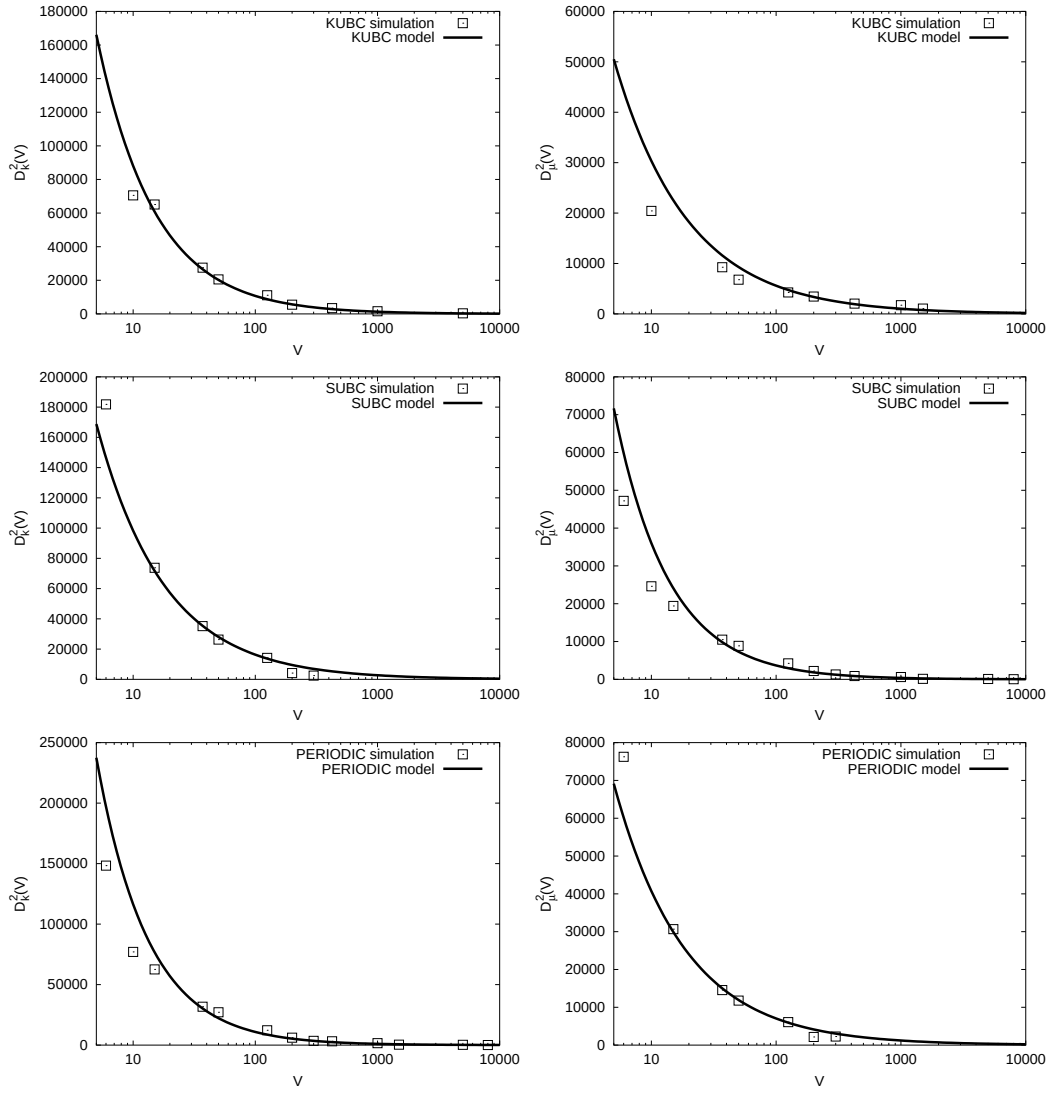

Figure I.10 : Variances of the apparent elastic moduli k^{app} and μ^{app} for different boundary conditions : simulations and model.

is investigated here in addition to the previous one $P_1 = 70\%$. These microstructures are also simulated and introduced in the finite element software with the same mechanical properties, given by (II.21) and (II.22). The objective is to study the effect of the volume fraction on the integral ranges of the apparent bulk and shear moduli k^{app} and μ^{app}. The numerical simulations using the finite element method were performed in this case only for the PERIODIC boundary conditions. The mean values and variances are given in figure I.11 as a function of the domain size. The mean value varies slowly as a function of the size of the domain. Again, an important bias in the mean value for small sizes of specimens is observed. For domain sizes larger than :

$$V = 37\ grains \tag{I.96}$$

The mean values are almost constant, and coincide with the effective properties. This size is larger than for $P = 70\%$ (where $V \simeq 15$ according to figure I.7). The values of the integral ranges and of the coefficient α, obtained by identification of the power law model (equation (I.89)) from the numerical results, are given in the table I.3. It can be noticed that the values of the integral ranges and those of the coefficient α obtained in the case of $P = 50\%$ are larger than those obtained in the case of $P = 70\%$, for a given contrast of properties. The coefficients α remains close to 1 for all investigated volume fractions.

Another important source of fluctuations of apparent moduli of finite domains is the contrast of properties $c = E_1/E_2$. So far, only the case $c = 100$ has been investigated. Let us now consider a contrast $c = 1000$ (E_1 keeping its value 2500 MPa), for $P = 70\%$. The objective is to study the effect of the contrast on the integral ranges of the effective elastic properties. The numerical simulations are performed for PERIODIC boundary conditions. Results are shown in figure I.12. A bias in the mean value in this case is observed when :

$$V < 15\ grains \tag{I.97}$$

(as in the case of a contrast $c = 100$). The values of the integral ranges and of the coefficient α, obtained by fitting the numerical results, using the model (equation (I.89)), are given in table I.3. The values of the integral ranges obtained in the case of $(c = 1000,\ P = 70\%)$ are much larger than those obtained in the case of $(c = 100,\ P = 70\%)$. The values of the coefficient α remain close to 1.

Thermal Conductivity

The power law model proposed in the case of elastic properties (equation (I.89)) can be used also for apparent thermal properties. The point variance D^2_λ is :

$$D^2_\lambda = P(1-P)(\lambda_1 - \lambda_2)^2 = 1.2253\ (W/mK)^2 \tag{I.98}$$

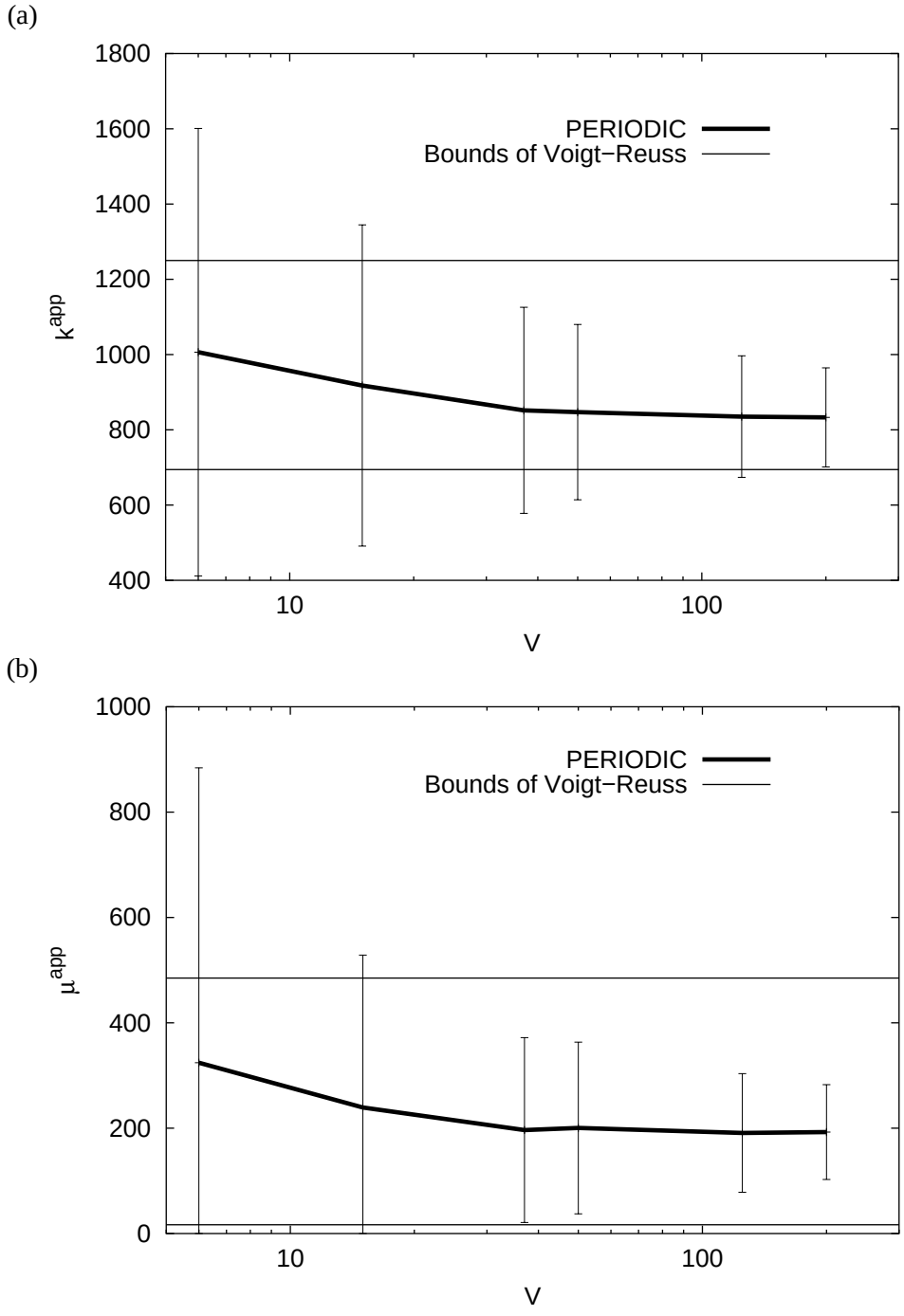

Figure I.11 : Dispersion and mean value of the apparent elastic properties (given in MPa) as a function of the domain size for periodic boundary conditions in the case of $(c = 100,\ P = 50\%)$, (a) evolution of k and (b) evolution of μ.

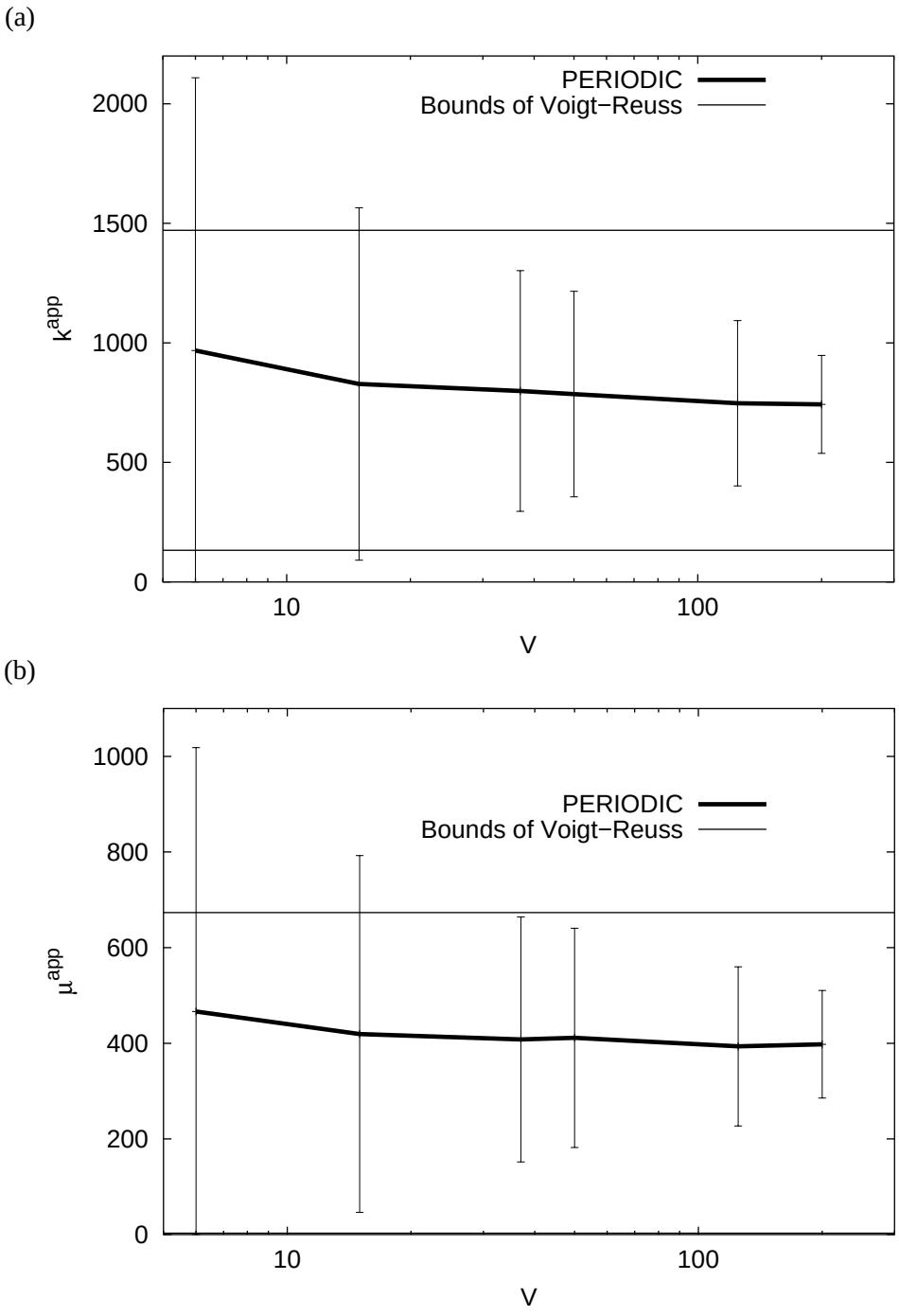

Figure I.12 : Dispersion and mean value of the apparent elastic properties as a function of the domain size for periodic boundary conditions in the case $(c = 1000,\ P = 70\%)$: (a) evolution of k^{app} and (b) evolution of μ^{app}.

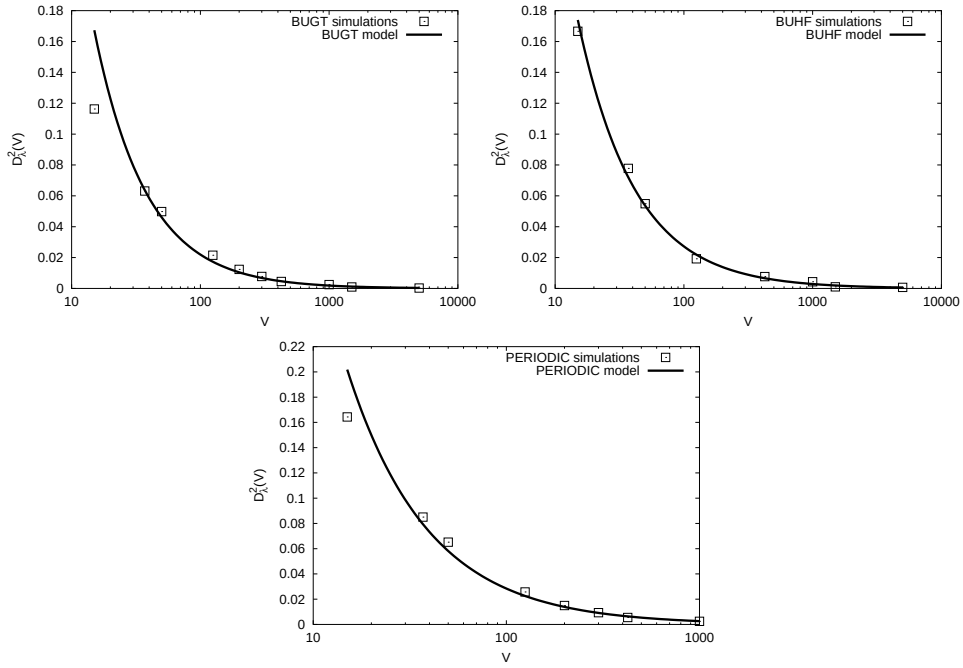

Figure I.13 : Variances of apparent thermal conductivity λ^{app} for different boundary conditions $P = 70\%$.

The values of the integral ranges and of the coefficient α identified from the simulations are given in table I.3 for different boundary conditions. They are found to depend on the type of boundary conditions. The largest integral range for the thermal conductivity is obtained for the periodic boundary conditions and the coefficient α is close to 1. These parameters are larger than for the case of elasticity. Figure I.13 shows the quality of the model. The power law is especially well-suited for periodic boundary conditions.

I.6 Determination of the Size of the Representative Volume Element

When considering a material as a realization of a random set or of a random function, we will show that the idea that there exists one single possible minimal RVE size must be abandoned. Instead, the size of a RVE can be defined for a given physical property, a given contrast and, above all, a given precision in the estimation of the effective properties and given number of realizations that one is ready to generate. This is explicited later for the three situations encountered in the previous sections.

The size of a RVE for an estimated property Z can be related directly to the precision of the mean value of the results of different realizations for each domain size. So, theoretically, if the domain V is a RVE for the property Z, the dispersion

must vanish. In practice one must determine the size of the RVE for a *given error* ϵ.

In the theory of samples, the absolute error ϵ_{abs} on the mean value obtained with n independent realizations of volume V is deduced from the interval of confidence by:

$$\epsilon_{abs} = \frac{2D_Z(V)}{\sqrt{n}} \tag{I.99}$$

Hence the relative error ϵ_{rela} is :

$$\epsilon_{rela} = \frac{\epsilon_{abs}}{Z} = \frac{2D_Z(V)}{Z\sqrt{n}} \tag{I.100}$$

The size of the RVE can now be defined as the volume for which for instance :

$$n = 1\ realization \tag{I.101}$$

is necessary to estimate the mean property Z with a relative error :

$$\epsilon_{rela} = 1\% \tag{I.102}$$

provided we know the function $D_Z(V)$.

Alternatively, we can decide to operate on smaller volumes (provided no bias is introduced), and consider n realizations to obtain the same relative error. Equation (I.100) gives :

$$n = \frac{4D_Z^2(V)}{Z^2\epsilon_{rela}^2} \tag{I.103}$$

I.6.1 Volume Fraction

In the case of the volume fraction, the exact mean value $P^{eff} = P$ is known. The relative error is given as a function of the sampled volume V by:

$$\epsilon_{rela}(V) = \frac{2D_P(V)}{P} = 2\sqrt{\frac{(1-P)A_3}{VP}} \tag{I.104}$$

which corresponds to the application of equation (I.99) for :

$$n = 1\ realization \tag{I.105}$$

This is illustrated in figure I.14 in the case of a volume fraction $P = 70\%$. Using equation (I.104), the minimum domain size that is necessary to reach a given precision are shown, for three different volume fractions, in table I.4.

The size of a RVE for the estimated volume fraction can be related directly to the precision of the mean value of the results of different realizations for each domain size. Figure I.14 shows three examples of this measurement: one obtains :

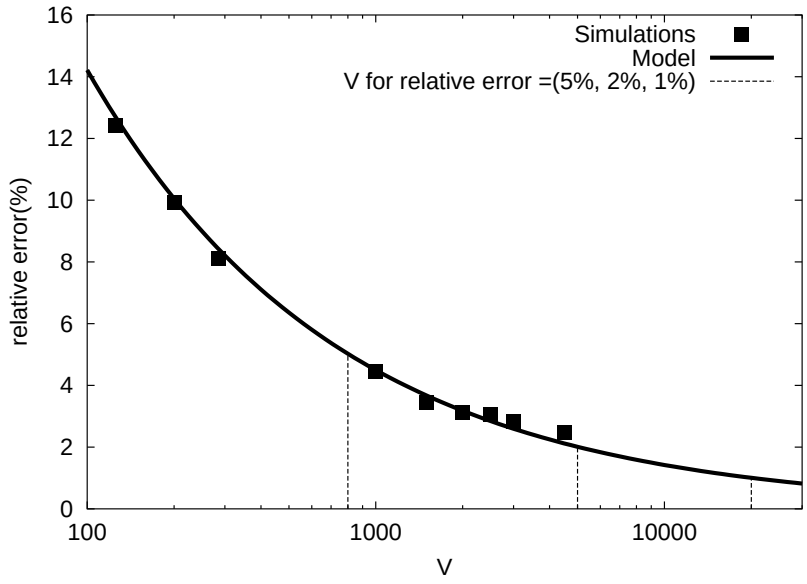

Figure I.14 : Relative precision ϵ_{rela} for volume fraction $P = 70\%$ and $n = 1$ realization : it decreases when the size of the domain increases.

Volume Fraction P	1%	2%	5%	10%
50%	47000	11790	1880	470
70%	20000	5050	800	200
90%	5240	1300	210	52

Table I.4 : RVE size for a given relative precision ϵ_{rela} and $n = 1$ realization of the estimated volume fraction, for three different volume fractions.

$$V_{5\%}^{RVE} = 800,\ V_{2\%}^{RVE} = 5050 \tag{I.106}$$

and :

$$V_{1\%}^{RVE} = 20000 \tag{I.107}$$

for the relative precision $\epsilon_{rela} = 5\%$, $\epsilon_{rela} = 2\%$ and $\epsilon_{rela} = 1\%$ of the mean value of the volume fraction, respectively.

The size of the RVE can also be defined as the volume for which for instance :

$$n = 10\ realizations \tag{I.108}$$

are necessary to estimate the mean property with a confidence $\epsilon_{rela} = 1\%$. Equation (I.104) gives :

$$V = \frac{4(1-P)A_3}{nP\epsilon_{rela}^2} \tag{I.109}$$

For $P = 70\%$ one finds $V^{RVE} = 2000$.

Conversely, the same equation also shows that one must use about $n = 1350$ realizations to find the mean value with an error $\epsilon_{rela} = 1\%$ for a fixed $V^{RVE} = 15$.

I.6.2 Elastic Moduli

In the case of effective elastic moduli, the exact mean value and variance for a given domain size are *a priori* unknown. Using the equation (I.89), the absolute error on the mean value can be evaluated as :

$$2D_Z(V) = 2D_Z\sqrt{\left(\frac{A_3}{V}\right)^{\alpha}} \tag{I.110}$$

where Z stands here for k^{app} or μ^{app}. The absolute error can be deduced from figure I.10 that shows the power law model and the variances of simulations as a function of domain size, for different boundary conditions.

The first important remark is that for the same absolute error, the periodic boundary conditions require the largest domain size, compared to kinematic uniform boundary conditions (KUBC) and static uniform boundary conditions (SUBC) for k and μ. This is due to higher fluctuations of apparent properties obtained with these conditions. The kinematic uniform boundary conditions require a smaller domain size than the static uniform boundary conditions for the same absolute error.

Using equation (I.99) in the case of the elastic moduli k^{app} and μ^{app}, the absolute error for the mean value is obtained with a sample of n realizations, Z standing for

k^{app} or μ^{app}. Hence the number of realizations n necessary for the estimation of the property with a given absolute error ϵ_{abs} and a volume V is:

$$n(V) = \frac{4}{\epsilon_{abs}^2} D_Z^2 \left(\frac{A_3}{V}\right)^{\alpha} \tag{I.111}$$

One must insist on the fact that the absolute error corresponds to the estimation of the mean apparent moduli which have been found to depend in general on the domain size and do not necessarily coincide with the wanted effective property, especially for small domain sizes. This corresponds to a bias of the estimation. This bias is bounded by the difference of the estimations obtained using KUBC and SUBC, since these boundary conditions can be shown to provide bounds of the the effective properties ((Huet, 1990; Hazanov and Huet, 1994)).

From the available results of figure I.7, the smallest domain size for which the bias can be neglected is :

$$V = 15\ grains \tag{I.112}$$

for k^{app} and μ^{app} in the case of periodic boundary conditions. For the conditions KUBC and SUBC, volumes larger than 1000 are necessary to obtained unbiased mean values, i.e. mean apparent moduli that almost coincide with the wanted effective ones.

Using the equation (I.100), and for a volume V providing unbiased moduli, we deduce the relative precision of the effective property Z^{eff} (namely the effective bulk modulus k^{eff} or the effective shear modulus μ^{eff}). Hence, the number n of realizations that must be considered is deduced from equations (I.103) and (I.110). This is illustrated in figure I.15 for $\epsilon_{rela} = 1\%$. For a given precision, the number of realizations decreases when the domain size increases. The periodic boundary conditions require the largest number of realizations, compared with other boundary conditions.

Let us give two explicit examples of the use of equation (I.103) for two unbiased volumes and periodic boundary conditions : $V = 50$ and $V = 125$. The minimal numbers n of realizations to obtain the overall bulk modulus k^{eff} and shear modulus μ^{eff}, for a given precision ϵ_{rela}, are given in table I.5.

Conversely, the minimum size of the RVE can be determined for a given ϵ_{rela} and a given number $n = 10$ of realizations. The results are shown on figure I.15. When $\epsilon_{rela} = 1\%$, it can be seen that one must take about $V^{RVE} = 13340$ (from the result given by the periodic boundary conditions) for k^{app} and $V^{RVE} = 71253$ for μ^{app}.

Using such sizes in a finite element code is rather prohibitive. One would prefer smaller volumes. This requires however a sufficient number of realizations. By

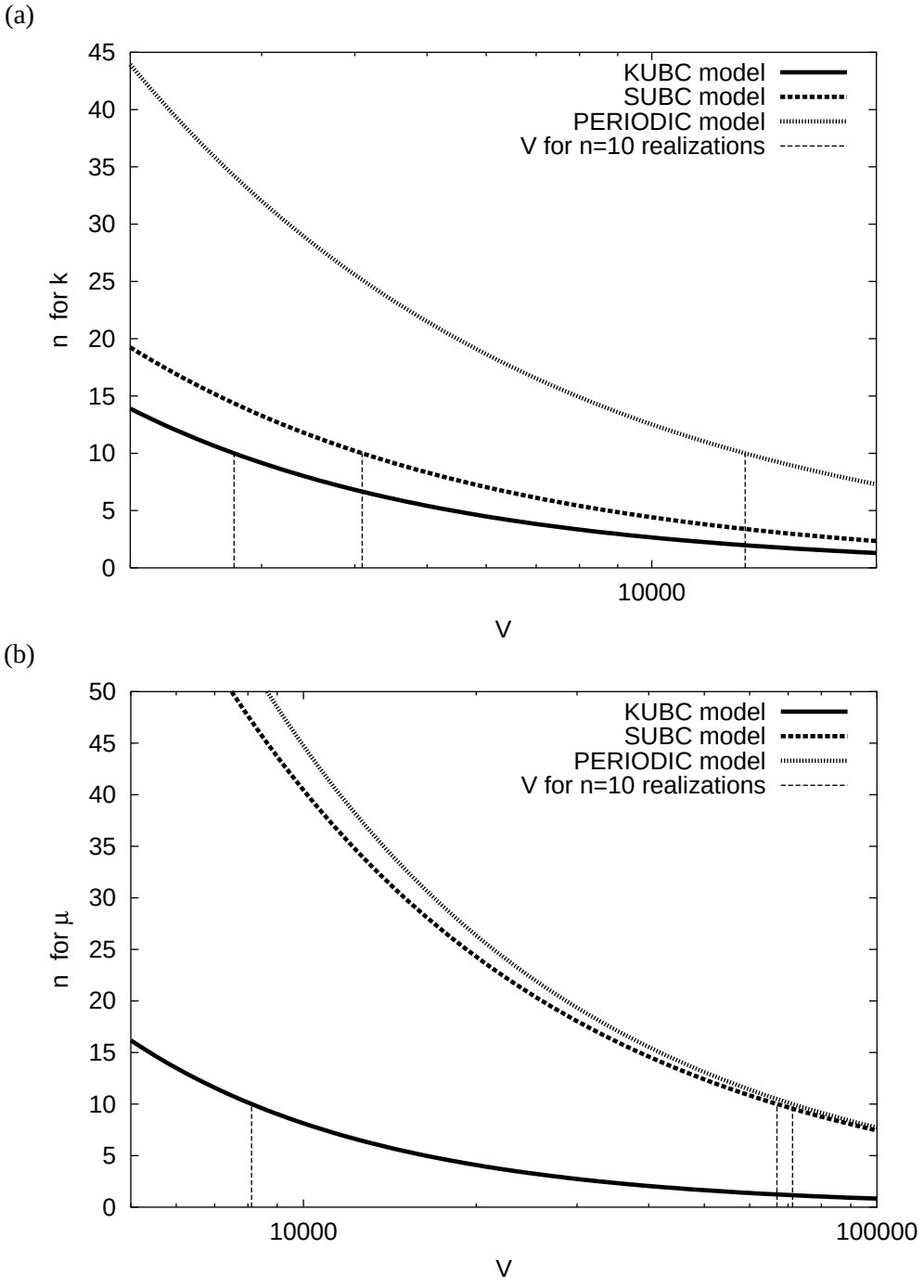

Figure I.15 : Number of realizations as a function of the domain size for a given relative error $\epsilon_{rela} = 1\%$: (a) case of k^{app}, (b) case of μ^{app}.

Relative Precision	$\epsilon_{rela} = 1\%$	$\epsilon_{rela} = 2\%$	$\epsilon_{rela} = 5\%$	$\epsilon_{rela} = 10\%$
Bulk Modulus (V=50)	700	175	28	7
Shear Modulus (V=50)	2500	625	100	25
Bulk Modulus (V=125)	400	100	16	4
Shear Modulus (V=125)	1300	325	52	13
Thermal Conductivity (V=50)	1950	490	80	20
Thermal Conductivity (V=125)	765	190	30	8

Table I.5 : Minimal number of realizations necessary to estimate the effective elastic moduli and thermal conductivity with given relative precision, for given volumes $V = 50, 125$ (for periodic boundary conditions, $P = 70\%$, $c = 100$).

comparison between these results and those for volume fraction in table I.4, it turns out that larger volumes are required to estimate the elastic moduli than to measure the volume fraction with the same precision (over three times more). In the present study, the shear modulus requires a larger number of realizations than the bulk modulus, for a given precision.

I.6.3 Thermal Conductivity

Similarly to the case of elastic properties, the absolute error on the mean value of apparent conductivity is given by relation (I.110). For the same absolute error on the mean value, the PERIODIC boundary conditions require the largest domain size compared to the other boundary conditions. The UGT conditions give a smaller domain size than the uniform heat flux for the same absolute error. The number of realizations n for a given relative error ϵ_{rela} on the effective conductivity λ^{eff} is deduced from equation (I.100). It is illustrated in figure I.16 for $\epsilon_{rela} = 1\%$. For a given precision, the required number of realizations decreases when the volume increases. The PERIODIC boundary conditions require the largest number of realizations, as compared to other boundary conditions. The size of the RVE, considered for instance as the volume requiring only $n = 10$ realizations, for $\epsilon_{rela} = 1\%$ is about :

$$V = 5504\ grains \tag{I.113}$$

obtained with PERIODIC boundary conditions.

One must again insist on the fact that the mean value of the apparent conductivity depends on the domain size. Volumes larger than $V = 100$ are necessary to obtain a mean apparent conductivity which is not too far from the effective one λ^{eff}, for the conditions BUGT and BUHF. The smallest domain size giving an unbiased mean value of apparent conductivity is about 10 for PERIODIC conditions. Using the equation (I.103) in the case of the effective thermal conductivity, the minimal numbers n of realizations to evaluate the effective thermal conductivity with a given precision ϵ_{rela}, are given in table I.5 for the fixed sizes $V_1 = 50$ grains and $V_2 = 125$ grains.

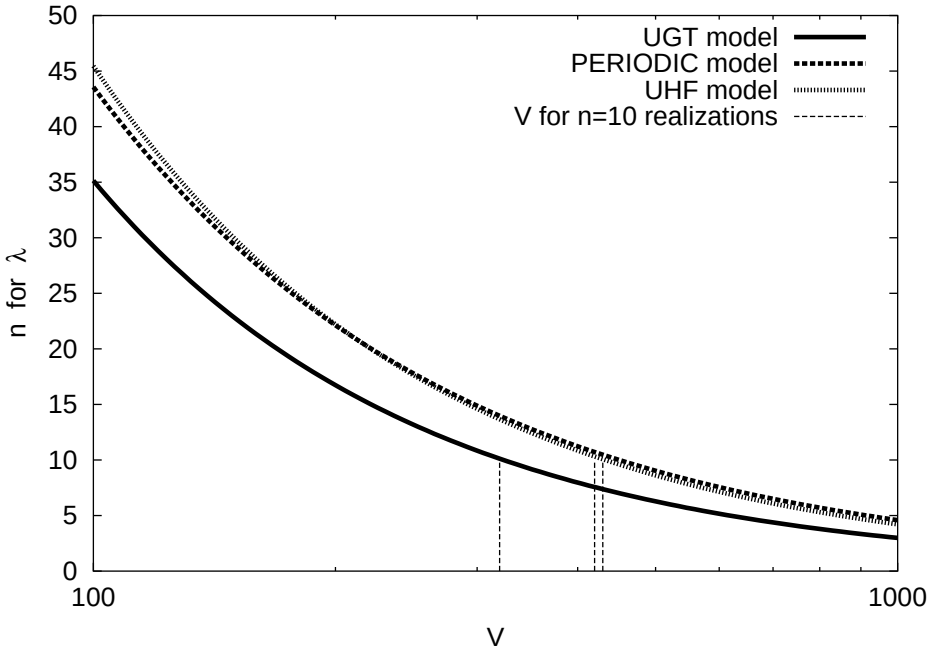

Figure I.16 : Number of realizations as a function of the domain size, necessary to obtain an absolute precision $\epsilon_{abs} = 0.05\ W/mK$ on the mean value of apparent thermal conductivity $P = 70\%$.

I.7 Conclusions

The effective linear properties of random composites can be determined not only by numerical simulations on large volume elements of heterogeneous material, but also as mean values of apparent properties of rather small volumes, providing that a sufficient number of realizations is considered. This is very important, since computations on large volumes are usually prohibitive. This corresponds also to an enlarged definition of Representative Volume Element. Its size V^{RVE} must be considered as a function of five parameters: the physical property Z, the contrast of properties c, the volume fractions of components, the wanted relative precision ϵ_{rela} for the estimation of the effective property and the number n of realizations of the microstructure associated with computations that one is ready to carry out. It depends also *in fine* on the special morphology of distribution of phases. Conversely, one can also choose a volume V^{RVE} allowing as many numerical simulations as necessary. The proposed methodology gives then the number of realizations that are necessary to reach a given precision ϵ_{rela} (see for instance equation (I.111)).

However, the chosen volume V^{RVE} cannot be taken as small as one may wish, because there exists in general a bias in the estimation of the effective properties. This bias is due to the type of boundary conditions. The mean apparent properties computed on finite size domains do not coincide with the effective ones if the domain size is too small. In the case of linear elasticity for instance, kinematic uniform boundary conditions overestimate the effective proper-

ties, whereas static uniform boundary conditions underestimate them. For both thermal conductivity and elasticity, the bias introduced by the periodic boundary conditions is found to be much smaller than for the other boundary conditions. In the case of Voronoï mosaics considered in this work, for domain sizes larger than $V = 15\ grains$ (resp. $V = 37\ grains$) for volume fraction $P_1 = 70\%$ (resp. $P_1 = 50\%$), the mean apparent property do not differ significantly from the effective one. However the dispersion of apparent properties obtained by periodicity conditions is always found to be larger than for the other types of boundary conditions. This means that more realizations are necessary (about 1700 for elasticity with $V = 15, \epsilon_{rela} = 5\%, P_1 = 70\%, c_E = 100$).

For the determination of RVE sizes of a given microstructure, the proposed methodology can be summarized as follows :

- generate different realizations of the microstructure for 4 to 5 different volume sizes V;
- submit each microstructure to loading with for instance PERIODIC boundary conditions and record the obtained apparent properties;
- compute mean value and variance of apparent property for the considered volume sizes; check that the number of realizations was sufficient for each volume (apply the sampling rule (I.99));
- identify the integral range A_3 and power α in model (I.110);
- set the wanted precision for the estimation of effective property ϵ_{rela} and a number of realizations n; use the model to deduce the final size V^{RVE}.

The notion of integral range plays the central role in the method. For additive properties (like volume fraction or mass density), it is simply related to the variance and domain size and does not depend on the effective property itself but only on the morphology. For more complex physical properties like elasticity and thermal conductivity, a power law model was proposed and identified. The generalized integral range A_3 is found to depend on the volume fraction, the contrast in properties, and the type of boundary conditions. The model seems to fit better to the data in the case of PERIODIC boundary conditions. This can be related to the fact that the observed bias in the estimation of effective properties is less pronounced in the case of periodic boundary conditions.

The case of three-dimensional Voronoï mosaics was studied in details, as an example of random microstructures. This model is relevant for polycrystals but also for two–phase materials in which both phases percolate. The fluctuations of apparent moduli on small domains can be attributed to the percolation level of the hard phase for the considered realization. This could explain the larger values found for the integral range A_3 found for the volume fraction $P_1 = 50\%$ than for $P_1 = 70\%$. This is synonymous of a larger dispersion of apparent moduli and finally to larger RVE sizes. Similarly, the increase in the contrast of properties leads to an increase

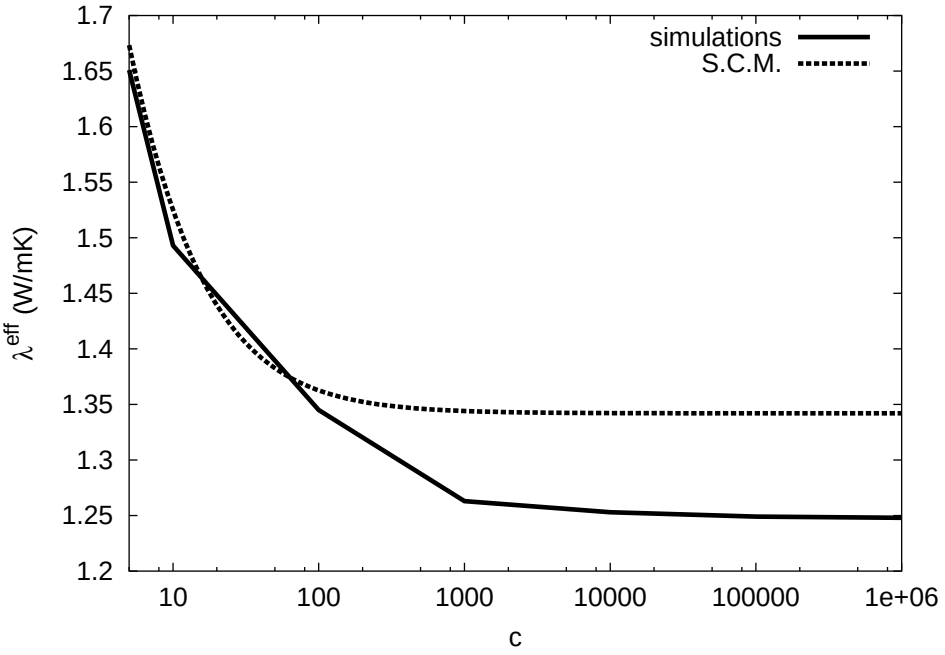

Figure I.17 : Effective thermal conductivity of Voronoï mosaics as function of the contrast of properties c (the thermal conductivity $\lambda_1 = 2.44W/mK$ is kept constant, $P_1 = 70\%$) : comparison with the self–consistent estimate. The numerical estimation of the effective conductivity is obtained by finite element simulations with periodic boundary conditions on a volume $V = 125$ and $n = 1020$ realizations for each value of c. The mean value is plotted.

of the integral range and of the RVE size. The RVE sizes found for different properties can be compared : the minimal domain size for a relative precision of 1% in the estimated property, $n = 10$ realizations and for $P_1 = 70\%, c_E = 100$ are $V = 2000, 5504, 13340, 71253$ for effective volume fraction, thermal conductivity, bulk modulus and shear modulus, respectively, in increasing order of volume size. These results depend on the specific values chosen for the material parameters of the components in the simulation, and do not have a general value. Note that the self–consistent estimate is often advocated to be a good model for polycrystalline microstructures. Indeed, a rather good agreement between the found effective properties of two–phase Voronoï mosaics and the self–consistent model can be seen in table II.6. This is however not the exact solution (for elasticity nor thermal conductivity) and the difference between numerical simulations and the self–consistent estimate is found to increase with the contrast of properties, as can be seen in figure I.17 for thermal properties. Another example of bi-continuous microstructure that is not described properly by the self–consistent scheme can be found in (Roberts and Garboczi, 1999), where computational homogenization methods are also used.

The procedure must now be applied to other microstructures and random models. It can also be applied to real three–dimensional images of heterogeneous materials obtained by tomography or confocal microscopy for instance ((Forest et al.,

2002)). Good agreement has been obtained between experimental results and the numerical estimation of the effective elastic and thermal properties of a two–phase material from food industry ((Kanit et al., 2003b)). In particular, it is shown in this forthcoming paper and in the next chapter that the methodology can be used to assess the representativity of available $3D$ images. In such cases, it may be necessary to estimate the properties using images smaller than the size of the deterministic RVE. On the other hand, the advantage of the method is that it is applicable also to nonlinear constitutive behaviors of the components (viscoplasticity, elastoplasticity). An increased dependence of the integral range on the contrast of properties may be expected in the nonlinear case, as a result of a higher heterogeneity of the fields.

Chapter -II-

COMPUTATION OF THREE-DIMENSIONAL REAL MICROSTRUCTURES : EFFECTIVE PROPERTIES AND REPRESENTATIVITY OF SAMPLES

Contents

II.1 Introduction

Applying a materials science approach to the characterization of composites of food industry requires consideration of its constituents on a microstructural level. Any change in the composite formulation or processing parameters gives rise to different morphologies of microstructures, which in turn dictate both the mechanical and sensory properties. Hence, via materials science, relationships may be established between the microstructure of a composite, and either physical properties or the sensory attributes (Colworth, 2000). These data may then be used as a predictive tool for the development of new composite microstructures that satisfy predetermined sensory criteria.

Digital image-based modeling technique for the finite element method is largely used in (Terada et al., 2000). It was developed by Hollister and Kikuchi (Hollister and Kikuchi, 1994) for a study of bone tissue as an example of computation of real composite materials. This technique is utilized for evaluating both macro and micro-mechanical behavior of composite materials that are given by $2D$ images (Terada et al., 1997). The finite element model obtained in this process is the direct representation of the scanned image using, for example, two-dimensional micrographs of real composite materials along with image-processing software. Thus, the homogenization analysis can reflect the effects of the original geometrical configuration.

In this work we propose a detailed study of the effective physical properties of a two-phase composite from food industry, regarding elastic properties : shear modulus μ^{eff} and bulk modulus k^{eff} and of the thermal conductivity λ^{eff}. These properties will be estimated by means of numerical simulations by the finite element method, using directly real images of the material in $3D$. The principle is to transform the real images obtained by confocal microscopy, and that are multilevel of gray into binary images. Two types of materials are studied to quantify the effect of the morphology on the macroscopic physical properties : one material called SA containing special additive, one material SB without additive. The additive affects only the morphology of the phases and not their behaviors. Both materials are made of a hard phase P_1 and a soft phase P_2 with a high contrast in elastic and thermal properties.

A strong difference in the effective properties is found experimentally for samples SA and SB; although the volume fractions of hard phase are the same in both materials. It will be shown that our finite element computations are able to reproduce the experimental results, based on the knowledge of the actual morphology. The last part is devoted to the study of geometrical and mechanical percolation ef-

fects associated with both microstructures.

For confidentiality reasons, the physical nature of the phases cannot be given. However, their mechanical and thermal properties are explicitly given in section II.2.2.

After a general description of morphological and physical aspects of the materials, we study the mesh density effect on finite element computations. We try to get an acceptable convergence in the computed apparent physical properties of the heterogeneous material. Our study is in $3D$, but a small comparison with the mesh density in $2D$ is also presented.

We begin with direct simulations on the set of all available microstructures, and quantify the anisotropy existing in the apparent elastic matrices. The obtained results allow us to quantify the representativity of the sizes of the samples. For that purpose, we apply some results of Huet (Huet, 1990), (Huet, 1991) and (Hazanov and Huet, 1994) on the apparent properties obtained by samples of heterogeneous material, smaller than the size of the RVE.

The statistical study proposed in chapter 1 and applied to the case of Voronoï mosaics is applied here to the real microstructures. This enables us to find the necessary sizes for the used samples and to compare them with experimental sizes to quantify the representativity of samples.

We close this chapter by a quantitative study of the phenomenon of the geometrical percolation on our real images. We present an example explaining phenomena of strain localization bands, while studying the percolation in the field of local strains, thus defining a notion of mechanical percolation.

II.2 Presentation of the Microstructures from Food Industry

II.2.1 Morphological Description

Experimental batches of our composite material are produced in ten blocks of $500\ g$ which are then stored at -18^0C (Bron et al., 1999). They are used for four-point bending tests and confocal imaging.

Two different types of microstructures are presented and studied here. The first one with additive (SA), the second one without additive (SB). The additive only changes the morphology of the microstructure, not the volume fraction of phases nor the properties of the individual phases. Three samples of each microstructure (SA_1 SA_2 SA_3, SB_1 SB_2 SB_3) are available. The samples without additive contain fairly round hard phase crystals while the samples with additive have more elongated hard phase crystals. Examples of each type of microstructure are given in figure II.1. The size of the images is $250\mu m \times 250\mu m \times 30\mu m$. The shortest direction is called OZ.

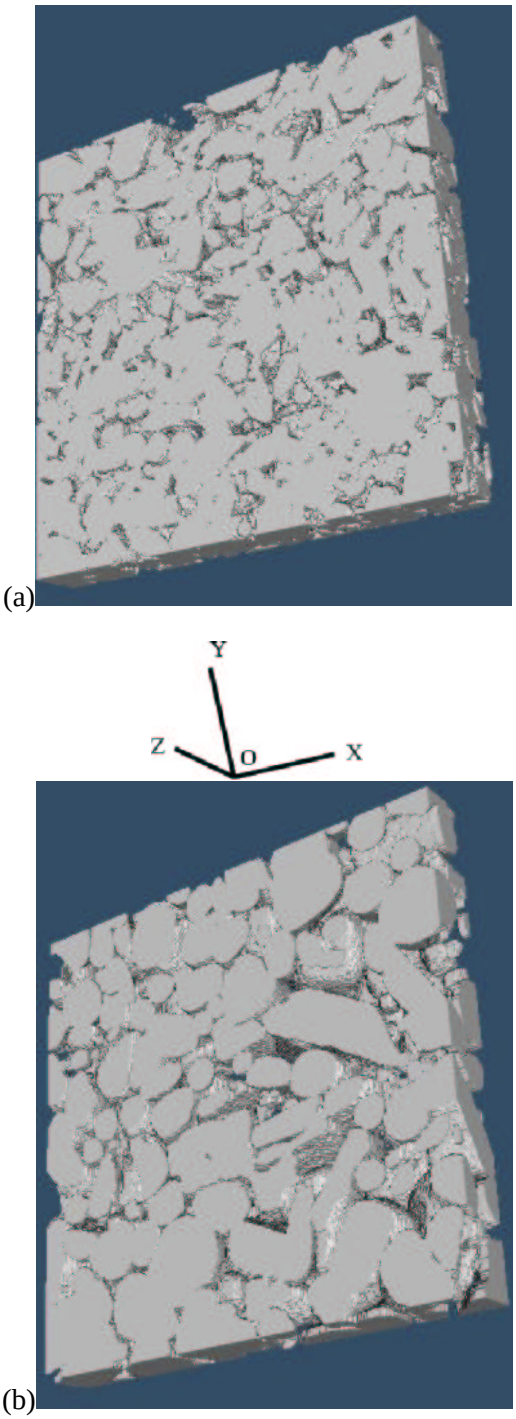

Figure II.1 : Examples of studied microstructures obtained by confocal imaging in $3D$, the size of the image is $250 \times 250 \times 30$ μm. The volume fraction of hard phase (in grey color) is about 70%. (a) Sample with additive SA and (b) sample without additive SB.

a) Segmentation

A difficult problem with the experimental micrographs is to differentiate the two different phases. This operation called *segmentation* or *threshold operation* takes a grey level image and transforms it into a binary image (each pixel is then or 0 or 1). The dark noise in the matrix is eliminated by a morphological closure by a square of size 2 pixels in every section; then the comparison of the grey level to a threshold enables us to generate the binary images. The first layers of the studied $3D$ images are given in figures II.3 and II.4.

b) Volume Fraction

The volume fraction of each phase was estimated using image analysis and stereology. This method consists in placing a regular grid of points over a cross-section image and recording the ratio of points landing over the hard phase by the total number of points hitting the reference volume. The obtained volume fractions of the introduced phases are given as the mean value of the area fractions on all the sections. The figure II.2 shows the evolution of the area fraction of phase 1 (hard phase named P_1) on all the sections (in the thickness direction OZ of the corresponding $3D$ images). In some specimens, important variations of the area fraction are observed along the thickness. This is the consequence of the small size of images as compared to the microstructure (see figures II.3 and II.4). For most samples, long range variations of P_1 occur in the thickness. The average values obtained by image analysis are given in the table II.1.

Specimens	SA_1	SA_2	SA_3	SB_1	SB_2	SB_3
Average Volume Fraction of Phase P_1 (%)	66.76	68.64	72.43	73.01	75.19	69.05

Table II.1 : The volume fractions of phase P_1 in different specimens.

The global volume fractions of phase P_1 introduced in the processing of these materials range from 65% to 75%, which is in agreement with the experimental values given in the table II.1.

c) Covariance and Covariogram

It is important to account for the presence of scales, size of heterogeneities, of the components of a microstructure. The basic morphological tools for these aspects are the covariance and covariance range L (Matheron, 1971), (Jeulin and Ostoja-Starzewski, 2002). In addition, it is sometimes important to account for the measurement of anisotropy of phase quantities.

Examples of experimental covariance of our real images are given in figure II.5 for material SA and figure II.6 for material SB. Note that, in general the covariance ranges L_{SB} of samples SB are larger than those for samples SA named L_{SA}

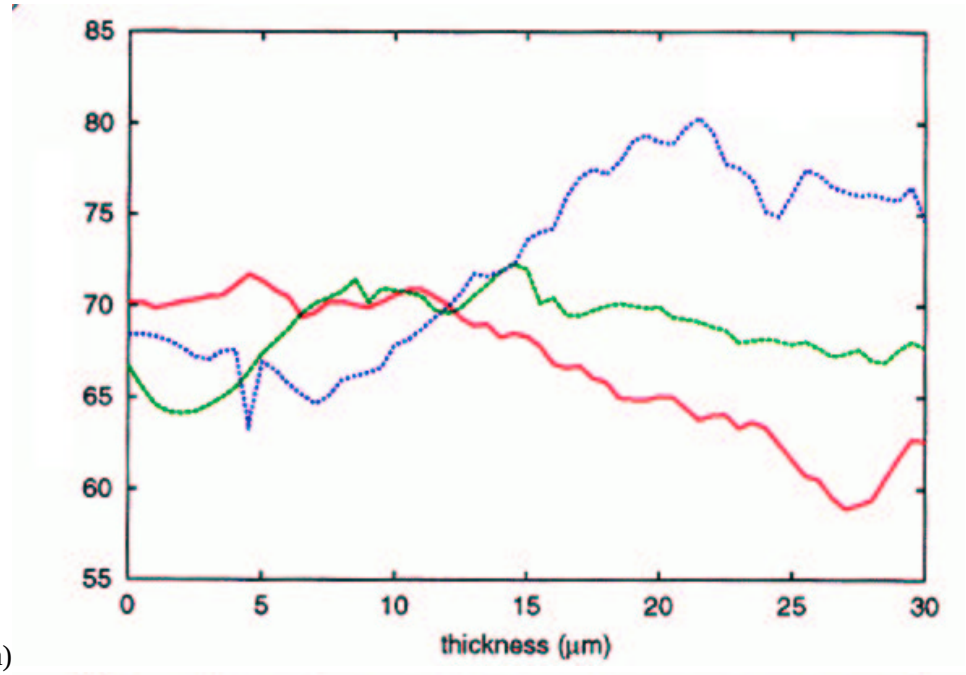

(a)

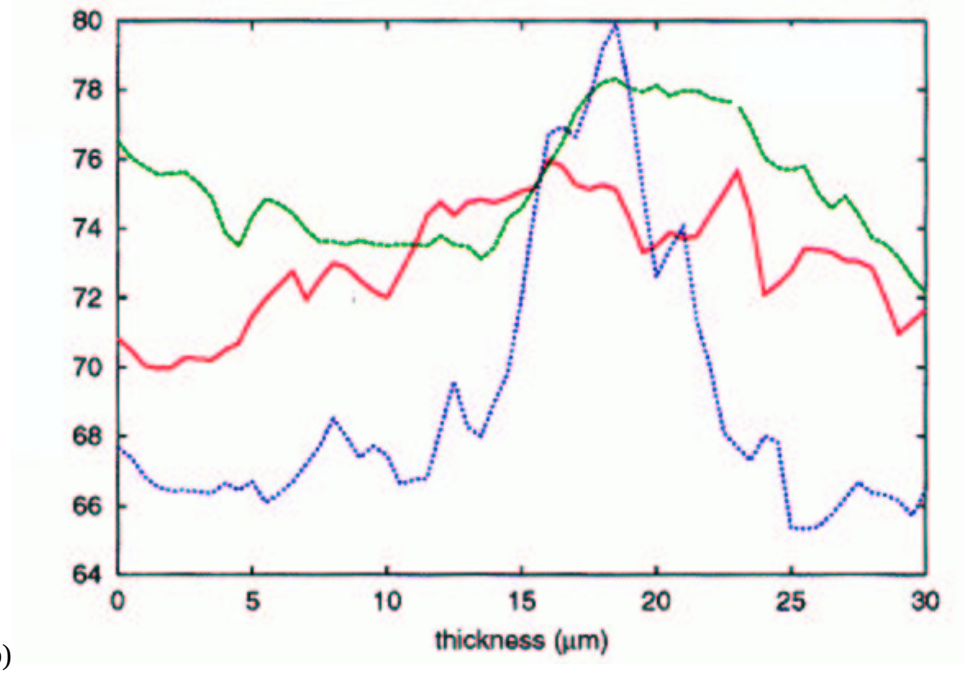

(b)

Figure II.2 : Evolution of the area fraction of hard phase P_1 $(\%)$ in thickness direction, (a) samples with additive SA and (b) samples without additive SB. An important variation is observed in samples with additive SA.

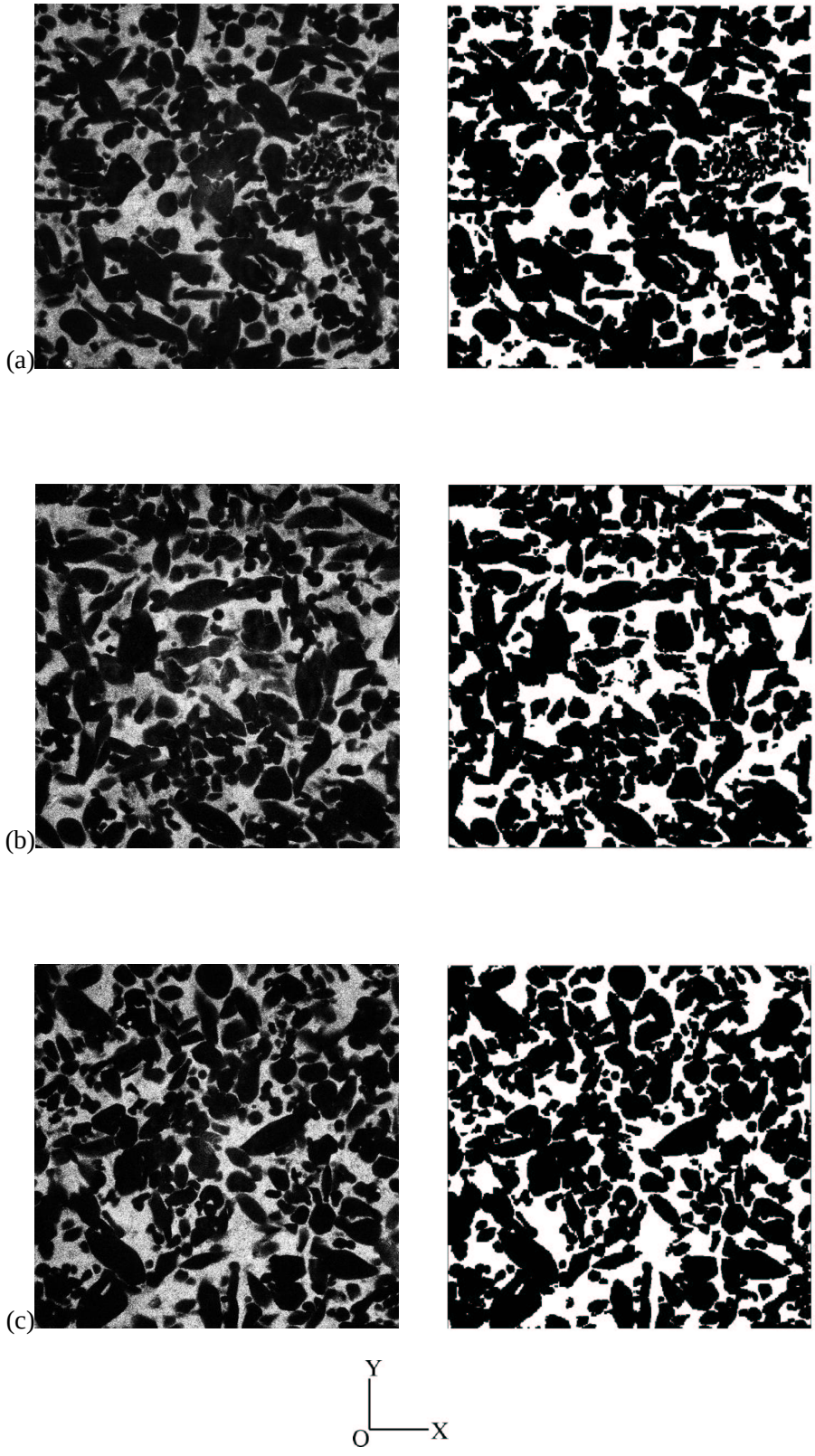

Figure II.3 : Specimens SA, confocal and thresholded images, (a) SA_1, (b) SA_2, (c) SA_3. The size of images is $250 \times 250\ \mu m$. The hard phase is in dark color in confocal and thresholded images.

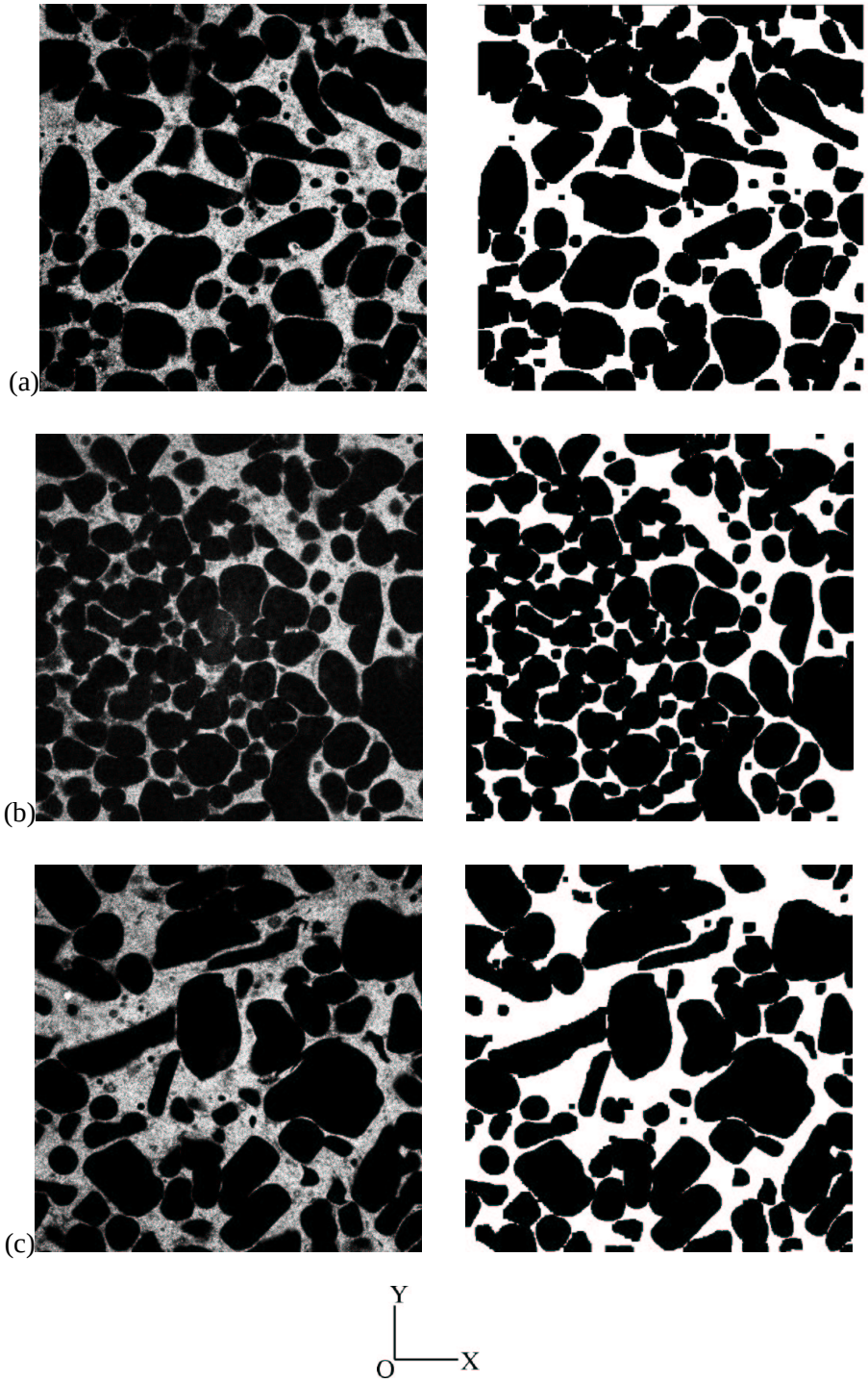

Figure II.4 : Specimens SB, confocal and thresholded images, (a) SB_1, (b) SB_2, (c) SB_3. The size of images is $250 \times 250\ \mu m$. The hard phase is in dark color in confocal and thresholded images.

which means that the size of heterogeneities is more important in samples SB than in samples SA. This will have a major influence on the estimation of RVE size for thermo-mechanical properties of the microstructures.

The covariances of the samples are given in figures II.5 and II.6. They are practically isotropic in two directions of observation (OX,OY) (horizontal, vertical), and they reach their asymptotic value for a finite range, which measures the scale of the microstructure.

A range (of hard phase P_1) close to :

$$L_{SA} = 15\ \mu m \tag{II.1}$$

is observed in samples SA and :

$$L_{SB} = 30\ \mu m \tag{II.2}$$

in samples SB (see table II.2).

Specimens	SA_1	SA_2	SA_3	SB_1	SB_2	SB_3
Covariance Range L (μm)	15	14	22	30	26	38

Table II.2 : Range of the covariance of samples SA and SB. The values of L are obtained from figures II.5 and II.6. The fairly round hard phase crystals in samples SB give an important range of covariance.

II.2.2 Physical properties

In all this work, the numerical simulations are made with these physical properties :

$$(E_1,\ \nu_1) = (2500\ MPa,\ 0.30), \quad (E_2,\ \nu_2) = (0.05\ MPa,\ 0.49) \tag{II.3}$$

for the elastic moduli, and :

$$(\lambda_1,\ \lambda_2) = (2.44\ W/mK,\ 0.0244\ W/mK) \tag{II.4}$$

for thermal conductivities.

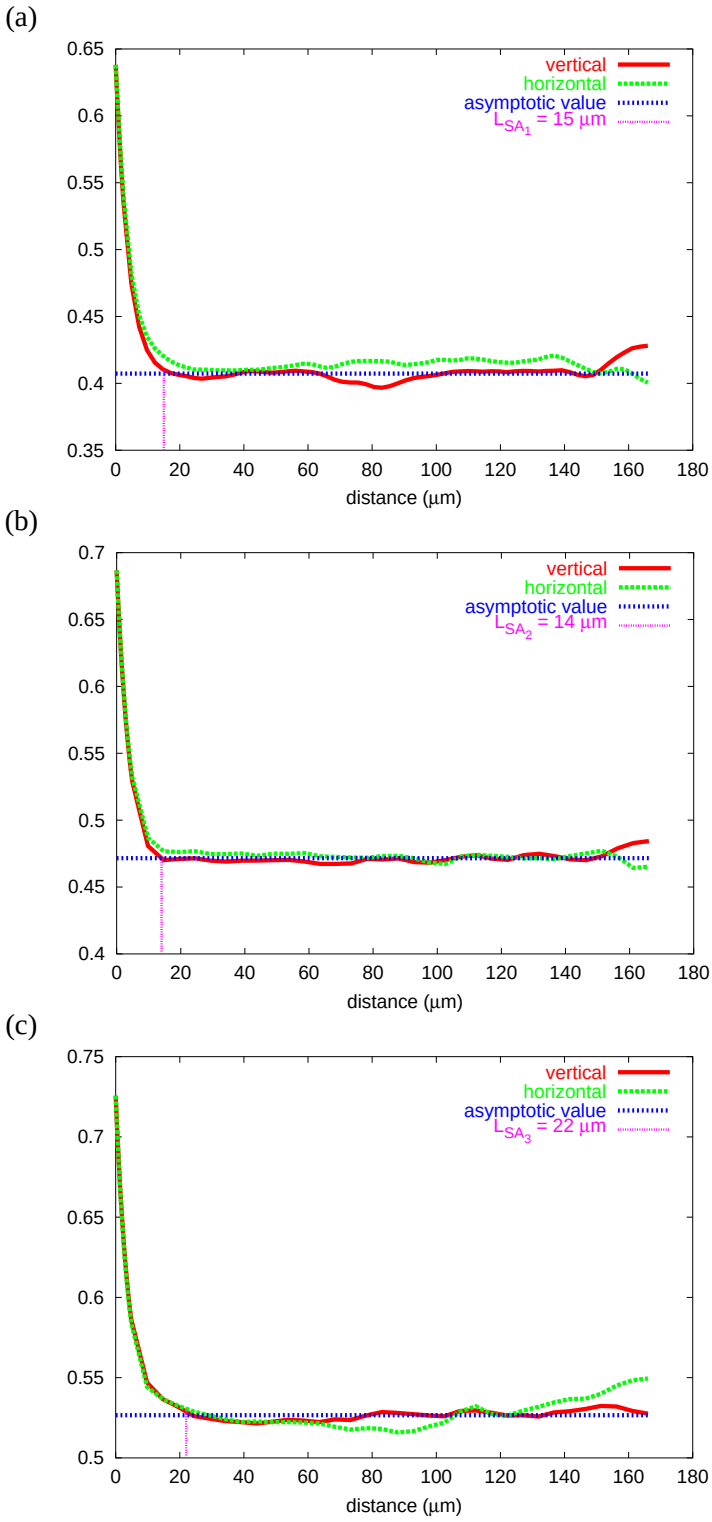

Figure II.5 : Covariance diagram and covariance range L of samples SA, (a) SA_1, (b) SA_2 and (c) SA_3.

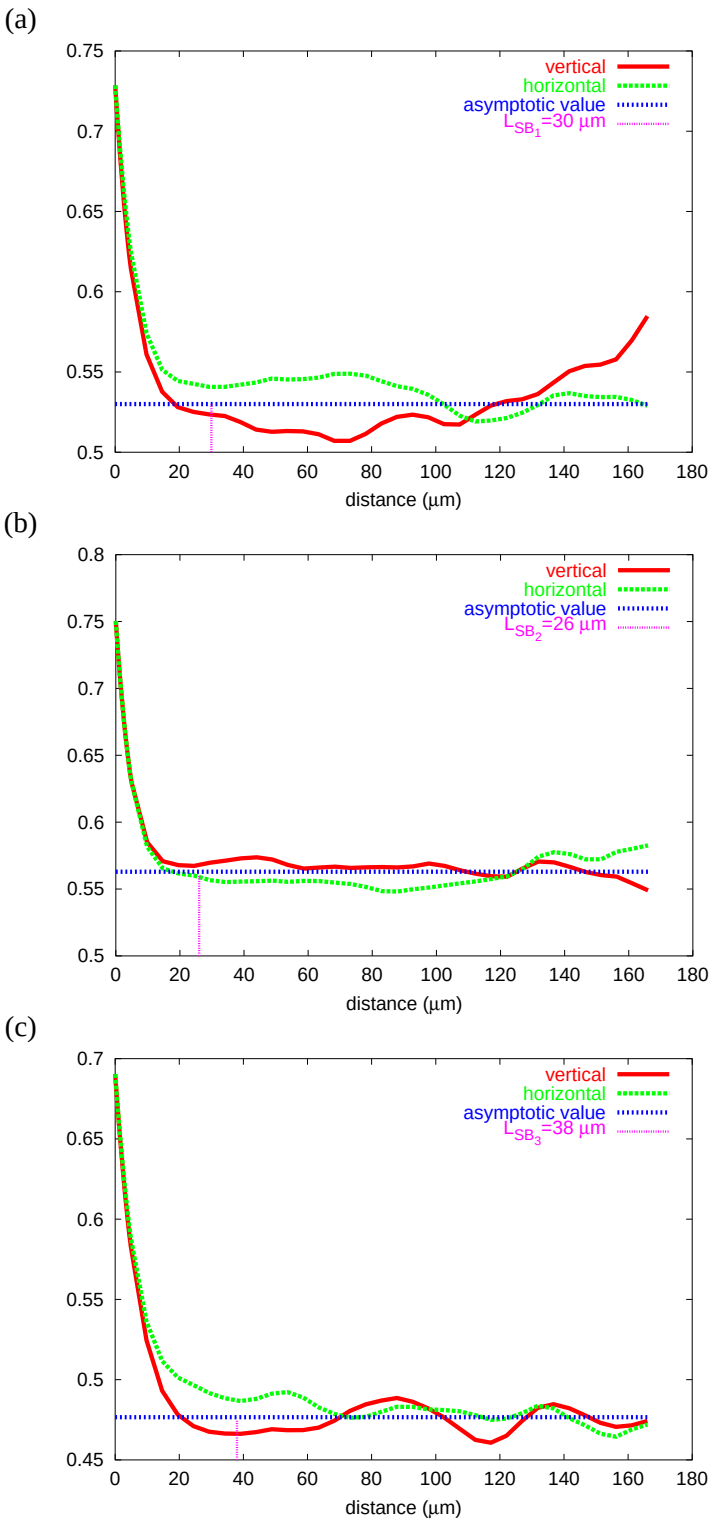

Figure II.6 : Covariance diagram and covariance range L of samples SB, (a) SB_1, (b) SB_2 and (c) SB_3.

a) Four-Point Bending Test

The mechanical test used for the determination of the effective mechanical properties of materials SA and SB is a four-point bend test (figure II.7). The samples used in those tests are $200 \times 200 \times 25\ mm$ bars, which are placed between two pairs of steel rolls used as load applicators. The two upper rolls are immobile while the two lower ones are able to apply a vertical displacement on the sample. The different values of the load F and the displacement of the lower rolls δ are the output of this test. Two ways of interpreting this test and obtaining the Young modulus are investigated : the Elastic Beam Model (EBM) and a finite element identification. The results are that the best estimation is given by finite element identification (El Ouarzazi et al., 2000).

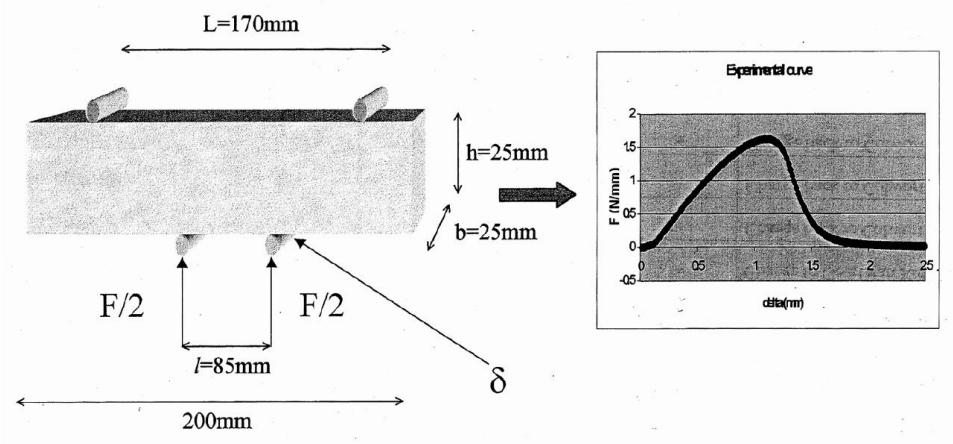

Figure II.7 : The four-point bend test used to estimate the Young modulus. The force-displacement curves obtained are interpreted using the elastic beam model.

The meaning of this chapter deals only with materials SA and SB with volume fraction P_1 close to 70%.

b) Experimental Effective Physical Properties

Four-point bending tests were performed to determine experimentally the Young's modulus E of materials over a large range of the volume fractions of phases P_1 and P_2 (Colworth, 2000). The results are reported in the figure II.8. Note that for all volume fractions, SA is found to be significantly stiffer than SB. This difference can be explained by the role of morphology of phases in each material. The tests were performed for a large interval of volume fractions, especially between 50% and 80% of hard phase P_1. The samples with additive SA give a higher value of Young's modulus by comparison with samples without additive SB for the same value of volume fraction, which can be explained by the role of more elongated hard phase crystals in samples with additive.

The homogenization theory provides us with bounds for the physical properties

(Voigt-Reuss, Hashin-Shtrikman). However, these bounds are not very useful due to the huge contrast between the physical properties of two phases, for example in our microstructures :

$$c_E = \frac{E_1}{E_2} = 50000 \tag{II.5}$$

The self-consistent model gives a fairly good estimation (especially of Young's modulus E) for the specimens with additive SA and for intermediate volume fractions, see figure II.8.

The Young's moduli obtained with the Hashin-Shtrikman bounds for shear and bulk moduli, E^{HS+} and E^{HS-}, are given by :

$$E^{HS+} = \frac{9k^{HS+}\mu^{HS+}}{3k^{HS+} + \mu^{HS+}} \tag{II.6}$$

$$E^{HS-} = \frac{9k^{HS-}\mu^{HS-}}{3k^{HS-} + \mu^{HS-}} \tag{II.7}$$

where : k^{HS+} and k^{HS-} (respectively μ^{HS+} and μ^{HS-}) are the Hashin-Shtrikman's bounds for k (respectively μ).

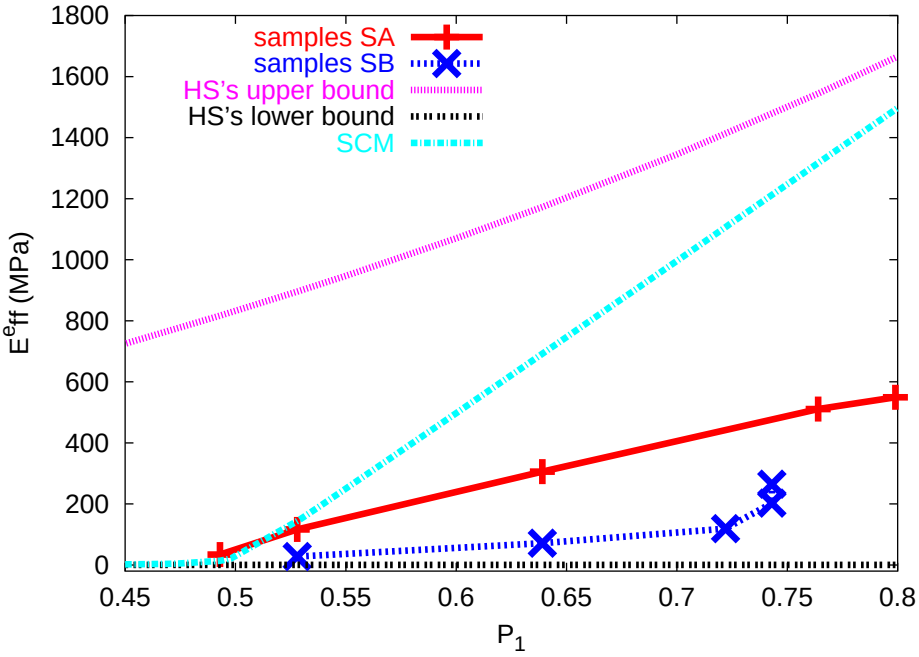

Figure II.8 : Experimental results compared to Hashin-Shtrikman's bounds and self-consistent model (SCM) for Young's modulus. The bounds are very far apart and the self-consistent model gives the same result for different morphologies.

II.3 Computational Tools

II.3.1 Meshing Microstructures

We have seen in the presentation of the studied microstructures that one needs to use a direct method to estimate the effective physical properties, especially, because on the one hand, the bounds (Voigt-Reuss's absolute bounds, Hashin-Shtrikman's bounds) are widely separated and the direct analytical solutions (self-consistent model for example) cannot be said *a priori* to be closer to one morphology than to the other one on the other hand (figure II.8). For this reason and to give a description of RVE sizes in the case of real microstructures, we choose to use the finite element method to compute the different apparent physical properties of our microstructures. The obtained results will be then used in a statistical description to relate the RVE sizes and the different parameters which influence it : that gives the relative precision ϵ_{rela} for the effective properties, the minimal number of realizations n, the contrast in the studied property c_k, c_μ, c_E and c_λ.

After obtaining the binary three-dimensional real images of the microstructures, a finite element mesh is used to mesh these images. Using a parallelepipedic mesh (to respect the parallelepipedic geometry of the samples), the VPOLY3D code attributes to each integration point of the finite element mesh the corresponding position in the $3D$ image (in phase P_1 or in phase P_2). This is the so-called multi-phase element technique.

The dimensions of the images are :

$$250 \times 250 \times 30\,\mu m = 1875000\,\mu m^3 \tag{II.8}$$

These dimensions lead to the image size :

$$512 \times 512 \times 60 = 15728640\,voxels \tag{II.9}$$

which means that the used resolution is about : $8\ voxels/\mu m^3$. The size of the image in $3D$ ($512 \times 512 \times 60\ voxels$) is imposed by our computation capacity. The original images are given with a size of :

$$1024 \times 1024 \times 60 = 62914560\,voxels \tag{II.10}$$

This reduction to $512 \times 512 \times 60\,voxels$ does not really change the morphology of the microstructures.

As we have seen in the case of Voronoï mosaics, the results given by the finite element method depend on the used mesh density. One must mesh sufficiently the microstructures to avoid the errors coming from the mesh density. In our case, the mesh density is the real volume of the microstructure (given in μm^3) represented by one finite element. To solve this problem, we need to use the parallel computing technique (see appendix B) instead a single workstation, on which we can only compute about 40000 degrees of freedom (d.o.f.). The $d.o.f.$ are the displacement component at the nodes. For parallel computing, we have used up to 32 PC to compute about $1.200.000$ degrees of freedom.

Figure II.9 explains the methodology followed in our work. The $3D$ image of the microstructure is meshed after the segmentation operation.

II.3.2 Mesh Density in $3D$

a) Global Convergence

Two examples of computations of Young's modulus E in the direction (OY) with mixed boundary conditions (see chapter 1) by finite element simulations from real microstructures are given, using the following contrast in Young's modulus :

$$c_E = \frac{E_1}{E_2} = 100 \tag{II.11}$$

on the specimen SA_1, and :

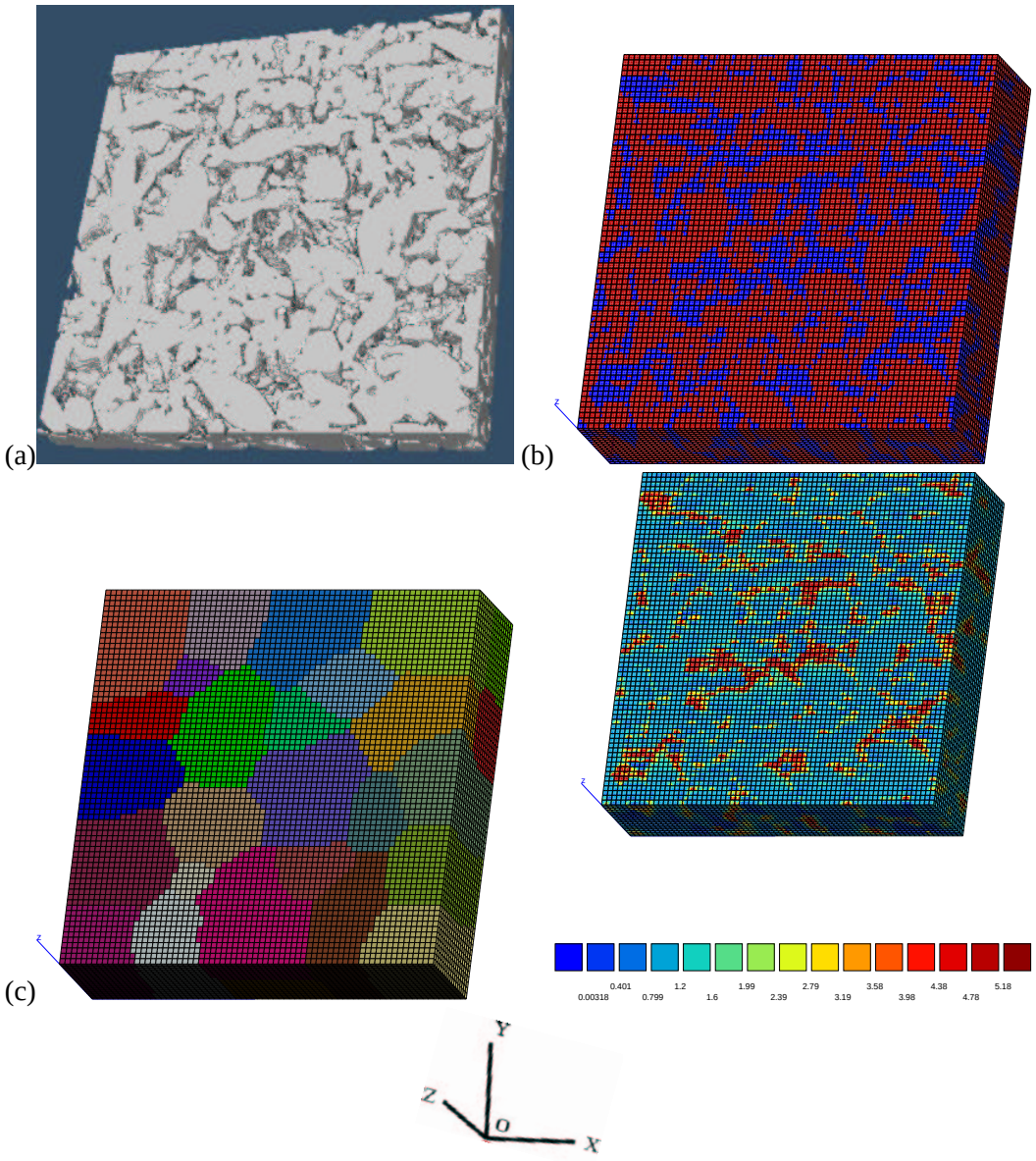

Figure II.9 : Methodology of computation of microstructures : (a) the image of the microstructure ($250 \times 250 \times 30\ \mu m$), 68.64% of hard phase P_1 in grey color, (b) the image of microstructure with the finite element mesh (with mesh density $= 20\ \mu m^3/finite\ element$), the red phase is P_1, (c) the size of computation is about $1.126.131\ d.o.f.$ divided into 32 sub-domains for parallel computing and (d) example of results of computation with imposed $E_{22} = 1$ in KUBC boundary conditions : the equivalent strain ε_{eq} given in equation (II.18).

$$c_E = \frac{E_1}{E_2} = 1000 \tag{II.12}$$

on the specimen SA_2, we keep :

$$E_1 = 2500\ MPa \tag{II.13}$$

$$\nu_1 = 0.3 \tag{II.14}$$

$$\nu_2 = 0.49 \tag{II.15}$$

We apply a displacement in direction (OY) on one face and keep the opposite face with $U_2 = 0$. The imposed displacement gives :

$$< \varepsilon_{22} >= 1 \tag{II.16}$$

so, the apparent Young's modulus in this direction is :

$$E = E_{OY} =< \sigma_{22} > \tag{II.17}$$

The first parameter studied is the mesh density defined as volume of material (μm^3) represented by one finite element. The figure II.10 shows the results of computations of Young's modulus E as a function of the number of degrees of freedom ($d.o.f.$) used to mesh the two microstructures. Figures II.11, II.12, II.13, II.14 and II.15 show an example of computation of Young's modulus on the specimen SA_1 in the direction (OY) for increasing mesh density ($d.o.f./element$ or $volume/element$) using mixed boundary conditions. The maps of the equivalent strain (ε_{eq} given by equation (II.18)) are given and compared with the map of phases (the phase in red is the hard one P_1). Note that we have large stresses in the hard phase and large strains in the soft one.

$$\varepsilon_{eq} = \sqrt{\varepsilon_{11}^2 + \varepsilon_{22}^2 + \varepsilon_{33}^2 + 2\varepsilon_{12}^2 + 2\varepsilon_{23}^2 + 2\varepsilon_{31}^2} \tag{II.18}$$

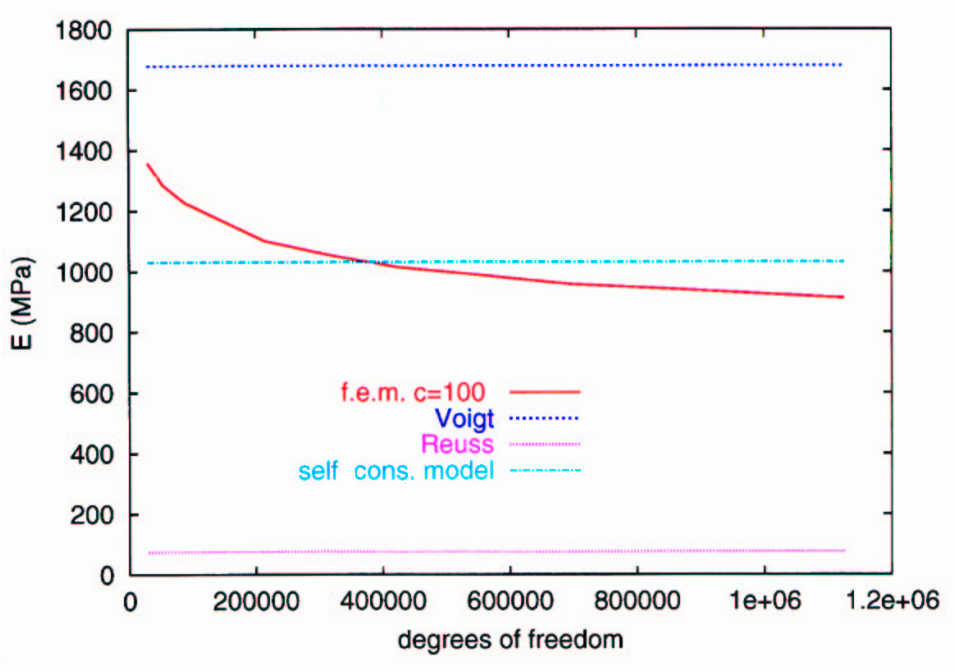

(a)

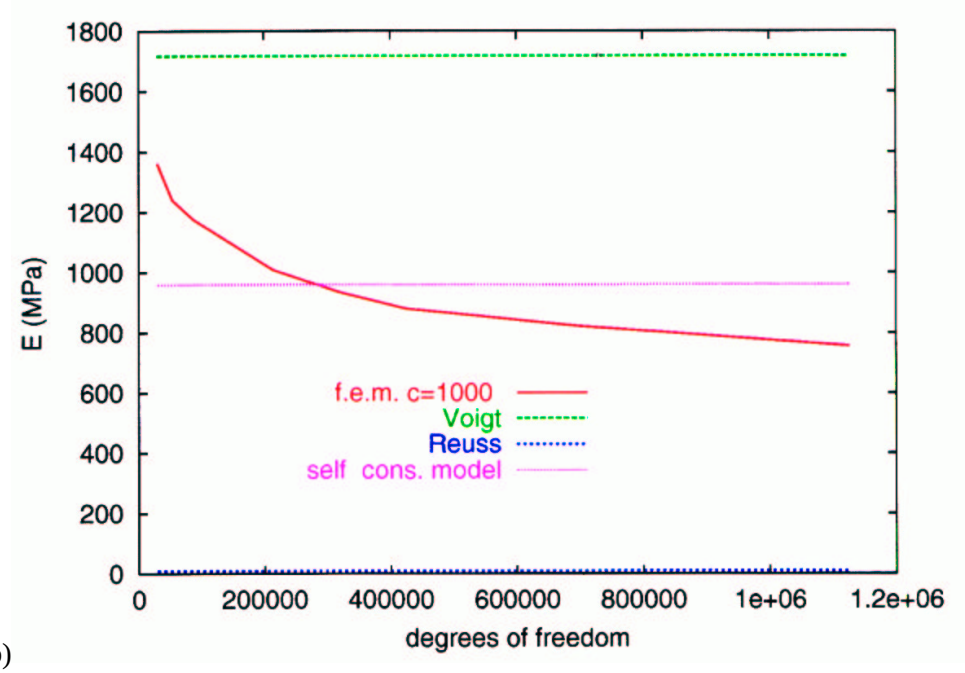

(b)

Figure II.10 : Effect of the mesh density in finite element simulations (f.e.m.) on the global convergence of the apparent Young's modulus. The Hashin-Shtrikman's bounds are (1322, 140 MPa) for the specimen (a) SA_1 and (1314, 16 MPa) for the specimen (b) SA_2. $c = c_E$ represents the contrast in the Young's moduli of the phases.

The number of degrees of freedom ($d.o.f.$) was changed from 30000 to 1150000. The size of the microstructures is $250 \times 250 \times 30\ \mu m = 1875000\ \mu m^3$. The number of finite elements was changed from 4096 to 88200 which means that the mesh density was changed from $458\ \mu m^3/element$ to $20\ \mu m^3/element$. First note that the absolute bounds are very far apart and the direct estimation of the self-consistent model overestimates the results for the two values of the contrast c_E. The computations with a contrast $c_E = 1000$ are more sensible than with $c_E = 100$, but the effect of the contrast becomes very slight for stronger contrasts. We accept an error on the apparent Young's modulus about 5% between a contrast $c_E = 1000$ and the real one : $c_E = 50000$.

As a result, we keep in all our computations on these microstructures a mesh density of $20\ \mu m^3/element$ in elastic properties and thermal conductivity.

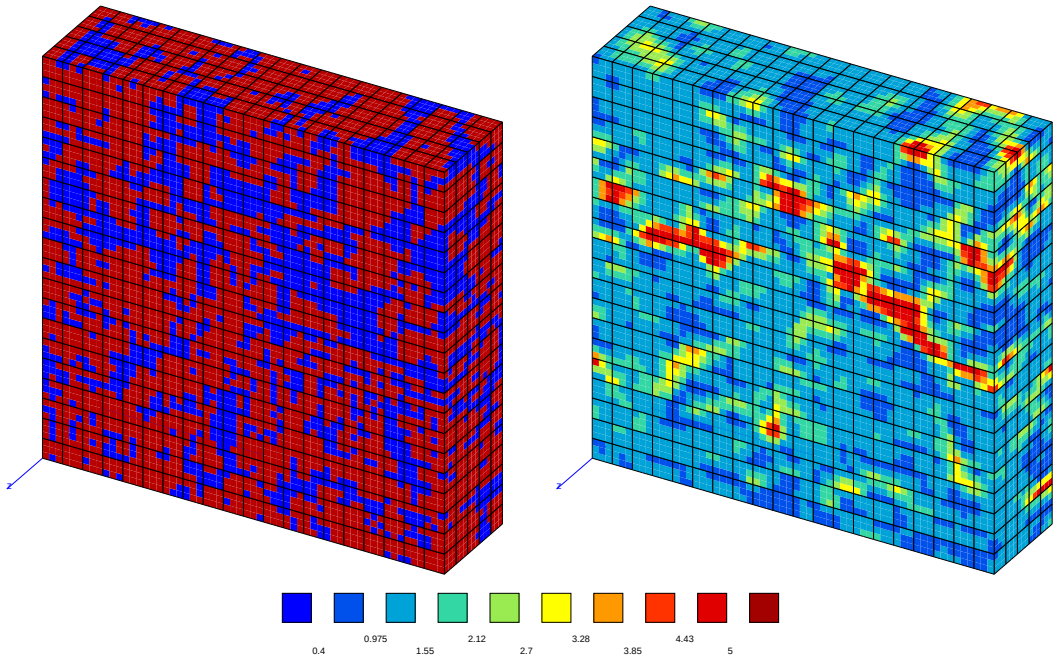

Figure II.11 : Mesh and computation with 2000 elements (29673 d.o.f.), or $938\ \mu m^3$/element and map of equivalent strain ε_{eq} for a mean prescribed strain $E_{22} = 1$.

b) Local Convergence

In our computations we need to compute the apparent physical properties. These properties are given as average values of the local fields in the microstructure. So the convergence shown in the figure II.10 is sufficient to validate our retained mesh density to compute the apparent physical properties. Now if one looks at the microscopic level, which means that we compare some maps of local fields obtained with different mesh densities, we see that we need more and more finite elements to obtain a good convergence in the local fields. The problem stems from the type of used finite elements. Our elements are multi-phase ones, which give a slow lo-

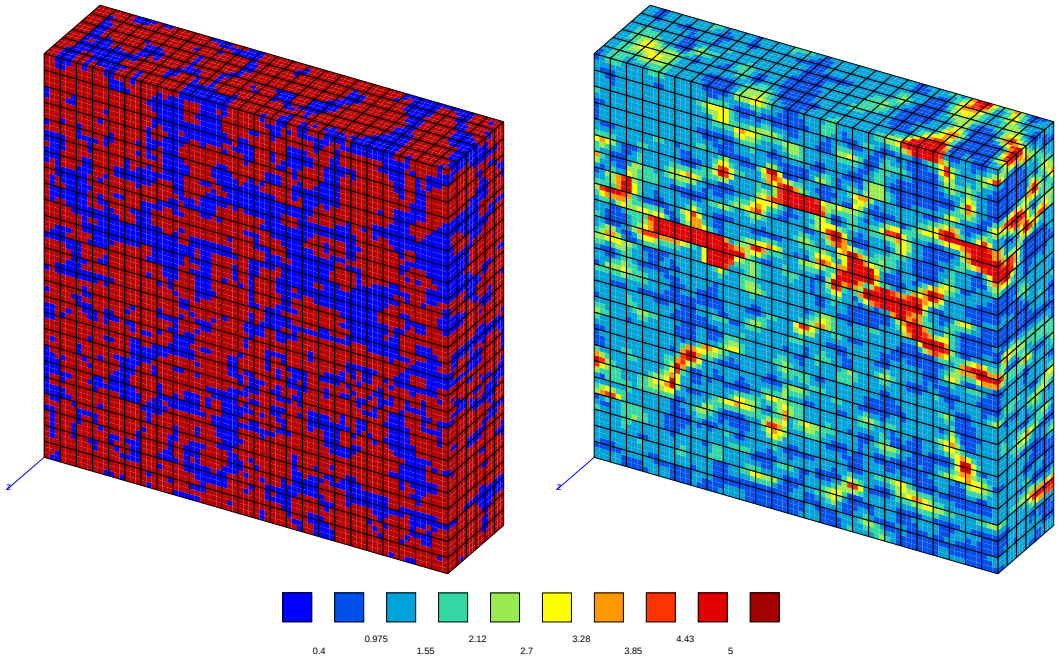

Figure II.12 : Mesh and computation with 3750 elements (53664 d.o.f.), or $500\ \mu m^3$/element and map of equivalent strain.

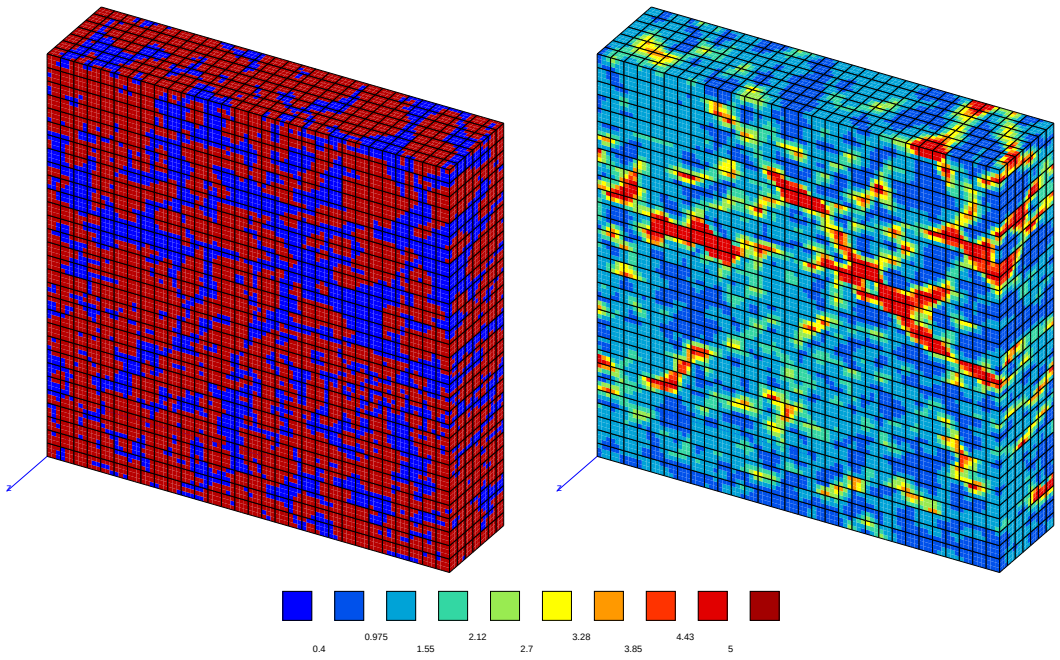

Figure II.13 : Mesh and computation with 6300 elements (87885 d.o.f.), or $298\ \mu m^3$/element and map of equivalent strain.

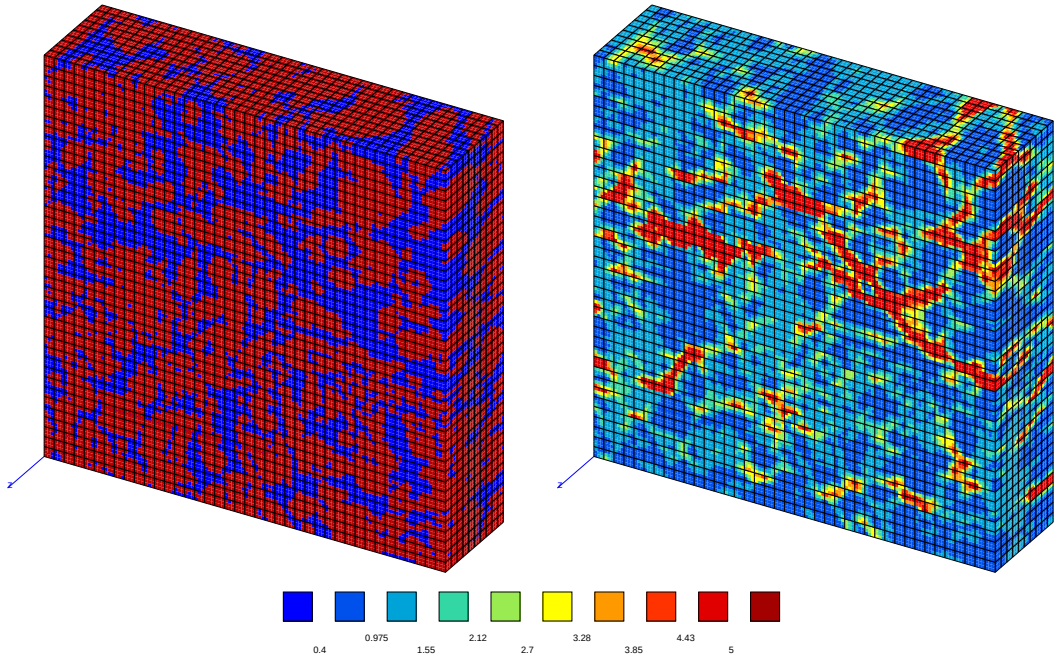

Figure II.14 : Mesh and computation with 16000 elements (214143 d.o.f.), or 117 μm^3/element and map of equivalent strain.

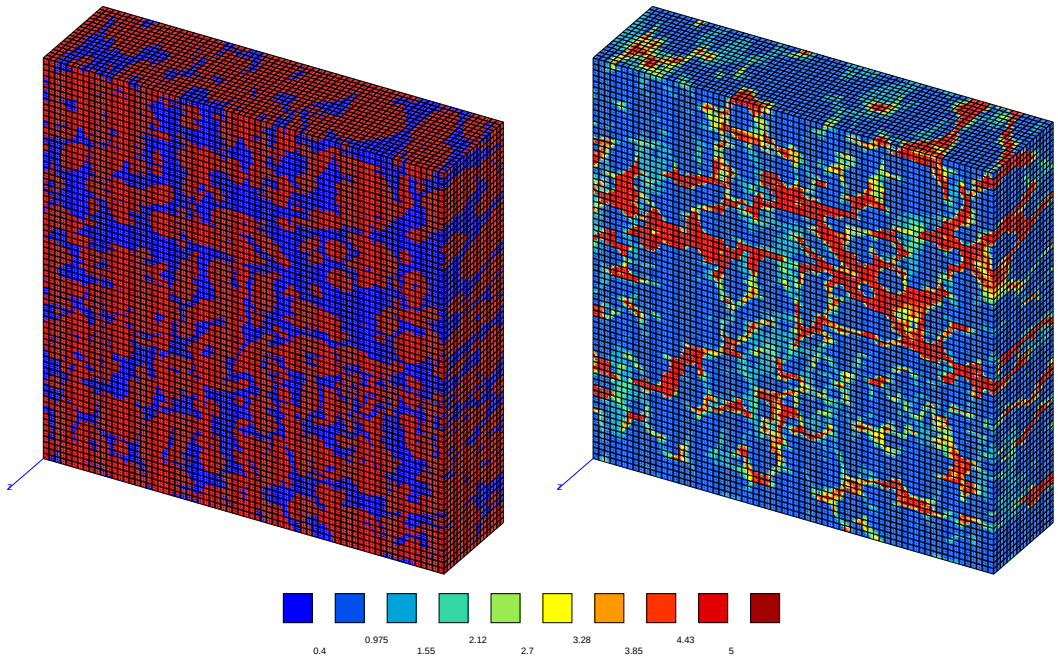

Figure II.15 : Mesh and computation with 88200 elements (1126131 d.o.f.), or 22 μm^3/element and map of equivalent strain.

cal convergence (figures II.11, II.12, II.13, II.14 and II.15). Figure II.16 shows the corresponding sections of the maps of equivalent strain given in figures II.11, II.12, II.13, II.14 and II.15.

As a result, the multi-phase elements are recommended for the macroscopic study and free meshing of figure I.3 (chapter 1) for a microscopic approach.

In order to quantify the effect of the mesh density in $3D$ on the variation of local fields, we have chosen to show the curve of displacement in the direction (OX) on the right edge parallel to the (OY) direction in our microstructure. Figure II.17 shows the curves of the displacement U_1 in the direction (OX) of the chosen edge. The length of this edge is $250\ \mu m$ and the displacement U_1 is negative because we have a traction in the direction (OY). One remarks the high sensitivity of the curve of the displacement U_1 to the mesh density given in figure II.17 by $volume\ (\mu m^3)/finite\ element$. We have a larger difference in the soft phase than in the hard one.

As a result, one can say that we need a higher mesh density when we compute with a larger contrast in the properties of the constituents. With our maximal used mesh density ($20\ \mu m^3/finite\ element$) we have not yet a very good local convergence. We have continued to study the effect of the mesh density on the local fields in $2D$ using the same first section of the microstructure used in this part.

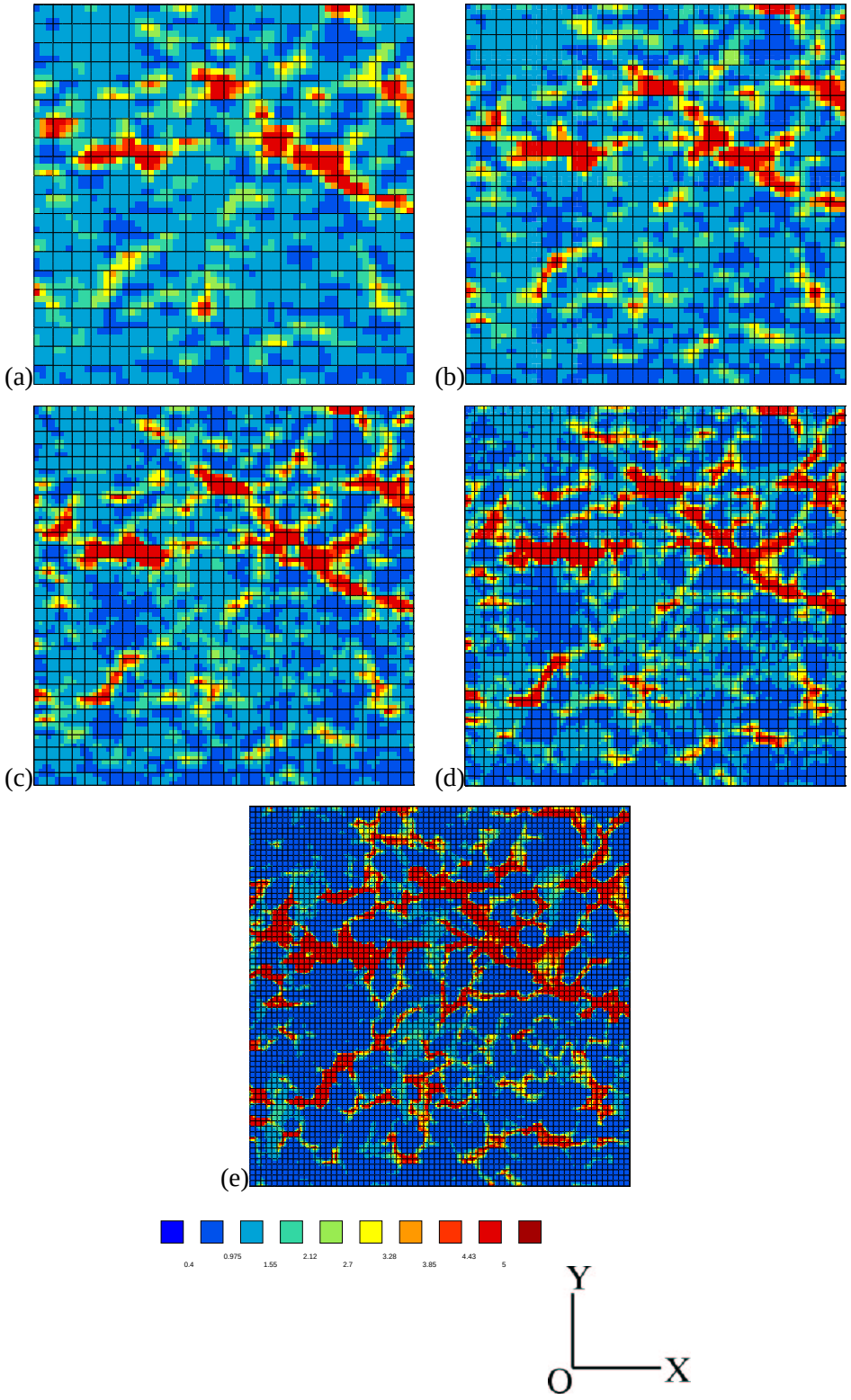

Figure II.16 : Local convergence as a function of mesh density in $3D$ case : (a) 2000 elements, (b) 3750 elements, (c) 6300 elements, (d) 16000 elements and (e) 88200 elements. These maps are the first section of figures II.11 to II.15.

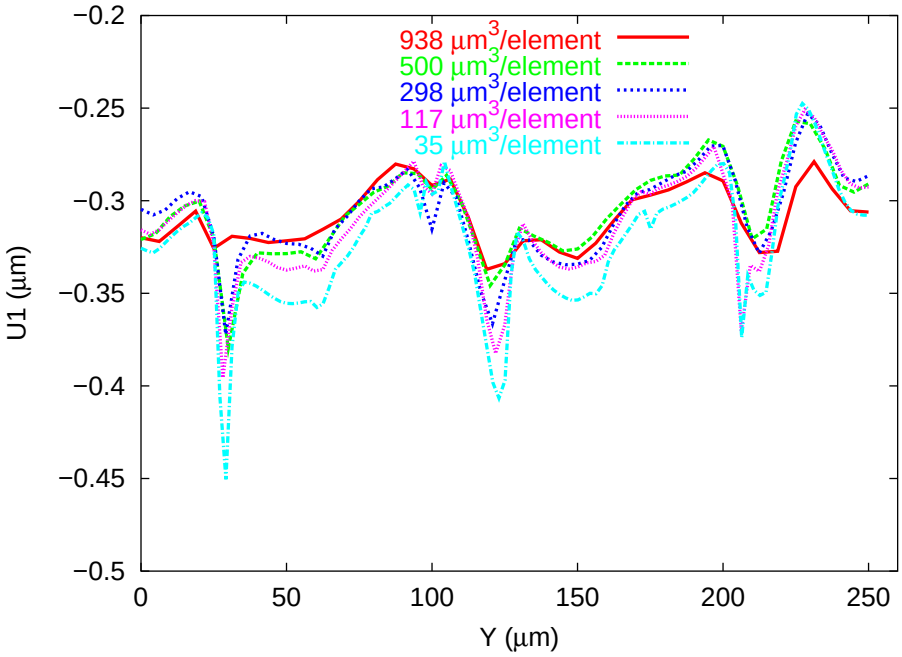

Figure II.17 : Effect of mesh density on the local convergence in $3D$.

II.3.3 Mesh Density in $2D$

We have seen, in the study of the effect of the mesh density in $3D$, that it is possible to obtain a good convergence in the macroscopic apparent properties. Regarding the local fields, this objective is very difficult to reach when using the multi-phase element technique for high contrasts of properties.

The computations in $2D$ are very easy as compared to the $3D$ case. For this reason, we can try to find the absolute convergence in the local fields.

Starting from the maximal mesh density which we have used in $3D$ (about $20\ \mu m^3/finite\ element$) and with a section of the same used microstructure, we will study the effect of the mesh density in $2D$ on the macroscopic apparent properties and on the local fields. For this, a series of computations of apparent Young's modulus in the direction (OY) are performed and observed its variation as a function of the mesh density; we have looked at the displacement U_1 in the same direction of the right edge.

a) Global Convergence

The used section covers :

$$250\ \times\ 250\ \mu m = 62500\ \mu m^2 \qquad \text{(II.19)}$$

The finite element mesh is designed according to the multi-phase element technique. The number of degrees of freedom ($d.o.f.$) was changed from 30000 to 240000. The number of finite elements was changed from 4900 to 40000. So the mesh density in $2D$ was changed from $12\ \mu m^2/finite\ element$ to $2\ \mu m^2/finite\ element$. As a macroscopic property, we consider the average value of the stress in the direction of the traction $(OY) : < \sigma_{22} >$. Figure II.18 shows the evolution of $< \sigma_{22} >$ as a function of the mesh density. The variation of $< \sigma_{22} >$ is very sensitive to coarse meshes and one can obtain the absolute convergence at about $150000\ d.o.f.$.

If one tries to use this mesh density in $3D$, ($150000\ d.o.f.$ corresponds to a mesh density of $6\ \mu m^2/finite\ element$, in $3D$ this gives about $14\ \mu m^3/finite\ element$), this requires about 134000 finite elements. With our code and using the parallel computing, about 54 PC are required to compute the microstructure.

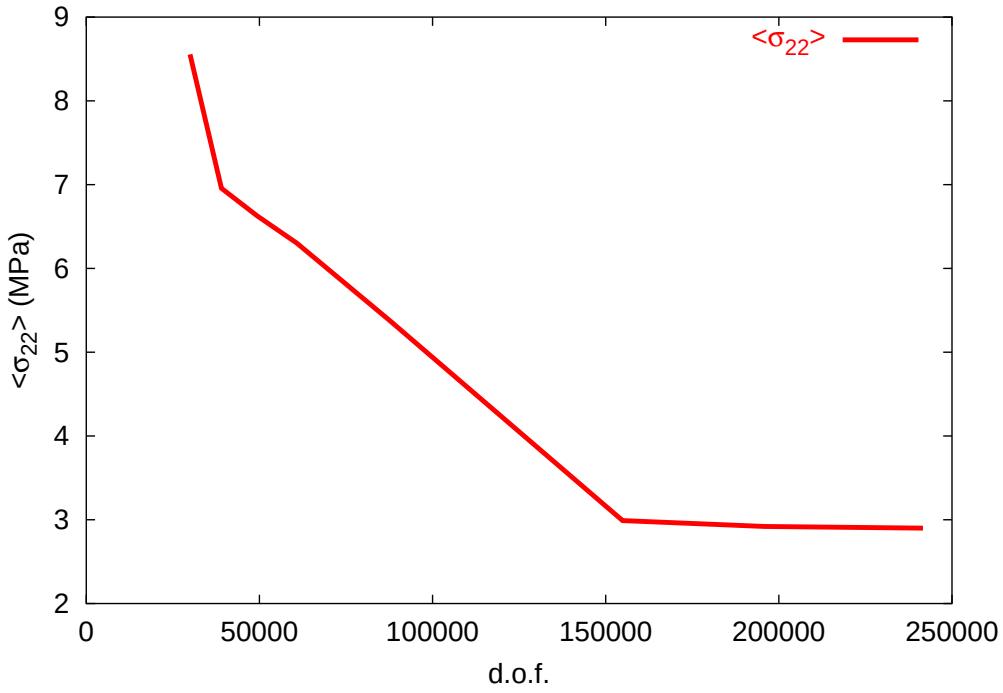

Figure II.18 : Convergence of results in $2D$, average value of $< \sigma_{22} >$.

b) Local Convergence

In the mesh density studied in the case of $3D$ we have seen that it is very difficult to obtain an absolute convergence in the local fields. Using the same technique of meshing, the multi-phase element technique in $2D$, figures II.19 and II.20 show the maps of equivalent strain ε_{eq} given in $2D$ by :

$$\varepsilon_{eq} = \sqrt{\varepsilon_{11}^2 + \varepsilon_{22}^2 + 2\varepsilon_{12}^2} \tag{II.20}$$

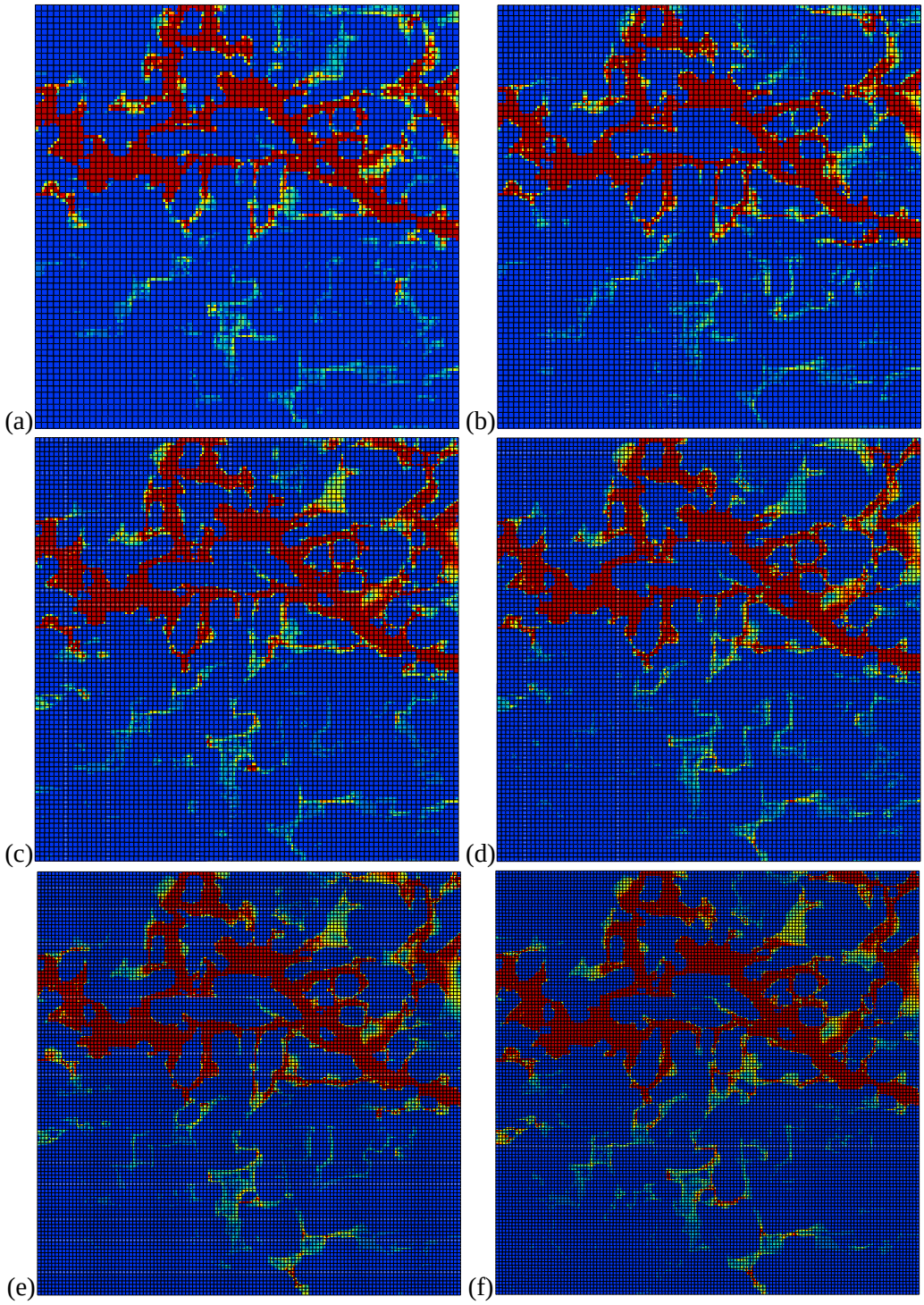

Figure II.19 : Effect of mesh density in $2D$. Maps of equivalent strain, (a) 4900 elements, (b) 6400 elements, (c) 8100 elements, (d) 10000 elements, (e) 14400 elements and (f) 16900 elements. The computations are performed with mixed boundary conditions.

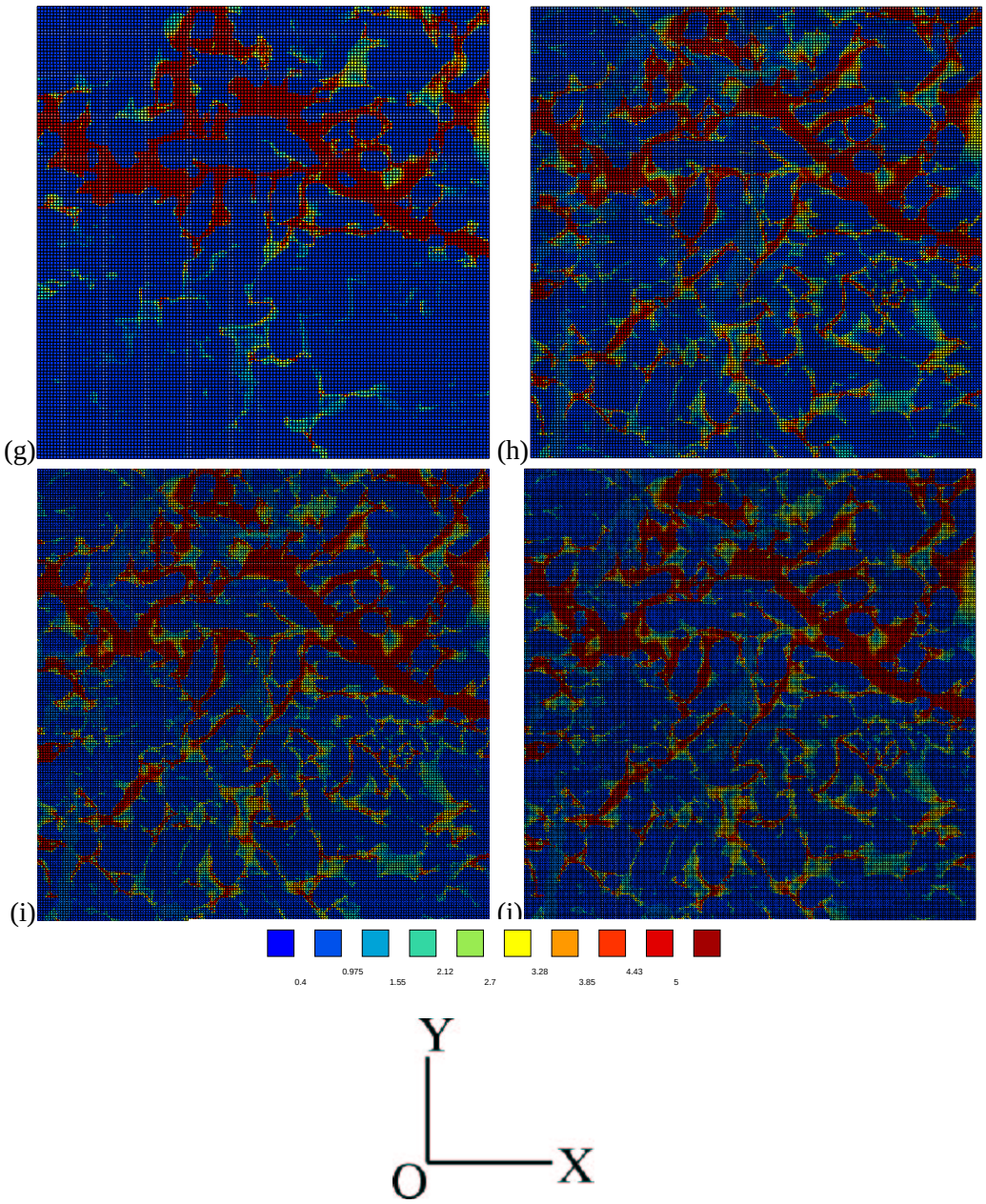

Figure II.20 : Effect of mesh density in $2D$. Maps of equivalent strain, (g) 19600 elements, (h) 25600 elements, (i) 32400 elements and (j) 40000 elements.

It is clear that one must use more and more finite elements to obtain an absolute local convergence with the multi-phase element mesh technique. In order to quantify this problem, we can say that the last three maps (figure II.20(h), (i) and (j)) of the equivalent strain ε_{eq} are equivalent. The corresponding three mesh densities are $2.44\ \mu m^2/finite\ element$, $1.93\ \mu m^2/finite\ element$ and $1.56\ \mu m^2/finite\ element$.

If one would use this last mesh density : $1.56\ \mu m^2/finite\ element$, which corresponds to a mesh density of about $1.95\ \mu m^3/finite\ element$ in $3D$, it would be necessary to use about 962300 finite elements to obtain the local convergence in $3D$. To compute with this number of finite elements with our code, we would need about 290 PC in parallel computing.

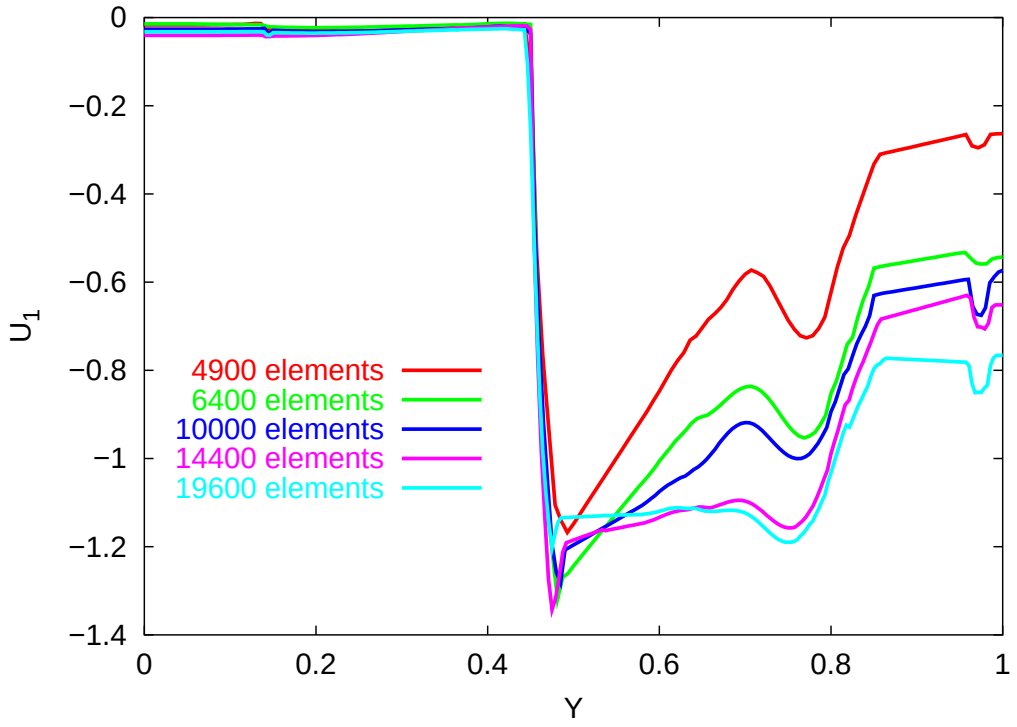

Figure II.21 : Convergence of results in $2D$, displacement U_1.

Figure II.21 gives the evolution of the displacement component U_1 on the right edge of the computed section, for different mesh densities. The last two mesh densities : $14400\ finite\ elements$ and $19600\ finite\ elements$ which corresponds to $4.34\ \mu m^2/finite\ element$ and $3.19\ \mu m^2/finite\ element$ give the same evolution of the displacement U_1. One notices that the value of the displacement U_1 is more sensitive in the soft phase P_2 ($0.5 \leq Y \leq 1$) than in the hard one P_1 ($0 \leq Y \leq 0.5$). In the hard phase, the first used mesh density $4900\ finite\ elements$, which corresponds to $12.76\ \mu m^2/finite\ element$, gives already a correct evolution of the displacement U_1.

II.4 Determination of Apparent Physical Properties

The elements and notations of homogenization theory necessary for the numerical determination of apparent linear properties carried out for real microstructures are presented in chapter 1 and in (Kanit et al., 2003a) for linear elasticity and for thermal conductivity.

II.4.1 Direct Estimation of Properties on Whole Microstructures

In this sub-section, the real microstructures are considered as a two–phase linear elastic material . The mechanical properties of the phases are :

$$(E_1,\ \nu_1,\ k_1,\ \mu_1) = (2500\ MPa,\ 0.3,\ 2083\ MPa,\ 962\ MPa) \tag{II.21}$$

$$(E_2,\ \nu_2,\ k_2,\ \mu_2) = (0.05\ MPa,\ 0.49,\ 0.8\ MPa,\ 0.02\ MPa) \tag{II.22}$$

So the contrast between different elastic properties is :

$$c_E = \frac{E_1}{E_2} = 50000 \tag{II.23}$$

$$c_\nu = \frac{\nu_1}{\nu_2} = 0.6 \tag{II.24}$$

$$c_k = \frac{k_1}{k_2} = 2600 \tag{II.25}$$

$$c_\mu = \frac{\mu_1}{\mu_2} = 48100 \tag{II.26}$$

Note that the contrast in shear modulus c_μ is very high whereas the contrast in bulk modulus c_k is smaller.

a) Apparent Elastic Properties

To study the mechanical anisotropy of our samples, we provide the apparent elastic matrices. These matrices can be anisotropic if the size of the samples is not large enough.

The apparent elastic matrix $\underset{\sim}{\underset{\sim}{\boldsymbol{C}}}^{app}$ is related to the macroscopic strain tensor (loading) $\underset{\sim}{\boldsymbol{E}}$ and the average microscopic stress tensor $< \underset{\sim}{\boldsymbol{\sigma}} >$ by :

$$< \underset{\sim}{\boldsymbol{\sigma}} >= \underset{\sim}{\underset{\sim}{\boldsymbol{C}}}^{app} : \underset{\sim}{\boldsymbol{E}} \tag{II.27}$$

To compute the apparent elastic coefficients C_{ij}^{app}, we impose a loading strain tensor $\underset{\sim}{\boldsymbol{E}}$ and with the average local stress tensor $< \underset{\sim}{\boldsymbol{\sigma}} >$ we compute the coefficients C_{ij}^{app} by the previous relation :

$$\begin{pmatrix} <\sigma_{11}> \\ <\sigma_{22}> \\ <\sigma_{33}> \\ <\sigma_{12}> \\ <\sigma_{23}> \\ <\sigma_{31}> \end{pmatrix} = \begin{pmatrix} C_{11}^{app} & C_{12}^{app} & C_{13}^{app} & C_{14}^{app} & C_{15}^{app} & C_{16}^{app} \\ & C_{22}^{app} & C_{23}^{app} & C_{24}^{app} & C_{25}^{app} & C_{26}^{app} \\ & & C_{33}^{app} & C_{34}^{app} & C_{35}^{app} & C_{36}^{app} \\ & & & C_{44}^{app} & C_{45}^{app} & C_{46}^{app} \\ & & & & C_{55}^{app} & C_{56}^{app} \\ & & & & & C_{66}^{app} \end{pmatrix} \begin{pmatrix} E_{11} \\ E_{22} \\ E_{33} \\ 2E_{12} \\ 2E_{23} \\ 2E_{31} \end{pmatrix} \quad \text{(II.28)}$$

To estimate all the coefficients of the apparent elastic matrix, we need to use six different computations with six different macroscopic strain tensors. The values of the macroscopic strain tensor (load) in each computation are given in the table II.3.

Loading	Imposed Field $\underset{\sim}{\boldsymbol{E}}$					
	E_{11}	E_{22}	E_{33}	E_{12}	E_{23}	E_{31}
1	1	0	0	0	0	0
2	0	1	0	0	0	0
3	0	0	1	0	0	0
4	0	0	0	0.5	0	0
5	0	0	0	0	0.5	0
6	0	0	0	0	0	0.5

Table II.3 : The six loading conditions used to compute the apparent elastic properties in KUBC boundary conditions.

All the samples are simulated using the six different loading conditions with KUBC boundary conditions.

We give the apparent elastic matrix of each sample : equations (II.29), (II.30) and (II.31) for samples with additive SA and equations (II.33), (II.34) and (II.35) for samples without additive SB. The mean apparent moduli are given by equations (II.36) and (II.32).

$$[C]_{SA_1} = \begin{pmatrix} 904 & 249 & 315 & 1 & 1 & 15 \\ & 813 & 290 & 1 & 5 & 3 \\ & & 1383 & 4 & 7 & 24 \\ & & & 301 & 3 & 1 \\ & & & & 363 & 2 \\ & & & & & 385 \end{pmatrix} \quad \text{(II.29)}$$

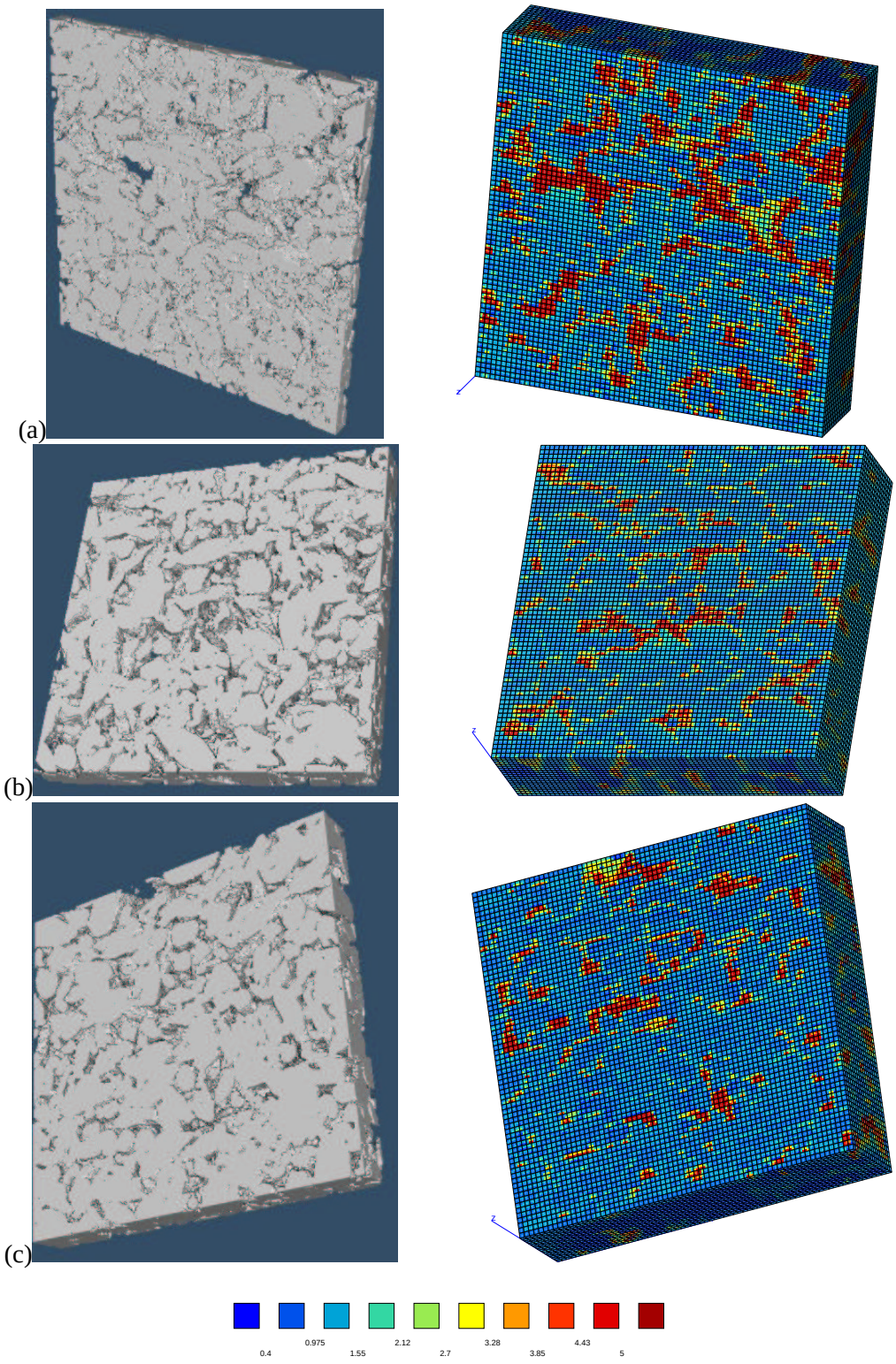

Figure II.22 : Direct numerical simulation of samples with additive SA, example of computation with $E_{22} = 1.$ in KUBC. The map of equivalent strain ε_{eq} is shown. The hard phase P_1 is in grey color.

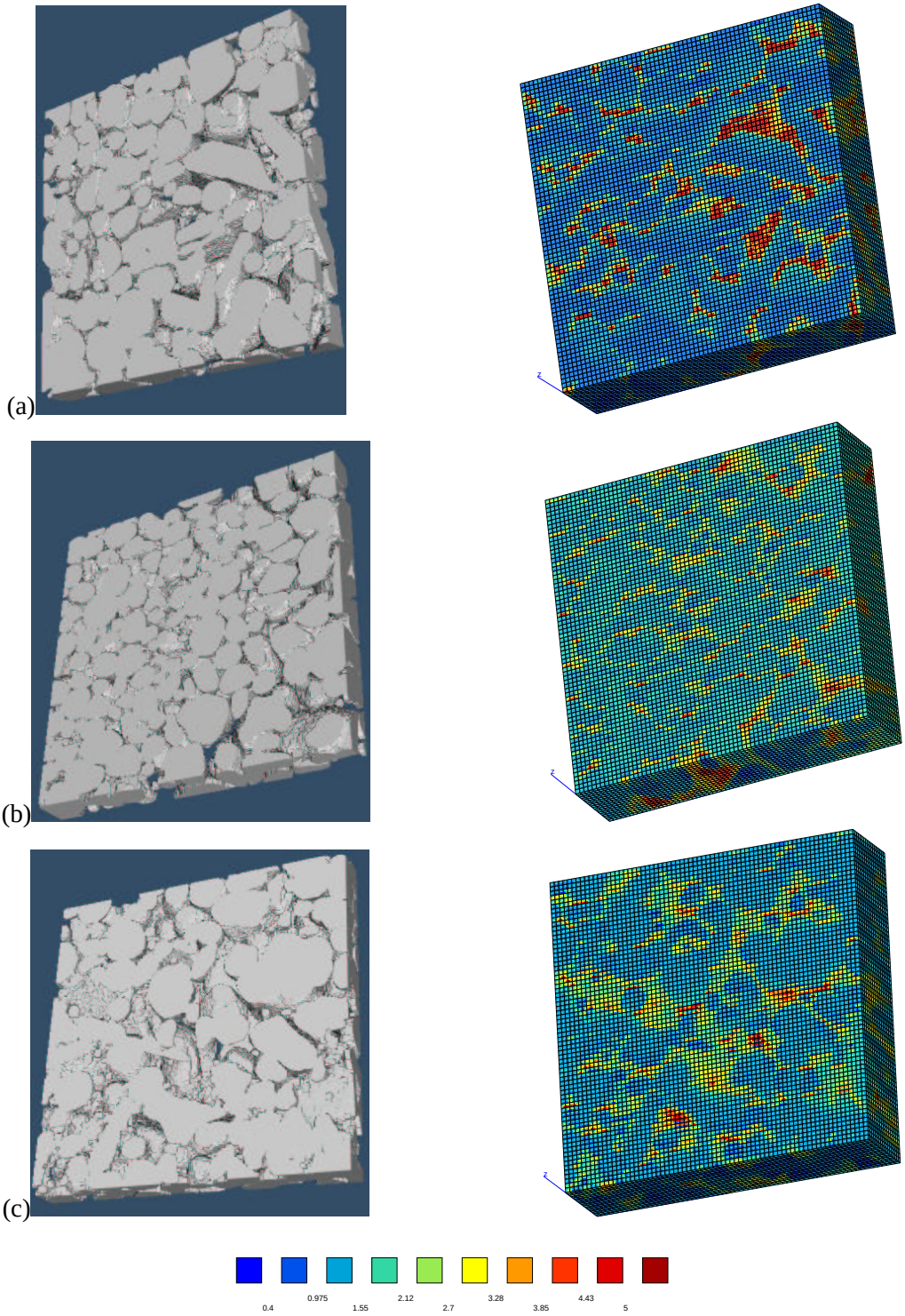

Figure II.23 : Direct numerical simulation of samples without additive SB, example of computation with $E_{22} = 1.$ in KUBC. The map of equivalent strain is shown.

$$[C]_{SA_2} = \begin{pmatrix} 1152 & 352 & 415 & 0 & 0 & 6 \\ & 1098 & 401 & 7 & 5 & 1 \\ & & 1597 & 1 & 9 & 12 \\ & & & 377 & 3 & 2 \\ & & & & 444 & 1 \\ & & & & & 451 \end{pmatrix} \quad \text{(II.30)}$$

$$[C]_{SA_3} = \begin{pmatrix} 674 & 166 & 16 & 1 & 0 & 1 \\ & 692 & 163 & 19 & 0 & 0 \\ & & 64 & 0 & 0 & 1 \\ & & & 258 & 0 & 1 \\ & & & & 228 & 0 \\ & & & & & 228 \end{pmatrix} \quad \text{(II.31)}$$

$$[C]_{SA_m} = \begin{pmatrix} 910 & 256 & 249 & 1 & 0 & 7 \\ & 868 & 285 & 9 & 3 & 1 \\ & & 1015 & 2 & 5 & 12 \\ & & & 312 & 2 & 1 \\ & & & & 345 & 1 \\ & & & & & 355 \end{pmatrix} \quad \text{(II.32)}$$

$$[C]_{SB_1} = \begin{pmatrix} 1197 & 333 & 416 & 1 & 12 & 23 \\ & 1060 & 384 & 5 & 20 & 7 \\ & & 1675 & 1 & 37 & 34 \\ & & & 387 & 12 & 0 \\ & & & & 457 & 1 \\ & & & & & 489 \end{pmatrix} \quad \text{(II.33)}$$

$$[C]_{SB_2} = \begin{pmatrix} 1998 & 958 & 966 & 13 & 0 & 11 \\ & 1985 & 960 & 5 & 4 & 1 \\ & & 2215 & 2 & 5 & 16 \\ & & & 500 & 3 & 1 \\ & & & & 537 & 2 \\ & & & & & 545 \end{pmatrix} \quad \text{(II.34)}$$

$$[C]_{SB_3} = \begin{pmatrix} 1739 & 859 & 860 & 1 & 5 & 14 \\ & 1661 & 864 & 8 & 29 & 2 \\ & & 1846 & 2 & 25 & 22 \\ & & & 401 & 9 & 13 \\ & & & & 442 & 1 \\ & & & & & 442 \end{pmatrix} \quad \text{(II.35)}$$

$$[C]_{SB_m} = \begin{pmatrix} 1645 & 717 & 747 & 5 & 6 & 16 \\ & 1569 & 736 & 6 & 18 & 3 \\ & & 1912 & 2 & 22 & 24 \\ & & & 429 & 8 & 5 \\ & & & & 479 & 1 \\ & & & & & 492 \end{pmatrix} \tag{II.36}$$

One can notice some anisotropy of the retained apparent elastic matrices computed for each sample. The values of the apparent elastic coefficients are in general not very different in dimensions (OX) and (OY). In the thickness direction OZ it is not the case.

As a result, our samples exhibit a significant anisotropy in the thickness direction. Physically, the value along the thickness of the sample is smaller by comparison with the two other directions. The small thickness of the samples is responsible for this anisotropy.

To quantify the anisotropy of these apparent elastic matrices, we give here the anisotropic index a for each sample. In the case of a matrix with a cubic symmetry, this index is given by :

$$a = \frac{2C_{44}}{C_{11} - C_{12}} \tag{II.37}$$

In our case, we take :

$$C_{44} = \frac{C_{44}^{app} + C_{55}^{app} + C_{66}^{app}}{3} \tag{II.38}$$

$$C_{11} = \frac{C_{11}^{app} + C_{22}^{app} + C_{33}^{app}}{3} \tag{II.39}$$

and :

$$C_{12} = \frac{C_{12}^{app} + C_{23}^{app} + C_{31}^{app}}{3} \tag{II.40}$$

We can also look at the anisotropy in the plane (XY). The in-plane anisotropy coefficient a_{XY} is defined as :

$$a_{XY} = \frac{2C_{44}^{app}}{C_{11}^{XY} - C_{12}^{app}} \tag{II.41}$$

with :

$$C_{11}^{XY} = \frac{C_{11}^{app} + C_{22}^{app}}{2} \tag{II.42}$$

The values of the retained anisotropy index for each sample and for the mean matrix of each type of microstructure are given in the table II.4.

Samples	SA_1	SA_2	SA_3	SA_m	SB_1	SB_2	SB_3	SB_m
a	0.934	0.950	1.316	1.010	0.952	0.954	0.966	0.956
a_{XY}	0.988	0.975	0.998	0.988	0.973	0.968	0.954	0.964

Table II.4 : The index of anisotropy of each sample and of the mean matrix of each type.

It appears that the rather small thickness of the samples introduces a bias in the determination of effective properties of the materials. Which means that their size is not representative. We use in the following a statistical approach (as it is proposed in the case of Voronoï mosaics) to estimate the effective physical properties of these microstructures, and the size of representative volumes of these materials.

b) Young's Modulus and Thermal Conductivity

Mixed boundary conditions have been used to estimate the apparent Young's modulus of the samples in direction (OY) (figure II.24). The simulations of Young's modulus on the whole sample is also given for the sample SA_2. As shown in this figure, the absolute bounds of Voigt-Reuss and those of Hashin-Shtrikman are very far apart. The experimental results in the case of the sample SA_2 are not close to the results of simulation on the whole sample, which can be explained by the non representativity of the size of the simulated samples.

In figure II.25 (a), the self-consistent model gives an apparent Young's modulus larger than the one given by the simulations of the whole map. This difference can be explained by the smaller size of the used sample or / and by the fact that this model is not good for this type of heterogeneous materials.

For the thermal conductivity, we have the experimental value only for the case of the material SB. This value gives an error of 9% by comparison with numerical simulations.

II.4.2 Quantifying the Representativity of the Investigated Samples

In many practical cases, as in our real microstructures, the concept of a representative volume element does not apply or cannot be used when the size of the investigated samples is limited. Especially, the thickness of our studied samples

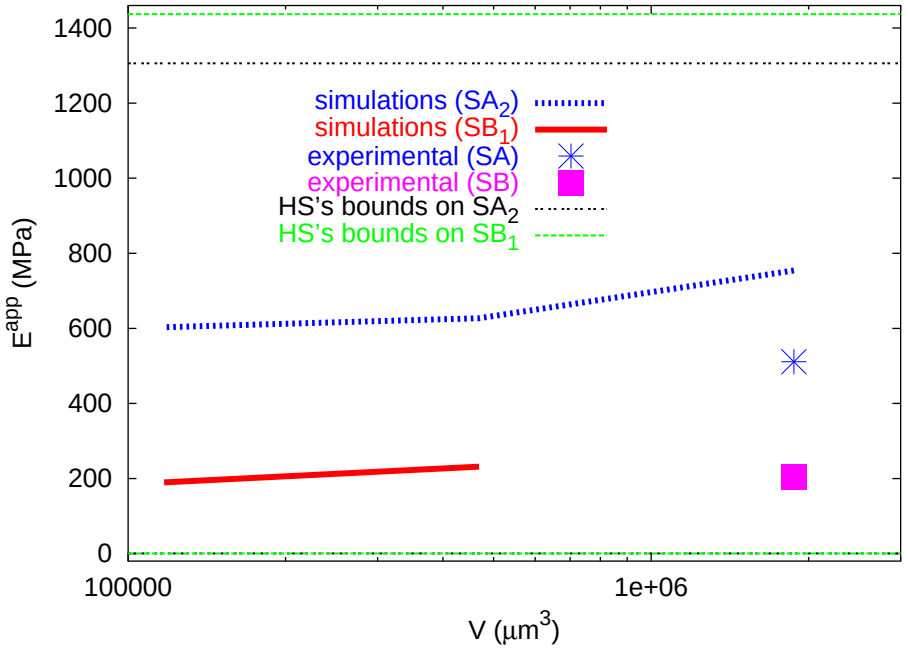

Figure II.24 : Simulation results of Young's modulus and comparison with the experimental values.

is not large enough by comparison with the two other dimensions (see figure II.1). Instead, using smaller sizes in this case is the only possible method to estimate the effective physical properties of the material.

The following aspects are investigated :

- Relationships between experimental results obtained on the whole sample but still smaller than the RVE, on the one hand, and on an appropriate set of smaller volumes (named uniform or regular partitions) and a random one on the other hand.
- Effect of the variation of the volume of the smaller specimens.
- Comparison between the results given by the absolute bounds on the one hand and the results given by two limiting cases : where the size of the smaller specimens goes to zero and where this size goes to that of the representative volume element on the other hand.
- Effect of applied boundary conditions : mixed and kinematic uniform boundary conditions (KUBC) to compute the Young's modulus E_{OY} in the direction (OY) of the sample SB_1.

a) Effect of Partitions

Figure II.24 shows an example of computation of apparent Young's modulus E^{app} for two samples of our studied microstructures : SA_2 and SB_1. The results of

(a)

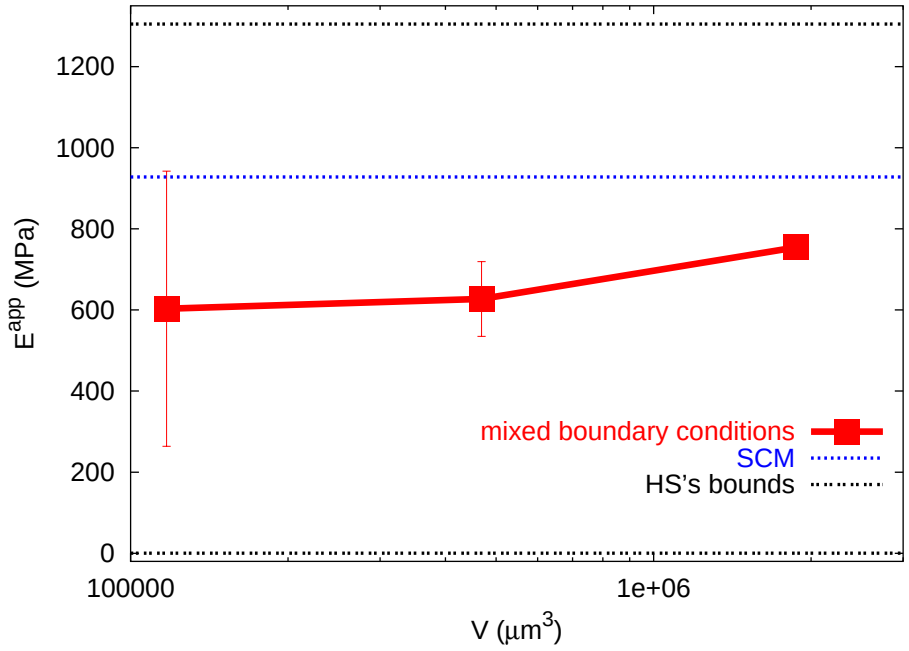

(b)

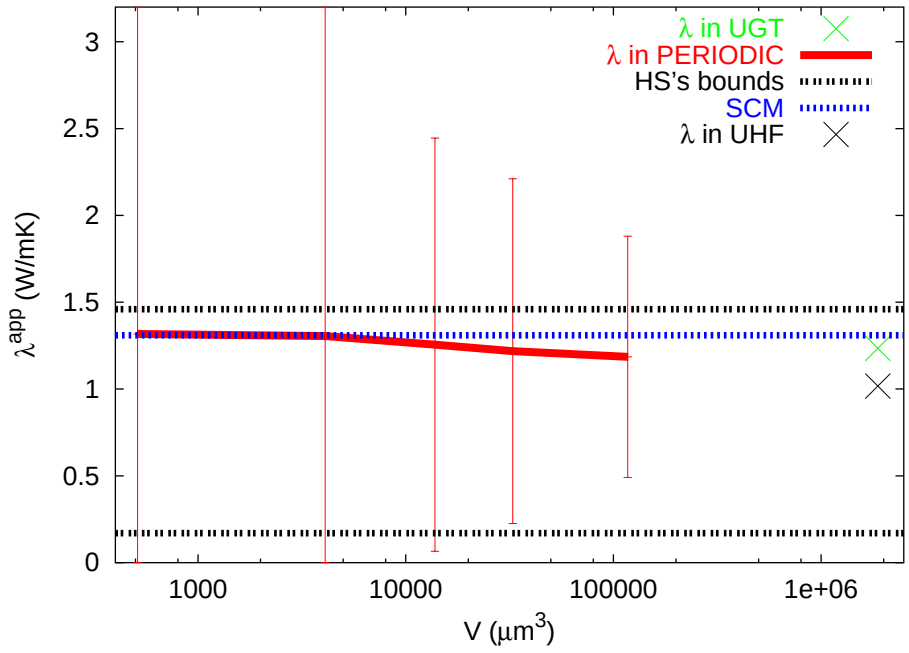

Figure II.25 : Mean values and intervals of confidence on the mean value for Young's modulus E^{app} (a) and thermal conductivity (b) as a function of the domain size for the specimen SA_2.

computations are given for the whole specimen with volume V_1 :

$$V_1 = V = 250 \times 250 \times 30 = 1875000\ \mu m^3 \tag{II.43}$$

and for two uniform partitions of the whole microstructure : the first partition is divided into 4 smaller samples with volume V_2 :

$$V_2 = \frac{1}{4} V_1 = 468750\ \mu m^3 \tag{II.44}$$

and the second one is divided into 16 smaller samples with volume V_3 :

$$V_3 = \frac{1}{16} V_1 = 117187.5\ \mu m^3 \tag{II.45}$$

The computations of Young's modulus are made with mixed boundary conditions on the whole specimen and on each smaller sample. In the case of two partitions, the average value is shown on figure II.24. One can clearly notice the bias existing when computing with smaller samples, in comparison with the obtained result on the whole specimen, even if the set of smaller samples builds a uniform partition of the whole microstructure. This bias is the due to boundary conditions. As an important result, one notes that the average value of the apparent Young's moduli computed with mixed boundary conditions and with a set of smaller samples, forming a uniform partition of the whole specimen, underestimates the apparent Young's modulus computed on the whole specimen with the same boundary conditions.

We can quantify the error made when computing with different uniform partitions : we have an error of $\epsilon_{rela} = 17\%$ using the first partition and $\epsilon_{rela} = 20\%$ using the second one for sample SA_2. This error increases when the number of smaller samples increases. These remarks hold true when using a random partition of the whole sample with the same number of smaller samples.

We have similar remarks when computing the apparent shear modulus, the apparent bulk modulus and the apparent thermal conductivity in different uniform boundary conditions with a random partition.

b) Sizes of Specimens

We have seen in the case of apparent Young's modulus, using mixed boundary conditions, that the error in computation with a set of smaller samples increases when the number of smaller samples increases. This means that, this error increases when the size of smaller samples decreases and the partition in this case underestimates the results obtained on the whole specimen.

In the case of apparent shear modulus μ^{app} and the apparent bulk modulus k^{app} (respectively the apparent thermal conductivity λ^{app}), the computation with a given partition with the kinematic uniform boundary conditions KUBC (respectively the uniform gradient of temperature at the boundaries UGT) overestimates the results obtained on the whole specimen. The computation with the static uniform boundary conditions SUBC (respectively the uniform heat flux at the boundaries UHF) underestimates the results obtained on the whole specimen. In both cases of boundary conditions, the error in computation increases when the size of smaller samples decreases.

When the sample is equal or larger than the representative volume element, the apparent properties coincide with the effective ones. In many cases, they are not the same (Huet, 1990), (Huet, 1991), (Sab, 1992), (Hazanov and Huet, 1994), (Ostoja-Starzewski, 1998) and (Jeulin and Ostoja-Starzewski, 2002).

c) Comparison with Absolute Bounds

The bounds of Voigt-Reuss (respectively Wiener's bounds) are the absolute bounds of the elastic moduli (respectively thermal conductivity). The partition into smaller samples overestimates or underestimates the results obtained on a partitioned sample. If the size of smaller samples goes to zero, the computation of the elastic properties (respectively thermal conductivity) with kinematic uniform boundary conditions KUBC (respectively UGT) gives the same results given by the absolute upper bound, or Voigt bound (respectively upper Wiener bound). The computation with static uniform boundary conditions SUBC (respectively UHF) gives the same results given by the absolute lower bound, or Reuss bound (respectively lower Wiener bound).

Now, if the partitioned specimen is a representative volume element, the results obtained with computation of this specimen are the effective ones and they are the same with both two types of uniform boundary conditions. Another case must be noted : if the partitioned specimen is larger than the representative volume element, and the partition into smaller volumes gives samples with sizes equal to the size of the representative volume element, in this case only the results obtained by averaging all the samples give the effective ones.

d) Influence of Boundary Conditions

Figure II.26 shows the results of computation of the apparent Young's modulus E^{app}_{OY} in the direction (OY) on the sample SB_1. The computations are made with mixed boundary conditions on the whole sample and on each smaller volume of the uniform partition into 16 smaller specimens. In each computation, the map of the equivalent strain (equation (II.18)) is shown.

As we have seen in the results of computations on smaller specimens, the average value of all apparent Young's moduli of smaller specimens differs from what is

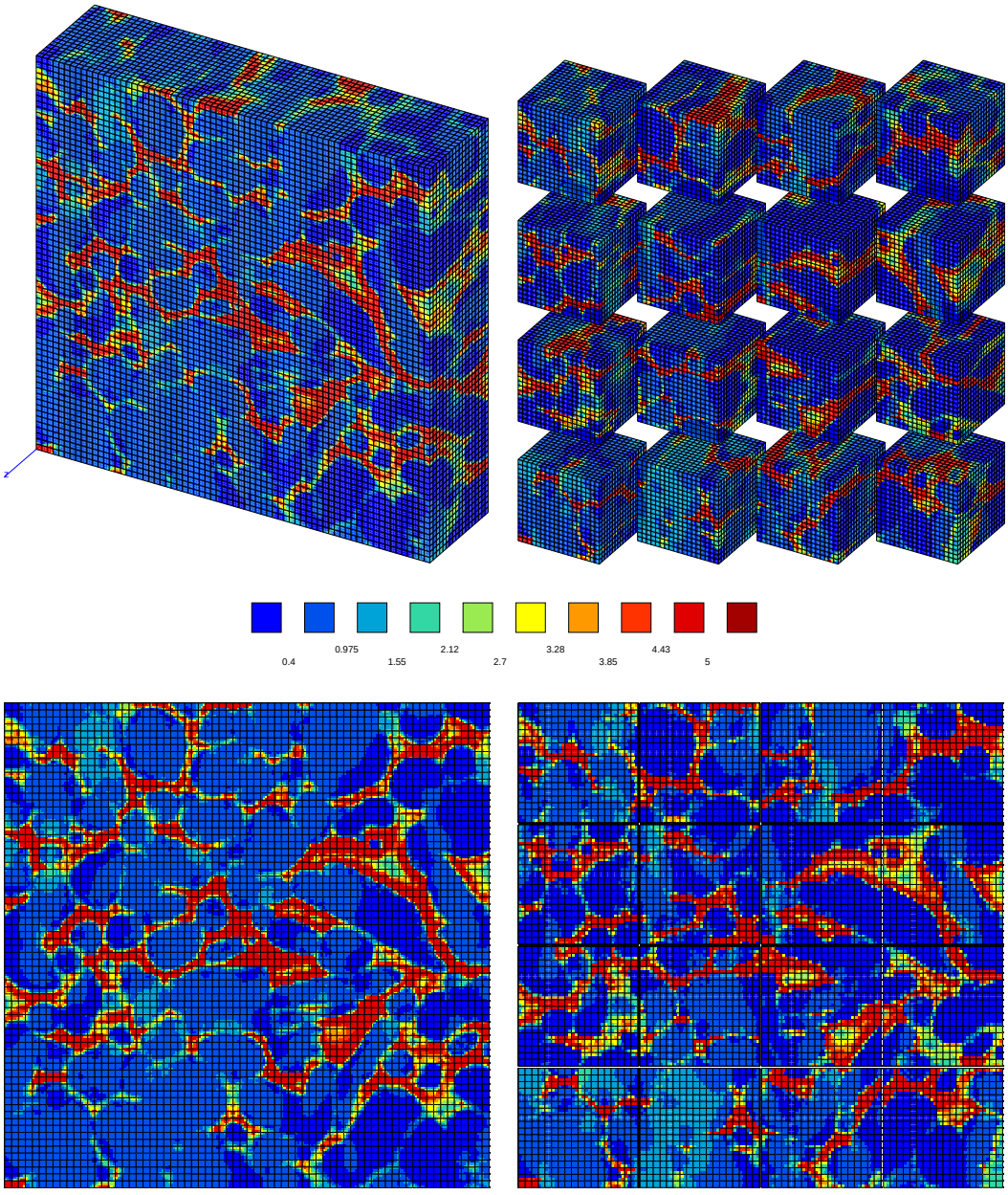

Figure II.26 : Application of mixed boundary conditions on sample SB_1 : effect of a regular distribution of volumes on local field of equivalent strain.

obtained with computation on the whole specimen. In figure II.26 one can remark this phenomenon clearly : the maps of the equivalent strain are not continuous between two neighboring sub-domains, which can be explained by the effect of the boundaries. We can make the same comments in the case of a random partition.

To study the case of kinematic uniform boundary conditions KUBC, we apply the value of the average strain tensor $< \underset{\sim}{\boldsymbol{\varepsilon}} >$ obtained in the computation given in figure II.26 (with mixed boundary conditions) as a uniform strain tensor $\underset{\sim}{\boldsymbol{E}}$ (equation (II.46)) at the boundary on the same microstructure (with KUBC boundary conditions). The results of these computations are shown in figure II.27. Results of computations on the whole sample and on a set of the same uniform partition are given. The strain tensor found in the first computation (figure II.26) and applied to the second one (figure II.27) is :

$$< \underset{\sim}{\boldsymbol{\varepsilon}} >= \begin{pmatrix} -0.367 & 0.018 & 0.010 \\ 0.018 & 1.000 & 0.013 \\ 0.010 & 0.013 & -0.356 \end{pmatrix} = \underset{\sim}{\boldsymbol{E}} \qquad \text{(II.46)}$$

Also in this case of boundary conditions, the result obtained by computation on the whole microstructure is not the same as the average value of the results obtained on a set of smaller volumes. In this case, the computations on smaller volumes overestimate the results on the whole sample. In figure II.27, we observe the discontinuity in the maps of the equivalent strain of smaller volumes, which can be explained also by the effect of the boundaries.

e) Comparison with Huet's Results

Our microstructures are a good example of studies of heterogeneous materials with samples smaller than the representative volume element. This problem is largely studied theoretically by Huet in several works, for instance in (Huet, 1990), (Huet, 1991) and (Hazanov and Huet, 1994). A reminder of his theories is given in the appendix A.

In this part, we validate some results by comparison with Huet's results given in appendix A.

The first result of Huet compares the apparent properties obtained on a large sample smaller than the representative volume element, using two different uniform boundary conditions. In the figure II.25(b), we present the results of numerical simulations on the whole sample SA_2, of the apparent thermal conductivity using two different uniform boundary conditions : the uniform gradient of temperature at the boundary (UGT) and the uniform flux at the boundary (UHF). One can remark clearly that the apparent thermal conductivity λ^{app}_{UHF} computed with the UHF boundary conditions is smaller than once computed with the UGT boundary conditions λ^{app}_{UGT} :

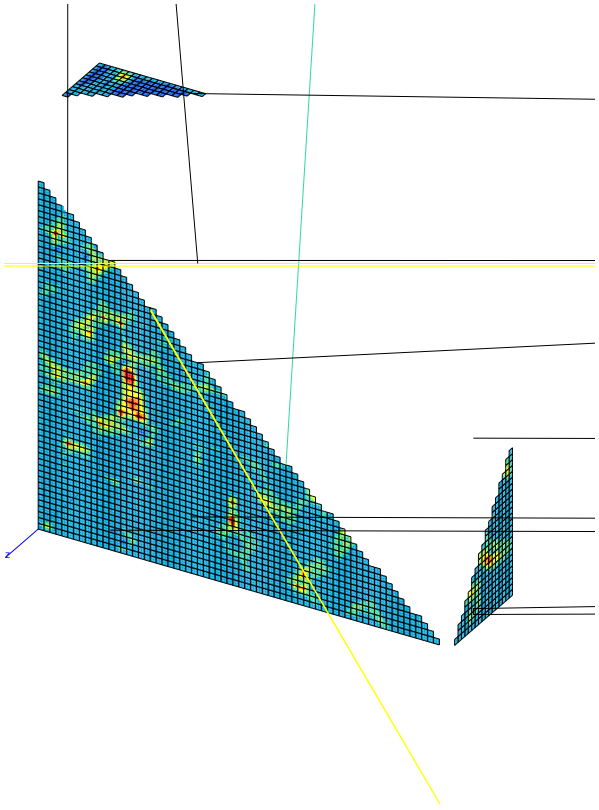

$$\lambda_{UHF}^{app} \leq \lambda_{UGT}^{app} \tag{II.47}$$

which satisfies the inequality (A.1) of the appendix A.

In the inequality (A.3), the apparent properties of a given sample smaller than the representative volume element (computed with KUBC or SUBC boundary conditions) are bounded on both sides by the average apparent properties computed on a set of smaller specimens forming a uniform or a random partition of the given sample.

In fact, this is true also in our microstructures. Especially, it is also true when using mixed boundary conditions to compute Young's modulus. In figure II.24, although bounding theorems are not available for effective Young's modulus, we find numerically that the apparent Young's modulus E_1^{app} computed on the whole sample SA_2 is larger than the average value of Young's moduli computed on sets of two examples of uniform partitions into 4 specimens and into 16 specimens, $\overline{E_4^{app}}$ and $\overline{E_{16}^{app}}$. In this example we have :

$$\overline{E_{16}^{app}} = 603\ MPa\ \leq \overline{E_4^{app}} = 627\ MPa\ \leq E_1^{app} = 754\ MPa \tag{II.48}$$

In the inequalities (II.48), the apparent Young's modulus computed on the whole sample SA_2 is bounded on one side by average value of Young's moduli of its sets of uniform partitions into 4 and into 16 smaller specimens.

Now, if the studied large sample has the size of the representative volume element, the computation on a set of smaller specimens obtained with a uniform or random partition of this sample gives bounds on both sides of the wanted effective properties.

This has an application in our real microstructure and in the case of Voronoï mosaics. In the case of real microstructures, figure II.28 shows clearly this phenomenon. The wanted effective properties are those given by the periodic boundary conditions and to which the results given by the uniform boundary conditions converge in the case of larger volumes. In this figure, the effective bulk modulus k^{eff} (respectively the effective shear modulus μ^{eff}) is bounded on one side by the average value of the apparent bulk moduli $\overline{k_{KUBC}^{app}}$ (respectively shear moduli $\overline{\mu_{KUBC}^{app}}$) computed on a set of smaller specimens with the KUBC boundary conditions.

For example, for a volume of the smaller specimens :

$$V = 32768\ \mu m^3 \tag{II.49}$$

we have :

$$k^{eff} = 634\ MPa \leq \overline{k^{app}_{KUBC}} = 737\ MPa \tag{II.50}$$

for the bulk modulus and :

$$\mu^{eff} = 345\ MPa \leq \overline{\mu^{app}_{KUBC}} = 480\ MPa \tag{II.51}$$

for the shear modulus, which correspond to the inequality (A.5) of appendix 1.

The inequality (A.5) is also verified in the case of physical properties of Voronoï mosaics. In the case of elastic properties, figure I.7 explains clearly this result. Taking an example of volume of smaller specimens : $V = 300\ grains$, the effective bulk modulus given by periodic boundary conditions k^{eff} (respectively effective shear modulus μ^{eff}) is bounded on both sides by the average value of apparent bulk moduli (respectively apparent shear moduli) computed on a set of smaller volumes with size equals to $V = 300\ grains$ with KUBC boundary conditions $\overline{k^{app}_{KUBC}}$ (respectively $\overline{\mu^{app}_{KUBC}}$) and SUBC boundary conditions $\overline{k^{app}_{SUBC}}$ (respectively $\overline{\mu^{app}_{SUBC}}$). So, we have :

$$\overline{k^{app}_{SUBC}} = 1095\ MPa \leq k^{eff} = 1198\ MPa \leq \overline{k^{app}_{KUBC}} = 1264\ MPa \tag{II.52}$$

for bulk modulus and :

$$\overline{\mu^{app}_{SUBC}} = 243\ MPa \leq \mu^{eff} = 433\ MPa \leq \overline{\mu^{app}_{KUBC}} = 514\ MPa \tag{II.53}$$

for shear modulus.

For the thermal conductivity of Voronoï mosaics, figure I.8 gives similar results. If we choose for the size of smaller specimens $V = 1000\ grains$ we have :

$$\overline{\lambda^{app}_{UHF}} = 0.821\ W/mK \leq \lambda^{eff} = 1.346\ W/mK \leq \overline{\lambda^{app}_{UGT}} = 1.410\ W/mK \tag{II.54}$$

The fourth result of Huet given in the appendix 1 (inequalities (A.7) and (A.8)) is also verified in the real microstructures and in the Voronoï mosaics, in elastic moduli and thermal conductivity.

In the sample SA_2, the mean value of apparent bulk moduli $\overline{k^{app}_{KUBC}}$ (respectively apparent shear moduli $\overline{\mu^{app}_{KUBC}}$) of a set of smaller specimens with a volume $V = 32768\ \mu m^3$ computed in KUBC boundary conditions (figure II.28) is bounded on both sides by the effective bulk modulus k^{eff} (respectively effective shear modulus μ^{eff}) on one hand and the upper bound k^{Voigt} (respectively μ^{Voigt}) on the other hand; so we have :

$$k^{eff} = 634\ MPa \leq \overline{k^{app}_{KUBC}} = 737\ MPa \leq k^{Voigt} = 1430\ MPa \qquad \text{(II.55)}$$

and :

$$\mu^{eff} = 345\ MPa \leq \overline{\mu^{app}_{KUBC}} = 480\ MPa \leq \mu^{Voigt} = 660\ MPa \qquad \text{(II.56)}$$

In the Voronoï mosaics (figure I.7), we have :

$$k^{eff} = 1198\ MPa \leq \overline{k^{app}_{KUBC}} = 1264\ MPa \leq k^{Voigt} = 1583\ MPa \qquad \text{(II.57)}$$

and :

$$\mu^{eff} = 345\ MPa \leq \overline{\mu^{app}_{KUBC}} = 480\ MPa \leq \mu^{Voigt} = 676\ MPa \qquad \text{(II.58)}$$

this is from the one hand, from the other hand we have :

$$k^{Reuss} = 947\ MPa \leq \overline{k^{app}_{SUBC}} = 1095\ MPa \leq k^{eff} = 1198\ MPa \qquad \text{(II.59)}$$

and :

$$\mu^{Reuss} = 27\ MPa \leq \overline{\mu^{app}_{SUBC}} = 243\ MPa \leq \mu^{eff} = 433\ MPa \qquad \text{(II.60)}$$

for a volume $V = 1000\ grains$ of smaller volumes.

The theoretical proof for the validity of these results is largely studied by Huet in (Huet, 1990) under the form of what he calls the *partition theorem*.

The results obtained theoretically by Huet and validated numerically in our work are also valid for shapes other than the parallelepipedic one. The type of partition is not important; one can use a random partition inside the uniform one but with a sufficiently large number of specimens n; this is well illustrated in figure II.28 for a uniform and a random partition with KUBC and periodic boundary conditions.

The results obtained here are also valid for shapes other than the cubic or parallelepipedic one used in this work, and which is the most suitable for the testing when applying the proposed method. In numerical simulations, use of other shapes of specimens and of samples will be possible, provided the sample will be decomposable into specimens with shapes filling the space in the case of uniform partition. A good example of numerical simulations with cubic specimens is given in (Zohdi et al., 2001).

II.5 Effective Properties and Representative Volume Element Size

The overall physical properties are studied in this part for a large range of volume sizes V and a large number of realizations n of small volumes taken in the whole real microstructures. The investigated physical properties are the elastic moduli (bulk modulus k and shear modulus μ) and the thermal conductivity λ.

For each property, the dispersion of the results when increasing the volume V and the integral ranges are reported in subsection (II.5.1).

II.5.1 Dispersions of Physical Properties

The microstructures presented in the introduction of this chapter (especially the specimens SA_2 as an example with additive and SB_1 as an example without additive, figures II.22 and II.23) are introduced in the finite element method for various boundary conditions : the kinematic uniform boundary conditions KUBC (the uniform gradient of temperature UGT in the case of thermal conductivity) and periodic boundary conditions (PERIODIC) with two different methods of decomposition into smaller volumes : regular and random decompositions. The objective of this part is to estimate the apparent physical properties (the bulk modulus k^{app}, the shear modulus μ^{app}, the Young's modulus E^{app} and the thermal conductivity λ^{app}), as a function of the size of the domain V taken in these microstructures.

a) Elastic Properties

The numerical simulations based on the finite element method are carried out for two different boundary conditions: kinematic uniform boundary conditions (KUBC) and the periodic boundary conditions (PERIODIC) for bulk modulus k and shear modulus μ and mixed boundary conditions for Young's modulus E. The mixed boundary conditions used here to compute the apparent Young's modulus are such that one face of the microstructure is fixed, and a given displacement is prescribed to the opposite face in the tensile direction. The studied specimens are SA_2 (as an example with additive, figure II.22(b)) with volume fraction of hard phase $P_1 = 68.64\%$ and SB_1 (as an example without additive, figure II.23(a)) with volume fraction of hard phase $P_1 = 73.01\%$. The number of fields (smaller volumes) n for each volume V is given in table II.5. The number n is found by subdivision of the global volume V_{global} of the microstructure :

$$V_{global} = 250 \times 250 \times 30 = 1875000\ \mu m^3 \tag{II.61}$$

by sub-domains V. For example, the number n of fields for the volume $V = 8 \times 8 \times 8 = 512\ \mu m^3$ is : 3662 fields. They are obtained from regular and random subdivisions of the whole microstructure.

(a)

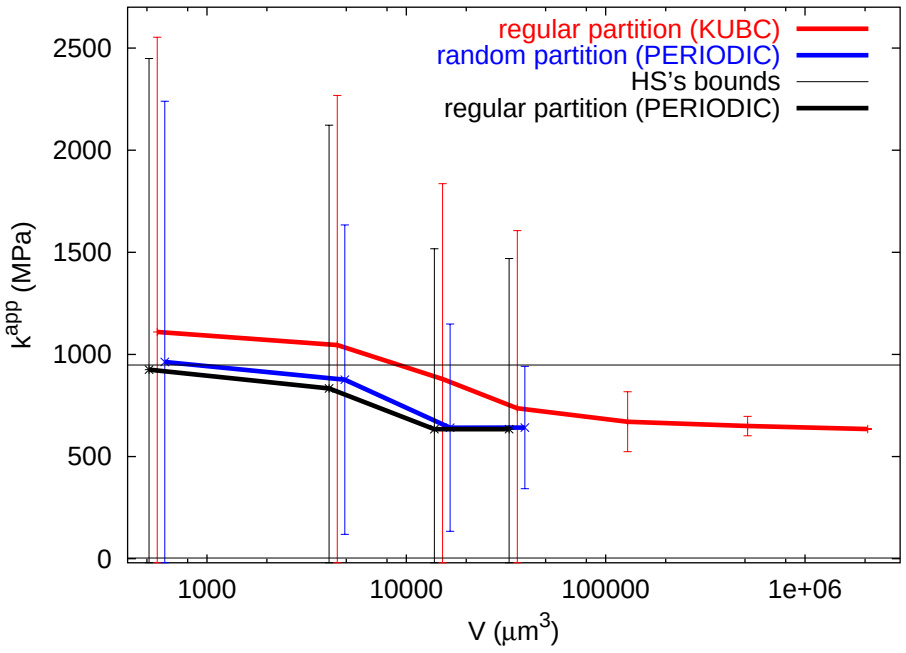

(b)

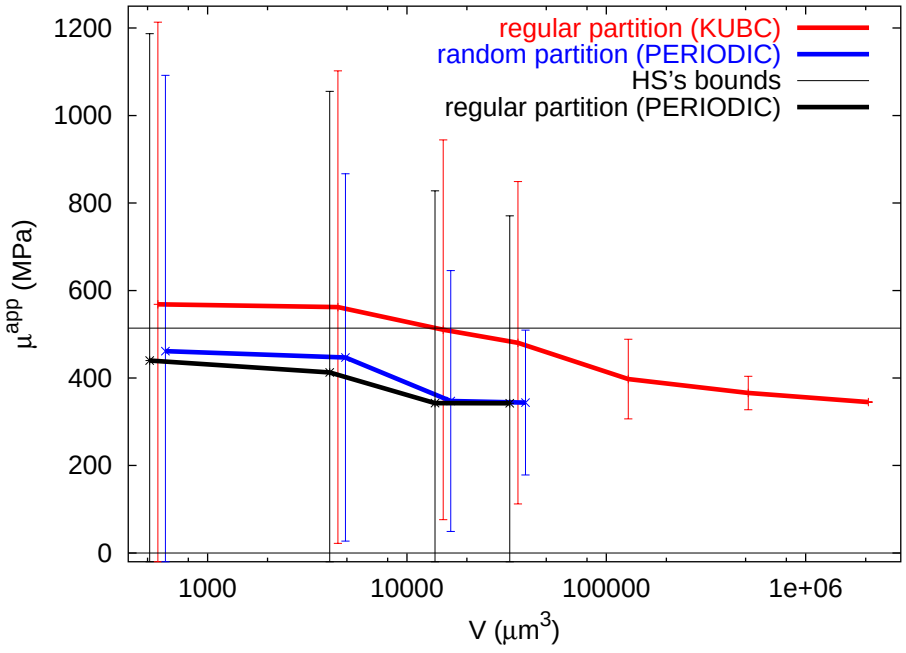

Figure II.28 : Mean values and intervals of confidence on the mean value for the bulk modulus k^{app} (a) and (b) for the shear modulus μ^{app} as a function of domain size for the specimen SA_2. The upper and lower bounds are (1430, 2.65 MPa) for k and (660, 0.05 MPa) for μ.

Volume of the Domain V (μm^3)	Number of Fields n
512	3662
4096	458
13824	136
32768	58
117188	16
468750	4
1875000 (the whole microstructure)	1

Table II.5 : Number of fields n used for all considered domain sizes, regular and random partitions.

Figures II.28 (a and b) and II.25 (a) give the obtained mean values and variances of the apparent moduli k^{app}, μ^{app} and E^{app} as a function of the volume size V. It shows that the dispersion of the results decreases when the size of the domain increases for all used boundary conditions.

The obtained mean values generally depend on the volume size, but also on the type of boundary conditions. For each modulus, the values converge towards the same limit for large volumes V, which is the wanted effective modulus. The values k^{eff}, μ^{eff} and E^{eff} found for large volume sizes are reported in table II.6 and compared to the Voigt-Reuss (upper bound and lower bound) and Hashin–Shtrikman's bounds (HS+ and HS-). The self–consistent model (SC), also given in table II.6, provides a fair estimate for specimen SA_2 . However, the self-consistent estimate strongly overestimates the effective properties of specimen SB_1.

Property	Simulation	Upper Bound	Lower Bound	HS+	HS-	SC
μ (SA_2)	345	660	0.05	514	0.11	371
μ (SB_1)	207	702	0.06	564	0.13	456
k (SA_2)	634	1430	2.65	948	2.70	618
k (SB_1)	334	1521	3.08	1058	3.14	791
λ (SA_2)	1.20	1.68	0.08	1.46	0.17	1.31
λ (SB_1)	0.77	1.79	0.09	1.58	0.20	1.47

Table II.6 : Values of numerical results (simulated on domains with volume $V = 32768$ μm^3), Voigt-Reuss or Wiener's bounds (upper and lower bounds), Hashin-Shtrikman's bounds (HS+, HS-) and self–consistent estimate (SC) for elastic and thermal properties for the specimens SA_2 and SB_1. The elastic moduli are given in (MPa), the thermal conductivity in (W/mK). The experimental value of λ for SB_1 is 0.85 (W/mK).

It can be noticed that, as in the case of simulations of the Voronoï mosaics (Kanit et al., 2003a) (and chapter 1), the mean value given by the periodic boundary conditions varies only slightly as a function of the size of the domain, as compared to the other boundary conditions. Figures II.25 and II.28 give the corresponding confidence intervals $[\overline{Z} - 2D_Z, \overline{Z} + 2D_Z]$, where Z is one of the apparent moduli, $\overline{Z}$

its mean value and D_Z^2 its variance.

Again in the case of real microstructures, an important bias is found in the mean value given by all boundary conditions (in this case it is just verified for kinematic uniform boundary conditions and periodic boundary conditions) for small volume sizes, the value being different from the effective one obtained for large samples. For small volumes, the average moduli obtained by simulations depend on the boundary conditions : KUBC produce results close to the upper bound. The result is that the mean value computed on small specimens cannot represent the effective response for the composite material even using the periodic boundary conditions and a sufficient number of realizations. It appears also that for sufficiently large sizes, here around :

$$V^* = 13824\ \mu m^3 \tag{II.62}$$

the mean value obtained with the periodic boundary conditions practically does not depend on the size of simulations. Any more it is claimed, in several works ((Terada et al., 2000), (Kouznetsova, 2002), (Kanit et al., 2003a)), that the periodic boundary conditions provide the most reasonable estimates among the class of possible boundary conditions for statistically homogeneous media. There is however no formal proof for that.

Note finally that the results of numerical simulations give a good agreement with the experimental results. Figure II.24 shows the case of Young's modulus E^{app} for the specimens SA_2 and SB_1 (the relative error is about $15\ \%$ for the microstructure with additive SA_2 and $6\ \%$ for the microstructure without additive SB_1 (Young's modulus) and $9\ \%$ (thermal conductivity) for the specimen SB_1).

b) Thermal Conductivity

The effective thermal conductivity of real microstructures is studied here using real thermal conductivities of phases. The same microstructures used in the study of the RVE for elasticity (the specimens SA_1 with $P_1 = 68.64\ \%$ and SB_2 with $P_1 = 73.01\ \%$) are used to estimate the apparent thermal properties. The objective is to estimate the apparent thermal conductivity λ^{app} of the effective homogeneous equivalent medium, as a function of the volume of the sub-domains. The real thermal conductivities of the phases are

$$(\lambda_1, \lambda_2) = (2.44\text{W/mK}, 0.0244\text{W/mK}) \tag{II.63}$$

which gives a contrast :

$$c_\lambda = \frac{\lambda_1}{\lambda_2} = 100 \tag{II.64}$$

The results of numerical simulations are obtained only for periodic boundary conditions, and validated with computations on large volumes with homogeneous boundary conditions : uniform temperature gradient at the boundary (UGT), uniform heat flux at the boundary (UHF). Figure II.25 (b) gives the obtained mean values and variances of the apparent thermal conductivity λ^{app} as a function of the volume size. The value of λ^{eff} found for large volume sizes is reported in table II.6 and compared to the Wiener and Hashin-Shtrikman bounds. The self-consistent model gives a fair estimate for SA_2 but overestimates strongly SB_1.

II.5.2 Determination of the Integral Ranges

a) Elastic Moduli

As in the case of simulations of Voronoï mosaics, the effective properties are defined from spatial averages of fields $Z(x)$ over a volume V. The fluctuations of the average values over different realizations of the real microstructures inside the volume V are considered.

Using the scaling law, equation (I.89), for the elastic properties used in real microstructures, from the equation (I.90), we have :

$$D_k^2 = P_1(1-P_1)(k_1-k_2)^2 = 933784\ (MPa)^2 \tag{II.65}$$

$$D_\mu^2 = P_1(1-P_1)(\mu_1-\mu_2)^2 = 198988\ (MPa)^2 \tag{II.66}$$

in the case of the specimen SA_1 and :

$$D_k^2 = P_1(1-P_1)(k_1-k_2)^2 = 855978\ (MPa)^2 \tag{II.67}$$

$$D_\mu^2 = P_1(1-P_1)(\mu_1-\mu_2)^2 = 181680\ (MPa)^2 \tag{II.68}$$

in the case of the specimen SB_2.

Our data were fit to relation (I.94) for the elastic moduli k^{app} and μ^{app} in the case of periodic boundary conditions and kinematic uniform boundary conditions (KUBC) in the case of the specimen SA_2. The found parameters A_3 (in this case it is a volume of material in μm^3) and α are given in table II.7. The quality of the model can be seen in figure II.29 (a, b, c and d), where the variances of simulated results and the model are compared for the periodic boundary conditions and kinematic uniform boundary conditions. The power law is also well-suited for periodic boundary conditions in this case of real microstructures.

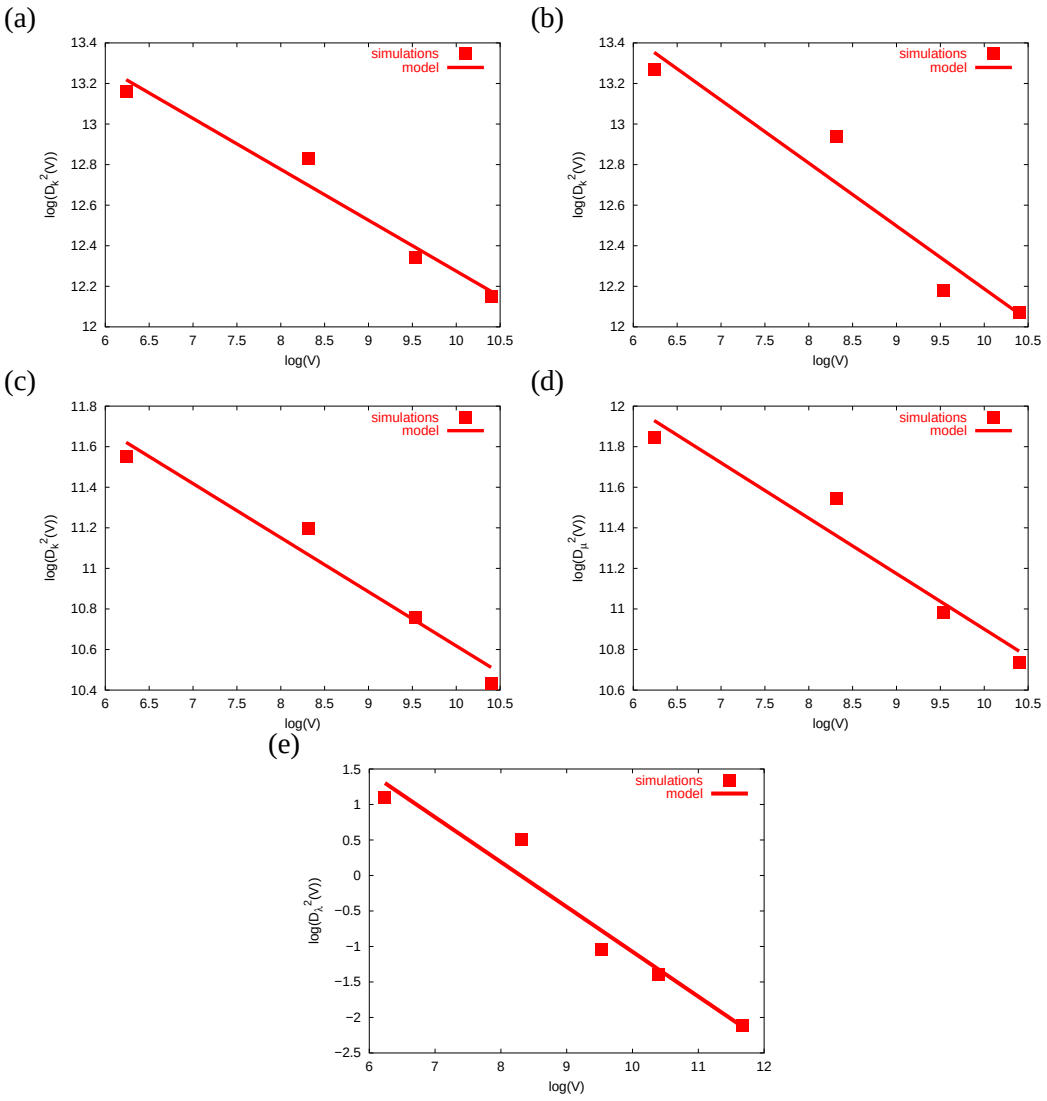

Figure II.29 : Quality of the fit for the specimen SA_2 in regular decomposition, (a) k for KUBC, (b) k for periodic, (c) μ for KUBC, (d) μ for periodic and (e) λ for periodic boundary conditions.

Physical Properties	Integral Range A_3 in μm^3	Coefficient α
$\mu\ (SA_2)$	869 ± 104	0.845 ± 0.202
$\mu\ (SB_1)$	1254 ± 125	0.750 ± 0.172
$k\ (SA_2)$	1161 ± 151	1.012 ± 0.263
$k\ (SB_1)$	1860 ± 298	0.921 ± 0.175
$\lambda\ (SA_2)$	2803 ± 420	0.632 ± 0.082
$\lambda\ (SB_1)$	5112 ± 460	0.696 ± 0.063

Table II.7 : Values of the integral range A_3 and of the coefficient α for elastic moduli k and μ and thermal conductivity λ in the case of periodic boundary conditions for the specimens SA_2 and SB_1.

From the coefficients given in table II.7, we see that the proposed scaling law in relation (I.89) can be accepted for our simulations also in the case of real microstructures. The value of the integral range is comparable to the size of the heterogeneities in the microstructures defined as the covariance range (figures II.5 and II.6). The largest integral range of the elastic moduli is found for the bulk modulus k in both microstructures (SA_2 and SB_1). The specimen SB_1 gives a larger integral range than specimen SA_2. The coefficient α is less than 1 for μ, meaning that the variance of the elastic moduli decreases more slowly with the volume than the variance of the volume fraction.

b) Thermal Conductivity

The power law model proposed in the case of elastic properties can be used also for apparent thermal properties. The point variance D^2_λ is :

$$D^2_\lambda = P(1-P)(\lambda_1 - \lambda_2)^2 = 1.2560\ (W/mK)^2 \tag{II.69}$$

in the specimen SA_2 and :

$$D^2_\lambda = P(1-P)(\lambda_1 - \lambda_2)^2 = 1.1498\ (W/mK)^2 \tag{II.70}$$

for the specimen SB_1.

The values of the integral ranges A_3 and of the coefficient α identified from the simulations are given in table II.7 for periodic boundary conditions. They are found to depend on the type of boundary conditions. The largest integral range for the thermal conductivity is obtained for the specimen SB_1 (as for the elasticity) and the coefficient α is lower than 1. These integral ranges are larger than for the case of elasticity. Figure II.29 (e) shows the quality of the model in the case of specimen SA_2.

II.5.3 Size of the Representative Volume Element

The real microstructures studied here can be considered as realizations of a random set. Therefore, as in the case of Voronoï mosaics, the idea that there exists one single possible minimal RVE size is not verified. It means that the size of a RVE must be given for a specific physical or morphological property, a given contrast in this property in different phases, and a given precision in the estimation of the effective studied property for a given number of different realizations that one is able to generate.

We recall that, in the theory of samples, the absolute error ϵ_{abs} on the mean value of a studied property Z, obtained with n independent (different) realizations of volume V, is given as a function of the variance $2D_Z(V)$ by :

$$\epsilon_{abs} = \frac{2D_Z(V)}{\sqrt{n}} \tag{II.71}$$

which gives the relative error ϵ_{rela} by :

$$\epsilon_{rela} = \frac{\epsilon_{abs}}{\overline{Z}} = \frac{2D_Z(V)}{\overline{Z}\sqrt{n}} \tag{II.72}$$

For sufficiently large volumes, the size of the RVE can be defined as the volume V_{RVE} for which $n = 1$ realization is necessary and sufficient to estimate the mean (effective) property Z with a relative error $\epsilon_{rela} = 1\%$ for instance, provided we know the function $D_Z(V)$. On the other hand, we can estimate the effective property using smaller volumes, and consider n different realizations to obtain the same relative error ϵ_{rela}. Equation (II.72) gives :

$$n = \frac{4D_Z^2(V)}{\overline{Z}^2\epsilon_{rela}^2} \tag{II.73}$$

The exact mean value $\overline{Z}$ and its variance for a given domain size are *a priori* unknown in the case of effective elastic moduli and effective thermal conductivity. The absolute error $2D_Z(V)$ on the mean value is given in equation (I.110) as :

$$2D_Z(V) = 2D_Z\sqrt{\left(\frac{A_3}{V}\right)^{\alpha}} \tag{II.74}$$

where Z stands here for k^{app}, μ^{app} or λ^{app}.

As in the case of Voronoï mosaics, we can note that for both types of microstructures (specimens SA and SB) and for the same absolute error ϵ_{abs}, the periodic boundary conditions require the largest domain size, compared to kinematic uniform boundary conditions (KUBC) (respectively UGT) and static uniform boundary conditions (SUBC) (respectively UHF) for k and μ (respectively λ). This is due to higher fluctuations of apparent properties obtained with these conditions. The kinematic uniform boundary conditions (respectively the uniform gradient of temperature at the boundary) require a smaller domain size than the static uniform boundary conditions (respectively uniform heat flux) for the same absolute error ϵ_{abs}.

The minimal number of different realizations n necessary and sufficient for the estimation of the effective property Z with a given absolute error ϵ_{abs} and a volume V is :

$$n(V) = \frac{4}{\epsilon_{abs}^2} D_Z^2 \left(\frac{A_3}{V}\right)^{\alpha} \tag{II.75}$$

The absolute error ϵ_{abs} corresponds to the estimation of the mean apparent moduli $\overline{Z^{app}}$ which have been found to depend in general on domain size and do not necessarily coincide with the wanted effective property Z^{eff}, especially for small domain sizes and uniform boundary conditions (KUBC and SUBC) (UGT and UHF

in thermal conductivity). This corresponds to a bias of the estimation. From the results of figures II.28 and II.25, the smallest domain size for which the bias can be neglected is about :

$$V^* = 13824\ \mu m^3 \tag{II.76}$$

(that represents a cube of $24 \times 24 \times 24\ \mu m^3$) for k^{app}, μ^{app} and λ^{app} in the case of periodic boundary conditions for both types of microstructures (specimens SA_2 and SB_1). For the uniform boundary conditions (KUBC and SUBC) (UGT and UHF in thermal conductivity), we need large volumes (the whole volume of microstructure : $250 \times 250 \times 30\ \mu m^3$ at least) to obtain unbiased mean values, i.e. mean apparent moduli $\overline{Z^{app}}$ that almost coincide with the wanted effective ones Z^{eff}.

Using equation (II.72), and for a volume V providing unbiased moduli ($V^* = 13824\ \mu m^3$ at least), we deduce the relative precision ϵ_{rela} of the effective property Z^{eff} (namely the effective bulk modulus k^{eff}, the effective shear modulus μ^{eff} or the effective thermal conductivity λ^{eff}). Hence, the minimal number n of fields that must be considered is deduced from equations (II.73) and (II.74). This is illustrated in figures II.30 and II.31 ((a) for specimen SA_2 and (b) for specimen SB_1) for $\epsilon_{rela} = 1\%$ in the case of periodic boundary conditions.

For a given precision ϵ_{rela}, the minimal number of necessary realizations decreases when the domain size increases for all the properties. The results are given only in the case of periodic conditions, which require the largest number of fields, compared with other boundary conditions. We give some interesting examples as applications of equation (II.73) for two unbiased volumes and periodic boundary conditions for all properties :

$$V_1 = V^* = 13824\ \mu m^3 \tag{II.77}$$

and :

$$V_2 = 32768\ \mu m^3 \tag{II.78}$$

The minimal numbers n of fields to obtain the effective bulk modulus k^{eff}, the effective shear modulus μ^{eff} and the effective thermal conductivity λ^{eff}, for a given precision ϵ_{rela} (1%, 2%, 5% and 10%), are given in table II.8 for the studied specimens (SA_2 and SB_1).

On the other hand, one can define the minimum size of the RVE V^{RVE} for a given ϵ_{rela} and a given number $n = 100$ of fields (for instance). The results are shown in figure II.32. When $\epsilon_{rela} = 1\%$, we give the values of V^{RVE} for both two types of studied microstructures and for all the physical properties (k, μ and λ) in

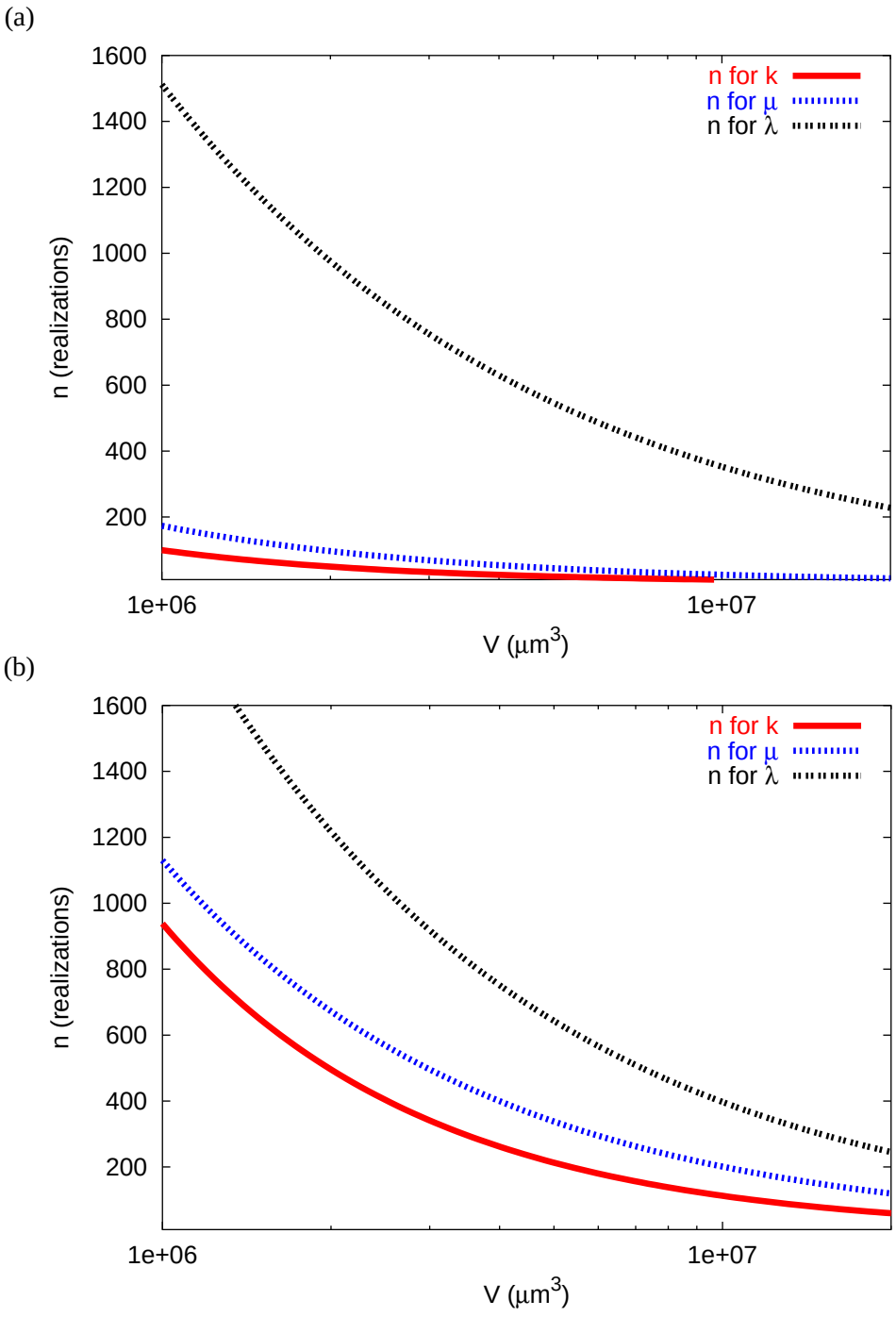

Figure II.30 : Number of fields (for bulk modulus k, shear modulus μ and thermal conductivity λ) as a function of the domain size (for large domain size) for a given relative error $\epsilon_{rela} = 1\%$: (a) for the specimen SA_2 and (b) for the specimen SB_1.

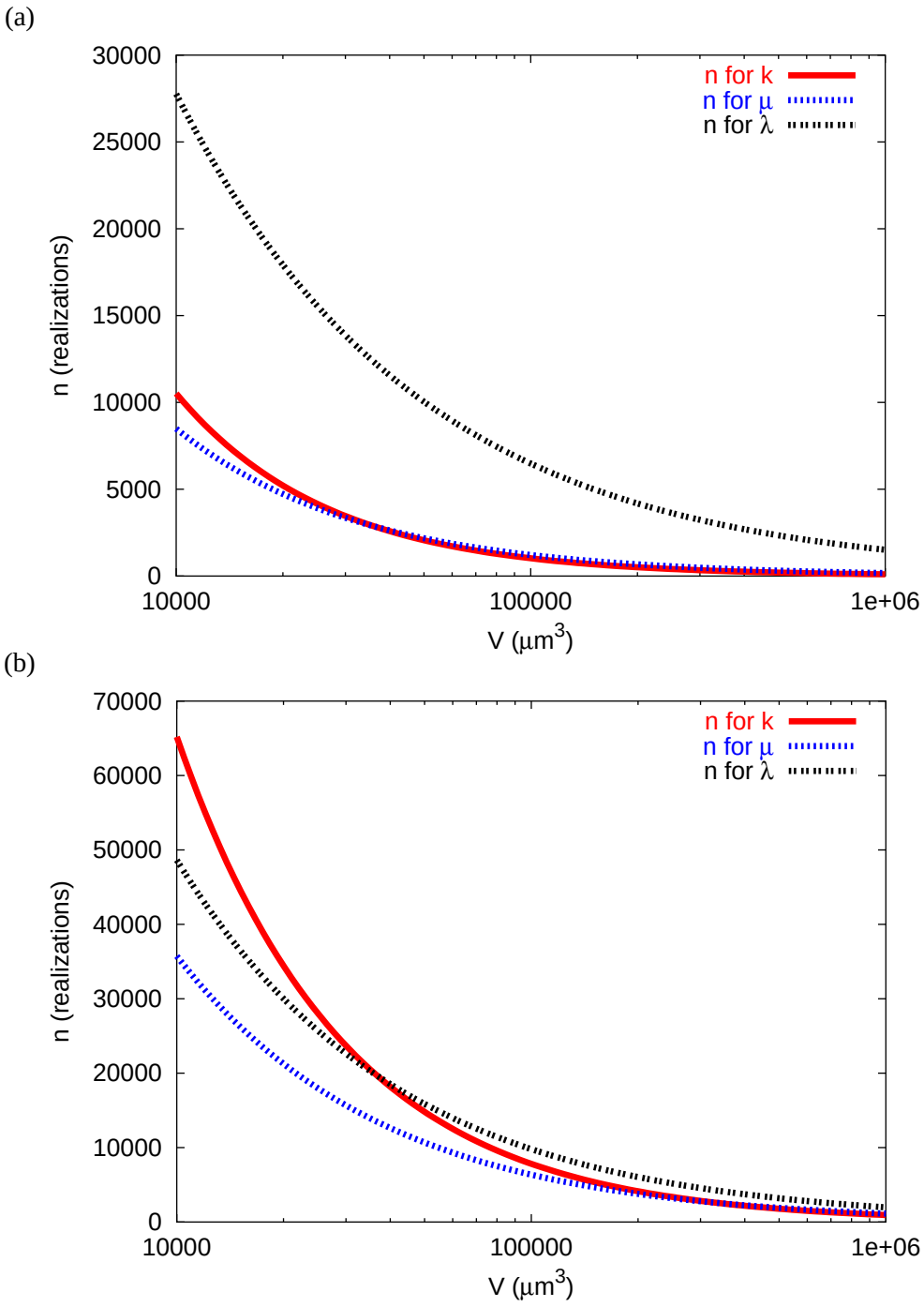

Figure II.31 : Number of fields (for bulk modulus k, shear modulus μ and thermal conductivity λ) as a function of the domain size (for small domain size) for a given relative error $\epsilon_{rela} = 1\%$: (a) for the specimen SA_2 and (b) for the specimen SB_1.

Relative Precision	$\epsilon_{rela} = 1\%$	$\epsilon_{rela} = 2\%$	$\epsilon_{rela} = 5\%$	$\epsilon_{rela} = 10\%$
k for SA_2 ($V_1 = 13824\ \mu m^3$)	7576	1894	300	75
k for SA_2 ($V_2 = 32768\ \mu m^3$)	3163	790	126	30
μ for SA_2 ($V_1 = 13824\ \mu m^3$)	6455	1613	258	64
μ for SA_2 ($V_2 = 32768\ \mu m^3$)	3113	778	124	30
λ for SA_2 ($V_1 = 13824\ \mu m^3$)	22624	5656	900	226
λ for SA_2 ($V_2 = 32768\ \mu m^3$)	13112	3278	524	130
k for SB_1 ($V_1 = 13824\ \mu m^3$)	48386	12096	1935	480
k for SB_1 ($V_2 = 32768\ \mu m^3$)	21853	5463	874	218
μ for SB_1 ($V_1 = 13824\ \mu m^3$)	28033	7000	1121	280
μ for SB_1 ($V_2 = 32768\ \mu m^3$)	14674	3668	586	146
λ for SB_1 ($V_1 = 13824\ \mu m^3$)	38814	9700	1552	388
λ for SB_1 ($V_2 = 32768\ \mu m^3$)	21287	5321	850	212

Table II.8 : Minimal number of fields necessary to estimate the effective elastic moduli and thermal conductivity with given relative precision, for given volume $V_1 = 13824\ \mu m^3$, $V_2 = 32768\ \mu m^3$ (for periodic boundary conditions).

Sample SA_2	Sample SB_1
$V_k^{RVE} = 100 \times 100 \times 100\ \mu m^3$	$V_k^{RVE} = 215 \times 215 \times 215\ \mu m^3$
$V_\mu^{RVE} = 126 \times 126 \times 126\ \mu m^3$	$V_\mu^{RVE} = 292 \times 292 \times 292\ \mu m^3$
$V_\lambda^{RVE} = 390 \times 390 \times 390\ \mu m^3$	$V_\lambda^{RVE} = 412 \times 412 \times 412\ \mu m^3$

Table II.9 : The minimal size of the RVE V^{RVE} for different physical properties obtained by the periodic boundary conditions. The results are given for $n = 100$ realizations and for the precision $\epsilon_{rela} = 1\%$.

the table II.9.

The computation of such sizes in a finite element code (with a mesh density sufficiently large) is possible only when using a parallel computing. One would compute on smaller volumes when using a simple workstation or PC. The last solution requires however a sufficient number of independent samples. As a comparison between all these results, we remark that for the same relative precision ϵ_{rela} and number of fields n, the thermal conductivity λ requires a volume larger than the volume required for the shear modulus μ and the bulk modulus k although the contrast in shear modulus c_μ is the largest one. This result is true in both specimens. One must note also that the specimen without additive SB_1 requires a volume larger than the volume required by the specimen with additive SA_2. This is due to the values of the integral ranges A_3 and the covariance ranges L, and this result is true for k, μ and λ (10 times for k, 12 times for μ and 2 times for λ).

II.6 Analysis of Local Fields : Localization and Percolation Phenomena

The term *percolation* is used extensively in a great variety of situations and evokes the notion of transport in a medium partially interconnected like a porous medium. The concept of percolation used in this work was introduced firstly by the mathematicians Broadbent and Hammersley in (Broadbent and Hammersley, 1957). The mathematical description of the percolation is associated with the notion of *percolation threshold*, or *critical value* of the volume fraction describing the connectivity.

This notion can be illustrated by a simple example : let's imagine that one mixes two powders, physically indiscernible except that one has a large electric conductivity and the other is insulating. Grains of powder are very small and fill in a compact way a very big volume. We can consider the number of grains as infinite. It is obvious that, if the amount of conductive powder is small, the whole behaves like an insulator. The original character of the percolation resides in the fact that the passage of a state to the other takes place suddenly for a precise value of the powder conductor percentage in the mixture. This percentage marks the percolation threshold.

The works of Shante and Kirkpatrick (Shante and Kirkpatrick, 1971) and those of Kirkpatrick (Kirkpatrick, 1973) served as an introduction to the percolation to the increasing number of physicists interested by the problem in the last decade. These articles are relative to problems of threshold or conductivity, they remain extensively valid. More lately the book and magazine of Stauffer (Stauffer, 1985) and (Stauffer, 1979), leaning on statistics, and the one of Essam and Bhatti (Essam and Bhatti, 1985) and the works of Domb (Domb et al., 1980) brought points of complementary view to those exposed in the previous works.

The interest that is currently drawn to the theory of the percolation is justified

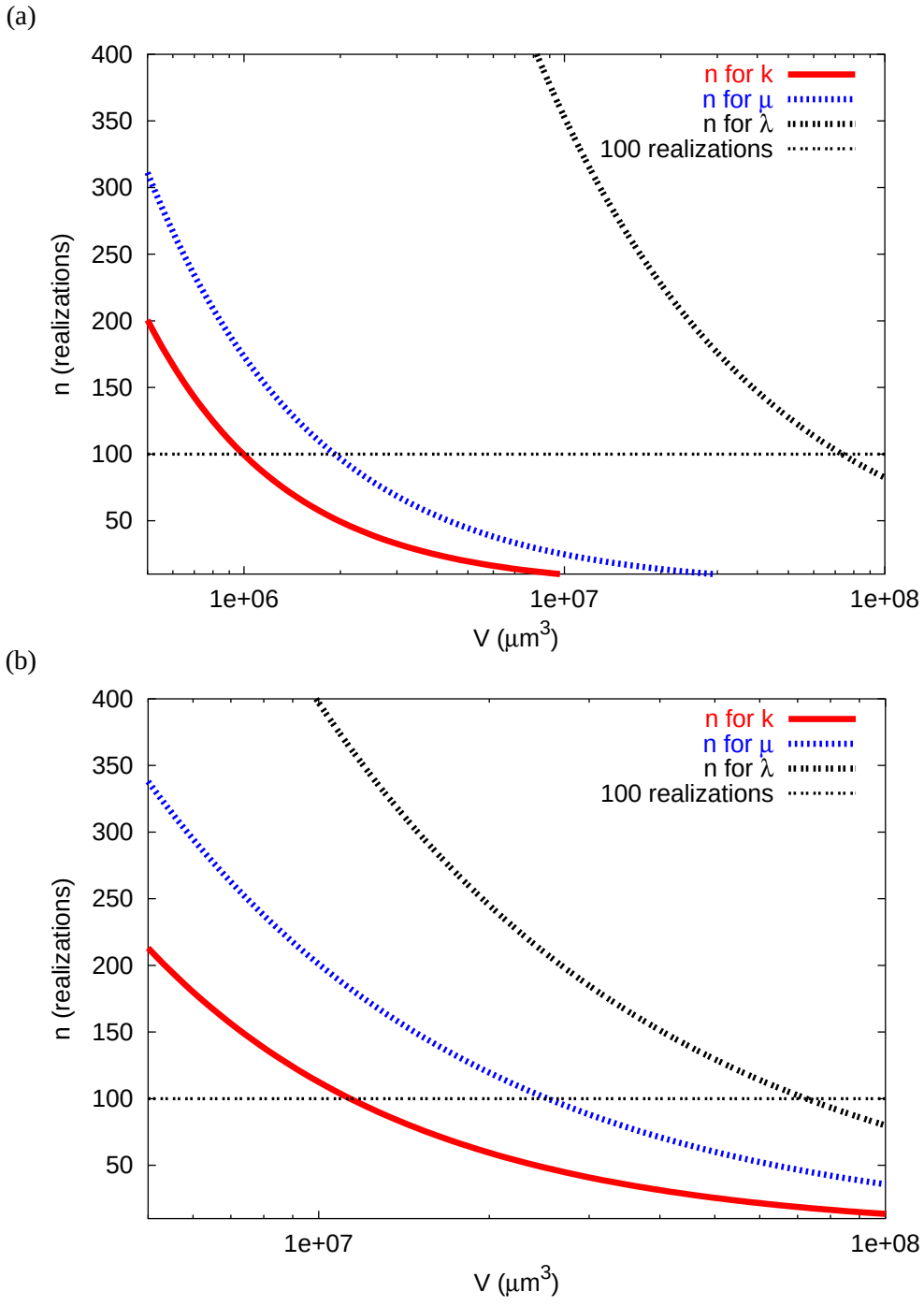

Figure II.32 : Number of fields as a function of the domain size for a given relative error $\epsilon_{rela} = 1\%$: (a) for the specimen SA_2 and (b) for the specimen SB_1.

by the fact that it is unifying concept (De Gennes, 1976) permitting to establish ties between the physical phenomena in very different disorganized systems. Also, there is an analogy between the problem of the permeability of a porous media and the one of the passage of the electric current in the disorganized medium and with geometrical percolation and once of the mechanical fields studied in this work.

Let us try now to characterize the percolation properties of the microstructures studied in this chapter. To compare the percolation properties of two microstructures, one needs to specify the investigated property and to define a percolation index. One tries to detect whether phase percolates "more" than the other in one microstructure. A first proposal for such an index related to mechanical properties is the matricity parameter introduced in (Dong and Schmauder, 1996), (Lele et al., 1998) and (Schmauder et al., 1999)

The matricity of phase α in such an α-β two-phase composite was recently introduced as an additional structural parameter and can be determined from a representative micrograph, which shows the different phases. The phases of the composite are reduced to lines from an image analysis system by maintaining its topology (Lele et al., 1998). The length of these skeleton lines in one phase, S_α, is then related to the length of all skeleton lines in both phases, $S_\alpha + S_\beta$. This ratio is called matricity of phase α :

$$M_\alpha = \frac{S_\alpha}{S_\alpha + S_\beta} \tag{II.79}$$

By definition, $0 \leq M_\alpha \leq 1$ and the sum of the matricities of all phases equals to one :

$$M_\alpha + M_\beta = 1 \tag{II.80}$$

Thus, M characterizes the degree of mutual interpenetration of the phases in the composite. M_α varies from a value close to 0 to a value close to 1 when the microstructure changes from a microstructure with α-inclusions to a microstructure with β-inclusions. The values 0 and 1 are obtained if the corresponding microstructures contain nicely separated inclusions with zero skeleton line length such as in the case of spheres. However, a certain M-value can describe different microstructures of a composite with a given volume fraction and with possibly different mechanical behaviors. This matricity index can be shown however to be flawed.

A self-consistent matricity model has been developed to simulate the mechanical behavior of an isotropic two-phase composite with coarse interpenetrating microstructure in (Lele et al., 1998). The model is an extension of a recently developed self-consistent model for matrices with randomly distributed inclusions (Dong and Schmauder, 1996). The model is applied to an Fe/Ag composite in (Lele et al.,

1998) and to a W/Cu composites in (Schmauder et al., 1999).

The aim of the present section is to see whether the huge difference in the effective properties of materials SA and SB can be attributed to the percolation behavior of the hard phase within both mixtures.

A percolation index is first defined to characterize the rate of percolation of a given field. Note that contrary to the initial naive view of percolation mainly based on binary arguments *("percolate or not")*, percolation can be seen as a continuous process in the case of continuous systems, and not necessary a sudden one. With the help of tools of image analysis and of the morphological processes of image reconstruction, this notion is applied to geometrical percolation of the hard phase investigated in this chapter, on the one hand, and to mechanical fields (strain) to quantify strain localization phenomena on the other hand.

II.6.1 Percolation Index

The geometrical percolation in random structures can result in changes in the macroscopic physical properties of the system near the corresponding percolation threshold (Stauffer, 1985), (Deutscher et al., 1983), (Deutscher, 1987) and (Zallen, 1983). Since the physical properties are easily measured experimentally, the percolation transition phenomena are easily studied by the changes in the physical properties. We first define and quantify what is called here *geometrical percolation*.

For that purpose, we need the notion of $3D$ image re-construction. Let's consider the set Y completely situated in another large set X ($Y \subset X$). The geodesic dilatation with size l of Y in X is :

$$D_x^l(Y) = \{x \in X,\ d(x,Y) \leq l\} \tag{II.81}$$

$d(x,Y)$ is the smallest distance between the point x and the set Y. We define the geodesic re-construction by successive geodesic dilatations with size $l = 1\ pixel$ of Y in X, until the whole set X has been explored.

The volume fraction P_p of percolating phase P in direction (OX) is defined by the following procedure :

1. Determine the $3D$ re-construction of the first section $x = 1\ pixel$ of the image of phase P in direction (OX). Call it P_p^x.

2. Determine the $3D$ re-construction of the last section $x = 512\ pixels$ of the image of phase P in direction $(-OX)$. Call it P_p^{-x}.

   $-x$ means that the successive geodesic dilatations are made in the negative direction of (OX).

3. The percolating phase in (OX) direction is then defined as the intersection of P_p^x and P_p^{-x}, so :

$$P_p = P_p^x \cap P_p^{-x} \tag{II.82}$$

It is clear, especially in the case of the heterogeneous materials like inclusions in matrices, that the volume fraction of percolating phase P_p is lower than or equal to the volume fraction of phase P studied in the heterogeneous material. It enables us to quantify the volume of phase that percolates and to compare it to the whole volume of this phase. It is then possible to define a *percolation index* P_r or *percolation ratio*. The percolation index is the ratio between the volume fraction of the percolating phase to the whole volume fraction in the microstructure of this phase, equation (II.83) :

$$P_r = \frac{P_p}{P} \tag{II.83}$$

It is always lower than or equal to 1. It is equal to 1 if the whole phase percolates, and equal to zero if there is no percolation of this phase (physically it means that this phase is a set of separated inclusions). Figures II.33 and II.34 illustrate the three steps in the $2D$ and $3D$ image re-construction.

II.6.2 Geometrical Percolation

In this part we study the phenomenon of geometrical percolation, and to quantify it, the curves of the geometrical percolation ratio are represented in figures II.35, II.36, II.38 and II.39. The previous definition of percolating phase P_p substantiates the notion of geometrical percolation. In particular, we will say there is a geometrical percolation of phase P as soon as the volume fraction of percolating phase P_p does not vanish.

Because of the size of our microstructures, especially the small thickness with respect to the (OZ) axis, we have chosen to study the evolution of the geometrical percolation ratio of each of the two present phases according to the number of sections in the plan (XY) added in the thickness (the OZ axis).

To each number of sections included in the $3D$ image we draw the geometrical percolation ratio in the two directions of sections : (OX) and (OY). One finds these results in figures II.35 and II.36 for microstructureses SA and in figures II.38 and II.39 for microstructures SB.

a) Samples With Additive SA

The evolution of the geometrical percolation ratio P_r, according to the thickness, is given in figure II.35 for the phase P_1 and in figure II.36 for the phase P_2 for

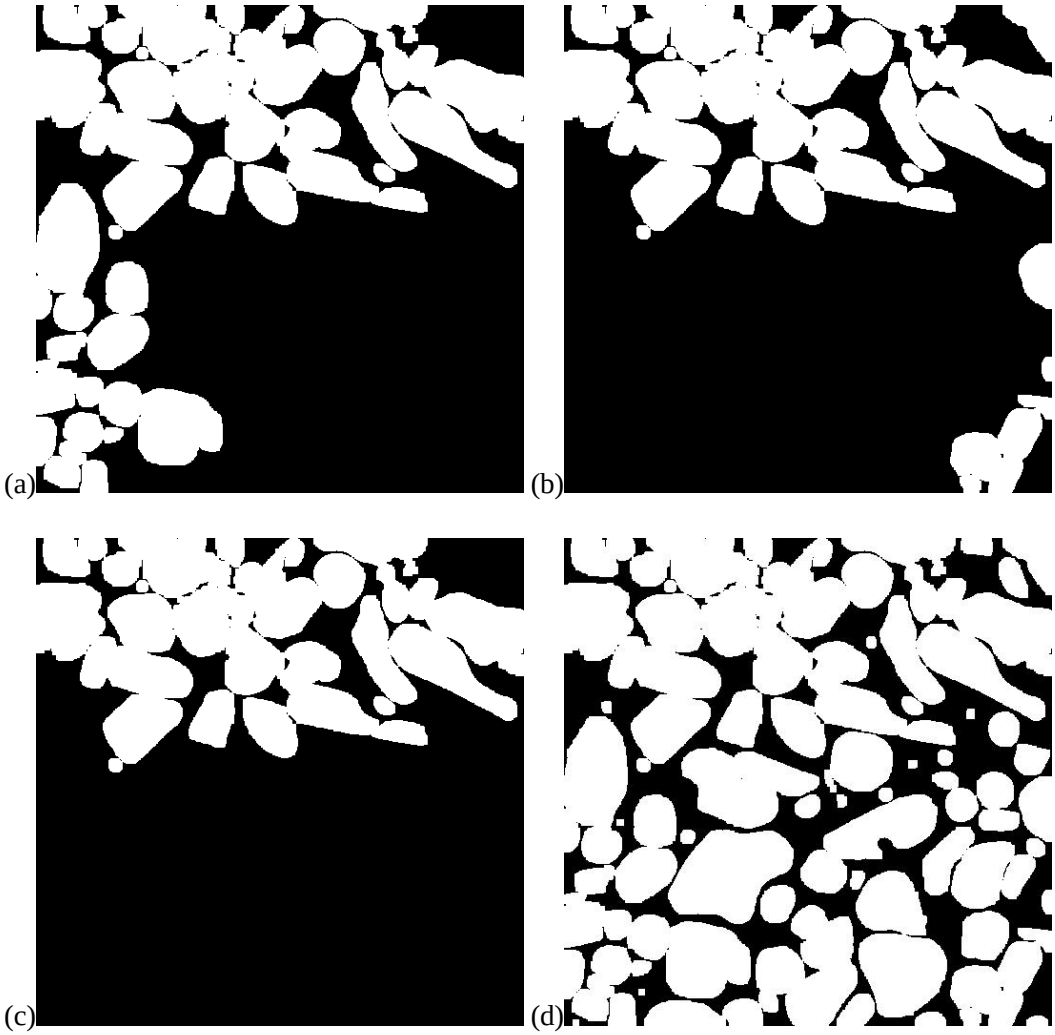

Figure II.33 : Example of $2D$ image re-construction. (a) Image of P_p^x, (b) image of P_p^{-x}, (c) image of P_p and (d) image of the whole image (set X).

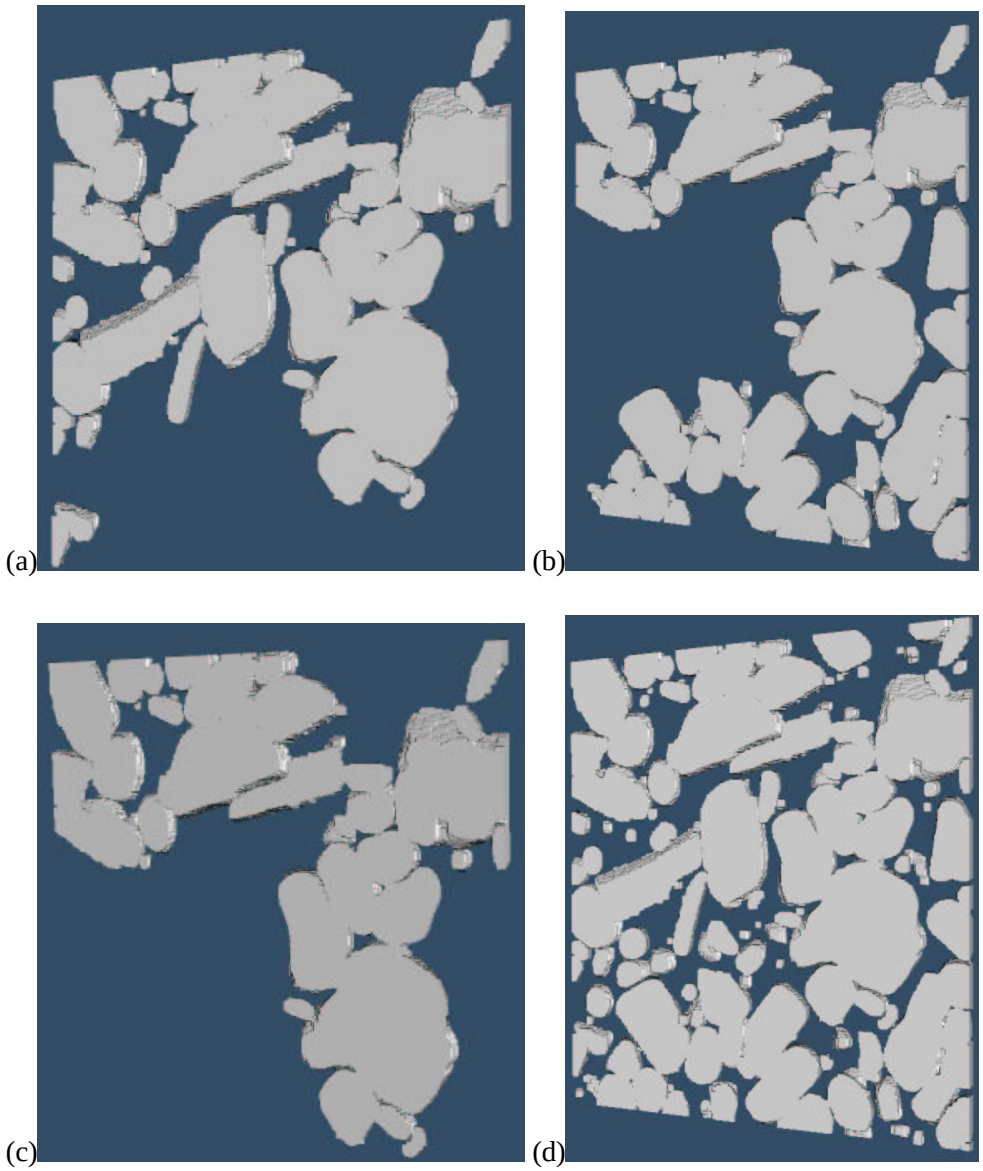

Figure II.34 : Example of $3D$ image re-construction. (a) Image of P_p^x, (b) image of P_p^{-x}, (c) image of P_p and (d) image of the whole image (set X).

microstructures SA. For each phase, these figures show the variation of the percolation ratio following two directions (OX) and (OY). The number of sections added according to the thickness is equal to 60 sections for a length of 30 μm.

One notices that for the phase P_1, one finds cases where this phase does not percolate in the first section. It is the case for specimen SA_2 according to the direction (OX) and the specimen SA_1 according to the direction (OY) (figure II.37). In the four remaining : SA_1 and SA_3 following the direction (OX) and SA_2 and SA_3 following the direction (OY), the percolation following the two directions starts at the first section. The largest percolation ratio on the first section is recorded for the specimen SA_3 following the two directions (OX) and (OY). While adding sections according to the direction of the thickness, the percolation ratio increases until it reaches the maximal value, that is 1 in any case, after a certain number of sections. This evolution is relatively fast since one only reaches the maximal value of the percolation ratio after about twenty sections (about one third of the whole thickness). One can notice, in short, that in all these cases, the global percolation ratio on the set of $3D$ image of each specimen is equal to 1, meaning that all the phase P_1 percolates in the two directions (OX) and (OY). They are no isolated inclusions of phase P_1.

Figure II.36 presents the evolution of the geometrical percolation ratio for the phase P_2 in samples SA. In this type of microstructure one finds only one case where the geometrical percolation ratio is vanishing on the first section (sample SA_3) with respect to the direction (OX). All the other rates of percolation have a non zero value on the first section. As in the case of the phase P_1 the evolution of the geometrical percolation ratio is relatively fast. One reaches the maximal value after about twenty sections (ie. 10 μm). One also notice that all the rates of percolation are equal to 1 on the totality of the image as for the phase P_1. This allows us to say that the phases P_1 and P_2 are interconnected or bi-percolated in all samples.

b) Samples Without Additive SB

Figures II.38 and II.39 present curves of the geometrical percolation ratio for the phases P_1 and P_2 in the case of the microstructure SB. On the first section one doesn't find any geometrical percolation in the case of specimen SB_3 following the two directions (OX) and (OY) (figure II.40), and in the case of the one of SB_1 in direction (OY), for the phase P_1. For the phase P_2, specimen SB_2 doesn't present a geometrical percolation in any direction in the first section, and it is also the case for specimen SB_1 in the direction (OY).

One notices that there are cases where the geometrical percolation of the phase P_1 increases only after a certain number of sections added. Specimen SB_3 percolates according to direction (OX) after 4 sections (about 2 μm) and after 10 sections following (OY) (about 5 μm). Four sections are also necessary so that the sample SB_1 percolates according to direction (OY). It means, physically, that in these cases the phase P_1 is only made of separate inclusions in the matrix (the phase P_2) according to the studied direction.

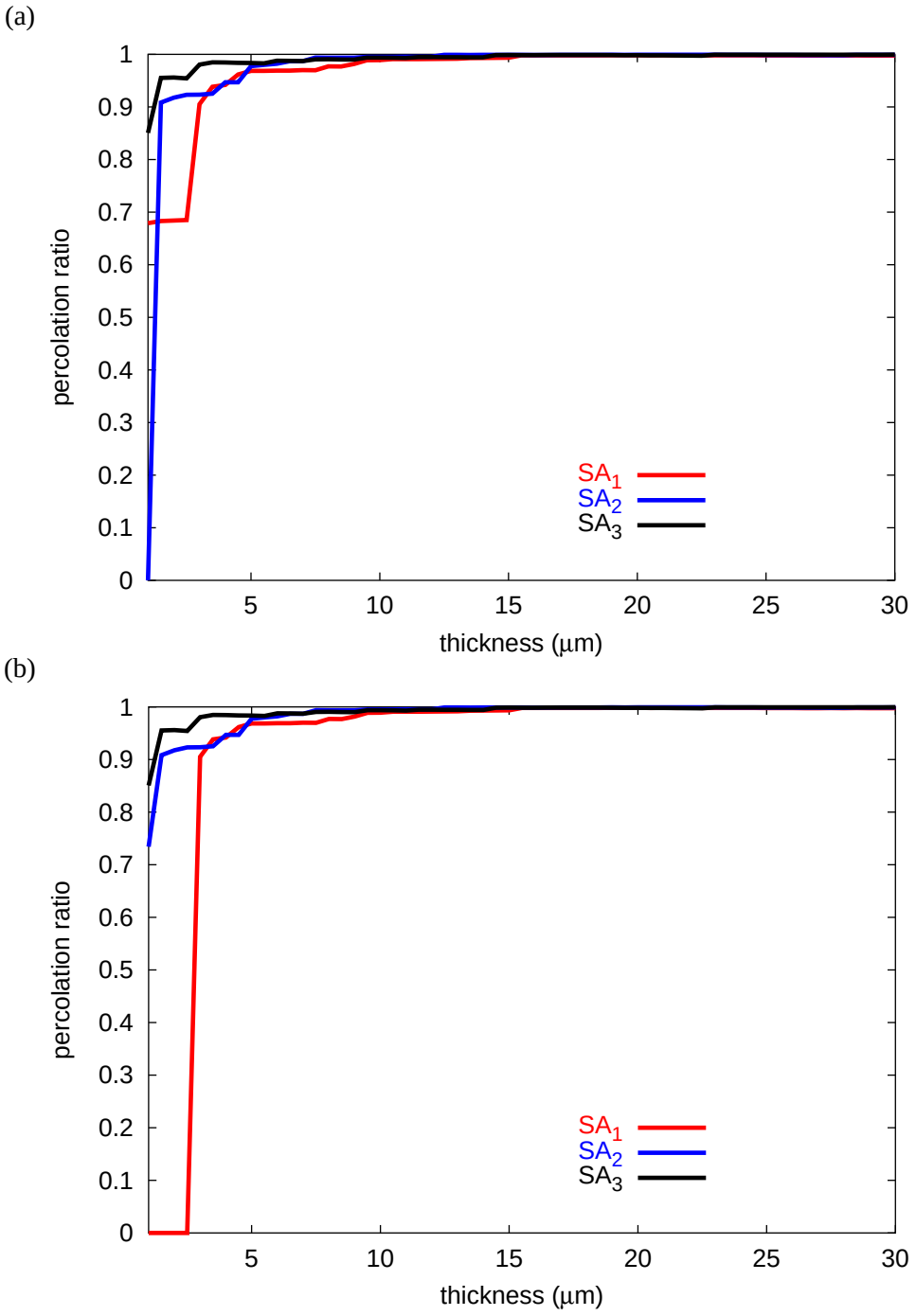

Figure II.35 : Evolution of the geometrical percolation ratio P_r of the hard phase P_1 for samples with additive SA. (a) In (OX) direction, (b) in (OY) direction.

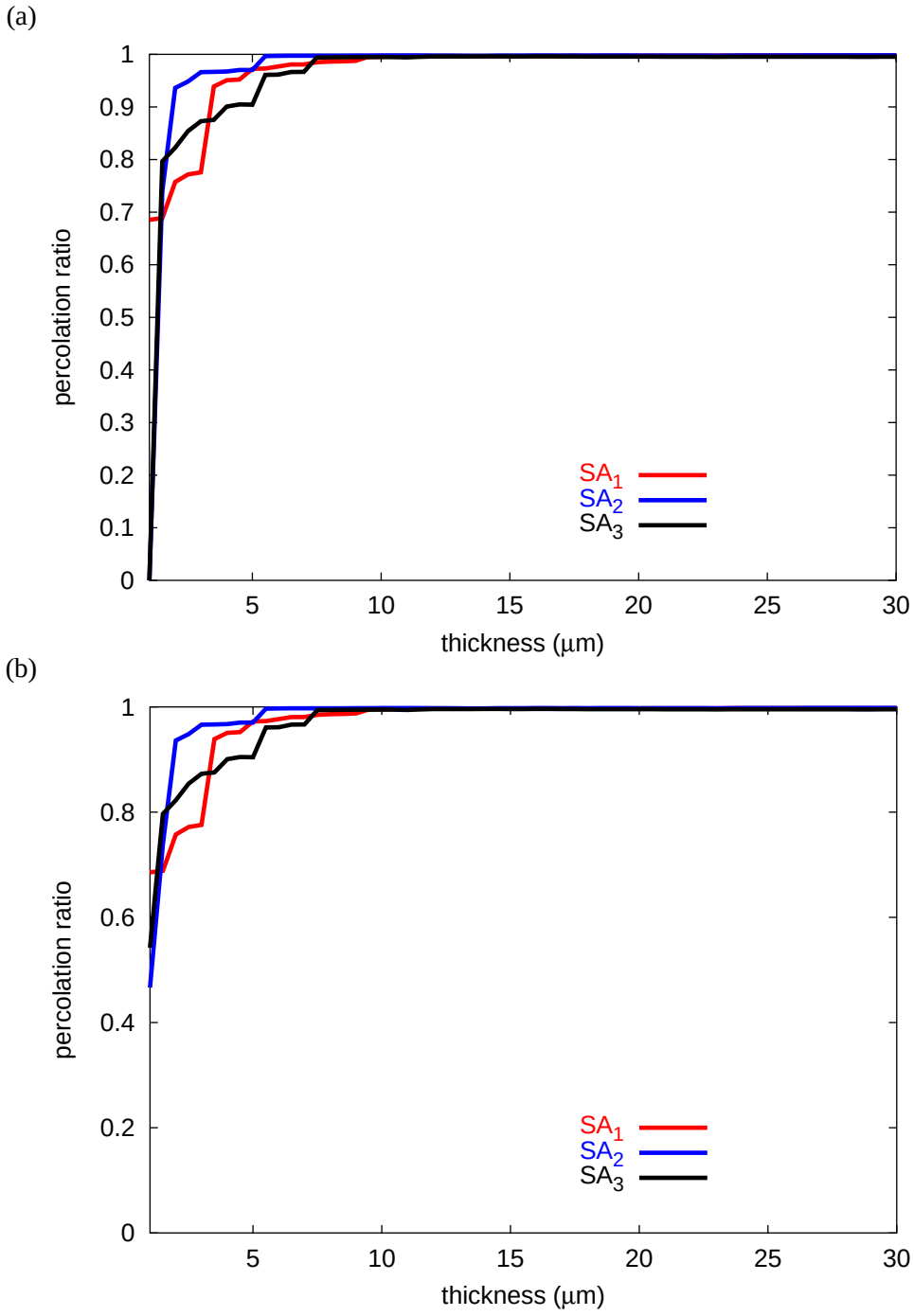

Figure II.36 : Evolution of the geometrical percolation ratio P_r of the soft phase P_2 for samples with additive SA. (a) In (OX) direction and (b) in (OY) direction.

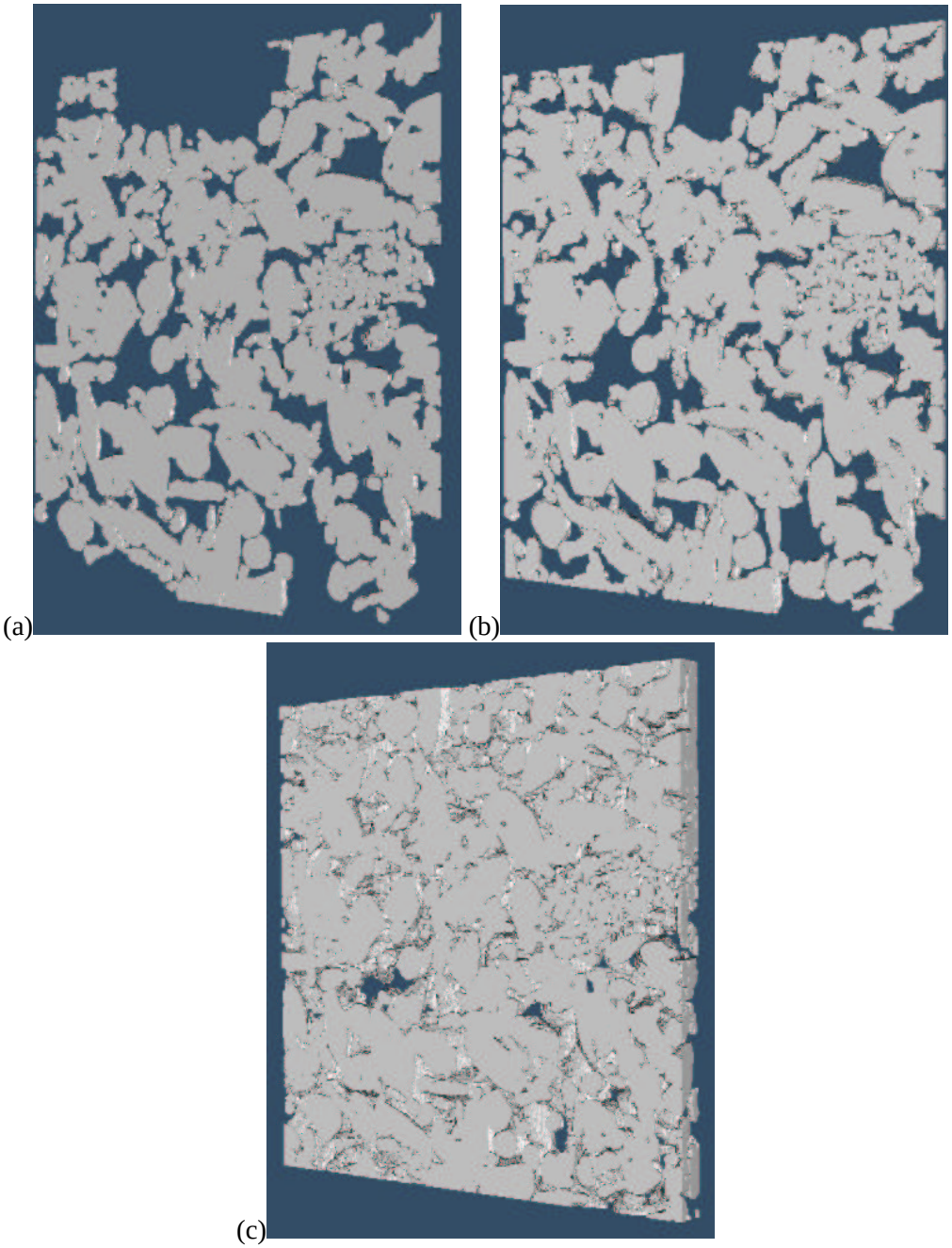

Figure II.37 : Evolution of the percolating phase of the hard phase P_1 for the sample SA_1 in (OY) direction. (a) After 3 μm ($P_r = 0.90$), (b) after 10 μm ($P_r = 0.98$) and (c) the whole sample, after 30 μm ($P_r = 1$).

It can be noted that in material SB, the phase P_1 percolates more slowly than the phase P_2. This microstructure is also bi-percolated.

By comparison with microstructures of the type SA, the phase P_1 percolates more slowly in type SB (after about $15\ \mu m$) than for the type SA (only $10\ \mu m$ are necessary), which can be related to the fact that the size of the RVE of type SB is larger than the one of the type SA.

II.6.3 Mechanical Percolation

After having studied the phenomenon of the geometrical percolation in our microstructures, we consider the case of the percolation of the mechanical fields. The objective is to study paths of high strain or high stress in a microstructure submitted to a given load. The survey of strain paths can explain phenomena like strain localization bands that exist in some deformed samples. Indeed, the strain bands in a microstructure can be defined as paths of percolation of this variable in this microstructure. For example, places of the microstructure where the value of the local equivalent strain is larger than a fixed threshold.

We define the percolation of a mechanical field as follows : a value of mechanical variable (ε_{eq} for instance) is attributed to each voxel of the microstructure according to the results of a finite element computation. A threshold image is obtained by selecting the domain where the variable is greater than a given threshold. One studies then the geometrical percolation property of this domain. In particular the percolation index can be computed in the same way as in the previous section.

To understand this phenomenon we used the microstructure SA_1 (SB_1 respectively) and we submit it to an external loading of type $E_{22} = 1$ under KUBC boundary conditions. The chosen local variable is the equivalent strain ε_{eq}. This local variable strongly varies in the microstructure. One calls percolated phase in this case, the set of Gauss integration points of the microstructure that have a value of the equivalent strain larger than a fixed threshold, and one checks if this set percolates or not.

Following two directions (OX) and (OY), the figure II.41 shows the percolation ratio of the calculated equivalent strain, above a given threshold. It is obvious that one finds that the percolation ratio is equal to 1 for a threshold equals to 0, because necessarily all the points have an equivalent strain superior or equal to zero. When the value of the threshold increases, the percolation ratio decreases until 0.

Figure II.42 (figure II.43 respectively) gives an example of the percolated domain of the equivalent strain of the examples mentioned before. The skeletons present the domain of the microstructure with an equivalent strain superior to $\varepsilon_{eq} = 0.4$ for the sample SA_1 and to $\varepsilon_{eq} = 0.5$ for the sample SB_1 that is percolating geometrically following direction (OX). If we look at the figure II.41,

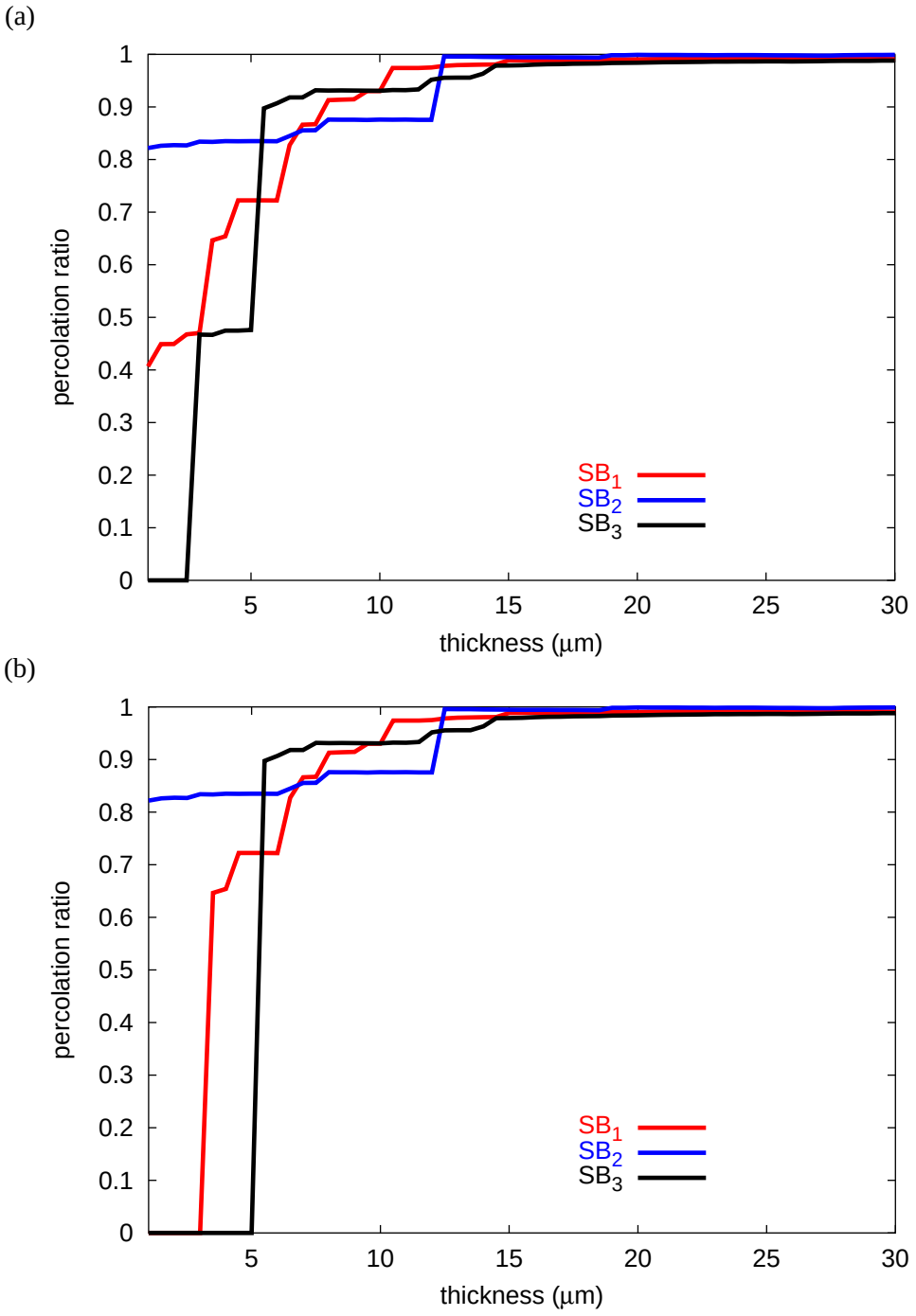

Figure II.38 : Evolution of the geometrical percolation ratio P_r of the hard phase P_1 for samples without additive SB. (a) In (OX) direction, (b) in (OY) direction.

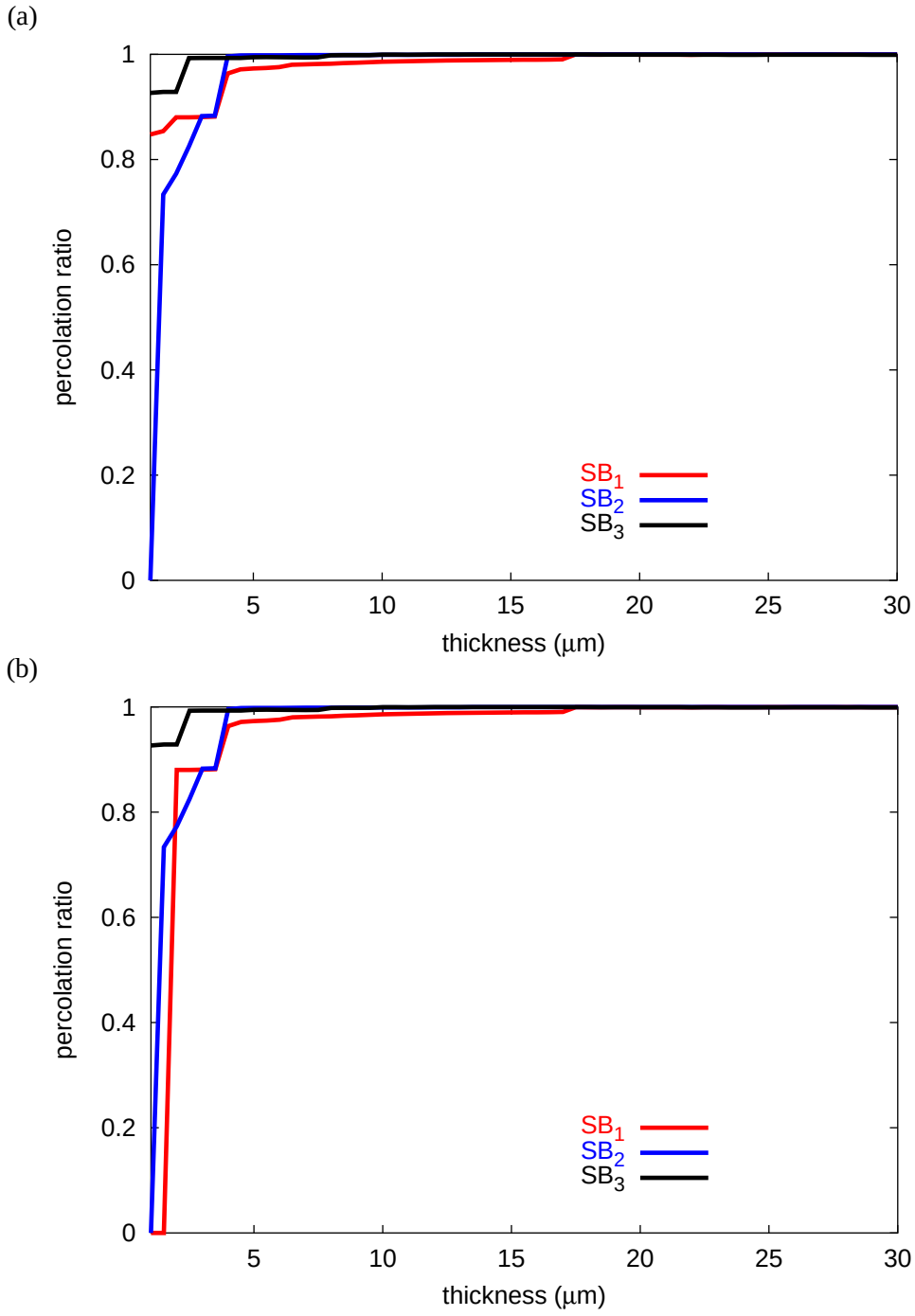

Figure II.39 : Evolution of the geometrical percolation ratio P_r of the soft phase P_2 for samples without additive SB. (a) In (OX) direction and (b) in (OY) direction.

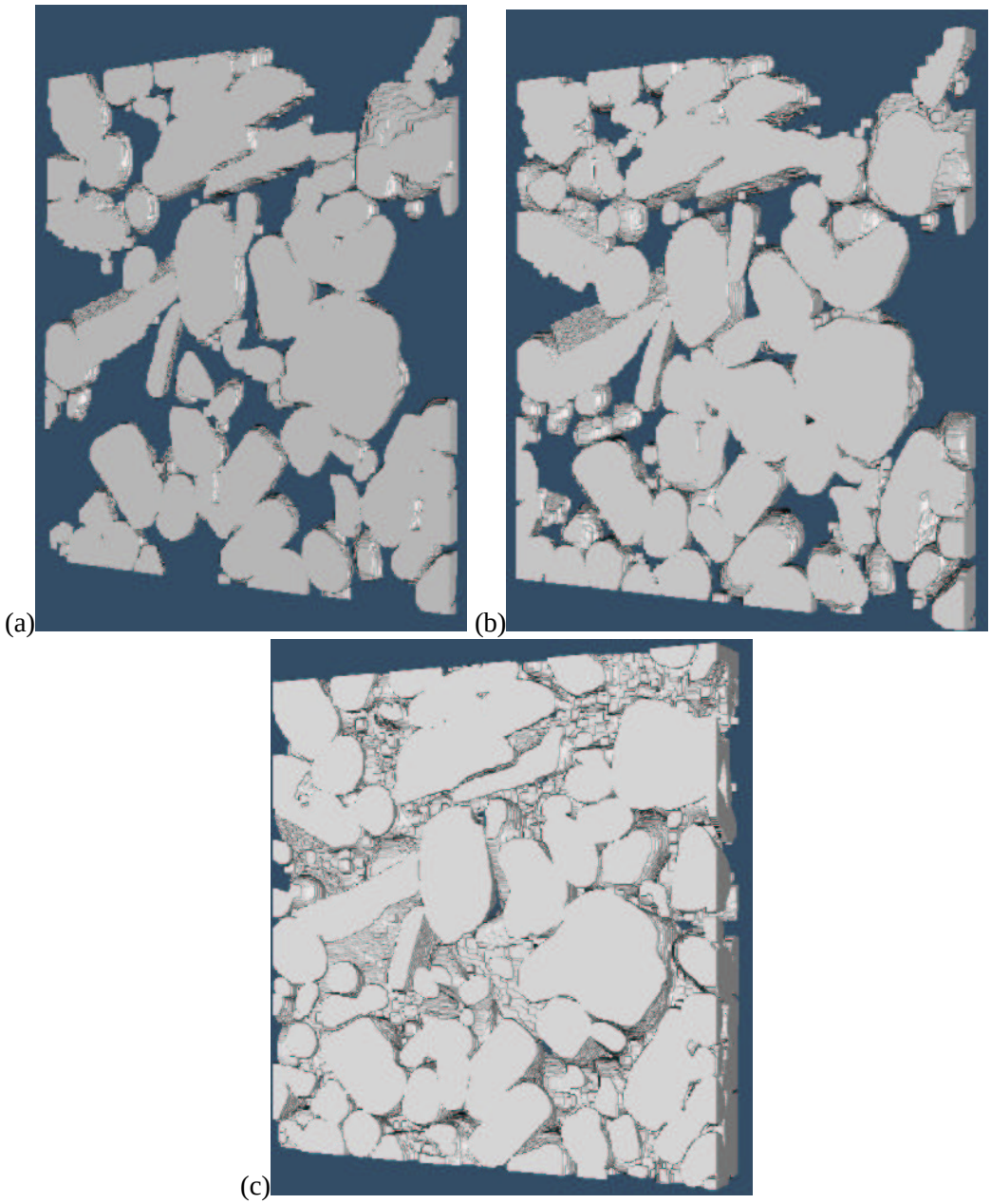

Figure II.40 : Evolution of the percolating phase of the hard phase P_1 for the sample SB_3 in (OY) direction. (a) After 6 μm ($P_r = 0.89$), (b) after 10 μm ($P_r = 0.93$) and (c) the whole sample, after 30 μm ($P_r = 1$).

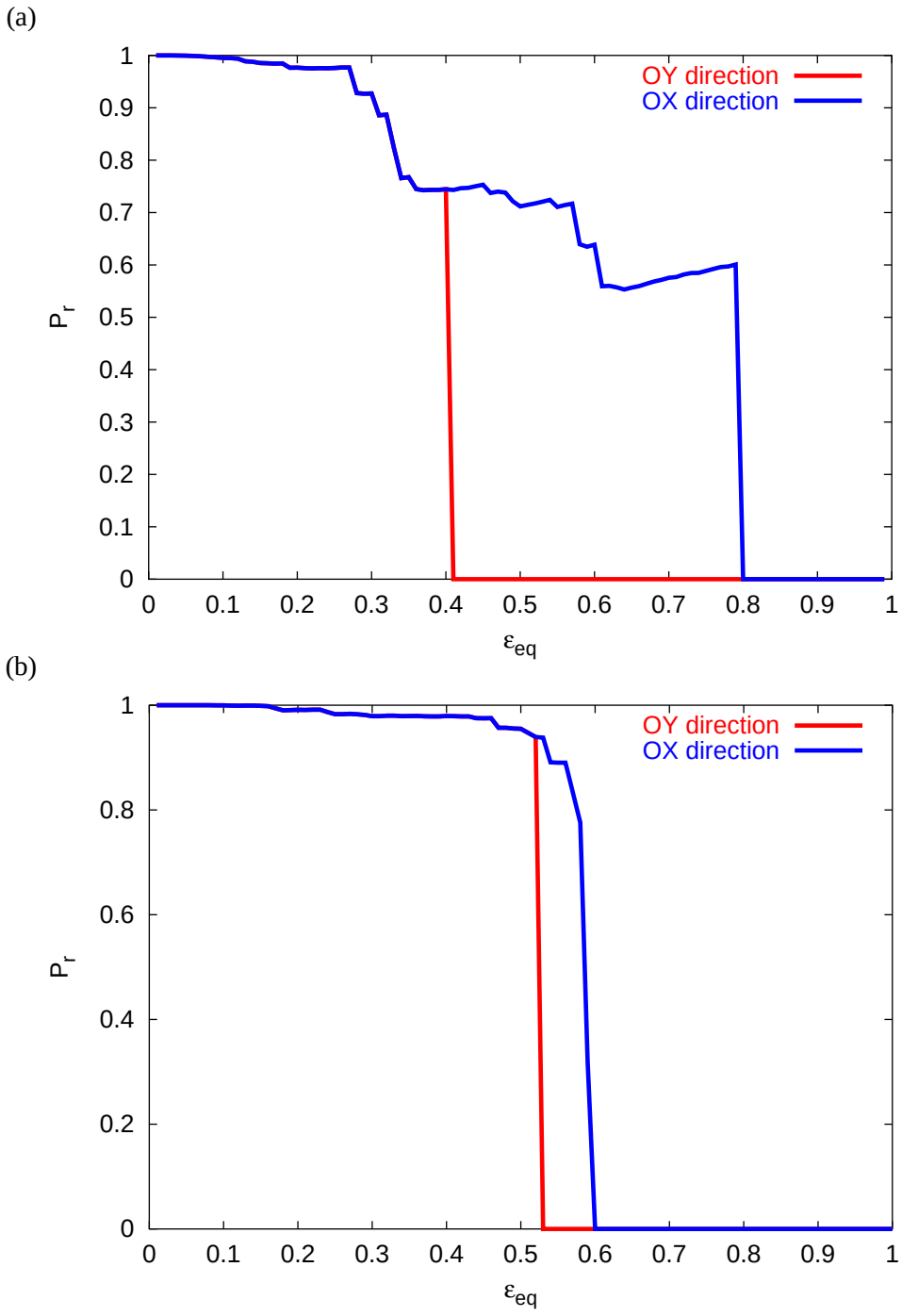

Figure II.41 : Evolution of the strain field percolation ratio as a function of the equivalent strain threshold. (a) Example of computation of the sample SA_1 with $E_{22} = 1$ and (b) computation of the sample SB_1 with $E_{22} = 1$.

we find that the percolation ratio in the case of the sample SA_1 is equal to about $P_r = 0.74$ for $\varepsilon_{eq} = 0.4$ and $P_r = 0.95$ for $\varepsilon_{eq} = 0.5$ for the sample SB_1 in (OX) direction. This is a rather small connected domain associated with strain localization in the soft phase. This band of intense deformation can be seen also on the strain map of figure II.42b (figure II.43b).

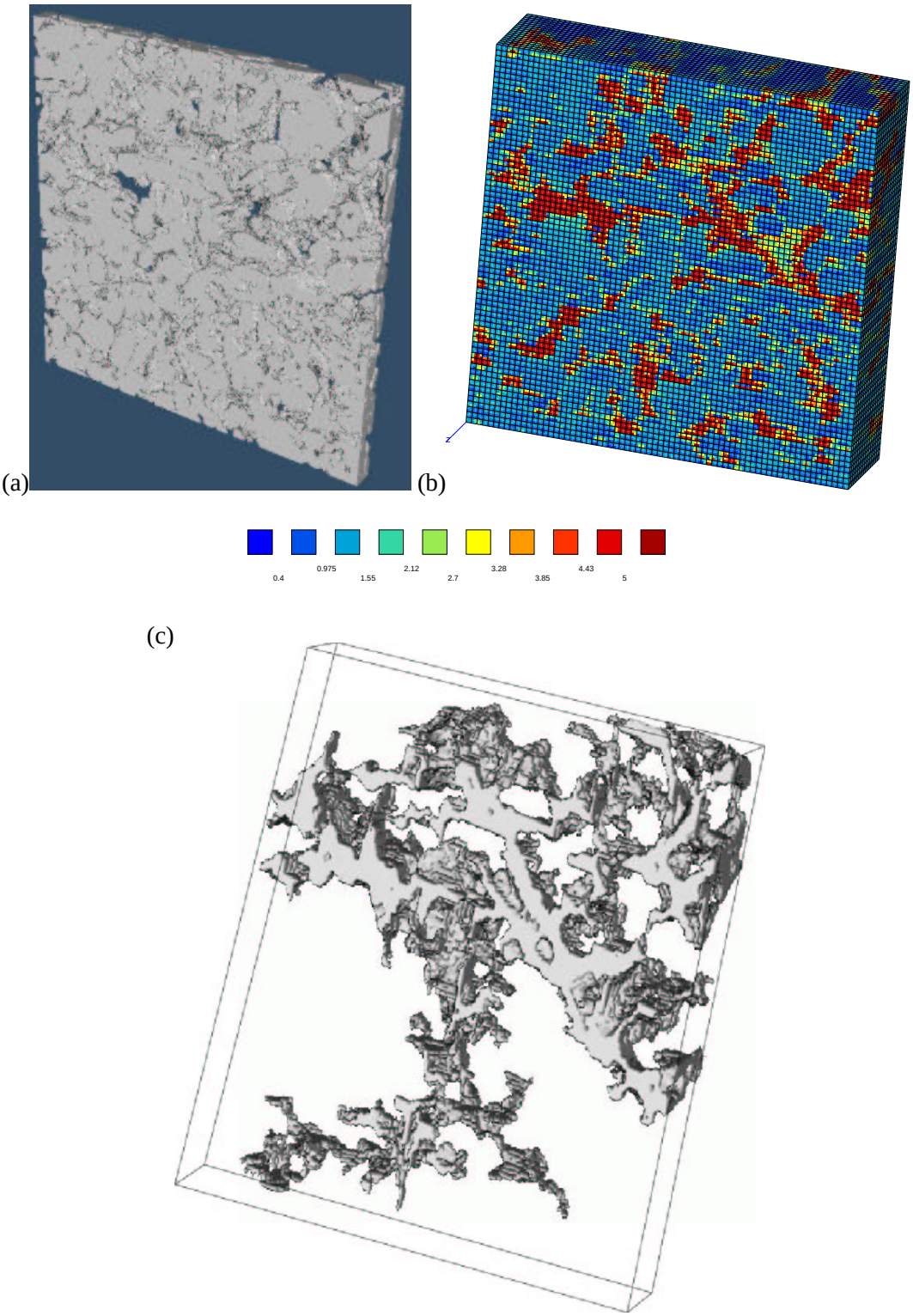

Figure II.42 : Image of the percolated volume P_p for the variable ε_{eq} for the computation using the sample SA_1. The imposed strain tensor (loading) is $E_{22} = 1$. The percolation is given in the direction (OX). (a) The whole sample, (b) map of ε_{eq} and (c) percolated volume for $\varepsilon_{eq} = 0.4$ ($P_r = 0.74$).

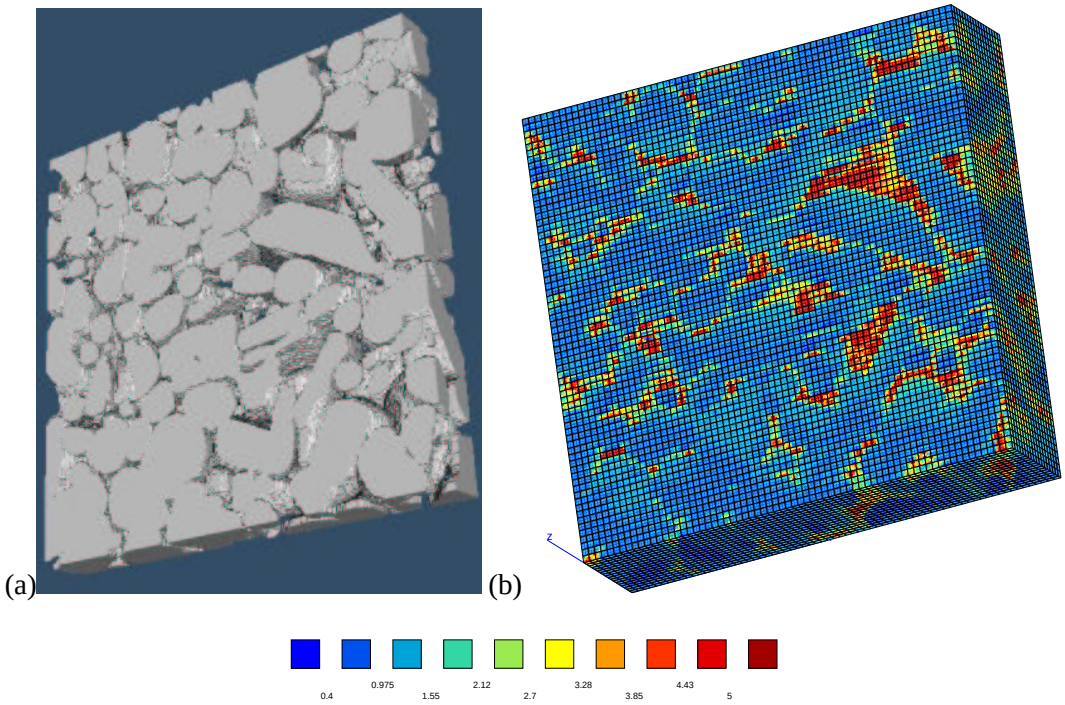

Figure II.43 : Image of the percolated volume P_p for the variable ε_{eq} for the computation using the sample SB_1. The imposed strain tensor (loading) is $E_{22} = 1$. The percolation is given in the direction (OX). (a) The whole sample, (b) map of ε_{eq} and (c) percolated volume for $\varepsilon_{eq} = 0.5$ ($P_r = 0.95$).

Chapter -III-

ELASTIC PROPERTIES OF BOOLEAN MODELS WITH HEXAGONAL PRISMATIC GRAINS

Contents

III.1 Introduction

For the economic and industrial reasons, the practical experiences are very costly. To solve this problem and to understand better and control relations between the morphology of microstructures and their physical properties, the recent studies in this domain try to replace the real images of microstructures by simulated ones using tools of mathematical morphology and a image analysis. Simulated images are easier to generate and to manipulate in the numerical simulations.

The aim of this chapter is to estimate the effective properties of new simulated microstructures and to compare them with the previous real microstructures.

We have chosen boolean schemes of hexagonal rods and plates, as examples of microstructures that we expect to be stiffer than the previous real samples.

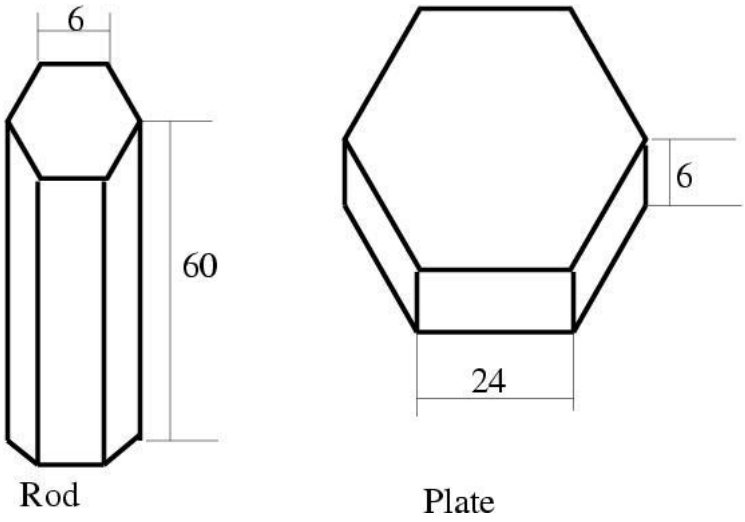

Figure III.1 : Geometry and dimensions of the used primary grains in hexagonal microstructures. The dimensions are given in pixels.

III.2 Morphological Construction

The generation of boolean scheme starts with the definition of the used primary grain. In the studied microstructures here, one uses a hexagon as primary grain. Two different types of geometry have been studied : one based on the hexagonal plate (microstructures P) and the other based on hexagonal rod (microstructure R). Two volume fractions of the hard phase, represented by hexagons, have also been generated, 50% of the hard phase (microstructures $P50$ and $R50$) and 70% of the hard phase (microstructures $P70$ and $R70$). The geometry and the dimensions of the used primary hexagons are shown in figure III.1.

The distributions of hexagons in the space are random. The position of each hexagon in the space is defined completely by the knowledge of its three angles that makes its axis with axes of the Euclidean reference OX, OY and OZ. Indeed, generation of the random positions of hexagons in the space amounts to generate the three random values of the components of the unit vector $\underline{n}$, axis of the plates and rods. Capacities of calculation require a size of the $3D$ image equals to a cube of $256 \times 256 \times 256$ pixels.

III.3 Finite Element Simulations

The same methodology as for the direct computations of the apparent elastic moduli for the real microstructures is used here to find the apparent elastic moduli for the Boolean models with hexagonal prismatic grains. Values of the elastic properties of the two phases used for the real microstructures are also the same used in this case. The different apparent coefficients of the elasticity matrix are computed with KUBC boundary conditions. Figures III.2, III.3, III.4 and III.5 show the nature of

the generated microstructures and the map of the equivalent strain in a computation where the imposed loading is $E_{22} = 1$. The apparent elastic matrices are given by equations (III.1), (III.2), (III.3) and (III.4).

$$[C]_{R50} = \begin{pmatrix} 886 & 284 & 283 & 6 & 2 & 4 \\ & 783 & 273 & 5 & 3 & 1 \\ & & 654 & 0 & 4 & 1 \\ & & & 260 & 3 & 2 \\ & & & & 240 & 3 \\ & & & & & 259 \end{pmatrix} \quad \text{(III.1)}$$

$$[C]_{R70} = \begin{pmatrix} 1520 & 574 & 574 & 3 & 2 & 1 \\ & 1670 & 601 & 5 & 3 & 7 \\ & & 1653 & 3 & 4 & 3 \\ & & & 492 & 8 & 2 \\ & & & & 514 & 2 \\ & & & & & 492 \end{pmatrix} \quad \text{(III.2)}$$

$$[C]_{P50} = \begin{pmatrix} 527 & 200 & 199 & 5 & 2 & 2 \\ & 668 & 220 & 5 & 1 & 6 \\ & & 654 & 7 & 2 & 3 \\ & & & 185 & 5 & 2 \\ & & & & 208 & 2 \\ & & & & & 181 \end{pmatrix} \quad \text{(III.3)}$$

$$[C]_{P70} = \begin{pmatrix} 1487 & 494 & 493 & 4 & 2 & 1 \\ & 1339 & 476 & 2 & 5 & 1 \\ & & 1357 & 1 & 8 & 1 \\ & & & 447 & 1 & 3 \\ & & & & 422 & 1 \\ & & & & & 447 \end{pmatrix} \quad \text{(III.4)}$$

The apparent matrices of elasticity found are not anisotropic. While looking at the table III.1, one finds that we can consider that the size of our microstructures is representative.

Microstructure	$R50$	$R70$	$P50$	$P70$
Anisotropy index a	1.02	0.97	0.93	0.97

Table III.1 : The index of anisotropy of each microstructure.

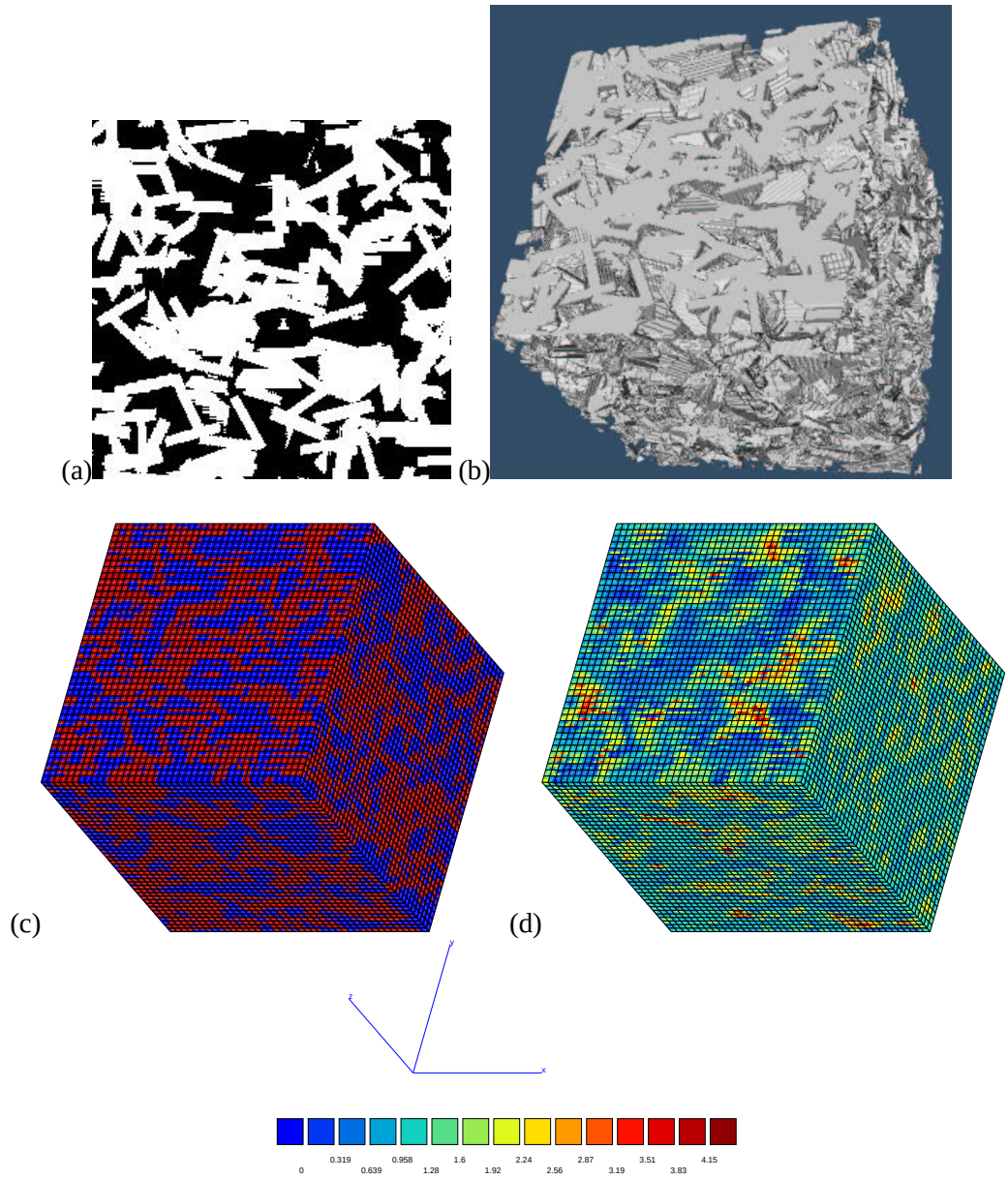

Figure III.2 : Boolean model with 50% of plate hexagons ($P50$). (a) The first section in plane XY, (b) the $3D$ image, (c) finite element mesh and (d) map of equivalent strain ε_{eq} with loading $E_{22} = 1$ under KUBC boundary conditions.

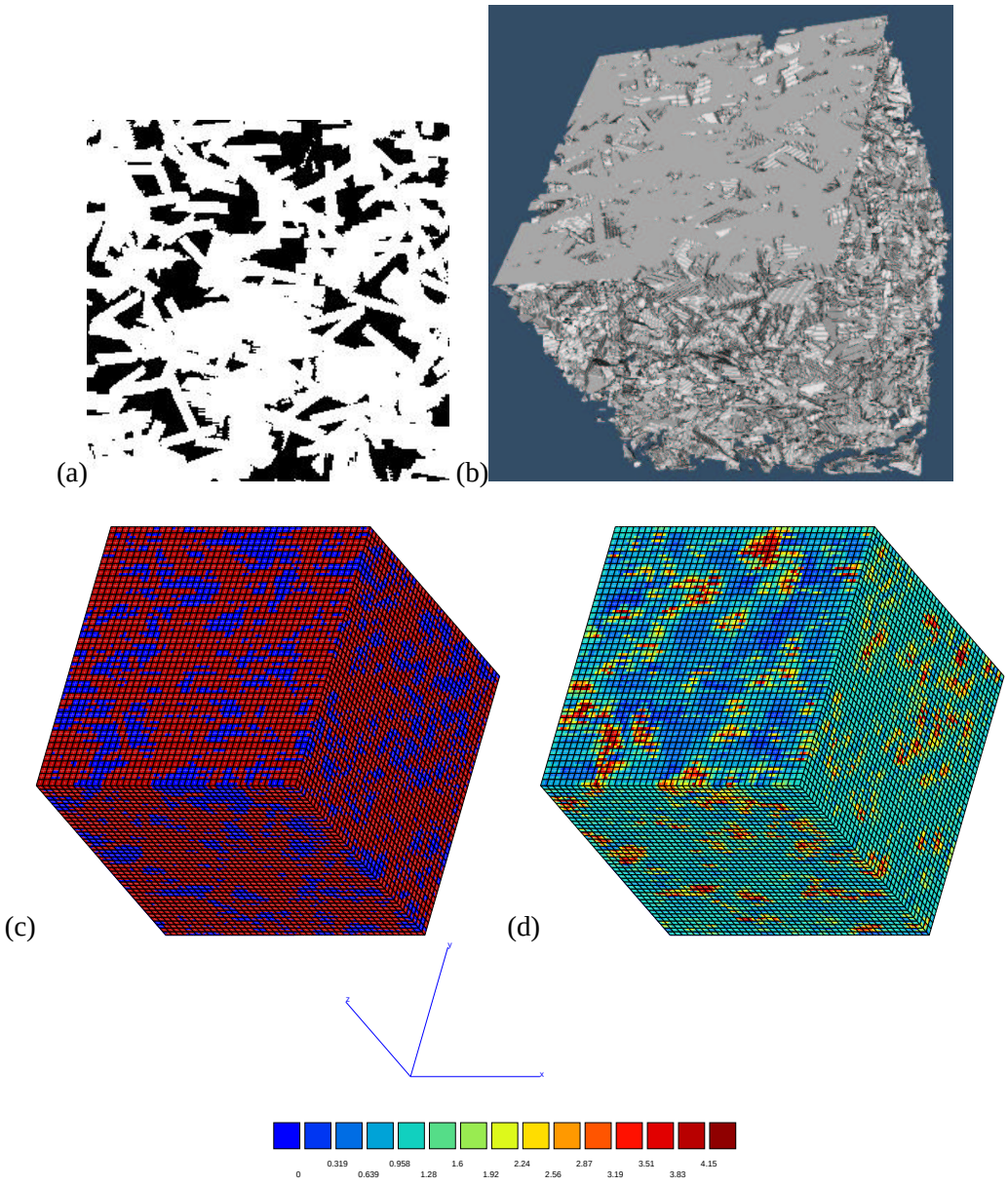

Figure III.3 : Boolean model with 70% of plate hexagons ($P70$). (a) The first section in plane XY, (b) the $3D$ image, (c) finite element mesh and (d) map of equivalent strain ε_{eq} with loading $E_{22} = 1$ under KUBC boundary conditions.

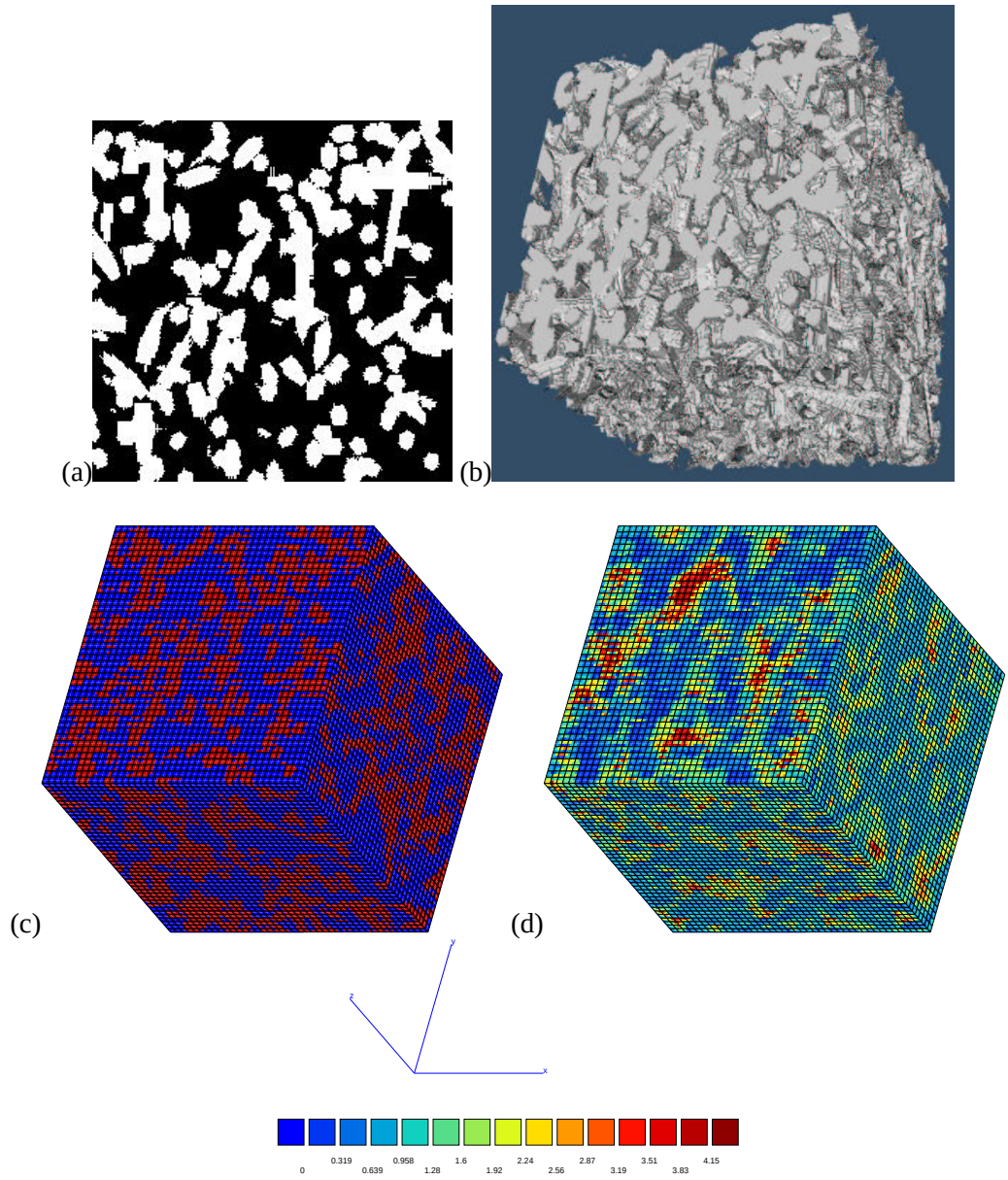

Figure III.4 : Boolean model with 50% of rod hexagons ($R50$). (a) The first section in plane XY, (b) the $3D$ image, (c) finite element mesh and (d) map of equivalent strain ε_{eq} with loading $E_{22} = 1$ under KUBC boundary conditions.

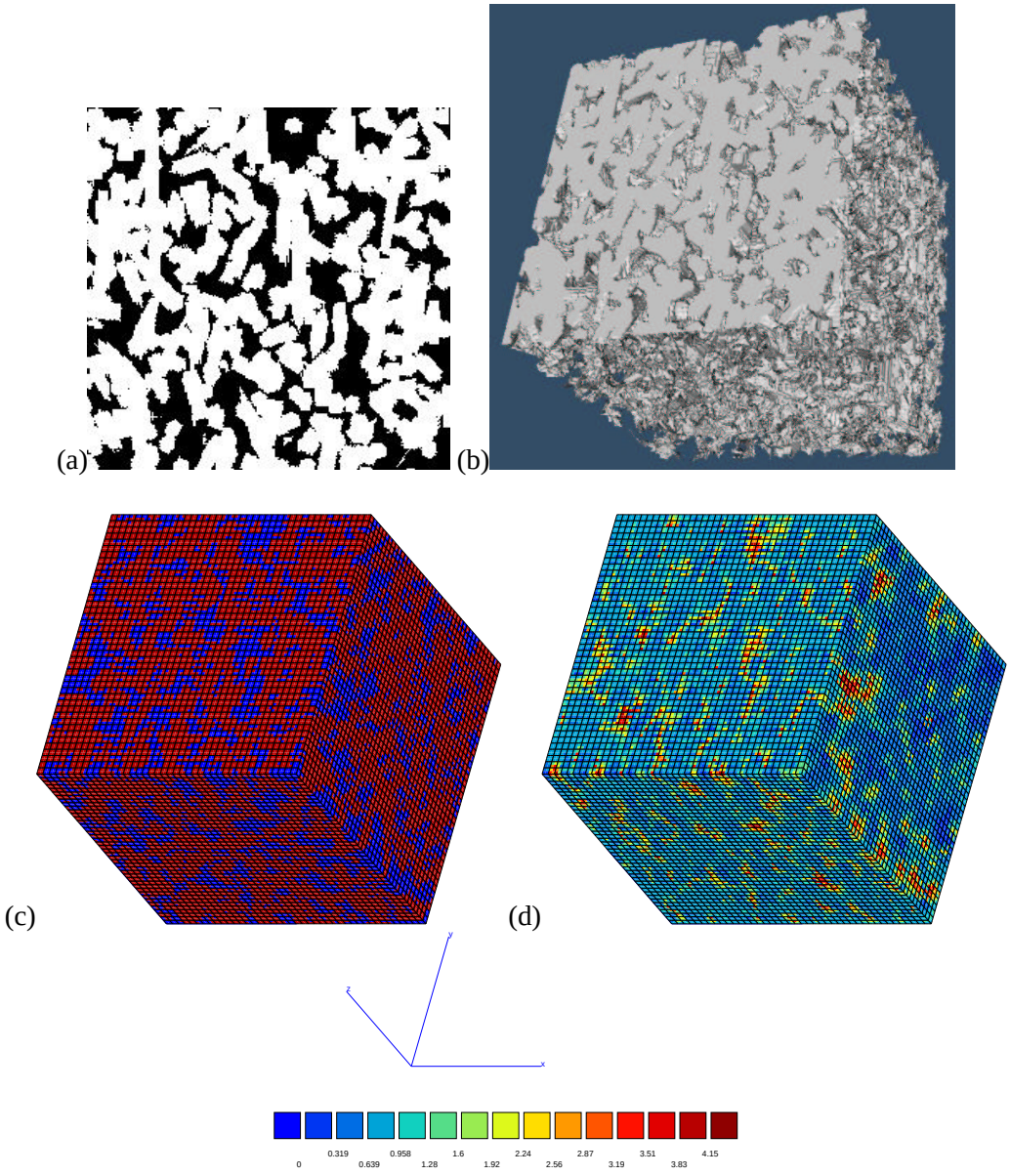

Figure III.5 : Boolean model with 70% of rod hexagons ($R70$). (a) The first section in plane XY, (b) the $3D$ image, (c) finite element mesh and (d) map of equivalent strain ε_{eq} with loading $E_{22} = 1$ under KUBC boundary conditions.

In the table III.2, one finds a comparison of values of the effective elastic properties of the simulated Boolean models and those of the real microstructures. Microstructures with hexagonal rod ($R50$ and $R70$) are more rigid than those with hexagonal plate ($P50$ and $P70$). It can be explained by the fact that the hard phase in the microstructures with rod hexagons is connected more that in the other case because of the geometry of primary grains. The effect is more pronounced for $P_1 = 50\%$.

Microstructure	$R50$	$R70$	$P50$	$P70$	SA_2	SB_1
$\mu\ (MPa)$	253	449	191	439	345	207
$k\ (MPa)$	449	916	333	781	634	334
$E\ (MPa)$	639	1158	481	1109	876	515

Table III.2 : Results of numerical simulations and comparison with samples of real microstructures.

III.4 Conclusions

This chapter contains only rough estimates of the effective properties, without any statistical analysis, for the sake of brievety. Two important conclusions are noted :

- The effective elastic moduli given by hexagonal boolean microstructures are higher than those given by the real materials. This is true for both types (with and without additive).
- The boolean microstructures with rod hexagons are more rigid than with plate hexagons.

This chapter is a step towards the optimization or the design of microstructures. Corresponding process conditions to obtain real microstructures close to these Boolean schemes must be found for practical applications.

Chapter -IV-

GENERAL CONCLUSION

At the end of this work, one important message for the mechanics of heterogeneous media is to abandon the idea of the uniqueness of the size of the Representative Volume Element. Even though a deterministic size of a RVE can be defined as the volume size for which apparent moduli computed with KUBC and SUBC boundary conditions coincide for a given precision, it is possible to consider smaller volume sizes to estimate the effective properties. The fluctuations of apparent properties from sample to sample are then compensated by the use of a sufficient number of realizations of given size.

The effective properties found by this procedure are related directly to several parameters. The average computed on a set of different samples depends on the number of considered samples. This relation can be expressed by a relative precision. Therefore the effective property is related to a minimal number of samples that must be considered to reach a given precision for the mean apparent property. It is clear, as shown numerically, that the minimal number of samples used to have a certain effective property with a given precision is larger when smaller sizes are considered. When the size of samples increases, the required number of samples decreases. The limit case is the deterministic size of the RVE for which one sample is sufficient.

To characterize the dependence of the amplitude of the fluctuation of apparent properties on volume size, we have introduced and extended the notion of *integral range*. The integral range, from the physical view point, is related to the average size of the heterogeneities existing in the studied heterogeneous medium. The simplest case that permits us to understand the physical meaning of the integral range is the case of a morphological property, for instance the volume fraction studied in this work for Voronoï mosaics. The integral range in the case of volume fraction is simply the average size of grains that are distributed randomly among the different phases. Computations with different samples or different realizations leads to an interval of apparent properties. This interval is related to the variance of the results.

It decreases when the sample size increases. This dependence is approximated in this work by a power law. The coefficient in this power law is in general equal to 1 for additive properties like volume fraction and it is only slightly different from 1 for the non-additive physical properties as the elastic moduli and the thermal conductivity studied in this work.

The methodology followed to obtain the effective properties, presented and validated in this work, requires the use of particular boundary conditions. Three types of boundary conditions have been studied for the determination of effective elastic properties : kinematic uniform boundary conditions KUBC, static uniform boundary conditions SUBC and periodic boundary conditions PERIODIC. The three corresponding boundary conditions for the thermal conductivity are : uniform gradient of temperature at the boundary UGT, uniform heat flux at the boundary UHF and periodic boundary conditions PERIODIC. The boundary conditions introduce a *bias* in the estimation of effective properties. The average of apparent properties computed on samples with constant volume are different for the three different boundary conditions. This result is expected because one works with volumes smaller than the deterministic RVE size. The necessary volume to have an average of the apparent properties equal to the effective property is different for each boundary conditions. According to the numerical simulations, the two boundary conditions that use homogeneous fields at the boundary (KUBC and SUBCS) require a size equal to that of the deterministic RVE per definition. All smallest volumes used for these two boundary conditions give some biased averages. In the limit case of very small volumes, the apparent properties coincide with the absolute bounds. The most interesting case is the one of periodic boundary conditions, that gives apparent property averages equal to the effective properties, even when using volumes smaller than the deterministic representative volume. However, for too small volumes, periodic boundary conditions also lead to biased effective properties. It must be noted also that periodic boundary conditions lead in general to higher variances than for the two other conditions. This requires a larger number of simulations to get a given precision for the effective property. The conclusions drawn in the case of elasticity and thermal conductivity are similar.

It is necessary to recall the effect of other parameters that can have an influence on the estimation of the effective properties. The contrast between the properties of constituents of the heterogeneous material acts directly on volumes and number of necessary realizations to estimate the effective properties with a good precision. Indeed, if the contrast is very important, it requires to increase volume sizes and the number of realizations. The volume fractions of constituents also have an important effect. Larger RVE sizes are found for volume fractions around 50% in the case of the studied microstructures.

This study was carried out on a model of random microstructures, that is the Voronoï mosaics. An application of this approach was also made to the case of real microstructures, using three-dimensional real images obtained by confocal microscopy. Our approach allows us to give the effective physical properties for the

real microstructures, and also, what is again very important, to answer the question of the representativity of the used samples. For that purpose, we took two types of materials that have approximatively the same volume fractions of constituents and with two different morphologies. The sizes of used samples are related to the confocal imaging technique. The direct calculation of elastic matrices of the samples reveals an anisotropy in the elastic and thermal properties. It means that the used sizes are not representative since macroscopic samples do not exhibit such anisotropy. Smaller volumes are taken randomly or uniformly out of the available samples for simulation, following the methodology explained for the Voronoï mosaics. One finds the same effect of boundary conditions and the bias found for volumes with small sizes. The size of the deterministic RVE for these microstructures is found to be more important than the size of the used samples. Huet's results for the theory of homogenization with volumes smaller than the deterministic RVE were verified here systematically. Verification is correct for uniform and also random volume decomposition. The numerical simulations are able to distinguish the stiffest microstructure out of the two investigated materials.

Percolation aspects of the hard and soft phase were also studied for the case of the real microstructures as possible explanation in the difference in effective properties. Two types of percolation phenomena are presented here with qualitative and quantitative view points : the geometrical percolation and the percolation of the local fields of strains or stresses. The used methodology is the re-construction of binary images of phases or local field values transformed into binary images, using a threshold operation with a suited value of the threshold. We have defined, to quantify these phenomena, an index of percolation, that is the ratio between the volume of the phase that percolates and the total volume fraction of this phase in the whole heterogeneous material. For the geometrical percolation, one finds that all the phases in the studied samples percolate with a ratio 100% in the two directions (OX and OY) of our sections. It is true for both phases. This allows us to say that the two phases are interconnected or the material is bi-percolated. The index of percolation is very sensitive to the thickness (OZ direction), about one third of the thickness is sufficient to have the complete geometrical percolation at 100%. In general, and always for the geometrical percolation, samples with additive percolate more quickly than samples without additive; this can be explained by the shape of the two phases in the two microstructures. It is true for both phases. The percolation of strain fields can be related to the presence or not of bands of strain localization. This phenomenon deserves further analysis.

A general comparison, concerning the elastic and thermal properties can be drawn between three types of random two-phase materials. The first type is the Voronoï mosaics, that are a model of virtual random distribution. The second type is an example of real microstructures from food industry obtained by confocal microscopy. The last is another virtual model, a boolean model of hexagonal prisms. Two different morphologies are studied : rod-like or plate-like hard phase inclusions.

The comparison is made in particular for the Young's modulus and the thermal conductivity, but can be generalized to other physical properties. The elastic properties and the thermal conductivities of components of these heterogeneous microstructures are the same in the three models. The volume fraction is also the same, which means that the only difference between the three types of microstructures is the morphology of phases. Two volume fractions of the hard phase were compared : 50% and 70%. Results of the comparison are given in figure IV.1.

Because of the strong contrast in properties of phases, the Hashin-Shtrikmann's upper and lower bounds are very far from each other. The self-consistent estimate is given in an interval of volume fraction of the hard phase between 45% and 100%. For virtual microstructures models, the self-consistent model underestimates the effective elastic properties and gives a good estimation of the effective thermal conductivity, and for the real microstructures, it overestimates these effective properties. This difference between the estimation of the self-consistent model and numerical simulation results become more important for volume fractions close to 50%. One finds no direct relation between the relevance of the self-consistent estimate and a specific morphology.

The two virtual microstructures (the Voronoï mosaics and the hexagonal microstructures) give higher effective properties than those given by the real microstructures. It is due to the more elongated shape of grains of the existing hard phase in the virtual models by comparison to the real microstructures. The Voronoï mosaics and the hexagonal microstructures give similar effective properties. A higher stiffness for the hexagonal microstructures with rod-like hard phase is found for volume fractions around 50%.

The present work can be regarded as a first step towards a computational approach of the design of microstructures for wanted overall properties. The aim is to explore new morphologies that can lead to unexpected properties like outstanding stiffness or conductivity, or controlled compliance. Such systematic computations can be a prelude for the experimental development of material processing in order to obtain the wanted properties. As shown in this work, in the case of products from food industry, the computation homogenization approach makes it possible to explore new morphologies that are currently not investigated experimentally, and possibly discover new products.

(a)

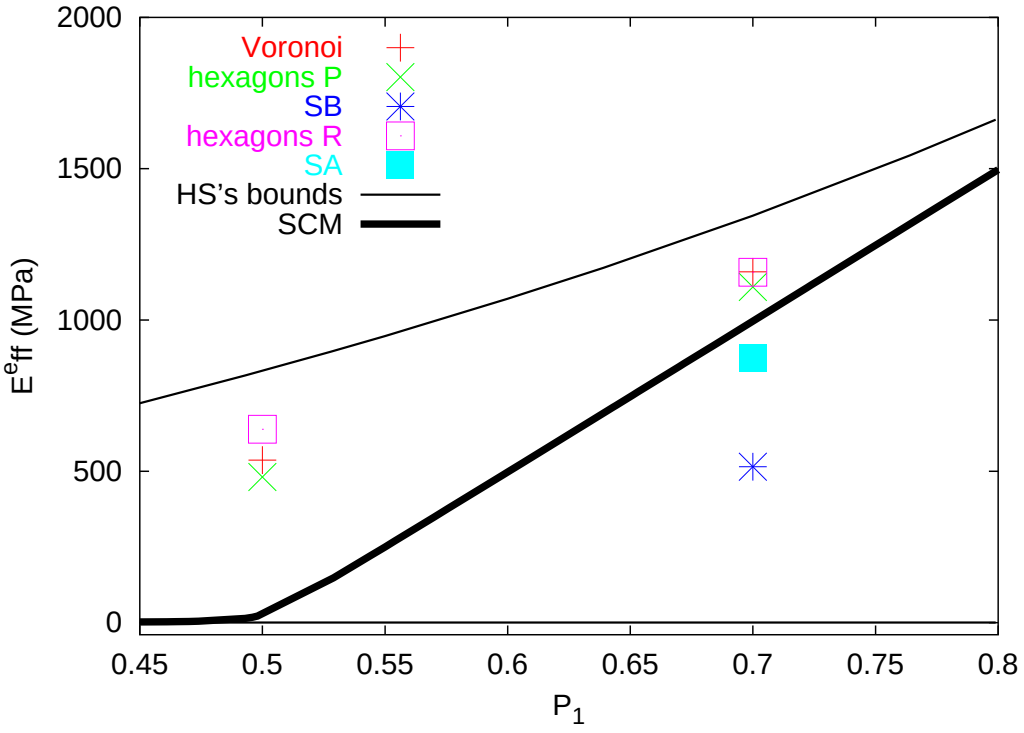

(b)

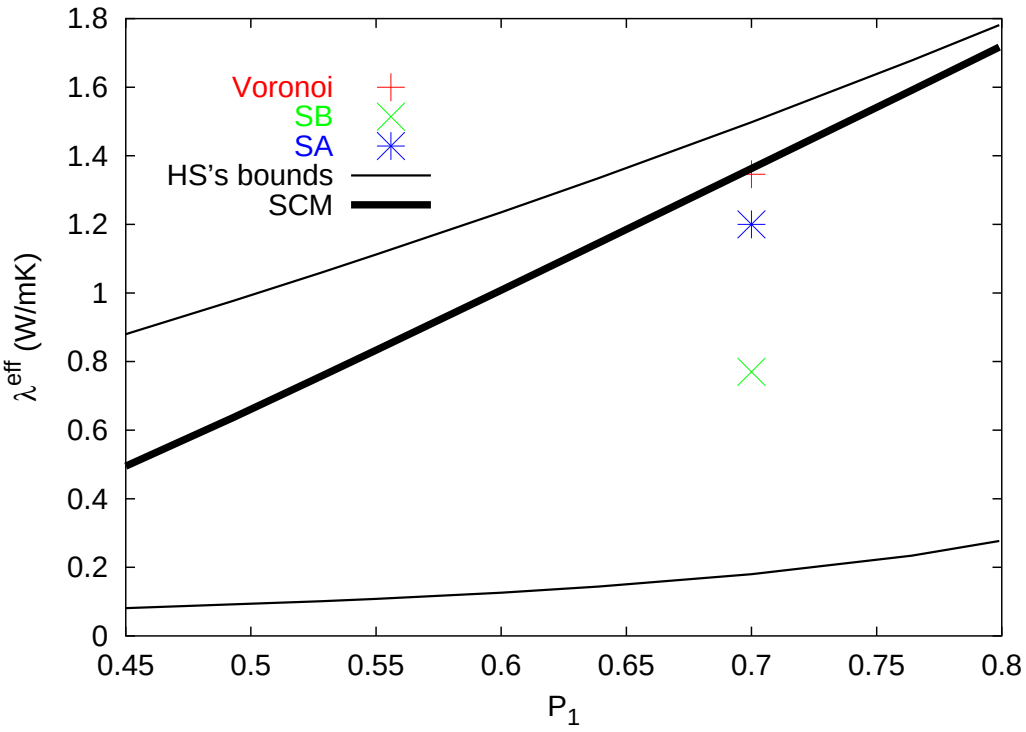

Figure IV.1 : Comparison of effective physical properties of three types of random two-phase elastic materials. (a) Effective Young's modulus and (b) effective thermal conductivity.

Appendix -A-

HUET'S THEOREMS ON THE APPARENT PHYSICAL PROPERTIES OF HETEROGENEOUS SAMPLES SMALLER THAN THE REPRESENTATIVE VOLUME ELEMENT

Contents

The practically important homogenization problem of heterogeneous elastic bodies was first studied in (Huet, 1990) and (Huet, 1991) in the case of samples smaller than the RVE.

It illustrates the relationships between apparent physical properties obtained on a large specimen (not necessarily a RVE) and on a set of smaller ones obtained as a uniform partition of the considered large specimen. It introduces hierarchies between sets of specimens of different sizes, and the absolute bounds where the size of specimens goes to zero, or to that of the RVE.

A.1 First Result

The apparent moduli of a large specimen found by the SUBC boundary conditions are smaller than the ones obtained by the KUBC boundary conditions (equation (A.1)). The apparent compliance tensor of a large specimen found by the KUBC boundary conditions is smaller than once obtained by the SUBC boundary conditions (equation (A.2)).

$$\underset{\sim}{\underset{\sim}{\boldsymbol{C}}}^{app}_{SUBC} \leq \underset{\sim}{\underset{\sim}{\boldsymbol{C}}}^{app}_{KUBC} \tag{A.1}$$

$$\underset{\sim}{\underset{\sim}{\boldsymbol{S}}}^{app}_{KUBC} \leq \underset{\sim}{\underset{\sim}{\boldsymbol{S}}}^{app}_{SUBC} \tag{A.2}$$

where :

$\underset{\sim}{\underset{\sim}{\boldsymbol{C}}}^{app}_{SUBC}$: the apparent modulus tensor of the body obtained with SUBC boundary conditions.
$\underset{\sim}{\underset{\sim}{\boldsymbol{C}}}^{app}_{KUBC}$: the apparent modulus tensor of the body obtained with KUBC boundary conditions.

$\underset{\sim}{\underset{\sim}{\boldsymbol{S}}}^{app}_{KUBC}$: the apparent compliance tensor of the body obtained with KUBC boundary conditions.
$\underset{\sim}{\underset{\sim}{\boldsymbol{S}}}^{app}_{SUBC}$: the apparent compliance tensor of the body obtained with SUBC boundary conditions.

The inequalities hold in the sense of quadratic forms on the space of second order symmetric tensors.

A.2 Second Result

If the used body (large specimen) does not have the size of the RVE, its apparent properties (found in KUBC or SUBC boundary conditions) are bounded on both sides by the results obtained on sets of smaller specimens forming a uniform partition of this body (equations (A.3) and (A.4)) :

$$\overline{\underset{\sim}{\underset{\sim}{\boldsymbol{C}}}^{app}_{SUBC}} \leq \underset{\sim}{\underset{\sim}{\boldsymbol{C}}}^{app}_{SUBC} \leq \underset{\sim}{\underset{\sim}{\boldsymbol{C}}}^{app}_{KUBC} \leq \overline{\underset{\sim}{\underset{\sim}{\boldsymbol{C}}}^{app}_{KUBC}} \tag{A.3}$$

$$\overline{\underset{\sim}{\underset{\sim}{\boldsymbol{S}}}^{app}_{KUBC}} \leq \underset{\sim}{\underset{\sim}{\boldsymbol{S}}}^{app}_{KUBC} \leq \underset{\sim}{\underset{\sim}{\boldsymbol{S}}}^{app}_{SUBC} \leq \overline{\underset{\sim}{\underset{\sim}{\boldsymbol{S}}}^{app}_{SUBC}} \tag{A.4}$$

where :

$\overline{\underset{\sim}{\underset{\sim}{\boldsymbol{C}}^{app}_{SUBC}}}$: the statistical mean value of apparent modulus tensor obtained with SUBC boundary conditions on a partition of V.

$\overline{\underset{\sim}{\underset{\sim}{\boldsymbol{C}}^{app}_{KUBC}}}$: the statistical mean value of apparent modulus tensor obtained with KUBC boundary conditions on the set of smaller specimens.

$\overline{\underset{\sim}{\underset{\sim}{\boldsymbol{S}}^{app}_{KUBC}}}$: the statistical mean value of apparent compliance tensor obtained with KUBC boundary conditions on the set of smaller specimens.

$\overline{\underset{\sim}{\underset{\sim}{\boldsymbol{S}}^{app}_{SUBC}}}$: the statistical mean value of apparent compliance tensor obtained with SUBC boundary conditions on the set of smaller specimens.

A.3 Third Result

Take a representative volume element in the form of a parallelepiped (RVE). Saw it into n parallelepipedic specimens with equal dimensions from one specimen to the others. Perform a series of tests with KUBC on this set of specimens and take the statistical average of the apparent moduli thus obtained. What is obtained is an upper bound for the effective modulus of the considered heterogeneous material.

In addition, take another representative volume element of the same material, with the same external shape and dimensions than the first one. Saw it into n parallelepipedic specimens of the same external shape and dimensions as for the first one. Perform a series of tests with SUBC on this second set of specimens, and take the statistical average of the apparent compliances thus obtained. The reciprocal of this average is a lower bound for the effective modulus of the material under consideration. In other words, the third result is the second one when the large specimen used is a RVE (equations (A.5) and (A.6)). In this case, the effective properties found with both KUBC and SUBC boundary conditions are the same.

That means :

$$\overline{\underset{\sim}{\underset{\sim}{\boldsymbol{C}}^{app}_{SUBC}}} \leq \underset{\sim}{\underset{\sim}{\boldsymbol{C}}^{eff}} \leq \overline{\underset{\sim}{\underset{\sim}{\boldsymbol{C}}^{app}_{KUBC}}} \tag{A.5}$$

$$\overline{\underset{\sim}{\underset{\sim}{\boldsymbol{S}}^{app}_{KUBC}}} \leq \underset{\sim}{\underset{\sim}{\boldsymbol{S}}^{eff}} \leq \overline{\underset{\sim}{\underset{\sim}{\boldsymbol{S}}^{app}_{SUBC}}} \tag{A.6}$$

where :

$\underset{\sim}{\underset{\sim}{\boldsymbol{C}}^{eff}}$: the effective modulus tensor of the representative volume element.

$\underset{\sim}{\underset{\sim}{\boldsymbol{S}}^{eff}}$: the effective compliance tensor of the representative volume element.

A.4 Fourth Result

This result explains the situation of apparent properties found on large specimen (smaller than the RVE) and the set of its uniform partition on the one hand and the corresponding effective properties on the other hand. In words, that means :

- *The apparent elastic properties obtained using the KUBC boundary conditions are bounded on both sides by the effective elastic properties (as lower bound) on the one hand, and the corresponding absolute limit bound which is Voigt's bound (as upper bound), (equation (A.7)).*
- *The apparent elastic properties obtained using the SUBC boundary conditions are bounded on both sides by the effective elastic properties (as upper bound) on the one hand, and the corresponding absolute limit bound which is Reuss's bound (as lower bound), (equation (A.8)).*

$$\underset{\approx}{\boldsymbol{C}}^{eff} \leq \overline{\underset{\approx}{\boldsymbol{C}}^{app}_{KUBC}} \leq \underset{\approx}{\boldsymbol{C}}^{Voigt} \tag{A.7}$$

$$\underset{\approx}{\boldsymbol{C}}^{Reuss} \leq \overline{\underset{\approx}{\boldsymbol{C}}^{app}_{SUBC}} \leq \underset{\approx}{\boldsymbol{C}}^{eff} \tag{A.8}$$

These results are especially useful when the effective properties are known and when dealing with bodies with dimensions smaller than the representative volume.

A.5 Application to Numerical Simulations of Random Materials

The results obtained and proved theoretically by Huet in (Huet, 1990) and (Hazanov and Huet, 1994) are validated numerically in our work. The validation is good in the case of Voronoï mosaïcs and real microstrcutures. These results are also valid for shapes other than the parallelepipedic one. The type of partition is not important; as we have seen in our work, one can use a random partition inside the uniform one but with a sufficiently large number of specimens n. The different realizations of the microstructure can be interpreted as parts of a large volume (in fact a representative one where n is large enough) obtained by gluing the smaller volumes. Huet's theorems can then be applied in a straightforward manner, with KUBC or SUBC boundary conditions used in the small volumes. The results of Huet are also used in (Zohdi et al., 2001) to develop a method to decompose a large-scale micromechanical simulations into a set of computationally smaller problems.

Appendix -B-

PARALLEL COMPUTING

Contents

This appendix presents the main numerical tools of parallel computing used in this work (Farhat and Roux, 1991), (Roux, 1994), (Farhat and Roux, 1994), (Feyel et al., 1997) and (Feyel, 1998).

B.1 Usual Algorithm Limitation

In the Newton algorithm, the step of evaluation of behavior laws is constituted of two loops carrying on elements and points of integration. Its complexity is linear according to the total number of integration points of the structure. It is easy to distribute these calls of routine of integration between several machines, because the treatment is local.

This is not done in the present work because we worked only on linear elasticity.

B.2 Resolution of the Linear System

The linear system $\underset{\sim}{\boldsymbol{K}}\underline{\delta u} = \underline{R}$ has at least as many unknowns as the number of degrees of freedom of the mesh of the structure. Two numerical method classes permit to solve such systems : iterative methods and direct methods.

B.2.1 Iterative Methods

The most used algorithm in this case is the *conjugate gradient*. The cost of storage is weak when one proceeds to the computations element by element. The ratio of convergence depends of the conditioning of the matrix $\underset{\sim}{\boldsymbol{K}}$. The numerical convergence is not ensured necessarily.

B.2.2 Direct Methods

The direct methods are very robust. They have a high cost of computation and more important storage than the iterative methods. The time required for the resolution of a linear system with D degrees of freedom, having a front F, is, for the frontal method :

$$t \propto DF^2 \tag{B.1}$$

Let's consider the mesh of a cube with n^3 elements with 20 nodes. The number of degrees of freedom is :

$$D = 3((1+n)(2n+1)^2 + n(n+1)^2) \propto n^3 \tag{B.2}$$

The minimal front forehead is :

$$F = 3((1+n)(2n+1) + n(n+1) + ...) \propto n^2 \tag{B.3}$$

So :

$$t \propto n^7 \tag{B.4}$$

The time of resolution increases as the seventh power of the decomposition, and the necessary memory as the fifth power. Let's consider a mesh two times thinner in all the directions multiplies the cost of this phase therefore by a factor $2^7 = 128$. These methods are not used in parallel computing.

B.3 Methods of Parallel Resolution of Linear Systems

B.3.1 Conjugate Gradient

In the system $\underline{v} = \underset{\sim}{\boldsymbol{K}}\underline{u}$, lines of the $\underset{\sim}{\boldsymbol{K}}$ matrix are distributed between all available processors. Each processor will achieve the matrix - vector product for lines that it possesses, a global sum operation on all processors permitting to construct $\underline{v}$. One supposes that the non-zero coefficients of each sub-matrix on each processor are, as much that possible, on the diagonal of the complete matrix. Each processor needs then of a limited part of the vector $\underline{u}$.

a) Decomposition into Sub-domains

In the case of two processors, the sub-matrices block by processor are obtained for example, naturally by a regrouping of elements in two sub-domains of the mesh.

The global domain Ω is the union of the non-connected sub-domains Ω_1 and Ω_2 and of the interface Γ_3. If the degrees of freedom are numbered according to this decomposition (numbers 1 to k in Ω_1, $k+1$ to l in Ω_2 and $l+1$ to N in Γ_3), the matrix of rigidity of Ω is decomposable by blocks under the form :

$$[\underset{\sim}{\boldsymbol{K}}] = \begin{pmatrix} K_{11} & 0 & K_{13} \\ 0 & K_{22} & K_{23} \\ K_{13} & K_{23} & K_{33} \end{pmatrix} \tag{B.5}$$

Matrices of rigidity associated to the $\Omega_1 \cup \Gamma_3$ union, and $\Omega_2 \cup \Gamma_3$ can be written as the following way :

$$[\underset{\sim}{\boldsymbol{K}}_1] = \begin{pmatrix} K_{11} & K_{13} \\ K_{13} & K_{33}^1 \end{pmatrix} \tag{B.6}$$

and :

$$[\underset{\sim}{\boldsymbol{K}}_2] = \begin{pmatrix} K_{22} & K_{23} \\ K_{23} & K_{33}^2 \end{pmatrix} \tag{B.7}$$

Terms noted $\underset{\sim}{\boldsymbol{K}}^1_{33}$ and $\underset{\sim}{\boldsymbol{K}}^2_{33}$ are the contributions of each sub-domain to the rigidity of interface and one has :

$$\underset{\sim}{\boldsymbol{K}}_{33} = \underset{\sim}{\boldsymbol{K}}^1_{33} + \underset{\sim}{\boldsymbol{K}}^2_{33} \tag{B.8}$$

The calculation of the $\underset{\sim}{\boldsymbol{K}}\underline{u}$ product on the two sub-domains takes place in two steps :

1. local computation on each sub-domain :

$$\begin{pmatrix} v_1 \\ v_3^1 \end{pmatrix} = \begin{pmatrix} K_{11} & K_{13} \\ K_{13} & K_{33}^1 \end{pmatrix} \begin{pmatrix} u_1 \\ u_3 \end{pmatrix} \tag{B.9}$$

and :

$$\begin{pmatrix} v_2 \\ v_3^2 \end{pmatrix} = \begin{pmatrix} K_{22} & K_{23} \\ K_{23} & K_{33}^2 \end{pmatrix} \begin{pmatrix} u_2 \\ u_3 \end{pmatrix} \tag{B.10}$$

2. assemblage of the product :

$$\underline{v} = \begin{pmatrix} v_1 \\ v_2 \\ v_3^1 + v_3^1 \end{pmatrix} \tag{B.11}$$

The advantage of this decomposition is that if sub-domains are sufficiently large, the first step is major. The second that requires the consignment of contributions v_3^1 of Ω_1 to Ω_2 and *vice-versa*, can be neglected. If sub-domains are reduced to only one element, one recovers the classical conjugate gradient, where the product takes place element by element, follow-up of an assembly. This type of method has been used by Quilici and Débordes (Quilici and Débordes, 1996).

b) Limits of this Algorithm

Advantages of the method of the conjugate gradient, associated to a decomposition into sub-domains, are multiple. In particular, it is very easy to program since it remains a method of classical conjugate gradient. Additional programming is required by the exchange of information to rebuild the product.

Its most serious drawback, that limits its use, is of numerical order. Indeed, for good performances, in terms of convergence speed, the algorithm of the conjugate gradient requires the use of preconditioners.

Unfortunately, the only preconditioners easily parallelisable rest on the incomplete factorizations of matrices of each sub-domain. It is not very efficient when the number of sub-domains increases : the algorithm of the parallel conjugate gradient doesn't ensure the extensibility, its efficiency decreases quickly as the number of sub-domains increases, that forbidden its use on the massively parallel calculators.

B.3.2 Method of the Schur Complement

The method of the Schur complement gives a partial solution to the previous problem.

It means that it is partially possible to factorize, by the Gauss method, the matrix $\underset{\sim}{\boldsymbol{K}}$. This matrix is similar to the matrix :

$$\begin{pmatrix} K_{11} & 0 & 0 \\ 0 & K_{22} & 0 \\ 0 & 0 & S \end{pmatrix} \tag{B.12}$$

with :

$$S = K_{33} - K_{31}K_{11}^{-1}K_{13} - K_{32}K_{22}^{-1}K_{23} \tag{B.13}$$

S is also, symmetrical, definite and positive. It is called matrix of the Schur complement. To solve the linear system :

$$\underset{\sim}{\boldsymbol{K}} \begin{pmatrix} u_1 \\ u_2 \\ u_3 \end{pmatrix} = \begin{pmatrix} v_1 \\ v_2 \\ v_3 \end{pmatrix} \tag{B.14}$$

amounts to the resolution of the system condensed to interfaces :

$$\underset{\sim}{\boldsymbol{S}}\underline{u}_3 = \underline{c}_3 \tag{B.15}$$

with :

$$\underline{c}_3 = \underline{v}_3 - \underset{\sim}{\boldsymbol{K}}_{31}\underset{\sim}{\boldsymbol{K}}_{11}^{-1}\underline{v}_1 - \underset{\sim}{\boldsymbol{K}}_{32}\underset{\sim}{\boldsymbol{K}}_{22}^{-1}\underline{v}_2 \tag{B.16}$$

In the case of many sub-domains, therefore with numerous interfaces, it is not possible to construct explicitly and factorize $\underset{\sim}{\boldsymbol{S}}$ since it would imply, for each degree of freedom, to solve a local problem on each sub-domain. But the previous system can be solved by a method of conjugate gradient that requires products only by $\underset{\sim}{\boldsymbol{S}}$.

Once the matrix $\underset{\sim}{\boldsymbol{S}}$ is decomposed into two terms (contribution of each sub-domain) S^1 and S^2, the products $\underset{\sim}{\boldsymbol{S}}\underline{u}_3$ ($\underline{u}_3$ is defined on the interface) is computed on each sub-domain separately. An operation of sum is sufficient then on the two sub-domains to rebuild the solution. For the first sub-domain for example, two steps are necessary :

1. resolution of the local problem :

$$\underset{\sim}{\boldsymbol{K}}_{11}\underline{u}_1 = -\underset{\sim}{\boldsymbol{K}}_{13}\underline{u}_3 \tag{B.17}$$

which gives :

$$\begin{pmatrix} u_1 \\ u_3 \end{pmatrix} \tag{B.18}$$

2. calculation of the matrix product :

$$\begin{pmatrix} K_{11} & K_{13} \\ K_{13} & K_{33}^1 \end{pmatrix} \begin{pmatrix} u_1 \\ u_3 \end{pmatrix} = \begin{pmatrix} 0 \\ S^1 u_3 \end{pmatrix} \tag{B.19}$$

These two steps only require some local operations to each sub-domain, that one can make therefore in parallel.

Advantages and Limits of the Method of the Schur Complement

The interest of this approach, that consists in solving by conjugate gradient only a problem condensed to interfaces, is that its conditioning is distinctly better that the one of the complete problem (Bjϕrstad and Widlund, 1986). The speed of convergence is increased therefore as much. This method proposes a parallelism to large grains : the time of calculation (necessary to the resolution of the local equilibrium) is larger than the one necessary to exchange messages. Let's add the easiness of the implantation.

There are other efficient preconditioners (Le Tallec, 1994). Their use permits to arrange an optimal method, for which the speed of convergence only depends on the number of sub-domains, and not on their stiffness. For a fixed number of sub-domains this speed is independent of the number of elements that contains each sub-domain.

B.4 The FETI Method

B.4.1 The Dual Schur Method

The FETI method (Finite Element Tearing and Interconnecting (Farhat and Roux, 1991)) is an extension of the dual Schur method, implementing the global mechanism of passage of information. The unknowns of the primal Schur method are displacements of interface, those of dual method are the forces of interface. The residual of the problem is then the jump of displacement to interfaces.

Indeed, to solve the global equilibrium of the structure, that means to invert the linear system :

$$\underset{\sim}{\boldsymbol{K}}\,\underline{q} = \underline{F} \tag{B.20}$$

is equivalent to solve the following problem :

$$\underset{\sim}{\boldsymbol{K}}^i\,\underline{q^i} = \underline{F^i} + \left[\underset{\sim}{\boldsymbol{B^i}}\right]^t \underline{\lambda^i} \tag{B.21}$$

as local equilibrium of each sub-domain Ω_i and :

$$\sum_{i=1}^{N} \underset{\sim}{\boldsymbol{B}}^i\,\underline{q^i} = \underline{0} \tag{B.22}$$

as a continuity of the displacements at the interfaces.

The unknowns are the forces $\underline{\lambda^i}$ at the interfaces. The operators $\left[\underset{\sim}{\boldsymbol{B^i}}\right]^t$ are the operators of local trace signed of each sub-domain (restriction at the interfaces).

The problem in condensed forces at the interfaces can, here again, be solved by an iterative method of conjugate gradient. Each iteration yields then the local linear system resolution :

$$\underset{\sim}{\boldsymbol{K}}^i\,\underline{q^i} = \underline{F^i} + \left[\underset{\sim}{\boldsymbol{B^i}}\right]^t \underline{\lambda^i} \tag{B.23}$$

B.4.2 Coarse Grid Preconditioner

However, it can occur, because of the chosen decomposition, that these local systems are ill-posed. If one sub-domain doesn't contain any portion of outside surface of the global structure where displacement (conditions of Dirichlet) is prescribed, the system is non-invertible.

In practice, it means that some insufficiently fixed sub-domains, loaded only with conditions of Neumann (forces on interfaces), lead to undetermined rigid body motions.

The inversion of such systems requires the calculation of the rigid modes. Indeed, let a matrix $\underset{\sim}{\boldsymbol{A}}$ be symmetrical and non-invertible :

$$\underset{\sim}{\boldsymbol{A}} = \begin{bmatrix} A_{11} & A_{12} \\ A_{21} & A_{22} \end{bmatrix} \tag{B.24}$$

with :

$$dim\ A_{11} = rang\ A = k \tag{B.25}$$

By change of basis associated to the Gauss factorization of $\underset{\sim}{\boldsymbol{A}}$, it comes :

$$\begin{bmatrix} I & 0 \\ -A_{21}A_{11}^{-1} & I \end{bmatrix} \begin{bmatrix} A_{11} & A_{12} \\ A_{21} & A_{22} \end{bmatrix} \begin{bmatrix} I & -A_{11}^{-1}A_{12} \\ 0 & I \end{bmatrix} = \begin{bmatrix} A_{11} & 0 \\ 0 & A_{22} - A_{21}A_{11}^{-1}A_{12} \end{bmatrix} \tag{B.26}$$

Such a transformation doesn't change the rank of $\underset{\sim}{\boldsymbol{A}}$. Consequently, the rank of the right member is equal to the rank of $\underset{\sim}{\boldsymbol{A}}$, and therefore :

$$A_{22} - A_{21}A_{11}^{-1}A_{12} = 0 \tag{B.27}$$

It proves that columns of the following matrix $\underset{\sim}{\boldsymbol{N}}$ form a basis of the kernel of $\underset{\sim}{\boldsymbol{A}}$:

$$\underset{\sim}{\boldsymbol{N}} = \begin{bmatrix} -A_{11}^{-1}A_{12} \\ I \end{bmatrix} \tag{B.28}$$

With these properties, the system :

$$\begin{bmatrix} A_{11} & A_{12} \\ A_{21} & A_{22} \end{bmatrix} \begin{bmatrix} x_1 \\ x_2 \end{bmatrix} = \begin{bmatrix} b_1 \\ b_2 \end{bmatrix} \tag{B.29}$$

can be inverted, while using a pivot of Gauss associated to A_{11} in the following manner :

$$\begin{bmatrix} x_1 \\ x_2 \end{bmatrix} = \begin{bmatrix} A_{11}^{-1} & 0 \\ 0 & 0 \end{bmatrix} \begin{bmatrix} b_1 \\ b_2 \end{bmatrix} + \underset{\sim}{\boldsymbol{N}}\underline{\alpha} \tag{B.30}$$

It means that a solution is the sum of an element of the kernel and the pseudo-solution obtained on the left by product by the pseudo-inverse matrix :

$$\underset{\sim}{\boldsymbol{A}}^{+} = \begin{bmatrix} A_{11}^{-1} & 0 \\ 0 & 0 \end{bmatrix} \tag{B.31}$$

In practice, the decomposition (B.24) is obtained by a complete symmetrical pivot of the matrix during its factorization. The detection of null pivots allows to construct A_{11} and to calculate the columns of $\underset{\sim}{\boldsymbol{N}}$.

While using the previous relations, the system (B.21) and (B.22) can be re-written, by using relations of continuity of $\underline{q^i}$:

$$\underline{q^i} = \underset{\sim}{\boldsymbol{K}}^{\boldsymbol{i}+}(\underline{F^i} + \underset{\sim}{\boldsymbol{B}}^{\boldsymbol{i}t}\underline{\lambda}) + \underset{\sim}{\boldsymbol{N}}_i\underline{\alpha^i} \quad and \quad \underset{\sim}{\boldsymbol{N}}^{\boldsymbol{i}t}(\underline{F^i} + \underset{\sim}{\boldsymbol{B}}^{\boldsymbol{i}t}\underline{\lambda}) = \underline{0} \tag{B.32}$$

$$\sum_{i=1}^{N} \underset{\sim}{\boldsymbol{B}}^i \underset{\sim}{\boldsymbol{K}}^{\boldsymbol{i}+t} \underset{\sim}{\boldsymbol{B}}^i \underline{\lambda} + \sum_{i=1}^{N} \underset{\sim}{\boldsymbol{B}}^i \underset{\sim}{\boldsymbol{N}}^i \underline{\alpha^i} = -\sum_{i=1}^{N} \underset{\sim}{\boldsymbol{B}}^i \underset{\sim}{\boldsymbol{K}}^{\boldsymbol{i}+} \underline{F^i} \tag{B.33}$$

The second equation of (B.32) imposes that the second member : $\underline{F^i} + \underset{\sim}{\boldsymbol{B}}^{\boldsymbol{i}t}\underline{\lambda}$ is in the image of $\underset{\sim}{\boldsymbol{K}}$ (or that it is orthogonal to the kernel, which is equivalent). The last two equations form a hybrid system on $\underline{\lambda}$ and $\underline{\alpha^i}$, that one can summarize by :

$$\begin{bmatrix} \underset{\sim}{\boldsymbol{D}} & \underset{\sim}{\boldsymbol{E}} \\ \underset{\sim}{\boldsymbol{E}}^t & \underset{\sim}{0} \end{bmatrix} \begin{bmatrix} \underline{\lambda} \\ \underline{\alpha} \end{bmatrix} = \begin{bmatrix} \underline{c} \\ \underline{d} \end{bmatrix} \tag{B.34}$$

with :

$$\underset{\sim}{\boldsymbol{D}} \equiv \sum_{i=1}^{N} \underset{\sim}{\boldsymbol{B}}^i \underset{\sim}{\boldsymbol{K}}^{\boldsymbol{i}+t} \underset{\sim}{\boldsymbol{B}}^i \quad and \quad \underset{\sim}{\boldsymbol{E}}\underline{\alpha} = \sum_{i=1}^{N} \underset{\sim}{\boldsymbol{B}}^i \underset{\sim}{\boldsymbol{N}}^i \underline{\alpha^i} \tag{B.35}$$

This system is solved then by using a method of intented conjugate gradient. It is a method of classical conjugate gradient with, in addition, the projection $\underset{\sim}{\boldsymbol{P}}\underline{g}$ of the gradient $\underline{g}$ on the kernel of $\underset{\sim}{\boldsymbol{E}}^t$, in order to impose the constraint :

$$\underset{\sim}{\boldsymbol{E}}^t\underline{\lambda} = \underline{d} \tag{B.36}$$

This projection ensures that directions of research are in the kernel of $\underset{\sim}{\boldsymbol{E}}^t$, that satisfy automatically the constraint (B.36) if $\underline{\lambda}$ has been initialized correctly.

At convergence :

$$\underset{\sim}{\boldsymbol{P}}\underline{g} = \underline{0} \tag{B.37}$$

the gradient $\underline{g}$ is in the image of $\underset{\sim}{\boldsymbol{E}}^t$ and a vector $\underline{\alpha}$ has been found, as :

$$\underline{g} = \underset{\sim}{\boldsymbol{D}}\underline{\lambda} - \underline{c} = -\underset{\sim}{\boldsymbol{E}}\underline{\alpha} \tag{B.38}$$

under the constraint (B.36). The solutions $\underline{\lambda}$ and $\underline{\alpha}$ satisfy the system (B.34) and (B.35).

The only difficulty is the calculation of the operator of projection $\underset{\sim}{\boldsymbol{P}}$. It is about finding a vector $\underline{\alpha}$ such that :

$$\underset{\sim}{\boldsymbol{P}}\underline{g} = \underline{g} + \underset{\sim}{\boldsymbol{E}}\underline{\alpha} \tag{B.39}$$

with :

$$\underset{\sim}{\boldsymbol{E}}^t\underset{\sim}{\boldsymbol{P}}\underline{g} = \underline{0} \tag{B.40}$$

one deduces therefore that :

$$\underset{\sim}{\boldsymbol{P}} = \underset{\sim}{\mathbf{1}} - \underset{\sim}{\boldsymbol{E}}(\underset{\sim}{\boldsymbol{E}}^t\underset{\sim}{\boldsymbol{E}})^{-1}\underset{\sim}{\boldsymbol{E}}^t \tag{B.41}$$

This calculation only requires the product by $\underset{\sim}{\boldsymbol{E}}$ and $\underset{\sim}{\boldsymbol{E}}^t$ as well as the resolution of the hollow linear system :

$$\underset{\sim}{\boldsymbol{E}}^t\underset{\sim}{\boldsymbol{E}}\underline{\alpha} = -\underset{\sim}{\boldsymbol{E}}^t\underline{g} \tag{B.42}$$

Its dimension is at most six times the number of sub-domains. The additional computation cost is therefore small.

This system can be solved in two different ways :

1. by a second method of conjugate overlapped in the first. This approach is easy to implement since it only requires products by $\underset{\sim}{\boldsymbol{E}}^t\underset{\sim}{\boldsymbol{E}}$. It presents the drawback to require, at each iteration of this second level of conjugate gradient, the communication network. In fact, this approach (two levels of overlapped conjugate gradient) is only viable when the used computer architecture associates processors, to the middle performances, to a very fast communication network.

2. to collect the $\underset{\sim}{\boldsymbol{E}}^t\underset{\sim}{\boldsymbol{E}}$ matrix and to use a direct method of linear system resolution. This method presents the only drawback to be more delicate to implement. It has the advantage to be very fast and especially very robust : when the global system $\underset{\sim}{\boldsymbol{K}}\underline{q} = \underline{F}$ to solve is ill-conditioned, the system *"coarse grid"* is also and the classical numerical difficulties of convergence occur at the time of the use of a type of iterative conjugate gradient solver.

This projection has a very good convergence acceleration effect. Indeed, applying the projection amounts to calculate the constants $\underline{\alpha^i}$ by sub-domains, in order to minimize the jump of the complete solution to interfaces.

The FETI method is therefore a method at two levels :

- A local level in each sub-domain, associated to matrices of rigidity $\underset{\sim}{\boldsymbol{K}}_i$.
- A global level coarse grid, associated to the operator of projection. Elements of this grid are sub-domains, and the nodes are values of components of rigid body movement $\underline{\alpha^i}$.

The FETI method is numerically extensible : its speed of convergence doesn't depend on the number of sub-domains, contrary to the method of the primal Schur complement. In practice, for the local problems with constant size (same number of elements), the time of resolution must remain constant if one increases the number of sub-domains and the number of processors at the same time (provided that the cost of calculation of the projection remains negligible). It is well-adapted therefore to the massively parallel calculators. Nevertheless, when the number of sub-domains becomes very large, the cost of calculation of the projection operator becomes non-negligible.

B.4.3 Preconditionning of the FETI Method

The ideal is to calculate directly (by a supplementary local resolution) what is the field of forces at the interfaces that conducted to the observed gradient. One constructs an optimal Dirichlet preconditioner which is *a priori* the best one. Its principal drawback is to be very expensive to calculate since it is necessary to invert a linear system the size of which is that of the local system.

Another non-optimal preconditioner but economical to calculate has been proposed by Farhat and Roux (Farhat and Roux, 1991). This preconditioner is a simple product by the restricted rigidity matrix to interfaces :

$$\underset{\sim}{\boldsymbol{M}} = \sum_{i \in domains} \underset{\sim}{\boldsymbol{B}}^i \underset{\sim}{\boldsymbol{K}}^{i^t} \underset{\sim}{\boldsymbol{B}}^i = \sum_{i \in domains} \underset{\sim}{\boldsymbol{K}}^i_{\Gamma\Gamma} \tag{B.43}$$

where $\underset{\sim}{\boldsymbol{K}}^i_{\Gamma\Gamma}$ denotes the rigidity of interface of the i^{th} sub-domain.

When the number of sub-domains is small (typically lower than 64), the Dirichlet preconditioner is more efficient than the product by rigidity interfaces, but it requires a considerable growth of the cost of the calculation (cost of the iteration multiplied by two).

B.4.4 Initial Reprojection

Let's suppose that the matrix of rigidity, associated to the finite element problem, doesn't change. It is then possible, while preserving directions of descent between two FETI's iterations, to conjugate the gradient and the previous direction of descent on directions calculated initialy. If the second local members $\underline{F^i} + \underline{\lambda^i}$ didn't change, one recovers the previous solution, without iteration.

In general, the second member evolved (modified outside loading), and one doesn't find our solution (the projected gradient is not sufficiently close to zero). This reprojection on the previous descent directions can be seen as the application of a preconditioner. The Newton-Raphson algorithm, used by a large number of nonlinear finite element calculation codes, to a certain number of extensions that differs by the way of calculating the tangent matrix of the problem. The quadratic convergence (optimal convergence speed) is ensured only if the calculation of this matrix is exact. This calculation is however expensive, and in certain cases it is preferable to be satisfied with an approximate tangent matrix. The speed of convergence is then slower, but the time of calculation is better because the cost of each iteration is lower.

In the setting of the use of the FETI method, the modified Newton-Raphson algorithm, in which one doesn't reactualise the tangent matrix, is very interesting : the tangent matrix of the linear system doesn't change, and it is possible to apply the initial preconditioner. This method can lead to a significant gain of the computation time. In contrast when the tangent matrix changes during the calculation, it becomes imperative to reactualize the matrix during the calculation, to preserve a good rate of convergence. It is then possible, in the FETI method, to take in account this reactualization while using a particular initial preconditioner, as Roux shows in the case of nonlinear elasticity (Roux, 1994).

B.4.5 Gains of Memory

The FETI method, like all methods of domain decomposition, can give significant gains of memory. The necessary memory for the resolution of N local linear problems can become smaller than the necessary memory to the treatment of the same problem on one processor. This effect is especially appreciable for three-dimensional calculations, because of the reduction of the local problem front.

B.4.6 FETI Method and Computer Architecture

The FETI method being a method of domain partition, it seems natural to use it on multiprocessors machines. Each processor will have the load of one or several sub-domains. Two types of machines exist now :

- *Shared - Memory* : all processors can address the set of all the random-access memory. Processors can *exchange* between them through the RAM. The program can, in fact be unaffected by this structure of multiprocessor. As the number of processors increases, conflicts of access become more frequent and

the system of management of the memory can become very complex, which make the general performance drop.

- *Distributed - Memory* : each processor possesses its own memory and can communicate with the other through a network of high performance communication. This approach assumes that communication time is low with respect to the days of useful calculation. It is called the coarse-grained parallelism. Problems of the access memory conflict don't exist anymore, but now the programmer must manage himself exchanges of messages while using the dedicated bookstores (PVM or MPI, for example). A local network of workstations is well as a good example of such machines.

It is possible to use computers with shared memory as is well as with distributed memory : to restrict each task to a zone memory data, disconnected of the one allocated to the other tasks, is sufficient.

References

ADAMS D.F. AND DONER D.R. (1967). *Transverse normal loading of a unidirectional composite*. J. Comput. Mat., vol. 1, pp 152.

ADLER P.M., JACQUIN C.G., AND QUIBLIER J.A. (1990). *Flow in simulated porous media*. Int. J. Multiphase Flow, vol. 16, pp 691–712.

ADLER P.M., JACQUIN C.G., AND THOVERT J-F. (1992). *The formation factor of reconstructed model three-dimensional porous media*. Water Resources Res., vol. 28, pp 1571–1576.

BARBE F., DECKER L., JEULIN D., AND CAILLETAUD G. (2001a). *Intergranular and intragranular behavior of polycrystalline aggregates. Part 1 : F.E. model*. Int. J. Plasticity, vol. 17, pp 513–536.

BARBE F., FOREST S., AND CAILLETAUD G. (2001b). *Intergranular and intragranular behavior of polycrystalline aggregates. Part 2 : Results*. Int. J. Plasticity, vol. 17, pp 537–563.

BENDSOE M.P. AND KIKUCHI N. (1988). *Generating optimal topologies in structural design using a homogenization method*. Comput. Methods Appl. Mech. Engrg., vol. 71, pp 197–224.

BENSOUSSAN A., LIONS J.L., AND PAPANICOLAOU G. (1978). *Asymptotic Analysis for Periodic Structures*. North-Holland.

BENTZ D.P. AND MARTYS N.S. (1994). *Hydraulic radius and transport in reconstructed model three-dimensional porous media*. Trans. Porous Media, vol. 17, pp 221–238.

BERAN M. AND MOLYNEUX J. (1966). *Use of classical variational principles to determine bounds for the effective bulk modulus in heterogeneous media*. Q. Appl. Math., vol. 24, pp 107–118.

BERAN M. J. (1968). *Statistical Continuum Theories*. J. Wiley, New York.

BESSON J., CAILLETAUD G., CHABOCHE J. L., AND FOREST S. (2001). *Mécanique non linéaire des matériaux*. Hermès Science.

BJϕRSTAD P. E. AND WIDLUND O. B. (1986). *Iterative methods for the solution of elliptic problems on regions partitioned into sub-structures*. J. Numer. Anal., vol. 23, pp 1097–1120.

BORNERT M., BRETHEAU T., AND GILORMINI P. (2001). *Homogénéisation en mécanique des matériaux.* Hermès.

BOUCHITTE G. AND SUQUET P. (1991). *Homogenization, plasticity and yield design*. Composite Media and Homogenization Theory, pp 107–133.

BOURGAT J.F. (1977). *Numerical experiments of the homogenization method for operators with periodic coefficients*, vol. 704. Springer-Verlag, Berlin.

BROADBENT S.R. AND HAMMERSLEY J.M. (1957). *Percolation processes I. Crystals and mazes*. Proc. Camb. Phil. Soc., vol. 53, pp 629–641.

BROCKENBOROUGH J.R., SURESH S., AND WIENECKE H.A. (1991). *Deformation of metal-matrix composites with continuous fibers : geometrical effects of fiber distribution and shape*. Acta Mater., vol. 39, pp 735–752.

BRON F., REED M., AND JEULIN D. (1999). *Elastic properties of ice creams*. Ecole des Mines de Paris.

BUDIANSKY B. (1965). *On the elastic moduli of some heterogeneous materials*. J. Mech. Phys. Solids, vol. 13, pp 223–227.

CAILLETAUD G., JEULIN D., AND ROLLAND P. (1994). *Size effect on elastic properties of random composites*. Engineering Computations, vol. 11, pp 99–110.

CHRISTENSEN R.M. AND LO K.H. (1979). *Solutions for effective shear properties in three phase sphere and cylinder models*. J. Mech. Phys. Solids, vol. 27, pp 315–330.

COLWORTH UNILEVER RESEARCH (2000). *Unilever Laboratory Progress Report*. Unilever Research Colworth.

COSTER M. AND CHERMANT J. L. (1989). *Précis d'Analyse d'Images*. Presses du CNRS.

DE GENNES P. G. (1976). *La percolation : un concept unificateur*. La Recherche, n° 72, pp 919–927.

DECKER L. AND JEULIN D. (2000). *Simulation 3D de matériaux aléatoires polycristallins*. La Revue de Métallurgie-CIT/Science et Génie des Matériaux, vol. Février 2000, pp 271–275.

DEUTSCHER G. (1987). *Chance and Matter*. J. Souletie, J. Vannimenus and R. Stora, North-Holland.

DEUTSCHER G., ZALLEN R., AND ADLER J. (1983). *Percolation Structures and Processes*. Ann. Israel Phys. Soc. Hilger, London, vol. 5.

DEVRIES F., DUMONTET H., DUVAUT G., AND LÉNÉ F. (1989). *Homogenization and damage for composite structures*. Int. J. Numer. Methods Engrg., vol. 27, pp 285–298.

DOMB C., STOLL E., AND SCHNEIDER T. (1980). *Percolation clusters*. Contemp. Phys., vol. 21, pp 577–592.

DONG M. AND SCHMAUDER S. (1996). *Modelling of Metal Matrix Composites by a Self-Consistent Embedded Cell Model*. Acta Mater., vol. 44 n° 6, pp 2465–2478.

DRUGAN W. J. AND WILLIS J. R. (1996). *A micromechanics-based nonlocal constitutive equations and estimates of representative volume element size for elastic composites*. J. Mech. Phys. Solids, vol. 44, pp 497–524.

EL OUARZAZI Y., FOREST S., JEULIN D., SINGLETON S., AND REED M. (2000). *Elastic behaviour of ice creams*. Ecole des Mines de Paris.

ESSAM J. W. AND BHATTI F. M. (1985). *Series expansion evidence supporting the Alexander-Orbach conjecture in two dimensions*. J. Phys., vol. A 18, pp 3577–3584.

FARHAT C. AND ROUX F. X. (1991). *A method of finite element tearing and interconnecting and its parallel solution algorithm*. Int. J. for Numerical Methods in Engineering, vol. 32, pp 1205–1227.

FARHAT C. AND ROUX F. X. (1994). *Implicit parallel processing in structural mechanics*. Comput. Mech. Adv., vol. 2, pp 47–72.

FEYEL F. (1998). *Application du calcul parallèle aux modèles à grand nombre de variables internes, Thèse de Doctorat*. Ecole des Mines de Paris.

FEYEL F., CAILLETAUD G., KRUCH S., AND ROUX F. X. (1997). *Application du calcul parallèle aux modèles à grand nombre de variables internes*. Colloque national en calcul de structures, May 20-23, Giens, France.

FLANNERY B.P., DECKMAN H.W., ROBERTS W.G., AND DAMICO K.L. (1987). *Three-dimensional X-ray microtomography*. Science, vol. 237, pp 1439.

FOREST S., BARBE F., AND CAILLETAUD G. (2000). *Cosserat modelling of size effects in the mechanical behavior of polycrystals and multi-phase materials*. Int. J. Solids and Str., vol. 37, pp 7105–7126.

FOREST S., CAILLETAUD G., JEULIN D., FEYEL F., GALLIET I., MOUNOURY V., AND QUILICI S. (2002). *Introduction au calcul de microstructures*. Mécanique et Industries, vol. 3, pp 439–456.

GARBOCZI E.J. AND DAY A.R. (1995). *An algorithm for computing the effective linear elastic properties of heterogeneous materials; Three-dimensional results for composites with equal phase Poisson ratios*. J. Mech. Phys. Solids, vol. 43, pp 1349–1362.

GHOSH S. AND MOORTHEY S. (1995). *Elastic-plastic analysis of arbitrary heterogeneous materials with the Voronoi Cell finite element method*. Comput. Methods. Appl. Mech. Engrg., vol. 121, pp 373–409.

GILBERT E. N. (1962). *Random subdivisions of space into crystals*. Ann. Math. Stat., vol. 33, pp 958–972.

GUEDES J.M. AND KIKUCHI N. (1990). *Preprocessing and postprocessing for materials based on the homogenization method with adaptative finite element methods*. Comput. Methods Appl. Mech. Engrg., vol. 83, pp 143–198.

GUSEV A. (1997). *Representative volume element size for elastic composites : a numerical study*. J. Mech. Phys. Solids, vol. 45, pp 1449–1459.

HASHIN Z. (1983). *Analysis of composite materials*. J. Appl. Mech., vol. 50, pp 481–505.

HASHIN Z. AND SHTRIKMAN S. (1963). *A variational approach to the theory of elastic behavior of multiphase materials.* J. Mech. Phys. Solids, vol. 11, pp 127–140.

HAZANOV S. AND HUET C. (1994). *Order relationships for boundary conditions effect in heterogeneous bodies smaller than the representative volume*. J. Mech. Phys. Solids, vol. 42, pp 1995–2011.

HERSHEY A. V. (1954). *The elasticity of an isotropic aggregate of anisotropic cubic crystals*. J. Appl. Mech., vol. 21, pp 236–240.

HILL R. (1952). *The elastic behavior of a crystalline aggregates.* Proc. Phys. Soc. Lond., vol. A65, pp 349–354.

HILL R. (1963). *Elastic properties of reinforced solids: some theoretical principles.* J. Mech. Phys. Solids, vol. 11, pp 357–372.

HILL R. (1965). *A self-consistent mechanics of composite materials*. J. Mech. Phys. Solids, vol. 13, pp 213–222.

HOLLISTER S. J. AND KIKUCHI N. (1994). *Homogenization theory and digital imaging : a basis for studying the mechanics and design principles of bone tissue*. Biotech. Bioengin, vol. 43(7), pp (586–596.

HUET C. (1990). *Application of variational concepts to size effects in elastic heterogeneous bodies*. J. Mech. Phys. Solids, vol. 38, pp 813–841.

HUET C. (1991). *Hierarchies and bounds for size effects in heterogeneous bodies*. Proc. Sixth Symposium on Continuum Moels and Discrete Systems, Dijon, 1989 (ed. G. Maugin), vol. 2, pp 127–134.

JEULIN D. (1981). *Mathematical morphology and multiphase materials*. In : Proc. 3rd European Symposium of Stereology, vol. 3 suppl. 1, pp 265–286. Streol. Iugosl.

JEULIN D. (1987). *Random structure analysis and modelling by mathematical morphology*. Proc. CMDS5, ed. A.J.M., Spencer, Balkema, Rotterdam, pp 217–226.

JEULIN D. (1991). *Modèles morphologiques de structures aléatoires et de changement d'échelles*. Thèse de Doctorat d'Etat, University of Caen.

JEULIN D. (1998). *Bounds of physical properties of some random structure*. Proceeding of the CMDS9 Conference (Istanbul, Turkey, June 29-July 3, 1998), E. Inan & K.Z. Markov (ed), to appear in World Scientific Publishing Company. N-18/98/MM, Ecole des Mines de Paris.

JEULIN D. (2001). *Caractérisation Morphologique et Modèles de Structures Aléatoires, Extrait de : Homogénéisation en mécanique des matériaux (tome1)*. Hermès, France.

JEULIN D. AND OSTOJA-STARZEWSKI M. (2002). *Mechanics of Random and Multiscale Microstructures*. SpringerWientNewYork.

JEULIN D. AND SAVARY L. (1997). *Effective Complex Permitivity of Random Composites*. Journal de Physique I France, section Condensed Matter, pp 1123–1142.

KANIT T., FOREST S., MOUNOURY V., AND JEULIN D. (2002). *Determination of the Representative Volume Element for homogenization of a two-phase random medium*. Conférence Matériaux 2002, de la Conception à la Mise en Oeuvre, 21-25 octobre 2002, Tours, France, pp 92.

KANIT T., FOREST S., MOUNOURY V., AND JEULIN D. (2003a). *Determination of the size of the Representative Volume Element for random composites : statistical and numerical approach*. Int. Journal of Solids and Structures, vol. 40, pp 3647–3679.

KANIT T., FOREST S., MOUNOURY V., AND JEULIN D. (2003b). *Large–scale computations of two–phase microstructures from confocal 3D images : elastic and thermal properties*. manuscript in preparation.

KIRKPATRICK S. (1973). *Percolation and conduction*. Rev. Mod. Phys., vol. 45, pp 574–588.

KOUZNETSOVA V. (2002). *Computational homogenization for the multi-scale analysis of multi-phase materials*. Technische Universiteit Eindhoven.

KRÖNER E. (1958). *Berechnung der elastischen Konstanten des Vielkristalls aus des Konstanten des Einkristalls.* Z. Physik, vol. 151, pp 504–518.

KRÖNER E. (1972). *Statistical Continuum Mechanics*. Springer, Berlin.

KRÖNER E. (1977). *Bounds for effective elastic moduli of disordered materials.* J. Mech. Phys. Solids, vol. 25, pp 137–155.

KRÖNER E. (1980). *Linear properties of random media- The systematic theory*. Comportements rhéologiques et structure des matériaux- CR 15ème Coll. GFR. Paris.

KWIECIEN M.J., MACDONALD I.F., AND DULLIEN F.A.L. (1990). *Three-dimensional reconstruction of porous sandstone from serial section data*. J. Micros, vol. 159, pp 343–359.

LANTUÉJOUL CH. (1991). *Ergodicity and integral range*. Journal of Microscopy, vol. 161, pp 387–403.

LE TALLEC P. (1994). *Domain decomposition methods in computational mechanics*. Computational mechanics advances. North-Holland Publishing Company, vol. 314, pp 7–12.

LELE P., DONG M., SOPPA E., AND SCHMAUDER S. (1998). *Simulation of interpenetrating microstructures by self-consistent matricity models*. Scripta Materialia, vol. 38 n° 9, pp 1327–1332.

LIPPMANN N., STEINKOPF TH., SCHMAUDER S., AND GUMBSCH P. (1997). *3D-finite-element-modelling of microstructures with the method of multiphase elements*. Computational Materials Science, vol. 9, pp 28–35.

MARIGO J.J., MIALON P., MICHEL J.C., AND SUQUET P. (1987). *Plasticité et homogénéisation : un exemple de prévision des charges limites d'une structure périodiquement hétérogène*. J. Méca. Th. Appl., vol. 6, pp 47–75.

MATHERON G. (1968). *Composition des perméabilités en milieu poreux hétérogènes : critique de la règle de pondération géométrique*. Rev. IFP, vol. 23, pp 201–218.

MATHERON G. (1971). *The theory of regionalized variables and its applications*. Paris School of Mines publications.

MATHERON G. (1975). *Random sets and integral geometry*. J. Wiley, New York.

MATHERON G. (1989). *Estimating and Choosing*. Springer-Verlag, Berlin.

MEILLE S. AND GARBOCZI E.J. (2001). *Linear elastic properties of 2-D and 3-D models of porous materials made from elongated objects*. Mod. Sim. Mater. Sci. and Eng., vol. 9, pp 1–20.

MILLER M. (1969). *Bounds for the effective electrical, thermal and magnetic properties of heterogeneous materials*. J. Math. Phys., vol. 10, pp 1988–2004.

MILTON G. (1982). *Bounds on the elastic and transport properties of two component composites*. J. Mech. Phys. Solids, vol. 30, pp 177–191.

MILTON G.W. (1984). *Correlation of the electromagnetic and elastic properties of composites and microgeometries corresponding with effective medium approximations*. In : Physics and Chemistry of porous media, éds. Johnson D.L. and Sen P.N., vol. 3 suppl. 1. AIP.

MILTON G.W. (1985). *The Coherent Potential Approximation is a realizable effective medium scheme*. Commun. Math. Phys., vol. 99, pp 453–500.

MILTON G.W. AND PHAN-THIEN N. (1982). *New bounds on effective elastic moduli of two-component materials*. Proc. Roy. Soc. London, vol. A380, pp 305–331.

MOULINEC H. AND SUQUET P. (1995). *A FFT-based numerical method for computing the mechanical properties of composites from images of their microstructure*. Microstructure-Property Interactions in Composite Materials, pp 235–246.

MOULINEC H. AND SUQUET P. (1997). *A numerical method for computing the overall response of nonlinear composites with complex microstructure*. Comput. Methods Appl. Mech. Engrg., vol. 157, pp 69–94.

NEEDLEMAN A. (1972). *Void growth in an elastic plastic medium*. J. Appl. Mech., vol. 39, pp 964–970.

NEMAT-NASSER S. AND HORI M. (1993). *Micromechanics : Overall Properties of Heterogenous Materials*. North Holland, Amsterdam.

OSTOJA-STARZEWSKI M. (1993). *Micromechanics as a basis of random continuum approximations*. Probabilistic Engineering Mechanics, vol. 8, pp 107–114.

OSTOJA-STARZEWSKI M. (1996). *Bounding of effective thermal conductivities of multiscale materials by essential and natural boundary conditions*. Physical Review, vol. B54, pp 278–285.

OSTOJA-STARZEWSKI M. (1998). *Random field models of heterogeneous materials*. Int. J. Solids Structures, vol. 35 n° 19, pp 2429–2455.

PAUL B. (1960). *Prediction of the elastic constants of multiphase materials*. Trans. Am. Inst. Min. Metall. Petrol Engrs., vol. 218, pp 36–41.

PECULLAN S., GIBIANSKY L. V., AND TORQUATO S. (1998). *Scale effects on the elastic behavior of periodic and hierarchical two-dimensional composites*. J. Mech. Phys. Solids, vol. 47, pp 1509–1542.

PONTE CASTAÑEDA P. AND SUQUET P. (1998). *Nonlinear composites*. Adv. Appl. Mech., vol. 34.

POUTET J., MANZONI D., HAGE-CHEHADE F., JACQUIN C.G., BOUTECA M.J., THOVERT J.F., AND ADLER P.M. (1996). *The effective mechanical properties of random porous media*. J. Mech. Phys. Solids, vol. 44, pp 1587–1620.

POVIRK G. L. (1994). *Incorporation of microstructural information into models of two–phase materials*. Acta metall. mater., vol. 43, pp 3199–3206.

QUIBLIER J.A. (1984). *A new three-dimensional modeling technique for studying porous media*. J. Colloid Interface Sci., vol. 98, pp 84–102.

QUILICI S. AND DÉBORDES O. (1996). *Parallélisation des problèmes d'évolution non linéaires (plateformes SIC)*. Rapport technique, 1996. Synthèse des travaux 93-95, saut technologique. Nouveaux outils de conception et de modélisation en mécanique et discipline associées.

QUILICI S., FOREST S., AND CAILLETAUD G. (1998). *On size effects in torsion of multi- and polycrystalline specimens*. Journal de Physique IV, vol. 8, pp 325–332.

ROBERTS A.P. (1997). *Statistical reconstruction of three-dimensional porous media from two-dimensional images*. Phys. Rev., vol. E56, pp 3203–3212.

ROBERTS A.P. AND GARBOCZI E.J. (1999). *Elastic properties of a tungste–silver composite by reconstruction and computation*. J. Mech. Phys. Solids, vol. 47, pp 2029–2055.

ROBERTS A.P. AND GARBOCZI E.J. (2000). *Elastic Properties of Model Porous Ceramics*. J. Am. Ceram. Soc., vol. 83[12], pp 3041–3048.

ROBERTS A.P. AND GARBOCZI E.J. (2001). *Elastic moduli of model random three-dimensional closed-cell cellular solids*. Acta Mater., vol. 49, pp 189–197.

ROBERTS A.P. AND GARBOCZI E.J. (2002). *Elastic properties of model random three-dimensional open-cell solids*. J. Mech. Phys. Solids, vol. 50, pp 33–55.

ROBERTS A.P. AND KNACKSTEDT M.A. (1995). *Mechanical and transport properties of model foamed solids*. J. Mat. Sci. Lett., vol. 14, pp 1357–1359.

ROBERTS A.P. AND TEUBNER M. (1995). *Transport properties of heterogeneous materials derived from Gaussian random fields : Bounds and simulation*. Phys. Rev., vol. E51, pp 4141–4154.

ROUX F. X. (1994). *Parallel implementation of a domain decomposition method for non-linear elasticity problems*. SIAM.

SAB K. (1992). *On the homogenization and the simulation of random materials*. Eur. J. Mech. Solids, vol. 11, pp 585–607.

SANCHEZ-PALENCIA E. (1974). *Comportement local et macroscopique d'un type de milieux physiques hétérogènes*. Int. J. Engrg. Sci., vol. 12, pp 331–351.

SANCHEZ-PALENCIA E. (1980). *Nonhomogeneous Media and Vibration Theory*. Lecture Notes in Physics, vol. 127.

SANCHEZ-PALENCIA E. AND ZAOUI A. (1987). *Homogenization techniques for composite media*. Lecture Notes in Physics No. 272, Springer, Berlin.

SCHMAUDER S., WEBER U., HOFINGER I., AND NEUBRAND A. (1999). *Modelling the Deformation Behaviour of W/Cu Composites by a Self-Consistent Matricity Model*. Technische Mechanik, Band 19, Heft 4, pp 313–320.

SERRA J. (1982). *Image analysis and mathematical morphology*. Academic Press.

SHANTE V. K. S. AND KIRKPATRICK S. (1971). *An introduction to percolation theory*. Adv. Phys., vol. 20, pp 325–357.

STAUFFER D. (1979). *Scaling theory of percolation clusters*. Phys. Rep., vol. 54, pp 1–74.

STAUFFER D. (1985). *Introduction to Percolation Theory*. Taylor and Francis, London.

SUQUET P. (1983). *Analyse limite et homogénéisation*. C.R. Acad. Sci. Paris, vol. II 296, pp 1355–1358.

SUQUET P. (1997). *Continuum micromechanics*. CISM Courses and Lectures No. 377, Springer Verlag, Berlin.

TERADA K., HORI M., KYOYA T., AND KIKUCHI N. (2000). *Simulation of the multi-scale convergence in computational homogenization approaches*. International Joutnal of Solids and Structures, vol. 37, pp 2285–2311.

TERADA K., ITO T., AND KIKUCHI N. (1998). *Characterization of the mechanical behaviors of solid-fluid mixture by the homogenization method*. Comput. Methods. Appl. Engrg, vol. 153, pp 223–257.

TERADA K., MIURA T., AND KIKUCHI N. (1997). *Digital image-based modeling applied to the homogenization analysis of composite materials*. Comput. Mech., vol. 20, pp 331–346.

THOMPSON J.F., SONI B.K., AND WEATHERILL N.P. (1999). *Handbook of grid generation*. CRC Press.

TORQUATO S. (1991). *Random heterogeneous media: microstructure and improved bounds on effective properties.* Appl. Mech. Rev., vol. 44, pp 37–76.

TORQUATO S. (1998). *Effective stiffness tensor of composite media-II. Application to isotropic dispersions*. J. Mech. Phys. Solids, vol. 46, pp 1411–1440.

TORQUATO S. AND LADO F. (1986). *Effective properties of two phase disordered composite media: ii Evaluation of bounds on the conductivity and bulk modulus of disperions of impenetrable spheres*. Phys. Rev., vol. B33, pp 6428–6434.

TORQUATO S. AND STELL G. (1983). *Microstructure of two-phase random media III. The n-point matrix probability functions for fully penetrable spheres.* J. Chem. Phys., vol. 79, pp 1505.

WALPOLE L. (1966). *On bounds for the overall elastic moduli of inhomogeneous systems*. J. Mech. Phys. Solids, vol. 14, pp 151–162.

WILLIS J.R. (1981). *Variational and Related Methods for the Overall Properties of Composites*. Advances in Applied Mechanics, vol. 21, pp 1–78.

WILLIS J. R. AND TALBOT D. R. S. (1989). *Proc. Sixth Symp. on Contin. Models and Discrete Systems, Dijon, 1989 (Edited by G. Maugin)*, vol. 1. Longman Scientific & Technical, England.

ZALLEN R. (1983). *The Physics of Amorphous Solids*. Wiley, New York.

ZEMAN J. AND SEJNOHA M. (2001). *Numerical evaluation of effective elastic properties of graphite fiber tow impregnated by polymer matrix*. J. Mech. Phys. Solids, vol. 49, pp 69–90.

ZOHDI T.I., WRIGGERS P., AND HUET C. (2001). *A method of substructuring large-scale computational micromechanical problems*. Comput. Methods Appl. Mech. Engrg., vol. 190, pp 5639–5656.